

Extrusion bioprinting of hydrogel scaffolds: printability and mechanical behavior

A Dissertation Submitted to
the College of Graduate and Postdoctoral Studies
in Partial Fulfillment of the Requirements for
the Degree of Doctor of Philosophy in
the Division of Biomedical Engineering
University of Saskatchewan

By
Saman Naghieh

© Copyright Saman Naghieh, December 2020. All rights reserved.

PERMISSION TO USE

In presenting this dissertation in partial fulfillment of the requirements for a postgraduate degree from the University of Saskatchewan, I agree that the Libraries of this University may make it freely available for inspection. I further agree that permission for copying of this dissertation in any manner, in whole or in part, for the scholarly purpose may be granted by Prof. Xiongbiao Chen who supervised my dissertation work, or in their absence, by the Head of the Department or the Dean of the College in which my dissertation work was done. It is understood that any copying or publication or use of this dissertation or part thereof for financial gain shall not be allowed without my written permission. It is also understood that due recognition shall be given to me and to the University of Saskatchewan in any scholarly use which may be made of any material in my dissertation.

Requests for permission to copy or to make other use of the material in this dissertation in whole or part should be addressed to:

College of Graduate and Postdoctoral Studies
116 Thorvaldson Building
110 Science Place
University of Saskatchewan
Saskatoon, Saskatchewan (S7N 5C9)
Canada

OR

Head of the Division of Biomedical Engineering College of Engineering
57 Campus Dr.
University of Saskatchewan
Saskatoon, Saskatchewan (S7N 5A9)
Canada

ABSTRACT

Extrusion bioprinting (known as dispensing-based bioprinting as well) has been widely used to extrude or dispense continuous strands or fibers of biomaterials (e.g. hydrogel) and cells (such a mixture is referred to as "bioink"), layer-by-layer, to form three-dimensional (3D) scaffolds for tissue engineering. For extrusion bioprinting, one key issue is printability or the capability to print and maintain reproducible 3D scaffolds from bioink, which is typically measured by the difference in structure between the designed scaffold and the printed one. Due to the structural difference (or the difference caused by printability), the printed scaffold's mechanical properties are also different from those of the designed scaffold, notably affecting the scaffold performance as applied subsequently to tissue engineering. This dissertation aims to perform a comprehensive study on the printability and mechanical behavior of hydrogel scaffolds fabricated by extrusion bioprinting. The specific objectives are (1) to investigate the influence of design-, bioink-, and printing-related factors on the printability of hydrogel scaffolds, (2) develop an indirect printing technique to improve the printability of low-concentration hydrogels, (3) develop a numerical model representative of the elastic modulus of hydrogel scaffolds by considering the influence of printability, and (4) investigate the effect of crosslinkers on the scaffold's mechanical properties through experimental and numerical approaches.

While studies on printing scaffolds from hydrogel(s) have been conducted, limited knowledge has been documented on hydrogels' printability. Current studies often consider one aspect of studying hydrogel printability (for example, bioink properties solely). The first part of this dissertation studies the multiple dimensions of printability for hydrogel scaffolds, including identifying the influence of hydrogel composition and printing parameters/conditions. Specifically, by using the hydrogels synthesized from alginate, gelatin, and methylcellulose (MC), flow behavior and mechanical properties, as well as their influence on the printability of hydrogels, were investigated. Pore size, strand diameter, and other dimensions of the printed scaffolds were examined; then, pore/ strand/ angular/ printability and irregularity were studied to characterize the printability. The results revealed that the printability could be affected by many factors; among them, the most important are those related to the hydrogel composition and printing parameters.

This chapter also presents a framework to evaluate alginate hydrogel printability systematically, which can be adopted and used in the studies of other hydrogels for bioprinting.

Low-concentration hydrogels have favorable properties for many cell functions in tissue engineering, but they are considerably limited from a scaffold fabrication point of view due to poor 3D printability. The second part of this dissertation is developing an indirect printing method to fabricate scaffolds made from a low-concentration of hydrogels as the second objective. This chapter briefly presents an indirect bioprinting technique to biofabricate scaffolds with low (0.5% w/v) to moderate (3% w/v) concentrations of alginate hydrogel using gelatin as a sacrificial bioink. Indirect-fabricated scaffolds were evaluated using compression, swelling, degradation, biological (primary rat Schwann cells), and morphological assessments. Results indicated that 0.5% alginate scaffolds have steep swelling changes, while 3.0% alginate scaffolds had gradual changes. 0.5% alginate demonstrated better cell viability throughout the study than 3.0% counterparts, though. It was concluded that this indirect bioprinting approach could be extended to other types of hydrogels to improve the printability of low-concentration hydrogels along with the biological performance of cells and avoid high shear stress during direct 3D bioplotting causing cell damage.

One issue involved in 3D bioplotting is achieving the scaffold structure with the desired mechanical properties. To overcome this issue, various numerical methods have been developed to predict scaffolds' mechanical properties, but they are limited by the imperfect representation of scaffolds as fabricated. The third part of this dissertation is developing a numerical model to predict the elastic modulus (one important index of mechanical properties) of scaffolds, considering the penetration or fusion of strands in one layer into the previous layer as the third objective. For this purpose, the finite element method was used for the model development, while medium-viscosity alginate was selected for scaffold fabrication by the 3D bioplotting technique. The elastic modulus of the bioplotted scaffolds was characterized using mechanical testing; the results were compared with those predicted from the developed model, demonstrating a strong congruity amongst them. Our results showed that the penetration, pore size, and the number of printed layers have significant effects on the elastic modulus of bioplotted scaffolds and suggest that the developed model can be used as a powerful tool to modulate the mechanical behavior of bioplotted scaffolds.

For improvement, the fourth part of the dissertation (or the fourth objective) is improving the developed model by considering the crosslinker's effect on the modeling. The use of a cation solution (a crosslinker agent such as CaCl_2) is important for regulating the mechanical properties, but this use has not been well documented in the literature. Here, the effect of varied crosslinking agent volume and crosslinking time on 3D extrusion-based alginate scaffolds' mechanical behavior were evaluated using both experimental and numerical methods. Compression tests were used to measure each scaffold's elastic modulus; then, a finite element model was developed, and a power model was used to predict scaffold mechanical behavior. Results showed that crosslinking time and crosslinker volume both play a decisive role in modulating 3D bioprinted scaffolds' mechanical properties. Because scaffolds' mechanical properties can affect cell response, this study's findings can be implemented to modulate the elastic modulus of scaffolds according to the intended application.

In conclusion, this dissertation presents the development of methods/models to study/represent the printability and mechanical properties of hydrogel scaffolds by using extrusion bioprinting, along with meaningful experimental and model-simulation results. The developed methods/models/results would represent an advance in bioprinting scaffolds for tissue engineering.

ACKNOWLEDGMENTS

I would like to express my deep gratitude to my supervisor, Dr. Xiongbiao Chen, for his valuable guidance, suggestion, advice, and support all through my doctoral study. I am also grateful to my doctoral advisory committee Dr. Ning Zu, Dr. Donald Bergstrom, and Dr. Chris Zhang, for their valuable advice.

The financial support received from the Natural Sciences and Engineering Research Council of Canada (through the research grants to Dr. Chen), as well as the University of Saskatchewan (through the scholarship to me), is appreciably acknowledged.

Most of the experiments in this dissertation were conducted in the Bio-Fabrication Lab at the University of Saskatchewan. Some experiments in Chapter 4 were conducted at the Cameco MS Neuroscience Research Center at the Saskatoon City Hospital. I am grateful to have the privilege to work in this facility. I would particularly like to thank Dr. MD Sarker, for his assistance and technical advice/support. Besides, I am grateful to my colleagues in the Tissue Engineering Research Group, including Dr. Adam D McInnes, Dr. Nitin Sharma, and Dr. Fu You, for their advice, inspiration, and practical assistance.

I am thankful to my parents, Mehdi and Jaleh, for their affection, advice, encouragement, and support all through my Ph.D. program. Mainly, I would like to express my gratitude to my brothers, Payman and Sasan, who always supported me. Finally, yet importantly, I would like to say a special thanks to my wife, Sadra, for her affection, inspiration, support, and assistance during the journey of my Ph.D. program.

TABLE OF CONTENTS

PERMISSION TO USE	i
ABSTRACT.....	ii
ACKNOWLEDGMENTS	v
TABLE OF CONTENTS	vi
LIST OF TABLES	xi
LIST OF FIGURES.....	xii
LIST OF ABBREVIATIONS.....	xvi
Chapter 1 Introduction	1
1.1 Tissue scaffolds and three-dimensional (3D) printing.....	1
1.2 Extrusion-based bioprinting and printability	1
1.2.1 Printability and bioink	4
1.2.2 Printability and fabrication	5
1.2.3 Printability and mechanical behavior of scaffolds.....	5
1.2.4 Printability and the effect of crosslinker	7
1.3 Research aim and objectives	8
1.4 Organization of this dissertation	9
1.5 Contributions of the primary investigator.....	12
1.6 References	12
Chapter 2 Dispensing-Based Bioprinting of Mechanically-Functional Hybrid Scaffolds with Vessel-like Channels for Tissue Engineering Applications - A Brief Review.....	17
2.1 Abstract.....	17
2.2 Introduction	18
2.3 Fabrication of hybrid scaffolds for TE.....	20

2.4 Design of hybrid scaffolds for TE.....	22
2.4.1 Role of imaging techniques and support in the fabrication of custom-made hybrid scaffolds.....	23
2.4.2 Potential biomaterials used in the fabrication of hybrid scaffolds	25
2.5 Physical architecture of hybrid scaffolds.....	29
2.6 Mechanical properties: hybrid scaffolds with tailorable mechanical properties.....	33
2.7 Cell viability and scaffold activation in large hybrid constructs: the role of vessel-like hollow channels/vascular networks	34
2.8 Current challenges and the future of hybrid scaffolds.....	41
2.8.1 3D bioprinting and printability	41
2.8.2 Development of novel biomaterials for improved biological and/or mechanical properties ...	42
2.8.3 Manipulating multiple biomaterials	43
2.8.4 Cell viability and the creation of activated hybrid scaffolds.....	44
2.9 Conclusions	45
2.10 References	46
 Chapter 3 Printability of 3D Printed Hydrogel Scaffolds: Influence of Hydrogel Composition and Printing Parameters.....	 56
3.1 Abstract.....	56
3.2 Introduction	57
3.3 Materials and methods.....	59
3.3.1 Preparation of hydrogels.....	59
3.3.2 Scaffold fabrication	60
3.3.3 Testing hydrogel construct swelling properties.....	60
3.3.4 Testing the compressive strength of the hydrogel constructs.....	61
3.3.5 Testing hydrogel construct degradation properties	61
3.3.6 Flow behavior tests	61
3.3.7 Printability studies on printing parameters and condition	61
3.3.8 Printability evaluation.....	63

3.3.9 Statistical significance.....	64
3.4 Results	64
3.4.1 Mechanical characterization.....	64
3.4.2 Flow behavior results.....	66
3.4.3 Effect of printing parameters on 2D printability.....	67
3.4.4 Effect of printing parameters on 3D printability.....	73
3.5 Discussion	78
3.6 Conclusions	82
3.7 References.....	83
 Chapter 4 Indirect 3D bioprinting and characterization of alginate scaffolds for potential nerve tissue engineering applications	87
4.1 Abstract.....	88
4.2 Introduction	88
4.3 Materials and Methods.....	90
4.3.1 Materials and equipment.....	90
4.3.2 Directly bioprinting of scaffolds and preparation of cell-incorporated bulk gels.....	90
4.3.3 Indirect bioprinting of alginate scaffolds.....	93
4.3.4 Sterilization of scaffolds by ethanol disinfection or UV irradiation	94
4.3.5 Mechanical tests.....	95
4.3.6 Assessment of the swelling and degradation rates	95
4.3.7 Cell viability and morphological assessment.....	96
4.3.8 Statistical analysis	97
4.4 Results and discussion	97
4.4.1 Morphology of scaffolds.....	97
4.4.2 Mechanical properties	100
4.4.3 Swelling properties.....	101
4.4.4 Degradation properties.....	103

4.4.5 Cell viability and circularity assessment	105
4.5 Conclusions	113
4.6 References	114
Chapter 5 Modeling of the Mechanical Behavior of 3D-Bioploted Scaffolds Considering the Penetration in Interlocked Strands	119
5.1 Abstract.....	119
5.2 Introduction	120
5.3 Materials and methods.....	122
5.3.1 Material preparation for fabrication	122
5.3.2 Design and fabrication of scaffolds	123
5.3.3 Image analyzing	124
5.3.4 Mechanical testing.....	124
5.3.5 Finite element modeling	125
5.3.6 Statistical analysis	126
5.4 Results and discussion	126
5.4.1 Model verification.....	126
5.4.2 Some more simulation results.....	129
5.5 Conclusions	135
5.6 References	135
Chapter 6 Influence of crosslinking on the mechanical behavior of 3D printed alginate scaffolds: experimental and numerical approaches	140
6.1 Abstract.....	140
6.2 Introduction	141
6.3 Materials and methods.....	143
6.3.1 Preparation of alginate solution and other required materials	143

6.3.2 Design and fabrication of alginate scaffolds	143
6.3.3 Mechanical testing.....	144
6.3.4 Numerical modeling of the linear/non-linear behavior of 3D bioplotting scaffolds.....	145
6.3.5 Imaging and morphology evaluation	148
6.3.6 Statistical analysis	148
6.4 Results and discussion	148
6.4.1 Effect of the crosslinking time	148
6.4.2 Effect of crosslinker volume.....	149
6.5 Follow-up computational analysis.....	150
6.5.1 Linear elastic finite element model to predict the elastic modulus of scaffolds immediately after printing.....	150
6.5.2 Non-linear numerical model to predict the non-linear behavior of 3D bioplotting scaffolds and bulk gels	153
6.6 Conclusions	155
6.7 References	155
Chapter 7 Conclusions and future recommendations	159
7.1 Conclusions	159
7.2 Recommendations for future research.....	161
Appendix A: Images of Research Competition 2018	163
Appendix B: Images of Research Competition 2019	164

LIST OF TABLES

	Page
Table 2.1. Potential biomaterials and printing parameters used in the biofabrication of hybrid scaffolds.	27
Table 2.2. Physical architecture and mechanical properties of hybrid scaffolds.	30
Table 2.3. Printing parameters and reported cell viability for different kinds of cells.	38
Table 3.1. Viscosity behavior for different groups.	67
Table 3.2. Effect of nozzle speed on strand and pore printability.	71
Table 3.3. 3D printability results for bioplotted scaffolds made from groups 1 to 4 (✕ shows that biomaterials were not printable or a large deviation has been observed).	74
Table 3.4 Linear regression models created based on experimental results reported in Table 3.2.	81
Table 5.1. Printing condition used in scaffold fabrication.	124
Table 5.2. Parameter values used in simulation by the finite element model.	127
Table 6.1. Groups of scaffolds subjected to mechanical testing.	143
Table 6.2. Numerical models predicting the non-linear mechanical behavior of 3D bioplotted alginate gels and scaffolds.	154

-
- Figure 1.1.** Schematic of extrusion bioprinting technique (inset is a cell-incorporated alginate scaffold). 3
- Figure 1.2.** Idealistic and realistic views of printed scaffolds: top views with a) idealistically constant and b) fluctuated strand diameter, side views with c) no overlap among layers and no deflection, d) no overlap and deflection, and e) overlap and deflection. 6
- Figure 2.1.** Schematic of bioprinting techniques a) inkjet-based, b) laser-based, and c) dispensing-based. 19
- Figure 2.2.** Schematic of the fabrication process of a hybrid ear-shaped scaffold by a dispensing-based 3D bioprinting technique including I) conversion of the medical image to a CAD model, II) transformation of the data to the machine code, III) biomaterial and cell source selection, and IV) bioprinting of sacrificial support, auricular cartilage, and fat tissue. 20
- Figure 2.3.** 3D bioprinting of complex structures via sacrificial support for ear regeneration; obtaining CAD model from imaging data, [1 - converting CAD model to STL file, 2- investigation of the accuracy of STL file, 3- defining desired parts for bioprinting with different cells, 4- creation of the CAD model of sacrificial support based on main CAD model, 5- fabrication of porous scaffold via bioprinter]; a representative sample of ear fabricated by a 3D-Bioplotter (CAD model is available at <https://www.thingiverse.com/thing:304657> [42]). 24
- Figure 2.4.** Printing of vascular networks within hybrid scaffolds using: a) hydrogel reservoir, b) coaxial nozzle, c) sacrificial material: I) CAD models of main (hybrid biomaterials) and sacrificial parts, II) final scaffold before removing sacrificial material (inset is the top view during fabrication), III) final hybrid scaffold after removal of the sacrificial material. 37
- Figure 3.1.** The schematic diagram of an extrusion-based 3D bio-printer. 57
- Figure 3.2.** The rates of absorption of samples composed of various biomaterials were indicated by the change in mass of the samples over time. 64

Figure 3.3. The compressive strength of the scaffolds of varying composition over time is shown here. Statistical significance was calculated using a Student's t-test (* was and ** were used to represent $p < 0.05$ and $p < 0.01$, respectively).	65
Figure 3.4. Shear stress as a function of the Shear rate for each solution.	66
Figure 3.5. Effect of printing pressure on D_s for groups 2 and 4, as an illustration.	68
Figure 3.6. Effect of nozzle speed on printability of groups 1 to 3 (pressure: 0.2 bar) and 4 (pressure: 0.1 bar): comparison between D_s and experimental strand diameter (inset images are printed scaffolds for group 2 at different nozzle speeds of 6, 14, 18, and 26 mm/s, as an illustration).	70
Figure 3.7. Effect of offset on the strand diameter of scaffolds made of groups 1 to 4.	72
Figure 3.8. Effect of the angular pattern on printability of scaffolds with acute, right, and obtuse angles.	73
Figure 4.1. 3D biplotting of alginate hydrogels: a) cultivated Schwann cells mixed with alginate hydrogel and then biplotted, b) cell-incorporated alginate scaffold and staining result showing one strand, and c) poor printability of 0.5% alginate printed with a 100- μ m needle and staining result of cell-incorporated gel.	92
Figure 4.2. Indirect biofabrication: a) 3D bioplotter used for the fabrication of gelatin scaffolds, b) gelatin scaffold and bulk gel samples, and c) gelatin scaffold used for indirect biofabrication and a close-up view of this sacrificial framework.	94
Figure 4.3. Indirect biofabrication of alginate scaffolds using sacrificial gelatin [from left to right: 0.5, 1.5, and 3% alginate solutions, sacrificial framework (scale bar 5 mm), and pore of indirect-fabricated scaffold after freeze-drying (scale bar 100 μ m)]: a) impregnated gelatin scaffolds after 18 h refrigeration, b) removing the sacrificial material after 48 h incubation, and c) SEM images of the side view of indirectly fabricated scaffolds with 0.5%, 1.5% (scale bar 500 μ m), and 3% (scale bar 1 mm) alginate concentrations after freeze-drying.	98
Figure 4.4. A comparison of pore size, strand diameter, and sample thickness from sacrificial gelatin scaffolds to samples after a) 18 h of refrigeration and b) subsequent 48 h of incubation. (*) and (~) indicate a significant difference from the original scaffold and the two other sample types, respectively ($p \leq 0.05$, $n = 9$).	99
Figure 4.5. Elastic modulus for different scaffolds (fabricated from 0.5, 1.5, and 3% alginate) for control samples and those sterilized using UV or ethanol (results for all groups are significantly different at $p \leq 0.05$).	101

Figure 4.6. Percent a) swelling over 24 h and b) degradation over 48 h of the three types of alginate scaffolds created using the indirect fabrication technique.	103
Figure 4.7. Progression of degradation for 1.5 and 3.0% alginate scaffolds over 48 h: a) visual observation and b) SEM images of indirect-fabricated scaffolds with 0.5, 1.5, and 3% alginate.	105
Figure 4.8. Fractional cell viability in 0.5, 1.5, and 3% bulk alginate gels over 8 d. Based on ANOVA (general linear model), time, concentration, and their interaction are statistically significant ($p < 0.05$) (top pictures are fluorescence microscope images of the total (left) and dead (right) staining of Schwann cells using Hoechst and PI).	107
Figure 4.9. Fluorescence microscope images of live staining of Schwann cells (scale bar 20 μm) showing live cells: I) 0.5% alginate bulk gel: a) day 1, b) day 4, c) day 8; II) 1.5% alginate scaffold: d) day 1, e) day 4, f) day 8; III) 3% alginate scaffold: g) day 1, h) day 4, i) day 8 (optical images in II and III were captured after fabrication of the cell-incorporated scaffolds; all scale bars are 500 μm).	109
Figure 4.10. Fractional cell viability in each cell-incorporated scaffold after 8 d. Error bars are standard deviation. Based on ANOVA (general linear model), time, concentration, and their interaction are statistically significant ($p < 0.05$).	110
Figure 4.11. Cell circularity on bulk gels and cell-incorporated scaffolds over 8 d.	111
Figure 4.12. Cell circularity of Schwann cells in post-seeded scaffolds over 8 d: a) cell viability for different groups of indirect-fabricated scaffolds and b) optical images from samples from different days indicating the morphology of cells (100 \times magnification).	113
Figure 5.1. Schematic of 3D bioplotting.	121
Figure 5.2. Illustration of printing alginate scaffolds: a) CAD model, b) sliced layers, and c) 3D-Bioplotter used for scaffold printing, with an inserted image showing the alginate scaffold printed in a tissue culture plate.	123
Figure 5.3. a) Applied parameters in finite element model including the amount of penetration within layers (Δ_0), pore size in the X and Z directions (P_x and P_z), E_x and E_z as the extra material exceeding the main borders of the scaffold. Δ_L is also the amount of trimmed value of the upper and lower sides of the modeled scaffolds for applying the compressive load and D is the strand diameter b) applied boundary conditions and meshed part.	126
Figure 5.4. Mesh sensitivity study.	128

Figure 5.5. Effect of penetration within layers on the elastic modulus of alginate scaffolds with a strand diameter of 0.58 mm and a distance of 1 mm between two adjacent strands.	130
Figure 5.6. Effect of pore size on the elastic modulus (pattern fill column bars show experimental results for bioplotted scaffolds with ($P_x, z=0$), ($P_x=470$ and $P_z=390$), and ($P_x=551$ and $P_z=487$)).	131
Figure 5.7. Effect of the number of layers on the elastic modulus (pattern fill column bars show experimental results for bioplotted scaffolds with 16 (24.25 ± 0.64 KPa), 24 (26.85 ± 0.92 KPa), and 31 layers (32.1 ± 0.60 KPa)).	132
Figure 5.8. Effect of a) Δ_0 and N_y , b) Δ_0 and D , c) E_x and E_z , and d) P_z and P_x on the elastic modulus (E.M.).	134
Figure 6.1. a) 3D bioplotted bulk gel, b) first printed layer of the bulk gel, and c) corrected stress-strain curve using corrected zero strain point.	145
Figure 6.2. The model developed to represent the structure of the alginate scaffold fabricated using a 3D bioplotter: penetration within layers (Δ_0), strand diameter (D), pore size in the X (P_x) and Z (P_z) directions, exceeding distance after the last strand in X and Z directions (E_x and E_z), and the amount of deformation at the upper and lower sides of the scaffold (Δ_L).	147
Figure 6.3. Effect of crosslinking time on the elastic modulus of alginate scaffolds immersed in 3 mL of 50 mM CaCl_2 .	149
Figure 6.4. Effect of crosslinking time and crosslinker volume on the elastic modulus of alginate scaffolds immersed in 1 mL or 3 mL of crosslinking agent.	150
Figure 6.5. Morphology of bulk alginate gel (top left) and SEM images of an alginate scaffold immersed in 50 mM CaCl_2 for 24 h.	151
Figure 6.6. a) Stress-strain curves of alginate samples of scaffolds and bulk gels (compressed after 3D bioplotting), b) finite element model: I) applied boundary conditions, II) meshed part, and III) collapsed scaffold after compression.	152

LIST OF ABBREVIATIONS

Abbreviation	Elaboration
Δ_0	Penetration among layers
2D	Two dimensional
3D	Three-dimensional
AM	Additive manufacturing
Ca^{2+}	Calcium ions
CaCl_2	Calcium chloride
CAD	Computer-aided design
COOH^-	Carboxylate ions
DMEM	Dulbecco's modified Eagle's medium
ECM	Extracellular matrix
ECs	Endothelial cells
EDTA	Ethylene-diaminetetraacetic acid
E.M	Elastic modulus
FBS	Fetal bovine serum
FEM	Finite element modeling
HA	Hyaluronic acid
$I_{x,y}$	Irregularity
MC	Methylcellulose
N	Number of strands
Na^+	Sodium ions
Na-Alg	Sodium alginate
NFC	Nanofibrillated cellulose
PBS	Phosphate-buffered saline
PCL	Poly-caprolactone
PEG	Polyethylene glycol
PEI	Polyethyleneimine
PI	Propidium iodide
PNS	Peripheral nervous system
PRSCs	Primary rat Schwann cells
RP	Rapid prototyping
SEM	Scanning electron microscopy
TE	Tissue engineering
UV	Ultraviolet

Chapter 1 Introduction

1.1 Tissue scaffolds and three-dimensional (3D) printing

The unavailability of adequate organs to meet the worldwide increasing demand for transplantation has created an organ shortage crisis on a global scale [1]. In the United States alone, more than 70,000 patients are waiting for organ transplants [2]. In particular, scaffold-based TE aims to develop bio-structures, so-called ‘scaffolds’, to eventually replace, protect, restore or repair damaged tissues such as skin, bladder, trachea, and myocardium after implantation [4–10]. Three-dimensional (3D) printing has been driving significant innovations in TE, enabling the creation of variably complex biocompatible scaffolds that are suitable for transplantation [3]. One of the 3D printing techniques (also known as additive manufacturing (AM)) widely used in TE is extrusion- or dispensing-based bioprinting [11], where a mixture of biomaterials and cells (referred to as bioink) is dispensed or extruded, layer-by-layer, to form a 3D scaffold. Typically, the bioink needs to be crosslinked, a process that promotes solidification of the bioink’s liquid form during or after printing. Depending on their nature, bioinks can be crosslinked physically or chemically. Either way, scaffolds should be printed as designed to resemble the biological and mechanical properties of native tissue; these “biomimetic” scaffolds promote successful and functional tissue regeneration [12,13]. To this end, numerous efforts have been made to fabricate biomimetic scaffolds using extrusion-based bioprinting.

1.2 Extrusion-based bioprinting and printability

One of the AM techniques is extrusion-based bioprinting (Figure 1.1). Using this technique, a mixture of cells and biomaterials can be printed layer by layer. This technique has enabled the manipulation of two or more biomaterials of distinct, yet complementary, mechanical and/or biological properties to form so-called hybrid scaffolds mimicking native tissues. Among various biomaterials, hydrogels synthesized to incorporate living cells and/or biological molecules have dominated due to their hydrated tissue-like environment.

In scaffold extrusion-based bio-fabrication, one of the key issues is discovering significant factors affecting the 3D printability of hydrogel scaffolds used widely in TE. 3D printability of a hydrogel biomaterial is defined as the ability of a hydrogel to form and maintain a reproducible

3D structure with structural integrity. It is an index to measure the difference between the designed and fabricated scaffold. Printability affects the structure of printed scaffolds and, as a result, their mechanical and biological properties. Using the extrusion-based bioprinting technique, live cell-incorporated structures can be fabricated. For this purpose, hydrogels have been widely used due to their cell-friendly environment and high water content. Hydrogels can be cross-linked physically or chemically to facilitate the creation of a bioprinted 3D structure. The cross-linking of hydrogels takes time and, as such, the hydrogel can flow or spread, and thus drift far from the desired design. Due to the poor printability of hydrogels, printed scaffolds may sometimes even collapse and fail to form a 3D structure. The concept of printability is important because the difference between a printed scaffold and the ideal design can impact the mechanical and biological properties, including mechanical strength and cell functions [14–17].

Printability can affect the shape fidelity of bio-fabricated scaffolds made using the extrusion-based technique. Printability is important in the sense that the structure of a scaffold controls the morphology and growth of cells after printing, the cultivation of which is already a challenging issue in TE [18]. Cell-incorporated hydrogels should be deposited as per designs intended to mimic artificial organs or tissues because the printed structure can affect the fate of cells after printing [18]. Poor printability can cause cell damage and result in tissue malfunction. Cell printing studies are also often quite expensive, so determining the correct printing parameters by trial and error is impractical [19]. Finally, yet importantly, printability affects the mechanical behavior of 3D-printed scaffolds.

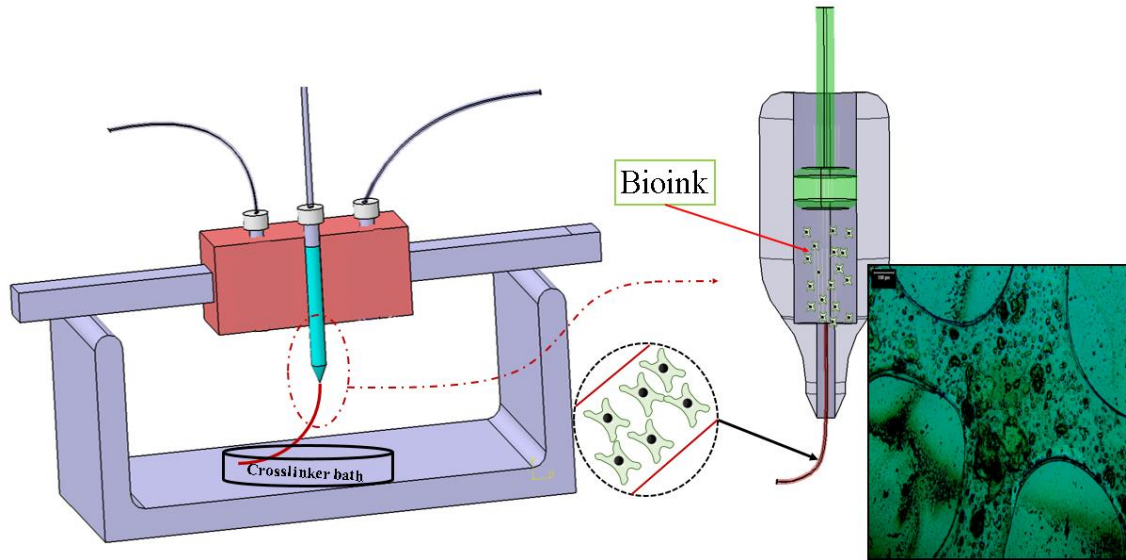


Figure 1.1. Schematic of extrusion bioprinting technique (inset is a cell-incorporated alginate scaffold).

Critical elements affecting printability include design, fabrication, and bioink. From a bioink perspective, two key factors influencing printability are flow behavior and physical properties of bioinks. Design parameters (e.g. pore size, strand diameter, layer thickness) and fabrication parameters (e.g. crosslinking mechanism and printing parameters such as pressure and speed) can influence printability as well. There are numerous studies on printability to investigate the effect of printing parameters, such as pressure and speed. It was reported that air pressure and nozzle speed play the most decisive role in the printability of scaffolds fabricated by the bioplotting technique as a dispensing-based technique [13,15,16]. Besides, the flow behavior of bioinks used for scaffolds biofabrication has thoroughly been studied in different studies [17–19]; recently, a study focused on the effect of loss and storage modulus on the printability of scaffolds [18]. Yet, there is a limited number of studies identifying key elements that play a significant role in printability from a design point of view. Design is a critical element influencing printability due to its effects on filament spacing, filament orientation, and, consequently, the mechanical properties of scaffolds. It may influence cell performance, such as cell seeding and cell proliferation as well, according to multiple sources [20–23]. In the design of scaffolds, different geometries can be achieved by changing the design-related parameters such as the orientation of strands, pore size, and layer thickness. Moreover, while there are many studies on the effect of a single bioink- and fabrication-related elements influencing printability, more in-depth studies are

required to explore the effect of fabrication parameters as well as bioinks for scaffolds made of a composition of biomaterials.

1.2.1 Printability and bioink

One factor affecting the printability is the composition of bioink used for scaffold fabrication, categorized under bioink-related elements. Flow behavior, viscoelasticity, and physical properties are different indexes used to characterize bioinks. Each of these factors can affect printability with positive or negative impacts. Several types of hydrocarbon biomaterials may be used for scaffold construction. Polysaccharide-based hydrogels are used frequently due to their positive effects on cell migration, axonal guidance, and synapse development [29,30]. One of the polysaccharide-based hydrogels that has been used widely in dispensing-based bioprinting is alginate due to its biocompatibility, low toxicity, and relatively high printability [31–33], as a good substrate to incorporate pancreatic islet cells, fibroblasts, myoblasts, and chondrocytes [34]. Sometimes, other types of biomaterials, such as gelatin as another biomaterial, are used with alginate to create hybrid or composite scaffolds. This strategy is implemented to improve the printability, mechanical properties, and biological characteristics of alginate scaffolds. For instance, alginate does not have adhesion sites required for cell attachment, and therefore, creating scaffolds made of alginate and gelatin can be a good solution to improve the biological properties of alginate scaffolds [35]. Gelatin is a collagen derivative that is less expensive relative to pure collagen and lacks the antigenicity of collagen; thus preventing the possibility of immunological response in the host into which it is implanted [36]. Gelatin is used widely to improve the mechanical/biological, as well as printability, of hydrogel scaffolds. Methylcellulose (MC) is another biocompatible hydrocarbon polymer which has shown promise in scaffold design, and its high hydrophilicity has been shown to allow for good water absorption, which is essential for nutrient delivery to the cells [37]. Hydrogels composed of multiple biomaterials have also been used in scaffold construction. For example, one study analyzed the properties of cell substrates composed of a scaffold containing both gelatin and alginate and found these scaffolds to have high water retention rates [38]. This suggests that combining different biomaterials may be a way to manipulate the scaffold characteristics and allow for better control in achieving desired scaffold functions. To this end, using a mixture of biomaterials, printability can be improved. For instance, it was reported that adding gelatin to alginate can improve the printability of alginate scaffolds

[17]. It should be noted that the creation of hybrid or non-hybrid scaffolds is challenging because of printability-related issues.

1.2.2 Printability and fabrication

While modulating the fabrication-, bioink-, and design-related elements is an approach to improve the printability of hydrogel scaffolds, as current research gaps, specifically from a fabrication point of view, there are some novel methods. One of these techniques is indirect bioprinting, which is quite useful for printing low-concentration hydrogels. Low-concentration hydrogel is demandable; for instance, efforts have been made to use soft and low-concentration hydrogels, which can enable the regeneration of neurons by providing an adhesive matrix [28,39]. For another example, Matyash et al. reported the utilization of soft alginate hydrogel with successful results for rat and human neurons [40]. While the mechanical properties of low-concentration hydrogels make them a favorable cellular environment, they are difficult to print into complex scaffolds [41,42]. The limited mechanical and physical stability makes scaffolds prone to collapse and deformation [13,43]. Indirect bioprinting is being explored to overcome these limitations. It involves the use of a sacrificial mold being developed through rapid prototyping (RP, another known term for AM), casting of biomaterial into the mold, and then mold removal to obtain the final construct [44,45]. This opens up the possibility of having a combination of many materials in one scaffold, including bioactive materials, with no worry of cell death caused by printing.

1.2.3 Printability and mechanical behavior of scaffolds

As a result of printability changes, the mechanical behavior of the printed scaffolds is different from the one of the original scaffold design. Beyond the importance of printability, the mechanical behavior of scaffolds should be matched with those of native tissue as discussed in the introduction. The mechanical behavior of scaffolds plays a decisive role in cell viability, and printability can affect the scaffolds' mechanical properties. Hence, performing either numerical or experimental studies to evaluate the mechanical properties of scaffolds is important. As a general fact, scaffolds should satisfy both the biological and mechanical requirements of the targeted tissue. Many researchers have focused on modulating the mechanical properties of scaffolds fabricated by 3D bioplotting technique [46,47]. An experimental study investigated the effect of

geometrical features of scaffolds (including pore size, strand diameter, and orientation of strands) on the mechanical properties of 3D-bioprinted scaffolds [48]. In another study, the mechanical properties of scaffolds were measured, and it was reported that varying geometrical features is an effective way to modulate scaffold mechanical properties [35]. Notably, experimental measurements and the characterization of the mechanical properties of scaffolds are time-consuming, even impractical, once scaffolds are implanted *in vivo*. Accordingly, it is needed to develop alternative methods, like numerical modeling [49], to predict the mechanical properties of scaffolds instead of the use of experimental tests. However, as the printability of bioinks affects the scaffold structure, the fabricated constructs are not always exactly as per design. It means that it is not easy to generate a model for numerical modeling so that it includes all features of a real structure of a scaffold. For instance, as Figure 1.2 shows, there is a fluctuation of strand diameter and deflection, and they are quite often neglected for numerical purposes. Furthermore, there is a penetration/overlap amongst layers, which is not considered for numerical modeling according to the literature [50] (Figure 1.2.e), and this matter will be discussed later on.

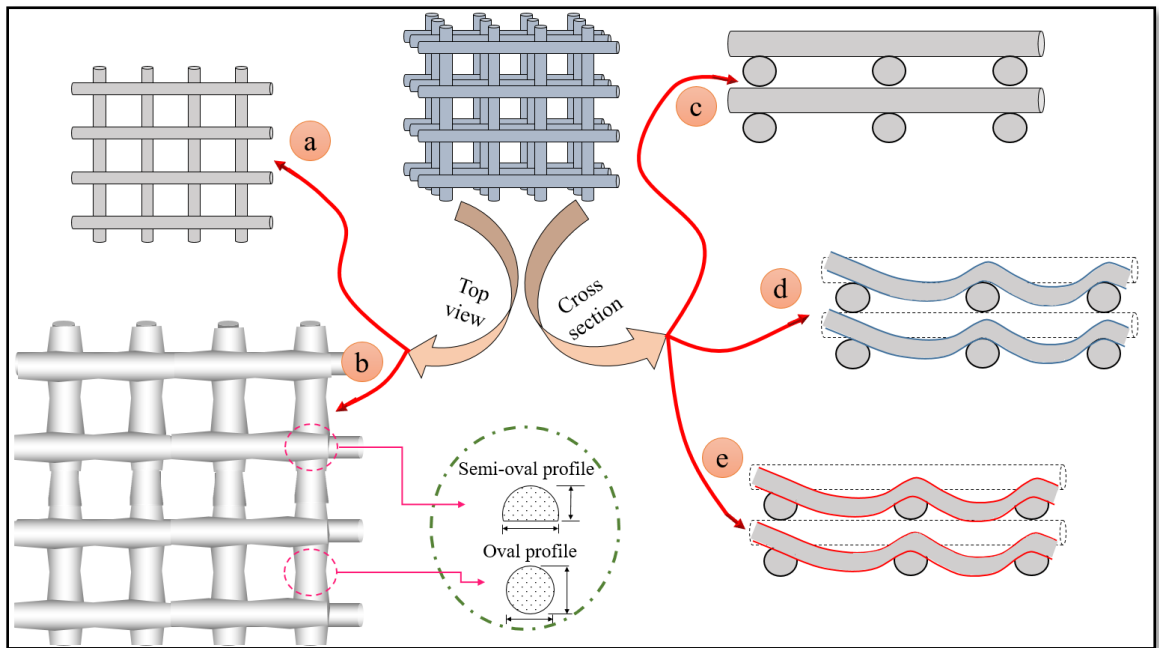


Figure 1.2. Idealistic and realistic views of printed scaffolds: top views with a) idealistically constant and b) fluctuated strand diameter, side views with c) no overlap among layers and no deflection, d) no overlap and deflection, and e) overlap and deflection.

Finite element modeling (FEM) has been introduced as a method to represent the mechanical properties of additive manufactured scaffolds. For instance, a method was reported to predict the mechanical response of scaffolds based on FEM during the cell differentiation at a microscopic level [51]; while in another research, a multi-scale finite element model was introduced to predict cell viability in scaffolds [52]. Particularly, FEM has been used to predict the mechanical behavior of scaffolds fabricated by extrusion-based 3D printers. For example, FEM was used to accurately predict the elastic modulus of scaffolds fabricated by fused deposition modeling, an extrusion-based 3D printing method, with the assistance of an accurate model representing the real structure of printed scaffolds. This model was used to reduce the trial and error, and using that, the elastic modulus of scaffolds was predicted with a good agreement [49]. Although FEM has many benefits, it can be inconvenient due to the complexities in representing the exact structural features of scaffolds fabricated by an AM method [53] due to limitations (i.e. unstable flow in extrusion-based bioprinting) [54]. Another issue is adapting the boundary conditions so that the elastic properties can be estimated using FEM; recently, a review paper has been published in this regard [55]. Specifically, in the extrusion-based 3D printing of hydrogels, one of the important factors that has been neglected in previous studies is the amount of penetration amongst interlocked strands, analogous to a saddle notch, which are printed layer by layer. This penetration may affect the mechanical properties significantly, as its effect has been reported on the mechanical behavior of scaffolds fabricated by another extrusion-based technique, previously [49]. There are limited studies on the effect of crosslinker on the developed numerical models, showing the importance of developing a numerical model to address this matter. Additionally, more studies should focus on how to predict the mechanical properties of hydrogel scaffolds, considering the real structure of scaffolds. It means that the designed model, used for numerical modeling, should be as similar to the real structure of scaffolds. That could happen by considering the penetration amongst layers, the effect of crosslinker, fluctuation of strand diameter, and composition of bioink used for scaffolds fabrication.

1.2.4 Printability and the effect of crosslinker

From a fabrication perspective, the crosslinking mechanism of scaffolds is important. Crosslinking is the procedure to solidify a hydrogel either physically (temperature-sensitive hydrogels such as gelation) or chemically (using a chemical crosslinker such as CaCl_2). However,

little is known about the effect of the crosslinking mechanism on printability. In an extrusion-based system, the cell-hydrogel precursor mixture is extruded layer-by-layer through a nozzle. The extruded hydrogel, such as alginate precursor (will be introduced later on), needs to be gelled quickly to assist the fabrication process and cell survival [24,25]. In this regard, divalent ionic crosslinkers, especially calcium chloride (CaCl_2), have frequently been used to crosslink extruded hydrogel-based bioink because the ions cause rapid gelation; the gelled bioink can have acceptable printability while supporting the viability of any incorporated cells. Two vital factors, which should be taken into account, are the crosslinking and stability of hydrogels after fabrication. Although crosslinking is a good method to improve the printability of hydrogels, it is not reproducible [26]. Several studies were also reported that excessive crosslinking causes a significant reduction in cell viability in biofabrication [27]. Furthermore, the type and concentration of crosslinkers regulate the printing parameters (e.g. dispensing pressure, needle speed) and mechanical properties of a 3D scaffold. There is a correlation between alginate network density, which can be affected by crosslinker type/concentration, and stiffness. Based on published reports, the higher stiffness, the more reduction in permeability of alginate and its subsequent decrease of cell viability and proliferation of neural stem cells encapsulated in alginate [28]. Therefore, using low-concentration crosslinkers is recommended. However, the critical challenge to address is the poor printability of hydrogels using a low-concentration of crosslinker during a printing process. In this regard, the effect of crosslinking time and amount of crosslinking agent have been neglected in the literature, and the concentration of crosslinker has been investigated solely. Accordingly, an appropriate quantity of low-concentration CaCl_2 solution should be taken in the biofabrication process to minimize the depletion effect of Ca^{2+} ions. However, this matter has not been studied until now so that scopes remain unexplored to determine the appropriate volume of CaCl_2 solution mandatory for an extrusion-based system without compromising the mechanical stability of hydrogel scaffolds.

1.3 Research aim and objectives

This dissertation aims to investigate the printability and mechanical behavior of hydrogel scaffolds fabricated by the extrusion bioprinting technique. To do so, the effect of design, bioink, and fabrication parameters on the printability of scaffolds created by the extrusion-based technique

are studied. Moreover, an indirect printing approach is developed to improve the printability of hydrogel scaffolds. Due to the printability-related issues, the mechanical behavior of the printed scaffolds is different from the designed one. Finally, a numerical model, considering the real structure of scaffolds affected by printability, was developed to predict the elastic modulus of scaffolds. The research objectives are:

- To study the printability and mechanical behavior of 3D printed hydrogel scaffolds (alginate, gelatin, and MC), with a focus on identifying the influence of hydrogel composition (e.g. viscosity) and printing parameters/conditions (e.g. crosslinking mechanism) on printability
 - ✓ Examining the flow behavior and mechanical properties, as well as their influence on the printability of hydrogels
 - ✓ Examining the pore size, strand diameter, and other dimensions of the printed scaffolds; and then evaluating their printability in terms of pore/ strand/ angular/ printability and irregularity
 - ✓ Presenting a framework to evaluate alginate hydrogel printability in a systematic manner, which can be adopted and used in the studies of other hydrogels for bioprinting,
- To develop an indirect printing technique to improve the printability of low-concentration hydrogels
 - ✓ Presenting an indirect bioprinting technique to biofabricate scaffolds with low (0.5% w/v) to moderate (3% w/v) concentrations of alginate hydrogel using gelatin as a sacrificial bioink,
 - ✓ Evaluating the indirect-fabricated scaffolds using compression, swelling, degradation, biological (primary rat Schwann cells), and morphological assessments,
- To develop a numerical model to predict the mechanical behavior of scaffolds
 - ✓ Introducing a numerical model to predict the elastic modulus (one important index of mechanical properties) of scaffolds considering the penetration or fusion of strands in one layer into the previous layer,
 - ✓ Validating the developed model using experimental approach (compression test),
- To improve the accuracy of the developed model by considering the effect of crosslinker
 - ✓ Evaluating the effect of varied crosslinking agent volume and crosslinking time on the mechanical behavior of alginate scaffolds experimentally and numerically.

1.4 Organization of this dissertation

This dissertation contains seven chapters, including this one, five chapters adapted from the five manuscripts that have been published, and a conclusion chapter that suggests future research directions.

Chapter 2 presents a brief review of printability as the key issue in extrusion bioprinting. In particular, design-, bioink-, and fabrication-related factors were studied to find significant elements affecting printability. According to the literature, printability can be affected by many factors, including those associated with bioink, printing process, and scaffold design, though far from certain. This chapter highlights the recent development in the discovery of printability for extrusion bioprinting. Key issues and challenges in the printability discovery are also identified and discussed, along with the approaches to improve the printability in extrusion bioprinting. In this review, rheological properties, printing parameters, and printing conditions are investigated systematically to map the relationship between these parameters and printability rather than considering each factor individually. This chapter aims to define printability, identifying factors that can affect it, and proposing methods to measure the 3D printability of hydrogel scaffolds. Here, a systematic study was implemented by characterizing the bioink flow behavior, 2D, and 3D printability of hydrogels with different compositions.

Chapter 3 examines the printability in terms of design, fabrication, and bioink to find significant factors affecting the printability of alginate-based hydrogels. In this chapter, alginate and a mixture of this hydrogel with gelatin and MC were studied. While studies have reportedly printed hydrogel scaffolds from one or more hydrogels, limited knowledge has been documented on the printability of such printing processes. This chapter presents a study on the printability of 3D printed hydrogel scaffolds, with a focus on identifying the influence of hydrogel composition and printing parameters/conditions on the printability. By using the hydrogels synthesized from pure alginate or alginate with gelatin and MC, flow behavior and mechanical properties, as well as their influence on the printability, were examined in this chapter. To characterize the printability, the pore size and strand diameter, and other dimensions of the printed scaffolds were examined; and then printability in terms of pore/strand/angular/printability and irregularity was evaluated. Results revealed that the printability could be affected by many factors; among the most important are those related to the hydrogel composition and printing parameters. This chapter also presents a framework to evaluate alginate hydrogel printability in a systematic manner, which can be adopted and used in the studies of other hydrogels for bioprinting.

Chapter 4 investigates a novel indirect printing technique to address the poor printability of low-concentration hydrogels. The indirect-bioprinting process involved (1) printing a sacrificial framework from gelatin, (2) impregnating the framework with low-concentration alginate, and (3) removing the gelatin framework by an incubation process, and thus forming low-concentration alginate scaffolds. The scaffolds were characterized by compression testing, swelling, degradation, morphological, and biological assessment of incorporated or seeded Schwann cells. Results indicated that scaffolds could be fabricated using the indirect-bioprinting process, wherein the scaffold properties are affected by the concentration of alginate and sterilization technique used. Furthermore, scaffolds showed better cell functionality when fabricated with a lower concentration of alginate compared to a higher concentration. The indirect-bioprinting process explained elaborately in this chapter could be extended to other types of low-concentration hydrogels to address the tradeoffs between printability and mechanical/biological properties for favorable cell functions.

In Chapter 5, the development of a novel numerical model to predict the elastic modulus (one important index of mechanical properties) of 3D bioplotting scaffolds is examined. One issue involved in 3D bioplotting is achieving the scaffold structure with the desired mechanical properties. To overcome this issue, various numerical methods have been developed to predict the mechanical properties of scaffolds, but they are limited by the imperfect representation of one key feature of scaffolds fabricated by 3D bioplotting, i.e., the penetration or fusion of strands in one layer into the previous layer. In this chapter, a finite element method was used for the model development, while medium-viscosity alginate was selected for scaffold fabrication by the 3D bioplotting technique. The elastic modulus of the bioplotting scaffolds was characterized using mechanical testing, and results were compared with those predicted from the developed model, demonstrating a strong congruity between them. Our results showed that the penetration, pore size, and the number of printed layers have significant effects on the elastic modulus of bioplotting scaffolds; and also suggest that the developed model can be used as a powerful tool to modulate the mechanical behavior of bioplotting scaffolds.

Chapter 6 investigates the effect of crosslinkers on the mechanical behavior of 3D printed scaffolds. In particular, this chapter is on the effect of varied crosslinking agent volume and

crosslinking time on the mechanical behavior of 3D bioprinted alginate scaffolds to evaluate scaffolds using both experimental and numerical methods. Compression tests were used to measure the elastic modulus of each scaffold; then, a finite element model was developed, and a power model was used to predict scaffold mechanical behavior. Results showed that crosslinking time and volume of crosslinker both play a decisive role in modulating the mechanical properties of 3D bioprinted scaffolds. Because mechanical properties of scaffolds can affect cell response, the findings of this study can be implemented to modulate the elastic modulus of scaffolds according to the intended application.

In Chapter 7, the developed methods and results obtained from the previous chapters are summarized and, on this basis, conclusions are drawn and highlighted. Moreover, suggestions for future research directions are presented and discussed.

1.5 Contributions of the primary investigator

The published articles included in this dissertation have multiple co-authors. However, the first author, Saman Naghieh, is the primary investigator of the research work as per the mutual understanding of all co-authors. In this dissertation, the co-authors are greatly appreciated and acknowledged for their valuable contributions.

1.6 References

- [1] H. Kang, S.J. Lee, I.K. Ko, C. Kengla, J.J. Yoo, A. Atala, A 3D bioprinting system to produce human-scale tissue constructs with structural integrity, *Nat. Biotechnol.* 34 (2016) 312–319. doi:10.1038/nbt.3413.
- [2] B. Starly, W. Lau, T. Bradbury, W. Sun, Internal architecture design and freeform fabrication of tissue replacement structures, *Comput. Des.* 38 (2006) 115–124.
- [3] S. Naghieh, M. Sarker, M. Izadifar, X. Chen, Dispensing-based bioprinting of mechanically-functional hybrid scaffolds with vessel-like channels for tissue engineering applications – a brief review, *J. Mech. Behav. Biomed. Mater.* 78 (2018) 298–314. doi:10.1016/j.jmbbm.2017.11.037.
- [4] R. Langer, Perspectives and challenges in tissue engineering and regenerative medicine, *Adv. Mater.* 21 (2009) 3235–3236.
- [5] H. Sekine, T. Shimizu, J. Yang, E. Kobayashi, T. Okano, Pulsatile myocardial tubes fabricated with cell sheet engineering, *Circulation.* 114 (2006) 1–87.
- [6] A. Atala, S.B. Bauer, S. Soker, J.J. Yoo, A.B. Retik, Tissue-engineered autologous bladders for

- patients needing cystoplasty, *Lancet*. 367 (2006) 1241–1246.
- [7] G. Matsumura, N. Hibino, Y. Ikada, H. Kurosawa, T. Shin'oka, Successful application of tissue engineered vascular autografts: clinical experience, *Biomaterials*. 24 (2003) 2303–2308.
- [8] N. Boucard, C. Viton, D. Agay, E. Mari, T. Roger, Y. Chancerelle, A. Domard, The use of physical hydrogels of chitosan for skin regeneration following third-degree burns, *Biomaterials*. 28 (2007) 3478–3488.
- [9] P. Macchiarini, P. Jungebluth, T. Go, M.A. Asnaghi, L.E. Rees, T.A. Cogan, A. Dodson, J. Martorell, S. Bellini, P.P. Parnigotto, Clinical transplantation of a tissue-engineered airway, *Lancet*. 372 (2008) 2023–2030.
- [10] S. Cebotari, A. Lichtenberg, I. Tudorache, A. Hilfiker, H. Mertsching, R. Leyh, T. Breyman, K. Kallenbach, L. Maniuc, A. Batrinac, Clinical application of tissue engineered human heart valves using autologous progenitor cells, *Circulation*. 114 (2006) I–132.
- [11] E. Boccardi, I. V. Belova, G.E. Murch, A.R. Boccaccini, T. Fiedler, Oxygen diffusion in marine-derived tissue engineering scaffolds, *J. Mater. Sci. Mater. Med.* 26 (2015) 1–9.
- [12] W. Teo, W. He, S. Ramakrishna, Electrospun scaffold tailored for tissue specific extracellular matrix, *Biotechnol. J.* 1 (2006) 918–929.
- [13] Y. He, F. Yang, H. Zhao, Q. Gao, B. Xia, J. Fu, Research on the printability of hydrogels in 3D bioprinting, *Sci. Rep.* 6 (2016) 29977. doi:10.1038/srep29977.
- [14] J. Göhl, K. Markstedt, A. Mark, K. Håkansson, P. Gatenholm, F. Edelvik, Simulations of 3D bioprinting: predicting bioprintability of nanofibrillar inks, *Biofabrication*. 10 (2018) 34105.
- [15] S. Kyle, S. Kyle, Z.M. Jessop, A. Al-sabah, I.S. Whitaker, 'Printability' of Candidate Biomaterials for Extrusion Based 3D Printing : State-of-the-Art 'Printability' of Candidate Biomaterials for Extrusion Based 3D Printing : State-of-the-Art, *Adv. Healthc. Mater.* (2017). doi:10.1002/adhm.201700264.
- [16] J.E. Trachtenberg, P.M. Mountziaris, J.S. Miller, M. Wettergreen, F.K. Kasper, A.G. Mikos, Open-source three-dimensional printing of biodegradable polymer scaffolds for tissue engineering, *J. Biomed. Mater. Res. Part A*. 102 (2014) 4326–4335.
- [17] L. Ouyang, R. Yao, Y. Zhao, W. Sun, Effect of bioink properties on printability and cell viability for 3D bioplotting of embryonic stem cells, *Biofabrication*. 8 (2016) 35020. doi:10.1088/1758-5090/8/3/035020.
- [18] T. Gao, G.J. Gillispie, J.S. Copus, A.K.P.R. Asari, Y.-J. Seol, A. Atala, J.J. Yoo, S.J.J. Lee, Optimization of gelatin-alginate composite bioink printability using rheological parameters: a systematic approach, *Biofabrication*. (2018).
- [19] J. Park, S.J. Lee, S. Chung, J.H. Lee, W.D. Kim, J.Y. Lee, S.A. Park, Cell-laden 3D bioprinting hydrogel matrix depending on different compositions for soft tissue engineering: characterization and evaluation, *Mater. Sci. Eng. C*. 71 (2017) 678–684.
- [20] A. Gleadall, D. Visscher, J. Yang, D. Thomas, J. Segal, Review of additive manufactured tissue engineering scaffolds: relationship between geometry and performance, *Burn. Trauma*. 6 (2018)

- 19.
- [21] J.M. Sobral, S.G. Caridade, R.A. Sousa, J.F. Mano, R.L. Reis, Three-dimensional plotted scaffolds with controlled pore size gradients: effect of scaffold geometry on mechanical performance and cell seeding efficiency, *Acta Biomater.* 7 (2011) 1009–1018.
- [22] M. Domingos, F. Chiellini, A. Gloria, L. Ambrosio, P. Bartolo, E. Chiellini, Effect of process parameters on the morphological and mechanical properties of 3D bioextruded poly (ϵ -caprolactone) scaffolds, *Rapid Prototyp. J.* 18 (2012) 56–67.
- [23] M. Domingos, F. Intranuovo, T. Russo, R. De Santis, A. Gloria, L. Ambrosio, J. Ciurana, P. Bartolo, The first systematic analysis of 3D rapid prototyped poly (ϵ -caprolactone) scaffolds manufactured through BioCell printing: the effect of pore size and geometry on compressive mechanical behaviour and in vitro hMSC viability, *Biofabrication.* 5 (2013) 45004.
- [24] R. Tripathi, B. Mishra, Development and evaluation of sodium alginate–polyacrylamide graft–copolymer-based stomach targeted hydrogels of famotidine, *AAPS PharmSciTech.* 13 (2012) 1091–1102.
- [25] C.H. Yang, M.X. Wang, H. Haider, J.H. Yang, J.-Y. Sun, Y.M. Chen, J. Zhou, Z. Suo, Strengthening alginate/polyacrylamide hydrogels using various multivalent cations, *ACS Appl. Mater. Interfaces.* 5 (2013) 10418–10422.
- [26] H. Lee, S. Ahn, L.J. Bonassar, G. Kim, Cell (MC3T3-E1)-Printed Poly (ϵ -caprolactone)/Alginate Hybrid Scaffolds for Tissue Regeneration, *Macromol. Rapid Commun.* 34 (2013) 142–149.
- [27] S. Ahn, H. Lee, L.J. Bonassar, G. Kim, Cells (MC3T3-E1)-laden alginate scaffolds fabricated by a modified solid-freeform fabrication process supplemented with an aerosol spraying, *Biomacromolecules.* 13 (2012) 2997–3003.
- [28] A. Banerjee, M. Arha, S. Choudhary, R.S. Ashton, S.R. Bhatia, D. V Schaffer, R.S. Kane, The influence of hydrogel modulus on the proliferation and differentiation of encapsulated neural stem cells, *Biomaterials.* 30 (2009) 4695–4699.
- [29] R. Frischknecht, C.I. Seidenbecher, The crosstalk of hyaluronan-based extracellular matrix and synapses, *Neuron Glia Biol.* 4 (2008) 249–257.
- [30] C. Rhiner, M.O. Hengartner, Sugar antennae for guidance signals: syndecans and glypicans integrate directional cues for navigating neurons, *Sci. World J.* 6 (2006) 1024–1036.
- [31] T. Andersen, P. Auk-Emblem, M. Dornish, 3D cell culture in alginate hydrogels, *Microarrays.* 4 (2015) 133–161.
- [32] S.H. Ahn, H.J. Lee, J.-S. Lee, H. Yoon, W. Chun, G.H. Kim, A novel cell-printing method and its application to hepatogenic differentiation of human adipose stem cell-embedded mesh structures, *Sci. Rep.* 5 (2015) 13427.
- [33] R.A. Perez, M. Kim, T.-H. Kim, J.-H. Kim, J.H. Lee, J.-H. Park, J.C. Knowles, H.-W. Kim, Utilizing core–shell fibrous collagen-alginate hydrogel cell delivery system for bone tissue engineering, *Tissue Eng. Part A.* 20 (2013) 103–114.
- [34] S.P.M. Bohari, D.W.L. Hukins, L.M. Grover, Effect of calcium alginate concentration on viability

- and proliferation of encapsulated fibroblasts, *Biomed. Mater. Eng.* 21 (2011) 159–170. doi:10.3233/BME-2011-0665.
- [35] F. You, X. Wu, X. Chen, 3D Printing of Porous Alginate/gelatin Hydrogel Scaffolds and Their Mechanical Property Characterization, *J. Int. J. Polym. Mater. Polym. Biomater.* 66 (2016) 299–306. doi:10.1080/00914037.2016.1201830.
- [36] A. Ito, A. Mase, Y. Takizawa, M. Shinkai, H. Honda, K.-I. Hata, M. Ueda, T. Kobayashi, Transglutaminase-mediated gelatin matrices incorporating cell adhesion factors as a biomaterial for tissue engineering, *J. Biosci. Bioeng.* 95 (2003) 196–199. doi:10.1263/jbb.95.196.
- [37] C. Ivanov, M. Popa, M. Ivanov, A.A. Popa, Synthesis of poly (vinyl alcohol) - methyl cellulose hydrogel as possible scaffolds in tissue engineering, *J. Optoelectron. Adv. Mater.* 9 (2007) 3440–3444.
- [38] T. Pan, W. Song, X. Cao, Y. Wang, 3D bioplotting of gelatin/alginate scaffolds for tissue engineering: influence of crosslinking degree and pore architecture on physicochemical properties, *J. Mater. Sci. Technol.* 32 (2016) 889–900.
- [39] E.K. Purcell, A. Singh, D.R. Kipke, Alginate composition effects on a neural stem cell–seeded scaffold, *Tissue Eng. Part C Methods.* 15 (2009) 541–550.
- [40] M. Matyash, F. Despang, R. Mandal, D. Fiore, M. Gelinsky, C. Ikonomidou, Novel Soft Alginate Hydrogel Strongly Supports Neurite Growth and Protects Neurons Against Oxidative Stress, *Tissue Eng. Part A.* 18 (2012) 55–66. doi:10.1089/ten.tea.2011.0097.
- [41] Y. Luo, A. Lode, A.R. Akkineni, M. Gelinsky, Concentrated gelatin/alginate composites for fabrication of predesigned scaffolds with a favorable cell response by 3D plotting, *RSC Adv.* 5 (2015) 43480–43488. doi:10.1039/C5RA04308E.
- [42] T. Pan, W. Song, X. Cao, Y. Wang, 3D Bioplotting of Gelatin/Alginate Scaffolds for Tissue Engineering: Influence of Crosslinking Degree and Pore Architecture on Physicochemical Properties, *J. Mater. Sci. Technol.* 32 (2016) 889–900. doi:10.1016/j.jmst.2016.01.007.
- [43] B.P. Chan, K.W. Leong, Scaffolding in tissue engineering: general approaches and tissue-specific considerations, *Eur. Spine J.* 17 (2008) 467–479.
- [44] C. De Maria, A. De Acutis, G. Vozzi, Chapter 8 – Indirect Rapid Prototyping for Tissue Engineering, *Essentials 3D Biofabrication Transl.* (2015) 153–164. doi:10.1016/B978-0-12-800972-7.00008-6.
- [45] A. Houben, J. Van Hoorick, J. Van Erps, H. Thienpont, S. Van Vlierberghe, P. Dubruel, Indirect Rapid Prototyping: Opening Up Unprecedented Opportunities in Scaffold Design and Applications, *Ann. Biomed. Eng.* 45 (2017) 58–83. doi:10.1007/s10439-016-1610-x.
- [46] L.G. Bracaglia, B.T. Smith, E. Watson, N. Arumugasaamy, A.G. Mikos, J.P. Fisher, 3D printing for the design and fabrication of polymer-based gradient scaffolds, *Acta Biomater.* (2017).
- [47] S. Gómez, M.D. Vlad, J. López, E. Fernández, Design and properties of 3D scaffolds for bone tissue engineering, *Acta Biomater.* 42 (2016) 341–350.
- [48] A.D. Olubamiji, Z. Izadifar, J.L. Si, D.M.L. Cooper, B.F. Eames, D.X. Chen, Modulating mechanical behaviour of 3D-printed cartilage-mimetic PCL scaffolds: influence of molecular weight and pore

- geometry, *Biofabrication*. 8 (2016) 025020. doi:10.1088/1758-5090/8/2/025020.
- [49] S. Naghieh, M.R.R. Karamooz Ravari, M. Badrossamay, E. Foroozmehr, M. Kadkhodaei, Numerical investigation of the mechanical properties of the additive manufactured bone scaffolds fabricated by FDM: the effect of layer penetration and post-heating, *J. Mech. Behav. Biomed. Mater.* 59 (2016) 241–250. doi:10.1016/j.jmbbm.2016.01.031.
- [50] S. Naghieh, M. Sarker, M. Karamooz-Ravari, A. McInnes, X. Chen, Modeling of the Mechanical Behavior of 3D Bioprinted Scaffolds Considering the Penetration in Interlocked Strands, *Appl. Sci.* 8 (2018) 1422. doi:10.3390/APP8091422.
- [51] N. Sahai, T. Jain, S. Kumar, P.K. Dutta, Development and Selection of Porous Scaffolds Using Computer-Aided Tissue Engineering, in: *Chitin Chitosan Regen. Med.*, Springer, 2016: pp. 351–388.
- [52] M. Elsaadany, K.C. Yan, E. Yildirim-Ayan, Predicting cell viability within tissue scaffolds under equiaxial strain: multi-scale finite element model of collagen–cardiomyocytes constructs, *Biomech. Model. Mechanobiol.* (2017) 1–15.
- [53] X.-Y. Zhang, G. Fang, J. Zhou, Additively Manufactured Scaffolds for Bone Tissue Engineering and the Prediction of their Mechanical Behavior: A Review, *Materials (Basel)*. 10 (2017) 50. doi:10.3390/ma10010050.
- [54] T. Jin, I. Stanciulescu, Numerical investigation of the influence of pattern topology on the mechanical behavior of PEGDA hydrogels, *Acta Biomater.* 49 (2017) 247–259.
- [55] A. Adessina, J.-F. Barthélémy, F. Lavergne, A. Ben Fraj, Effective elastic properties of materials with inclusions of complex structure, *Int. J. Eng. Sci.* 119 (2017) 1–15.

Chapter 2 Dispensing-Based Bioprinting of Mechanically-Functional Hybrid Scaffolds with Vessel-like Channels for Tissue Engineering Applications - A Brief Review

This chapter has been published as “Saman Naghieh, MD Sarker, Mohammad Izadifar, and Xiongbiao Chen, Dispensing-Based Bioprinting of Mechanically-Functional Hybrid Scaffolds with Vessel-like Channels for Tissue Engineering Applications - A Brief Review, Journal of the Mechanical Behavior of Biomedical Materials, 2018, DOI: <https://doi.org/10.1016/j.jmbbm.2017.11.037>, <https://www.youtube.com/watch?v=s8usVlz7AYs&t=63s>.” According to the Copyright Agreement, "the authors retain the right to include the journal article, in full or in part, in a thesis or dissertation."

(All the literature review was conducted by me. MD Sarker and Mohammad Izadifar helped me in preparing Tables and Figures. Professor Xiongbiao Chen guided and supervised the whole review work.)

2.1 Abstract

Over the past decades, significant progress has been achieved in the field of TE to restore/repair damaged tissues or organs and, in this regard, scaffolds made from biomaterials have played a critical role. Notably, recent advances in biomaterials and 3D printing have enabled the manipulation of two or more biomaterials of distinct, yet complementary, mechanical and/or biological properties to form so-called hybrid scaffolds mimicking native tissues. Among various biomaterials, hydrogels synthesized to incorporate living cells and/or biological molecules have dominated due to their hydrated tissue-like environment. Moreover, dispensing-based bioprinting has evolved to the point that it can now be used to create hybrid scaffolds with complex structures. However, the complexities associated with multi-material bioprinting and synthesis of hydrogels used for hybrid scaffolds pose many challenges for their fabrication. This paper presents a brief review of dispensing-based bioprinting of hybrid scaffolds for TE applications. The focus is on the design and fabrication of hybrid scaffolds, including imaging techniques, potential biomaterials, physical architecture, mechanical properties, cell viability, and the importance of

vessel-like channels. The key issues and challenges for dispensing-based bioprinting of hybrid scaffolds are also identified and discussed along with recommendations for future research directions. Addressing these issues will significantly enhance the design and fabrication of hybrid scaffolds to and pave the way for translating them into clinical applications.

2.2 Introduction

The paucity of adequate organs to meet the increasing demand for organ transplantation has created a global organ shortage crisis [1]. TE has emerged as a promising approach to regenerate human tissues and organs; and one TE strategy is to develop constructs or scaffolds for replacing/repairing damaged tissues. Driving significant innovations in TE, 3D printing (Figure 2.1) has enabled the creation of 3D scaffolds with a wide range of complexities. Different from conventional methods such as electrospinning [2], freeze-drying, gas foaming [3], and particle or porogen leaching [4], AM techniques allow for precise control layer-by-layer to create 3D scaffolds [5]. Among these three techniques, dispensing-based bioprinting offers many attractive features. It is less expensive than inkjet- and laser-based printings and operationally more flexible with respect to printing multiple materials and cell types. Over the last decade, dispensing-based technique has created new opportunities to achieve the goal of complex organ printing, where the cells are incorporated by means of hydrogels [6–12].

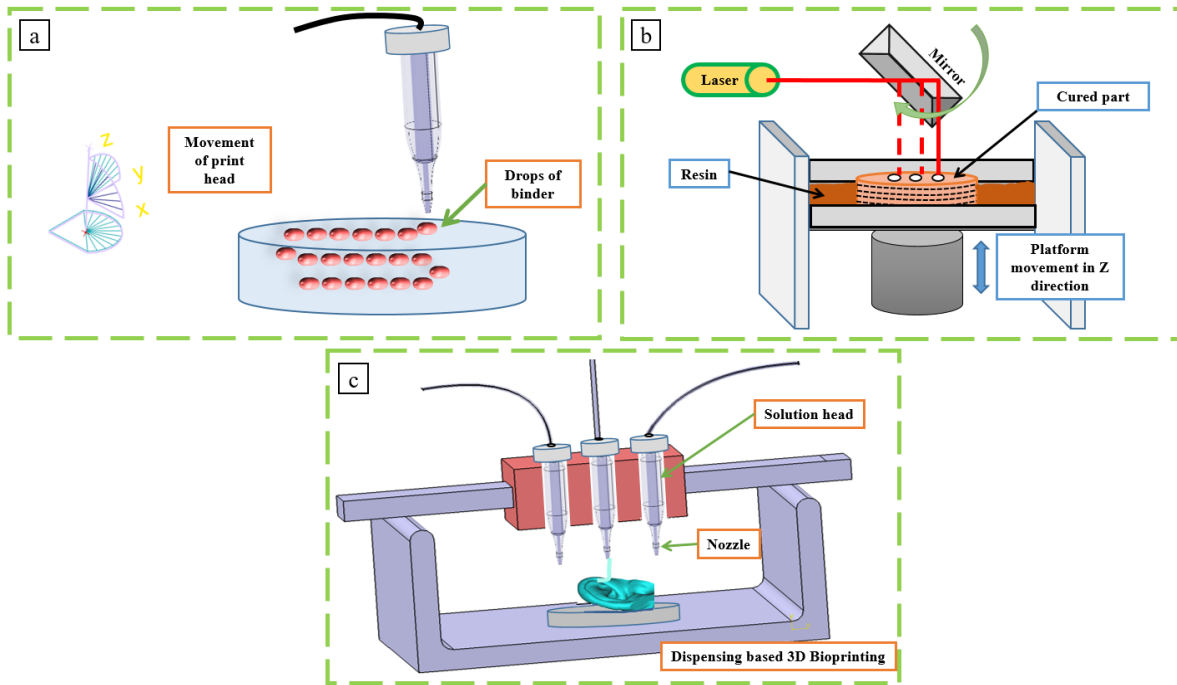


Figure 2.1. Schematic of bioprinting techniques a) inkjet-based, b) laser-based, and c) dispensing-based.

Although hydrogels provide an appropriate environment for cells due to their high water content, they have poor mechanical properties. Thus, hydrogels at higher concentrations have been used to improve printing fidelity but this results in insufficient in-growth of new tissue [13]. On the other hand, other components, such as some synthetic polymers, can provide the required mechanical properties but, in the majority of cases, are not biologically compatible [14]. Thus, researchers have combined synthetic/natural hydrogel polymers to improve the mechanical stability of cell-incorporated constructs. These constructs fabricated by combining two or more biomaterials to achieve synergistic biological and mechanical properties are called hybrid scaffolds in this paper.

This paper aims to review recent developments with respect to the design and fabrication of hybrid scaffolds based on dispensing-based bioprinting. In this regard, imaging techniques, potential biomaterials, physical architecture, and mechanical properties of hybrid scaffolds are discussed. The importance of vessel-like hollow channels/vascular networks and cell viability, as current challenges in TE, is then highlighted. Finally, the current limitations of 3D bioprinting and future directions for the development of hybrid scaffolds are discussed.

2.3 Fabrication of hybrid scaffolds for TE

Figure 2.2 shows the procedure for the fabrication of hybrid scaffolds, which involves capturing the imaging data from the patient, generating a computer-aided design (CAD) model, selecting biomaterials and sources, and fabricating the hybrid scaffold. To fabricate hybrid scaffolds, a mixture of materials can be printed layer-by-layer or multiple layers of various materials can be combined; in some cases, sacrificial supports are also utilized. Hence, issues including poor mechanical/biological properties of hydrogels can be addressed by combining cell-laden hydrogels with stiffer natural/synthetic polymers in addition to crosslinkers.

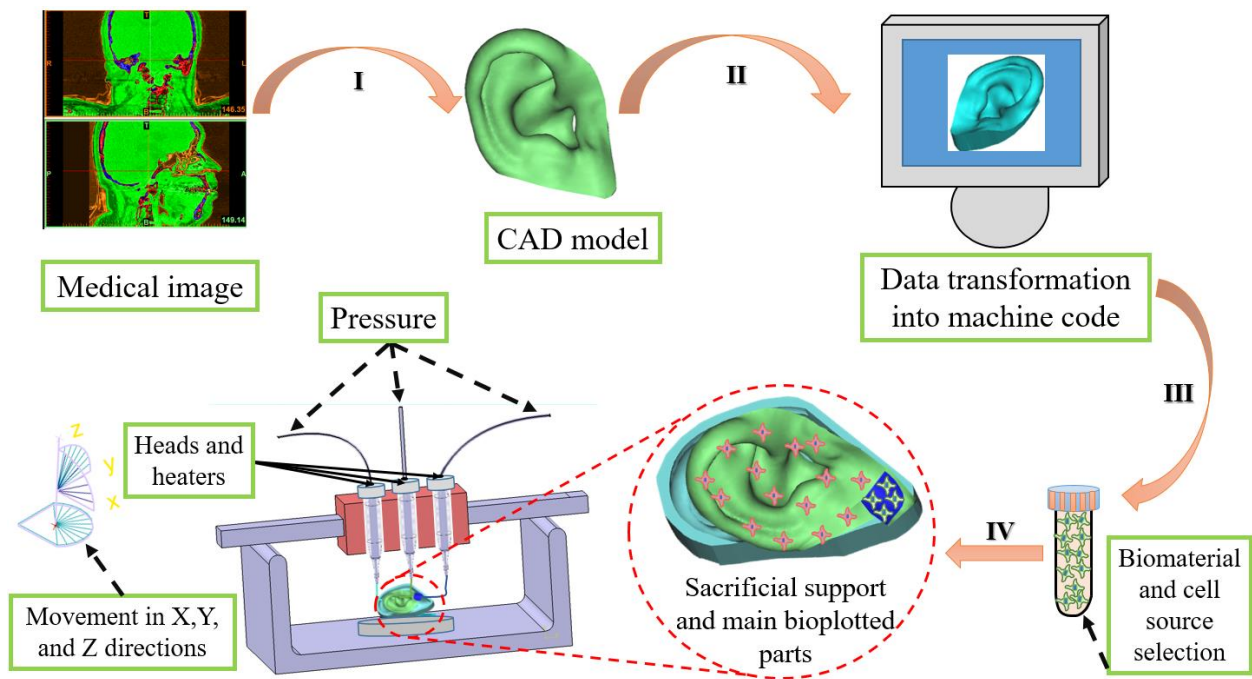


Figure 2.2. Schematic of the fabrication process of a hybrid ear-shaped scaffold by a dispensing-based 3D bioprinting technique including I) conversion of the medical image to a CAD model, II) transformation of the data to the machine code, III) biomaterial and cell source selection, and IV) bioprinting of sacrificial support, auricular cartilage, and fat tissue.

Conventional methods have been used to prepare hybrid scaffolds in which hydrogels were incorporated into the scaffold by perfusion, but inadequate reproducibility and heterogeneous cell positioning limit the application of them [14]. Dispensing-based 3D bioprinting can effectively overcome such limitations. For instance, poly-caprolactone (PCL) and cell-laden alginate hydrogels have been printed using a multi-head tissue/organ building system [15]. Using other

methods, hybrid scaffolds were fabricated by combining 3D cell printing and electrospinning techniques [16,17] or acellular scaffolds using electrospinning and 3D printing together [18,19].

Depositing biomaterials accurately is the key to mimicking the heterogeneous structures of native tissues. One challenge for both AM and conventional methods used to fabricate hybrid scaffolds is manipulating two or more biomaterials. A common method to manipulate multiple biomaterials is to use multiple dispensers, each depositing one biomaterial [20]; this approach has been widely used to create hybrid scaffolds [21,22]. The critical issue of this approach is to control the biomaterials accurately to be deposited as per the CAD model. In other words, the problem associated with this method is the inability to simultaneously and accurately deposit biomaterials/cells. The other possibility for the deposition of multiple biomaterials is to print a mixture of biomaterials, such as a mixture of alginate and gelatin [23]. Simple mixing of various biomaterials/cells and fabricating scaffolds is one of the techniques used to create composite structures and *in situ*-forming hydrogel scaffolds [24,25]. However, accurate control over the deposition of biomaterials/cells is a challenge of this method. To tackle this issue, researchers have leaned towards other techniques such as coaxial nozzle-assisted 3D bioprinting to print biomaterials simultaneously [26] and, particularly, to create vessel-like channels, as will be discussed in subsequent sections.

Because hybrid scaffold fabrication requires the handling of multiple biomaterials with different rheological properties, fabrication conditions might need to be rigorously determined and selected. In the dispensing-based technique, continuous and uniform printing of strands is associated with the moving speed of the needle, which is determined by [27]:

$$V = \frac{4Q}{\pi D^2} \quad (2.1)$$

where V , Q , and D are the moving speed, the flow rate of the dispensed biomaterial, and needle inner diameter, respectively.

Notably, the flow rate of the biomaterial dispensed is a function of operational parameters (e.g., pressure, temperature), the flow behavior of the biomaterial (e.g., viscosity, consistency, flow behavior indexes), and geometric parameters (e.g., needle diameter, length), as given by [28]:

$$Q = \pi \frac{r_i^3 r_o^3}{4} \left[\frac{3n \tan \theta \left(\Delta P + \frac{2\tau_y}{\tan \theta \ln \frac{r_i}{r_o}} \right)}{2K (r_i^{3n} - r_o^{3n})} \right]^{\frac{1}{n}} \quad (2.2)$$

This equation is for a tapered needle, where P is the applied pressure, r_i and r_o are the entrance and exit radius of the needle, respectively, and θ is the angle between needle and deposition surface. Moreover, τ_y , n , and K are the yield stress, flow index, and consistency index, respectively. Note that n and K are associated with temperature and θ is related to the length of the needle.

Hence, the manipulation of biomaterials used to fabricate hybrid scaffolds is quite challenging. For example, different fabrication parameters have been considered for printing PCL/alginate hybrid scaffolds [15,29]. Generally, a low driving force is needed for hydrogels due to their low viscosity. Furthermore, precise force control is required to print cell-laden hydrogels and arrange cells precisely at high resolution. On the other hand, dispensing materials such as PCL require a higher temperature and driving force. Thus, adequate cooling is required during the printing process of successive layers of hybrid scaffolds to overcome heat-induced cell damage in cell-laden hydrogels.

In addition to the problems associated with manipulating biomaterials in a dispensing-based bioprinting system, liquid polymers are required prior to fabrication. Natural and synthetic polymers require different conditions (e.g., temperature, solvent) to be dissolved and they also need specific conditions (e.g., low temperature, light, crosslinkers, pH) to be crosslinked [30]. Therefore, a key challenge in the fabrication of hybrid scaffolds is to manipulate multiple materials with different dissolution and crosslinking or gelation properties. Furthermore, more challenges arise to attach successive printed layers with different biomaterials and when it is required to meet specific fabrication parameters (e.g., extrusion pressure, speed, temperature, type of crosslinker) to achieve printability with geometric precision.

2.4 Design of hybrid scaffolds for TE

The first step regarding the design of a customized hybrid scaffold could be the creation of a CAD model using medical images (Figure 2.2). This step plays a decisive role in the biofabrication process with respect to the accuracy of the fabricated scaffold. Biochemical, as well

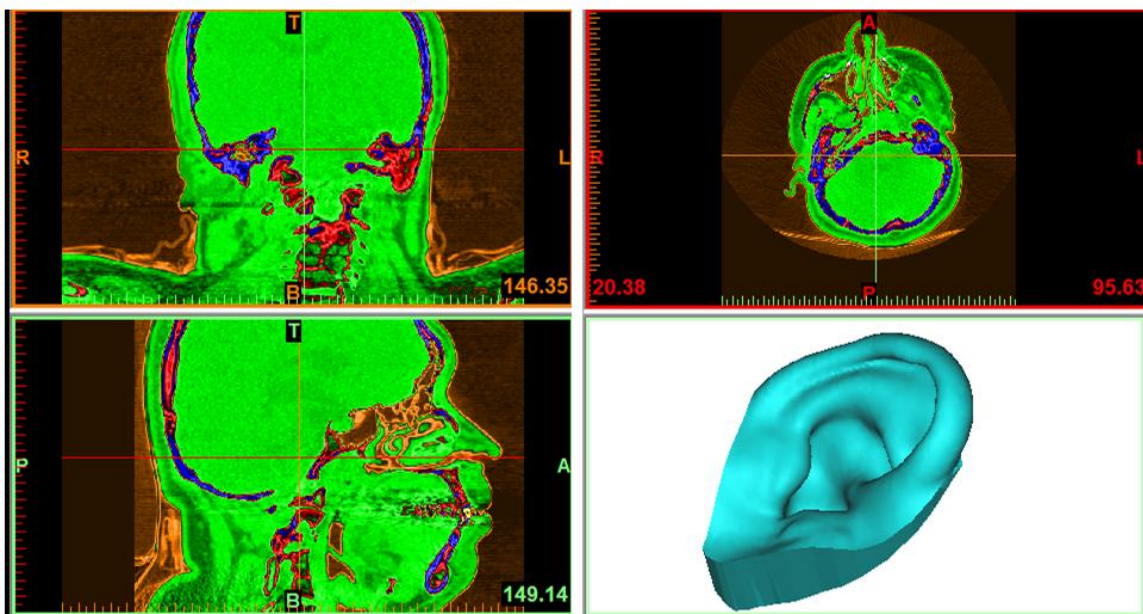
as physical aspects, should be considered in designing tissue scaffolds. Biochemical aspects are associated with the chemical composition and biological properties of the scaffold. Physical design is related to the morphology and mechanical properties of the scaffold. This section highlights imaging techniques and potential biomaterials for the fabrication of hybrid scaffolds. Some fabrication features, morphology, mechanical properties, and how to modulate the mechanical properties of hybrid scaffolds are also discussed.

2.4.1 Role of imaging techniques and support in the fabrication of custom-made hybrid scaffolds

Fabrication of customized hybrid scaffolds starts with processing medical image captured from the patient. Imaging data acquisition and conversion into the format recognized by the machine must have sufficient resolution [31]. Recently, AM and medical imaging techniques, as noninvasive medical imaging modalities, have been used to fabricate customized patient-specific scaffolds [32]. To this end, defects of the patient can be scanned using medical imaging and the data obtained then converted into a CAD model [33,34]. A comprehensive review has recently been published on the importance of imaging data, challenges, and practical steps needed to fabricate a 3D printed model from cardiovascular CT data [35].

Hybrid scaffolds with complex structures are used in various applications such as skeletal muscle [1] and articular cartilage reconstruction [14]. In most cases, only soft materials such as hydrogels are printed and the creation of complex structures remains a challenge [36,37]. Complex structures might be defined as large-size structures, such as the ear, that have complex curvatures. More considerations are necessary to fabricate such hybrid structures, one of which is having a sacrificial support during their printing. In this regard, polyethylene glycol (PEG) [38], gelatin slurry [39], and Pluronic F-127 hydrogel [1] have been used as sacrificial supports. Another study reported a supramolecular assembly (guest-host system) for the development of bioinks and support hydrogels, such that filaments were deposited in the support hydrogel [40]. Using a slurry of gelatin microparticles is another method to support complex 3D structures during printing [39]. Additionally, some researchers used a submerged-in-crosslinker approach to crosslink the hydrogel just after printing to create hybrid scaffolds with cell-laden hydrogels [26,41].

Sacrificial support is required for the fabrication of complex structures, as depicted for the ear in Figure 2.3. Supports are quiet useful assets to tolerate the weight of material during the printing process of a structure and specifically for situations, that material cannot be printed without support. The process starts with the generation of a CAD model using imaging data and progresses to the fabrication of a porous scaffold. The ear has a complex shape and composition and is a good candidate to illustrate the complexity of printing such structures. Notably, the ear has both auricular cartilage and fat tissue and, thus, bioprinting of the ear is also a good example of the fabrication of hybrid scaffolds using various biomaterials. Figure 2.3 shows the 3D model of the ear created using imaging data. This 3D model is then converted to an STL file and, after ensuring its accuracy, different parts, support, and the final porous structure can be designed (Figure 2.3). It is worth mentioning that the regeneration of ear tissue with traditional techniques is difficult.



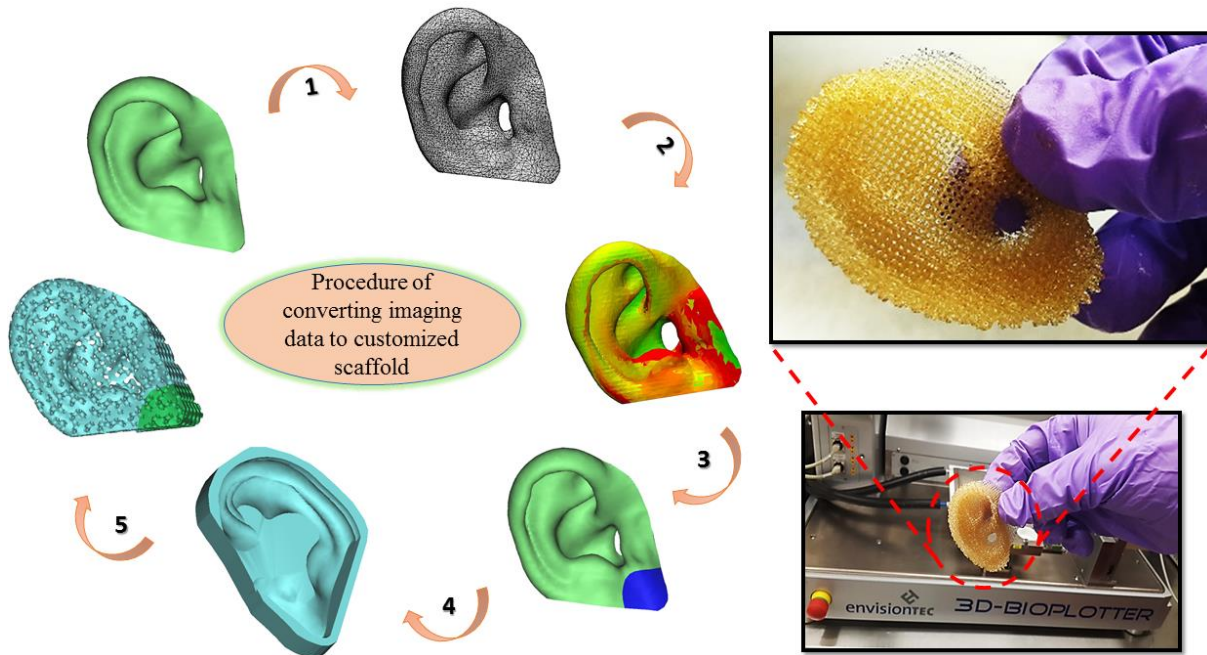


Figure 2.3. 3D biprinting of complex structures via sacrificial support for ear regeneration; obtaining CAD model from imaging data, [1- converting CAD model to STL file, 2- investigation of the accuracy of STL file, 3- defining desired parts for bioprinting with different cells, 4- creation of the CAD model of sacrificial support based on main CAD model, 5- fabrication of porous scaffold via bioprinter]; a representative sample of ear fabricated by a 3D-Bioplotter (CAD model is available at <https://www.thingiverse.com/thing:304657> [42]).

2.4.2 Potential biomaterials used in the fabrication of hybrid scaffolds

Biomaterials should act as a mechanical support and provide biological requirements for targeted cells selected based on application. Hydrogels, such as alginate, are good substrates for the incorporation of cells but they do not have appropriate mechanical properties. To address this issue, hybrid scaffolds, including hydrogels and other natural/synthetic components, are used. From the biological point of view, many efforts have been made to fabricate functionalized scaffolds. Moreover, extracellular mimetic hydrogels are outstanding examples used in various biomedical applications that provide an artificial extracellular microenvironment resembling both the mechanical and biological features of extracellular matrix (ECM). Such structures have been applied to cartilage, bone, tendon, and intervertebral disc regeneration [43].

In addition, the selected biomaterials should be biocompatible to support cell activities such as proliferation, migration, etc. [44]. Moreover, they should have a suitable degradation rate and non-toxic byproducts to degrade just after tissue regeneration and replacement of ECM

proteins. A degradation rate that is too fast/slow results in issues such as lack of stability of the biomaterial [45]. Moreover, the selected biomaterials should be printable with suitable fluidic viscosity. In this regard, some biomaterials have good printability [46]; for those with poor printability, methods such as the use of sacrificial materials can be utilized. When using hydrogels in a dispensing-based system, good crosslinkers should be used to prevent any collapse during the printing process [37]. Hence, many factors including printability, degradation rate, mechanical stability, biological requirements, etc. should be taken into account during biomaterial selection,

Both synthetic and natural polymers have been widely used in TE applications. Some synthetic polymers used in scaffold fabrication cannot provide an appropriate environment for cell attachment because they are hydrophobic and do not have cell attachment sites. In contrast, hydrogels are good candidates for cell encapsulation and 3D bioprinting but have poor mechanical properties. Hence, the combination of synthetic biomaterials (or other components) and hydrogels creates potential constructs for 3D biofabrication [47].

To overcome the poor mechanical properties of cell-laden hydrogels, several efforts have been made to combine hydrogels and other synthetic/natural polymers using a dispensing-based technique to support cell-laden hydrogels [17,48]. In this regard, Kang et al. reported the fabrication of hybrid scaffolds by combining cells with gelatin, fibrinogen, hyaluronic acid (HA), and glycerol mixed into Dulbecco's Modified Eagle Medium (DMEM) [1]. In a similar study, PCL improved the mechanical stability of cell-impregnated alginate for cartilage tissue regeneration [14]. In addition to mechanical properties, shear-thinning materials are generally desired candidates for 3D dispensing-based bioprinting due to the rapid decrease of viscosity of the material after extrusion from the nozzle [15].

Hydrogels can be functionalized to improve their biological properties. For instance, one polysaccharide-based hydrogel widely used in dispensing-based bioprinting is alginate, which has good biocompatibility, low toxicity, and high printability [49–51]. This biomaterial has been successfully used to incorporate pancreatic islet cells, fibroblasts, myoblasts, and chondrocytes [52]. In spite of many attractive features, lack of cell binding sites limits the application of sodium alginate (Na-Alg); for instance, Shim et al. reported that alginate (derived from brown seaweed) might not promote cellular activities because it has no bioactive proteins [15]. In this regard, many

efforts have been made to functionalize alginate. For example, carbodiimide chemistry is useful for forming covalent bonds between various peptides and the alginate molecule. Such peptides can significantly enhance the functionality of cell-laden alginate for neurite outgrowth [53]. In this regard, the lack of adhesion sites on alginate has led researchers to functionalize this polymer by adding peptides, fibronectin, laminin, fibronectin, collagen, gelatin, etc. [54–56]. Another option for functionalizing hydrogels is the addition of immobilized growth factors, e.g., to functionalize chitosan hydrogel for the differentiation of neural stem cells [43].

Another point to take into account is that selected biomaterials utilized in the fabrication of hybrid scaffolds should have a proper degradation rate. For example, hybrid scaffolds have been fabricated using cell-laden alginate hydrogel and PCL [14]; however, all of the pores were filled with gel and eliminated channels available for nutrient perfusion. Thus, the rate of degradation should be appropriate so that the scaffold degrades and provides some channels for perfusion. The issue of lack of nutrients, specifically for the inner parts of the scaffolds, has been extensively discussed elsewhere [57]. To address this issue, radio frequency heating has been used to accelerate the biodegradation of scaffolds and create a pathway for nutrient perfusion [58]. A recent review discusses the challenge of how to match the degradation rate of scaffolds with the growth of native tissue [59]. Other researchers have tried to fabricate hybrid scaffolds with pores intentionally left empty for oxygen and nutrient transport and as an example refer to [15].

Overall, the biomaterials selected for hybrid scaffolds should satisfy both mechanical and biological requirements. Table 2.1 lists the potential biomaterials that can be utilized in the fabrication of hybrid scaffolds as well as dispensing-based printing machines used in the biofabrication of hybrid scaffolds.

Table 2.1. Potential biomaterials and printing parameters used in the biofabrication of hybrid scaffolds.

Materials	Application	Description	Dispensing-based printing machines	Ref
PCL and alginate	Osteochondral tissue regeneration	PCL (molecular weight = 70000–90000 Da), 4% w/v alginate	MtoBS	[15]

PCL and alginate	Generation of organized living grafts with improved mechanical stability	PCL (molecular weight = 70000–90000 Da), 2% w/v medium viscosity Na-Alg	BioScaffolder dispensing: multi-arm dispensing-based bio-printing system	[22]
Nanofibrillated cellulose (NFC), PCL, and alginate	Auricular cartilage regeneration	2% (w/w) of plant-derived NFC, PCL Capa 6500, 0.5% (w/w) Na-Alg	3D Discovery [®] instrument	[60]
PCL, Pluronic F-127, hydrogel: gelatin, fibrinogen, HA and glycerol	Bone, cartilage, skeletal muscle	PCL (molecular weight =43000~50000 Da), gelatin (35~45 mg/mL), fibrinogen (20–30 mg/mL), HA (3 mg/mL), and glycerol (10% v/v), 33% w/v Pluronic F-127 added to a 10% v/v glycerol solution.	Integrated tissue and organ printing	[1]
PCL, PEG, alginate	Ear regeneration	PCL (molecular weight =45000-60000 Da), PEG (molecular weight = 20000 Da), 4% w/v alginate	MtoBS	[38]
Fibrinogen, collagen type I, and Matrigel	3D printed bifurcated tubes	-	MakerBot Replicator printer	[39]
Cell-laden Na-Alg and CaCl₂	Micro-channels for nutrients delivery	2-5% (w/v) Na-Alg solution 2-5% (w/v) CaCl ₂	Coaxial nozzle-assisted 3D bioprinting system	[26]
Alginate, HA	Peripheral nerve regeneration	Alginate and HA (2.5 % w/v alginate and 0.25 % w/v HA)	3D-Bioplotter [™] system, EnvisionTEC	[61]
PCL and alginate	Cartilage TE	PCL (molecular weight =48000-90000 Da); Alginate: 2 and 2.5% medium viscosity alginate	3D-Bioplotter [™] system, EnvisionTEC	[14]
Collagen hydrogel precursor, gelatin, fibrinogen, thrombin	Vascular Network System	10% (w/v) gelatin, collagen hydrogel precursor (rat tail, type I), fibrinogen (10 mg/mL), thrombin (3U/mL)	A developed bio-printing platform	[62]

PCL and alginate	Cartilage TE	PCL (molecular weight =70000-90000 Da), 4 and 6% alginate	Multihead deposition system	[47]
Collagen, gelatin	Fluidic channels	Collagen hydrogel precursor (rat tail, type I), 7% (w/v) gelatin	Bio-printer system	[63]
PCL, PEG, alginate/atelocollagen/decellularized ECM	Heterogeneous tissue regeneration	PCL (molecular weight =70000-90000 Da), PEG (molecular weight = 20000 Da),	MtoBS	[64]
Oxidized alginate, gelatin	Processability of the oxidized alginate-gelatin hydrogel in bioplotting applications	2% (w/v) Na-Alg (molecular weight of 100000–200000 g/mol), gelatin (type A)	Three axes moveable bioplotter (type BioScaffolder 2.1)	[65]
PCL and alginate	Soft and hard tissue regeneration	PCL (molecular weight =60000-80000 Da), 3.5 wt% alginate (low viscosity, high G-content non-medical grade LF10/60)	Dispensing system	[66]

2.5 Physical architecture of hybrid scaffolds

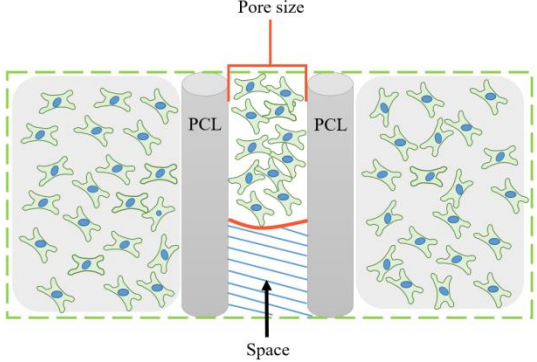
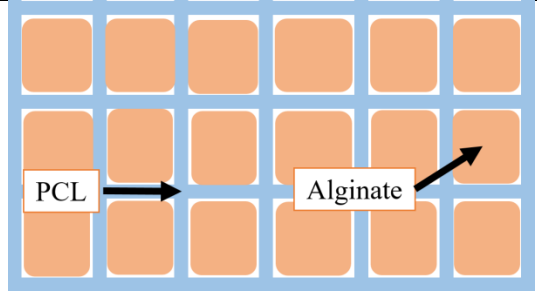
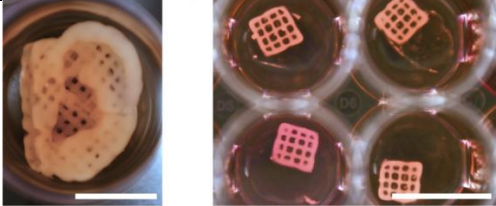
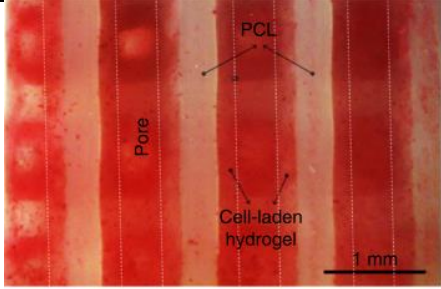
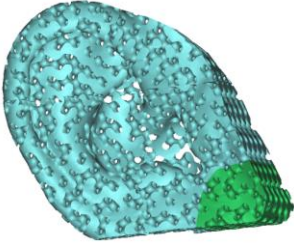
The morphology of a scaffold is defined by the geometry, distribution, and interconnectivity of pores, which are considered to be key parameters for 3D scaffold fabrication [67]. Due to the dependency of the mechanical properties into on the geometrical characteristics of the scaffold, here we emphasize the physical architecture; and in the next subsection, mechanical properties are discussed separately. In particular, in a porous scaffold, the macropores support cell migration whereas micropores promote cell-cell interactions and mass transport. Moreover, larger pores facilitate ECM extension and small pores enhance cell proliferation [68,69]. A recent review emphasizes the physical architecture of scaffolds in tissue regeneration [70]. To facilitate cell-cell interactions, mass transfer within the designed hybrid scaffold should be facilitated by sufficient mechanical stability in a porous structure with interconnected pores. Furthermore, interconnected pores ensure homogeneous cell seeding and better nutrient diffusion [69,71,72].

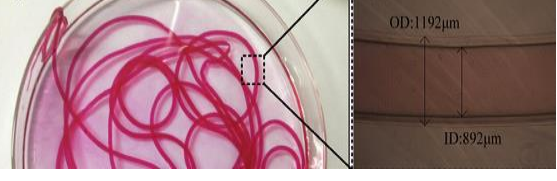
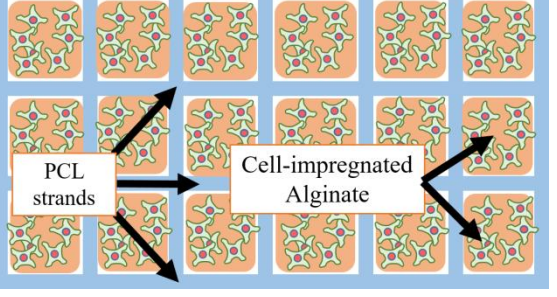
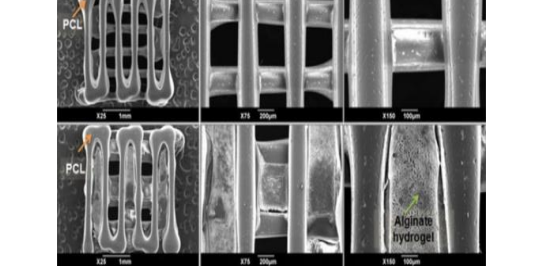
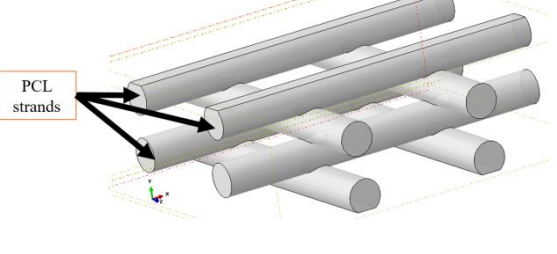
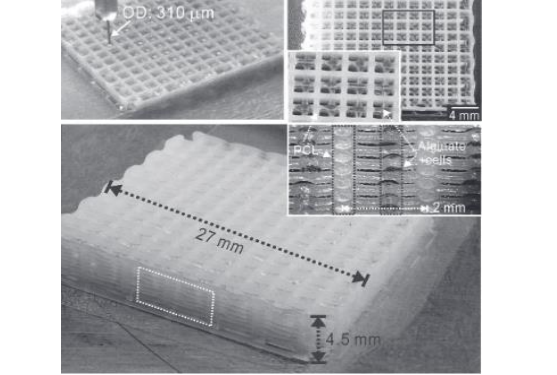
In general, hybrid scaffolds require a porous structure with interconnected pores due to the dependency of initial cell–carrier substance impregnation, cell-cell interactions, mass transfer of nutrients, and tissue growth to this factor. Therefore, balance among various design parameters must be achieved as strand thickness, pore geometry, and porosity significantly affect the mechanical and biological performance of the printed scaffold. In this regard, You et al. showed that the mechanical properties of hydrogel scaffolds can be modulated by altering internal structure parameters, including strand orientation and spacing, to manipulate the physical architecture of the scaffold [23]. In another study scaffolds with high porosity facilitate cell attachment were reported [73]. In a dispensing-based system, the main factors affecting the morphology of hybrid scaffolds are operating temperature, pressure, nozzle speed, and nozzle diameter. One of the advantages of developing hybrid scaffolds is that hydrogels cannot provide 3D constructs with pre-defined internal architectures; only a few reports are available in this regard [74,75]. Generally, changing the physical features of scaffolds (e.g., pore size, strand width) results in changes to mechanical properties, to be discussed in the next section.

Table 2.2 summarizes the physical and mechanical properties of bioprinted hybrid scaffolds. The diameter of the dispensed strands depends on the pressure, temperature, nozzle size, and nozzle speed. PCL strands with various diameters (50 to 275 μm) have been printed by adjusting the aforementioned fabrication variables [15]. In particular, changing these variables regulates the flow rate of the material dispensed from the needle/nozzle. In this regard, numerous models have been developed to predict the flow rate of the dispensed biomaterial to fabricate scaffolds with expected pore size and strand width [5,76].

Table 2.2. Physical architecture and mechanical properties of hybrid scaffolds.

Materials	Strand width (μm)	Pore size (μm)	Mechanical properties (KPa)	Description	Reference
------------------	--	---	------------------------------------	--------------------	------------------

PCL and alginate	50-275	50-600	-		[15]
PCL and alginate	-	2000	Young's modulus near 600		[22]
PCL, NFC (cellulose), alginate	Refer to picture	Theoretical porosity of 50%	-	 <p data-bbox="816 1108 1349 1178">Scale bar = 1 mm, with permission from the respective publisher</p>	[60]
PCL, Pluronic F-127, hydrogel: gelatin, fibrinogen, HA, and glycerol	~ 370	~ 750	Three-point bending test of the 3D bioprinted ear constructs for 1 mm extension: percentage of loading cycle 49.22 ± 12.54 (pre-implantation), 29.58 ± 3.45 (after one month)	 <p data-bbox="857 1499 1312 1528">With permission from the respective publisher</p>	[1]
PCL, PEG, alginate	200	600	Tensile modulus 14000–16000		[38]

<p>Cell-laden Na-Alg and CaCl₂</p>	<p>Outer diameter of hollow tube: 1192</p>	<p>Inner diameter of hollow tube: 892</p>	<p>Ultimate tensile strength of 3D structure based on fusion of adjacent hollow filaments: 46 (2% alginate), 77 (3% alginate), 116 (4% alginate)</p>	 <p>With permission from the respective publisher</p>	<p>[26]</p>
<p>PCL and alginate</p>	<p>~ 400</p>	<p>~ 650</p>	<p>-</p>		<p>[14]</p>
<p>PCL and alginate</p>	<p>200 ± 20</p>	<p>400 ± 20</p>	<p>-</p>	 <p>With permission from the respective publisher</p>	<p>[77]</p>
<p>PCL and alginate (only PCL was printed)</p>	<p>200-400</p>	<p>1000-2000</p>	<p>PCL compressive modulus: 6630-56460 PCL tensile modulus: 6030-46040 Compressive modulus of alginate was considered negligible</p>		<p>[78]</p>
<p>PCL and alginate</p>	<p>Alginate: 466 ± 63, PCL: 437 ± 11</p>	<p>88 ± 47</p>	<p>Tensile modulus: 15400 and 8300</p>		<p>[66]</p>

2.6 Mechanical properties: hybrid scaffolds with tailorable mechanical properties

As discussed above, stiffer materials are generally used to improve the mechanical properties of hydrogel biomaterials. Many studies cite the poor mechanical properties of hydrogels as evidence to justify the fabrication of hybrid scaffolds [14,15,78,79]. Because a hybrid scaffold might be a combination of a soft material and a stiff material, mimicking the mechanical properties of native tissue is quite challenging. Successful tissue regeneration largely depends on the mechanical properties of fabricated scaffold resembling native tissues. Different studies have made efforts to tailor the mechanical properties of scaffolds by exploring appropriate biomaterial and scaffold geometry [80,81]. In addition to experimental studies, some efforts have been made to predict the mechanical properties of scaffolds using numerical investigation. Numerical studies have been carried out to reduce the number of experiments to evaluate scaffolds using finite element models [82–85]. In this regard, more studies should be done to develop models that can predict the mechanical behavior of scaffolds considering the effects of geometric features. Inconsistency between the mechanical properties of scaffolds and native tissues provokes a stress-shielding phenomenon and, thus, inhibits ECM secretion by cells [78]. According to the literature, various mechanical properties are desired with respect to the application of hybrid scaffolds; Table 2.2 presents mechanical properties of some hybrid scaffolds utilized in different applications.

Hybrid scaffolds with tailorable mechanical stiffness (provided by thermoplastic polymers) have been printed together with cells [22]. In particular, hybrid scaffolds composed of an acellular and soft matrix were fabricated to mimic specific native tissues and achieve the desired biomechanical and biological function [86–89]. Likewise, the spacing, orientation, and thickness of the fibers of hybrid scaffolds have been modified to improve mechanical properties in order to for use in intervertebral disks, cartilage, bone, and ligaments, and even in large blood vessels [90–92]. Cardiac implants with modulated mechanical properties have been reported using hydrogel bioprinting with various patterns [93]. With respect to tailorable mechanical properties, more investigations are needed as this area is under-explored. Further, modulating the molecular weight of PCL and scaffold geometry has been attempted to fabricate hybrid constructs with similar mechanical properties to cartilage tissue [78]. Notably, conventional methods are unable to provide

scaffolds with tailorable mechanical properties due to random pore size and distribution, uncontrollable porosity, and poor pore interconnectivity [92,94–96].

Beyond the general goal of creating 3D scaffolds with mechanical properties similar to native tissues, the mechanical properties of scaffolds can affect vascularization. For example, cells respond to the mechanical properties of implanted scaffolds [97]. Santos et al. showed that human umbilical vein endothelial cells (ECs) grown on collagen-coated low and high stiff polyacrylamide hydrogels showed different functional expression [98]. Another study demonstrated that ECs respond differently to angiogenic growth factors according to the mechanical properties of the scaffold [99]. Consequently, a vascular organization can be controlled via scaffolds by modulating mechanical properties; this effect can be useful to better control the creation of vascular networks.

2.7 Cell viability and scaffold activation in large hybrid constructs: the role of vessel-like hollow channels/vascular networks

Creating vascular networks with perfusion capability within 3D thick scaffolds is one of the most critical challenges in the fabrication of large scaffolds for maintaining the viability of cells [100]; this important issue is the subject of a recent review [101]. The creation of large hybrid scaffolds is no exception as large hybrid structures require appropriate vessel-like hollow channels/vascular networks to support cell viability throughout the 3D construct regardless of application. The creation of vessel-like hollow channels/vascular networks is not only important for vascularization using ECs but also vital for other applications using various types of cells. Vessel-like hollow channels/vascular networks play a major role in maintaining cell viability by facilitating adequate transport of oxygen and nutrients to the cells [102–104]. The goal of the creation of hollow channels within scaffolds is to improve cell viability in bioprinted scaffolds compared to those created with traditional scaffold-based TE techniques. This is considered a promising approach allowing the fabrication of complicated tissues for major internal organs, handling and positioning of multiple cell types, and integrating a vascular network in 3D tissue structures [105,106]. As an example of the importance of a hollow channel/vascular network, the lack of a network within a PCL/alginate hybrid scaffold reduced cell viability after just three days of culture [22]. To address this issue, several attempts have been made to facilitate media transport within controlled scaffold geometry but failed due to the absence of integrated vascular networks

[107]. In this section, methods used to create vessel-like hollow channels/vascular networks and how to activate scaffolds for vascularization are discussed; the effect of printing parameters on cell viability is then summarized.

Notably, some approaches, such as chemical modification of biomaterials, optimization of pore sizes to facilitate blood vessel ingrowth, incorporation of angiogenic factors [108], and prevascularization of the scaffold in a bioreactor can enhance the formation of vasculature within a hybrid scaffold. Generally, microfabrication (e.g., photo patterning, micro-molding) and 3D bioprinting techniques are suitable for creating vascular networks [109]. Embedded microfluidic networks can improve perfusion in thick scaffolds but, in the majority of cases, microfluidic fabrication methods require various processes and, thus, direct fabrication of a vascular network is not possible [110]. Generation of a micro-pattern requires the knowledge of microfluidics to regulate the microenvironment (gas transfer, shear stress on cells, etc.) in cell culture. One example in this regard is using stacked multiple layers of poly (glycerol sebacate) embedded with microfluidic networks to promote the formation of a complex vascular network within a 3D scaffold [53]. Moreover, sacrificial filaments (carbohydrate glass) incorporated within a 3D scaffold are useful for generating a vascular pattern, but this approach is not free from the complexities introduced by ECs seeding and the need to remove the sacrificial material. With respect to vascular networks, Huang et al. reported the fabrication of 3D zigzag cellular tubes according to the fusion of Na-Alg droplets via inkjet printing. However, this method requires the precise deposition of Na-Alg droplets and long printing times [111]. Another technique uses matrix-assisted pulsed laser evaporation; however, this method requires highly viscous materials and thus results in poor cell survival [112]. Although seeding and encapsulation methods have been used to incorporate ECs within scaffolds, they can only form randomly organized vessels with poor interconnectivity.

Similar to the fabrication of complex structures with the assistance of sacrificial biomaterials as mentioned in the previous sections, several studies have used sacrificial techniques for vascular architecture fabrication. A recent review focuses on the utilization of sacrificial bioink materials for bioprinting of vascular tissue scaffolds [113]. However, ECs cannot be encapsulated during the fabrication of vascular channels in these methods [26,63,114]. For instance,

carbohydrate glass scaffolds were bioprinted but the sacrificial materials did not quickly dissolve after immersion in the culture medium [115]. In other studies, a perfused vascular channel was prepared in which a gelatin-based sacrificial filament was embedded into a collagen scaffold [116], and porous PCL bone grafts were vascularized through the post-seeding of human adipose-derived stem cells with a heterogeneous distribution [117]. Figure 2.4 illustrates the various techniques utilized in the creation of vascular networks within hybrid scaffolds. These techniques use a hydrogel reservoir to print in a bath of the hydrogel as a support. Second, coaxial nozzle printing can be utilized to create hollow channels using simultaneous crosslinking of the hydrogel. This technique is also known as core-shell printing and is a good candidate for the creation of hollow channels that can be used for drug delivery [118] or vessel-like channels as reported by many researchers [113,119,120]. Third, sacrificial materials act as a support that can be removed after chemically crosslinking of the main matrix. Using this method, Norotte et al. reported the creation of hollow channels of multicellular pig smooth muscle cells with the assistance of agarose cylinders as a sacrificial biomaterial [121].

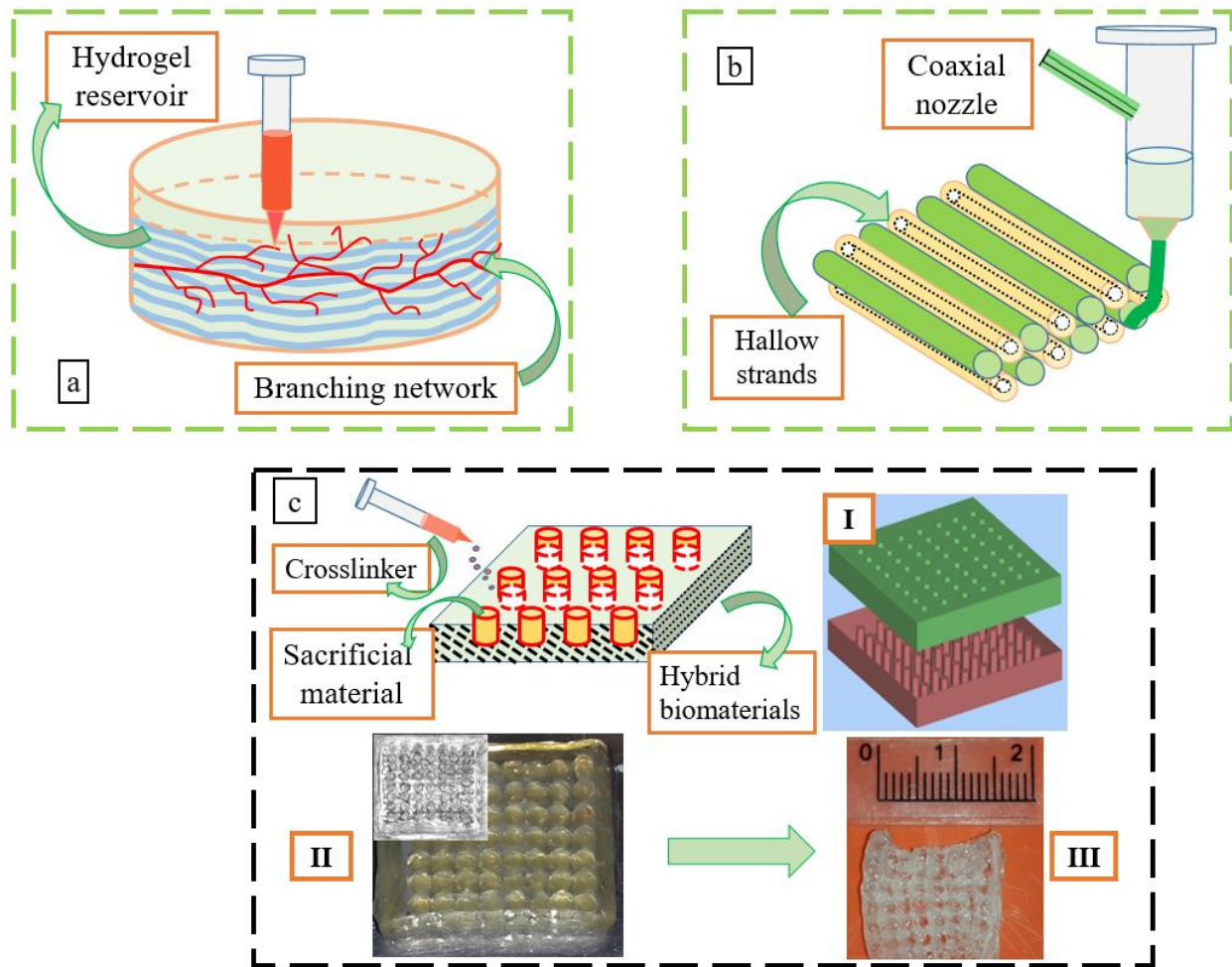


Figure 2.4. Printing of vascular networks within hybrid scaffolds using: a) hydrogel reservoir, b) coaxial nozzle, c) sacrificial material: I) CAD models of main (hybrid biomaterials) and sacrificial parts, II) final scaffold before removing sacrificial material (inset is the top view during fabrication), III) final hybrid scaffold after removal of the sacrificial material.

Moreover, hybrid scaffolds can be created from a 3D construct fabricated from functional biomaterials. Bioactive molecules such as cell-adhesion peptides, responsive moieties, and growth factors incorporated into 3D scaffold can enhance biological function and vascularization [122–124]. Sequential release of various angiogenic factors (such as vascular endothelial growth factors, basic fibroblast growth factor, and platelet-derived growth factor) from 3D scaffolds stimulates vasculature formation and therefore has frequently been explored [32]. Assembling multiple autologous cells, growth factors, and bioactive agents, mimicking the native tissue, is quite challenging; however, a 3D bioprinter with multiple nozzles can efficiently overcome this difficulty. A strategy to deploy stem cells and growth factors together in large constructs to form

vascular networks through the proliferation and differentiation of stem cells has been successful [125]. Hybrid scaffolds including tricalcium phosphate, PCL, and cells supported large blood vessel formation in calvarial bone reconstruction, while the control group promoted limited vascularization in the periphery of the implant [1]. The difficulty associated with thick tissue vascularization is forming an integrated vascular network within the 3D scaffold to allow the delivery of growth factors, oxygen, and other nutrients, and therefore this issue has been studied intensively [126,127].

The importance of using vessel-like hollow channels/vascular networks is to ensure cell viability. However, printing parameters also affect cell viability. Needle geometry and pneumatic pressure can affect cell viability in the 3D vascular pattern fabricated by a dispensing-based system. Using this method, many factors should be considered regarding cell viability and printing cell-laden hydrogels. For instance, conical needles are superior to cylindrical needles with respect to shear-induced cell damage, and therefore tapered needles are recommended [14]. Additionally, highly viscous hydrogels offer better printability but cause cell damage in the printing process due to higher dispensing pressure [128]. Some of the printing parameters and conditions used in the biofabrication of hybrid scaffolds for different TE applications are summarized in Table 2.3. A lower pneumatic pressure is recommended for cell-laden hydrogel printing to reduce the shear stress, which is one of the main factors influencing cell viability. Another factor is needle diameter, where smaller needle diameters result in more cell damage. Applied temperature and needle length are other paramount factors [129].

Table 2.3. Printing parameters and reported cell viability for different kinds of cells.

Materials	Nozzle speed/feed rate (mm/min)	Needle diameter (µm)/gauge size	Pressure (KPa)	Temperature (°C)	Crosslinking of hydrogel (mM)	Cell types	Cell viability	Description	Reference
PCL and alginate	Scan speed of the head PCL: 100 Alginate: 250	PCL: 200 and 150	PCL: 400 Alginate: piston-based system with a plunger speed of 1.2 mm/min	PCL: 80 Alginate: 20	CaCl ₂ : 100 and NaCl: 145	Chondrocytes isolated from human nasal septum cartilage and osteoblasts	Chondrocytes (~93.9%) and osteoblasts (~95.6%)	Cell viability for at least 7 days; chondrocytes retained their viability without remarkable proliferation after 7 days	[15]

PCL and alginate	PCL: feed rate of 176 Alginate: deposition speed of 100	PCL: 23G Alginate: 210	PCL: 500 Alginate: piston-based system with a plunger speed of 1.5 mm/min	PCL: 160 Alginate: room temperature	CaCl ₂ : 102	C20A4 cells	More than 60%	Only first day	[22]
NFC, PCL, and alginate	Feed rate PCL: 1200 NFC-Alginate: 300	PCL: 330 NFC-Alginate: 150	PCL: 250 NFC-Alginate: 40	PCL: 90 NFC-Alginate: 23	CaCl ₂ : 100	Human nasal chondrocytes	~70.9%	Throughout 28 days	[60]
PCL, Pluronic F-127, hydrogel: gelatin, fibrinogen, HA, and glycerol	-	PCL: 250 Pluronic F127: 250 Cell-laden hydrogel: 300	PCL: 800 Pluronic F127: 200-300 Cell-laden hydrogel: 50~80	PCL: 92.5 Others: 18	Thrombin solution (20 UI/mL)	3T3 fibroblasts and Human AFSCs, rabbit ear chondrocyte, mouse C2C12 myoblasts	3T3 fibroblasts ≥ 95% ~91% for AFSCs and chondrocyte and ~97% for myoblasts C2C12 myoblasts	3T3 fibroblasts: on day 0, maintained through days 3 and 6 and other cells for long durations	[1]
PCL, PEG, alginate	PCL: scan velocity 205 Alginate: piston velocity 0.48	-	PCL: 650 PEG: 300	PCL: 80 PEG: 80 Alginate: room temperature	CaCl ₂ : 100	Chondrocytes and adipocytes differentiated from adipose-derived stromal cells	~95%	During 7 days	[38]
PCL, PEG, Alginate/atelocollagen/decellularized ECM	Scan velocity, PCL: 205 PEG: 310 Alginate: 80 Atelocollagen: 60 dECM: 55	250	PCL: 650 PEG: 300 Piston velocity of alginate, Atelocollagen, and dECM: 0.008, 0.015, and 0.018	PCL: 80 PEG: 80 Others: room temperature	CaCl ₂	Human adipose-derived stem cells and human-turbinate-tissue-derived mesenchymal stem cells	>95%	-	[64]

			mm/s, respectively.						
Fibrinogen, collagen type I, and Matrigel	-	150	-	22	Printing in a gelatin slurry	C2C12 myoblasts	~99.7%	During 7 days	[39]
Cell-laden Na-Alg and CaCl₂	Movement speed around 1000 mm/min	21-23 G	Coaxial nozzle printing, flow rate alginate: 0.5-1.5 mL/min	-	Crosslinking via CaCl ₂ (coaxial nozzle)	L929 mouse fibroblast	~92.9%	Cell viability reduced from 92.9% on day 1 to 67.1% on day 7	[26]
PCL and alginate	Dispensing speed: PCL: 60 Alginate: 1500	PCL: 300 Alginate: 200	PCL: 800 Alginate: 10	PCL: 65-80, Alginate: 10	Partial crosslinking: CaCl ₂ : 170 Full crosslinking after fabrication: CaCl ₂ : 100	Rounded and fibroblastic cells isolated from primary cultures of embryonic chick chondrocytes	Minimum viability of 77% for both types of cells during 14 days	Up to 14 days of culture	[14]
PCL and alginate	Scan velocity: PCL: 80 Alginate: 400	PCL: 250 Alginate: 250	PCL: 650 Alginate: 9-20	PCL: 80 Alginate: room temperature	CaCl ₂ : 100 NaCl: 145	Chondrocyte	~85%	Over 10 days	[77]
PCL and alginate	Scan velocity: 450	Outer diameter: Alginate: 310, PCL: 350	Alginate: 220 ± 10 PCL: 350 ± 5	Alginate: 26 PCL: 130	Before cell loading: 0.5 wt% CaCl ₂ , after printing: 2 wt% CaCl ₂	MC3T3-E	~84%	During 7 days	[66]
Alginate/HA	Scan velocity: 240	100	120	-	CaCl ₂ : 100 0.1% w/v polyethyleneimine	RSC96 cells (ATTC), an immortalized rat Schwann cell line	83.2%	Over 3 weeks	[61]

Oxidized alginate, gelatin	Scan velocity: 600-3600	200	55 and 100	37	CaCl ₂ : 100	MG-63 osteoblast	Not reported statistically; high number of living cells	After the plotting process; 5 h of incubation	[65]
-----------------------------------	-------------------------	-----	------------	----	-------------------------	------------------	---	---	------

2.8 Current challenges and the future of hybrid scaffolds

Dispensing-based 3D bioprinting has revolutionized TE with respect to printing artificial tissues and organs but it is not free from limitations. Challenges remain with respect to fabricating hybrid scaffolds, such as the inclusion of vessel-like hollow channels/vascular networks and creation of scaffolds with geometrical features similar to those of native tissues. The following subsections present current limitations, solutions, and future directions.

2.8.1 3D bioprinting and printability

Challenges in 3D bioprinting include increasing the speed and resolution of biofabrication and the possibility of printing biocompatible materials. As depicted in Table 2.3, printing parameters and conditions significantly affect cell viability in the bioprinted strand. In a 3D bioprinting system, the viscosity of the biopolymer is a critical factor that needs to be considered to achieve superior printability and printing resolution. Because the viscosity of some polymers is associated with their concentration in solution, selection of higher viscosity materials requires the application of more concentrated biopolymer during biofabrication. However, a number of studies demonstrate the adverse effect of more concentrated biopolymers on tissue culture. For example, 4% alginate gels regenerated better cartilaginous tissue than 6% alginate gels [47].

Other vital factors are the crosslinking and stability of hydrogels after fabrication. Although crosslinking is a good method to improve the stability of hydrogels, it is not reproducible [66]. Several studies reported excessive crosslinking causing a significant reduction in cell viability in biofabrication [130]. In addition, the type and concentration of crosslinkers regulate printing parameters (dispensing pressure, needle speed) and the mechanical properties of the resulting 3D scaffolds. Therefore, the choice of crosslinkers and determining an appropriate concentration are critical challenges that need to be addressed. A viscous biomaterial used for 3D cell printing should

have good printability while ensuring that its chemical/physical crosslinking does not adversely influence cell viability.

2.8.2 Development of novel biomaterials for improved biological and/or mechanical properties

The range of biomaterials used in bioprinting is limited and includes natural polymers (collagen, HA, alginate, etc.) as well as synthetic ones (PCL, polylactic acid, polyglycolic acid, etc.). The ideal 3D complex tissue or organ has yet to be printed; the incorporation of cells in hydrogels that have poor mechanical properties is the main obstacle. Thus, researchers have used synthetic biomaterials to improve the mechanical stability of hydrogels [131,132]. The mechanism by which synthetic materials transfer mechanical stimuli to the encapsulated cells in the hydrogel is complex and requires more investigation. PCL, a synthetic polymer, has been used in some studies to improve the mechanical properties of hybrid structures [22]. However, the role of synthetic polymers in transferring customized mechanical stimuli to the cells encapsulated in hydrogels is important and should be addressed in future studies. Modulating the mechanical properties of a hybrid scaffold to match the structure of native tissues is another critical factor.

A number of biopolymers demonstrate superior printability but lack bioactive molecules in their structure. For example, Na-Alg demonstrates biocompatibility, low toxicity, and printability, and has frequently been used in 3D bioprinting [49–51]. In spite of many attractive features, the deficiency of cell binding moieties on the molecular chain limits the application of Na-Alg; as it has no bioactive proteins [15]. In this regard, carbodiimide chemistry is useful in forming a covalent bond between various peptides and alginate molecule [53]. Another biological issue is that cell-laden soft hydrogels degrade faster than synthetic materials in hybrid scaffolds. This non-uniform degradation affects the structure integrity of hybrid scaffolds within a short time during *in vivo* or *in vitro* tissue culture. Moreover, it is difficult to create attachments between successive layers of hydrogels and synthetic materials during bioprinting. Finally, synthetic materials take longer to degrade after *in vivo* implantation and result in inflammation and other biological complexities.

From the mechanical point of view, successful cell-laden hydrogel strands can generally be printed with synthetic polymers (e.g., PCL) to improve the mechanical properties of hybrid

scaffolds. However, the heat transferred from the printed synthetic polymers to the hydrogel filaments significantly reduces cell viability [133]. To limit such detrimental effects of synthetic polymers with a relatively high melting temperature, rapid cooling of PCL has been conducted after dispensing together with a microchannel distance gap between the PCL strands and cells to reduce cell damage in the cell-laden hydrogel [1]. Another study concluded that PCL printed at 65 to 75 °C did not have any effect on cell viability in the hybrid (PCL/alginate) scaffold due to the quick drop in the surface temperature of the PCL to room temperature [14].

Along with the development of novel biomaterials, conventional and AM techniques might be combined to create hierarchical hybrid scaffolds [19]. In this regard, the 3D biplotting technique might be combined with electrospinning method to achieve hybrid scaffolds with improved biological/mechanical properties. It is noticed that many efforts have been made to predict the mechanical properties of scaffolds using finite element models to reduce the number of time-consuming experiments, for example by developing accurate numerical models [82–84]. Such models can be utilized to predict the mechanical behavior of hybrid scaffolds in future studies.

2.8.3 Manipulating multiple biomaterials

Once a novel biomaterial is developed, the next question is how to manipulate various biomaterials to fabricate hybrid scaffolds. Control of the spatial distribution of materials is a key issue with respect to the manipulation of multiple materials. The capacity to manipulate multi-materials/cells during scaffold bio-fabrication is critical to mimic the heterogeneous structures of native tissue/organs. A straightforward approach is to blend multi-materials/cells for deposition to build scaffolds, resulting in hybrid scaffolds and *in situ*-forming hydrogel scaffolds. This approach is challenged by the need to control the spatial distribution of individual materials/cells within the scaffolds created. To address this challenge, the use of multiple dispensers has been applied over the last decade, wherein multiple materials/cells stored in different dispensers are alternatively applied to build the scaffolds. This approach has been successfully utilized to fabricate hybrid scaffolds comprised of a solid 3D synthetic polymer framework to impart mechanical strength and a hydrogel network to encapsulate cells. However, this approach lacks the ability to dispense multi-materials/cells simultaneously in a controllable manner in comparison with the simple blending

method. This limitation has been thoroughly addressed elsewhere, using a microfluidic device with a double-coaxial laminar flow as a novel method to manipulate multi-materials/cells [134].

2.8.4 Cell viability and the creation of activated hybrid scaffolds

In a 3D hybrid scaffold, a large proportion of the encapsulated cell population can experience necrosis due to limited diffusional mass transfer [135,136]. Consequently, cells encapsulated in a large 3D scaffold cannot survive for a long time. However, Shim et al. report a new approach to ensure the availability of interconnected pores within a few hundred microns [15]. Furthermore, because shear-induced cell damage is a common phenomenon in dispensing-based 3D bioprinting, more efforts are required to improve cell viability in this technology [37,137,138]. To address this issue, tapered needles have been introduced to reduce shear stress [45].

As mentioned above, a fundamental challenge in TE is vascularizing a large 3D cellular scaffold printed by a 3D bioprinting technique [1,108]. Because nutrient diffusion to cells without any vascular network is inefficient beyond a distance of 100 to 200 μm [1], cell viability in the scaffold is significantly reduced during *in vivo* or *in vitro* culture. In particular, new blood vessels take a considerable amount of time to grow into scaffolds by angiogenesis/vasculogenesis and this delay remarkably reduces cell viability due to hypoxia and necrosis [139]. Several strategic approaches have been considered to address this issue. Hollow channels prepared by sacrificial biomaterials have been perfused with ECs to form blood vessels [115]; the use of a coaxial nozzle to manage the flow of the hydrogel and crosslinker is another possibility to create 3D vasculature [140]. Moreover, a multi-nozzle bioprinter was used to fabricate complex tissue and a vascular network layer-by-layer to mimic native tissue [125]. In this regard, a co-axial nozzle was used to print tubular vascular networks, while a micro nozzle printed cells to fabricate large-scale vascularized tissues. Similarly, fibroblast tissue ligaments together with the vasculature network were printed [107]. Further, growth factors have been used to stimulate angiogenesis and create a vascular network [141,142]. Another remaining challenge in creating vascular networks is the generation of perfusable prevascularized tissues [32]. In this regard, *in vivo/in vitro* prevascularization was reported to be an effective approach in vasculature formation prior to *in vivo* implantation [143]. Finally, in addition to the importance of vascular networks in cell viability, fabrication parameters (e.g., applied pressure) can affect cell viability and therefore more

investigations are needed to determine optimal fabrication parameters for different biomaterials. As a future direction, techniques like coaxial nozzle printing might be implemented and combined with electrospinning to create hybrid scaffolds with vessel-like channels. Such a trend might improve cell viability within scaffolds, as the current critical challenge in TE.

2.9 Conclusions

Dispensing-based 3D bioprinting techniques have been widely used in the fabrication of tissue scaffolds with living cells, where hydrogels are regarded as the dominant biomaterials. Notably, poor mechanical/biological properties of hydrogels have led researchers to develop hybrid scaffolds from two or more biomaterials with distinct yet complementary properties. Many efforts have been made to address various challenges in the development of hybrid scaffolds with significant advances in terms of their design and fabrication. In terms of fabrication, one common trend to manipulate biomaterials is using multiple dispensers to deposit different biomaterials with dissimilar rheological properties and fabrication conditions (dissolution and crosslinking/gelation aspects). Challenges remain with respect to making attachments between successive layers printed with different biomaterials as well as determining appropriate fabrication parameters to achieve printability with geometric precision. In terms of design, critical issues are associated with the medical imaging used to fabricate customized patient-specific hybrid scaffolds, biomaterials, and the physical architecture of hybrid scaffolds with tailorable mechanical properties. This review highlights the technical (speed and resolution) and printability aspects, development of novel biomaterials, and fabrication of scaffolds with improved biological and mechanical properties. Many experimental and numerical studies have calculated/predicted the mechanical behavior of hybrid scaffolds and some advancements have occurred with respect to manipulating multiple materials, improving cell viability, creating vessel-like hollow channels/vascular networks, and fabricating large hybrid scaffolds. In spite of many successful achievements, more studies are needed to develop a range of printable biomaterials with appropriate biomechanical properties to create large hybrid scaffolds with vascular networks. The success of printing artificial tissues and organs with hybrid structures lies in the creation of an appropriate microenvironment in which a large cell population can function in an organized fashion to form respective tissues in the presence of a functional vasculature. In the near future, dispensing-based methods to produce bioprinted

hybrid scaffolds are predicted to evolve further towards the goal of printing entire organs or damaged tissues.

2.10 References

- [1] H. Kang, S.J. Lee, I.K. Ko, C. Kengla, J.J. Yoo, A. Atala, A 3D bioprinting system to produce human-scale tissue constructs with structural integrity, *Nat. Biotechnol.* 34 (2016) 312–319. doi:10.1038/nbt.3413.
- [2] A.P. Kishan, A.B. Robbins, S.F. Mohiuddin, M. Jiang, M.R. Moreno, E.M. Cosgriff-Hernandez, Fabrication of macromolecular gradients in aligned fiber scaffolds using a combination of in-line blending and air-gapelectrospinning, *Acta Biomater.* (2016).
- [3] G.S. Offeddu, J.C. Ashworth, R.E. Cameron, M.L. Oyen, Structural determinants of hydration, mechanics and fluid flow in freeze-dried collagen scaffolds, *Acta Biomater.* 41 (2016) 193–203.
- [4] T.G. Kim, H.J. Chung, T.G. Park, Macroporous and nanofibrous hyaluronic acid/collagen hybrid scaffold fabricated by concurrent electrospinning and deposition/leaching of salt particles, *Acta Biomater.* 4 (2008) 1611–1619.
- [5] M. Sarker, X.B. Chen, Modeling the flow behavior and flow rate of medium viscosity alginate for scaffold fabrication with a 3D bioplotter, (2017).
- [6] L.D. Albrecht, S.W. Sawyer, P. Soman, Developing 3D Scaffolds in the Field of Tissue Engineering to Treat Complex Bone Defects, *3D Print. Addit. Manuf.* 3 (2016) 106–112.
- [7] X. Zhao, X. Wang, Preparation of an adipose-derived stem cell/fibrin–poly (d, l-lactic-co-glycolic acid) construct based on a rapid prototyping technique, *J. Bioact. Compat. Polym.* 28 (2013) 191–203.
- [8] X. Zhou, X. Zhou, C. Liu, X.H. Wang, A 3D bioprinting liver tumor model for drug screening, *World J. Pharm. Pharm. Sci.* (2016).
- [9] X. Wang, Drug delivery design for regenerative medicine., *Curr. Pharm. Des.* 21 (2015) 1503.
- [10] L. Liu, X. Zhou, Y. Xu, W. Zhang, C.-H. Liu, X. Wang, Controlled release of growth factors for regenerative medicine, *Curr. Pharm. Des.* 21 (2015) 1627–1632.
- [11] Y. Xu, X. Wang, Application of 3D biomimetic models in drug delivery and regenerative medicine, *Curr. Pharm. Des.* 21 (2015) 1618–1626.
- [12] X. Zhao, L. Liu, J. Wang, Y. Xu, W. Zhang, G. Khang, X. Wang, In vitro vascularization of a combined system based on a 3D printing technique, *J. Tissue Eng. Regen. Med.* (2014).
- [13] A.D. Augst, H.J. Kong, D.J. Mooney, Alginate hydrogels as biomaterials, *Macromol. Biosci.* 6 (2006) 623–633.
- [14] Z. Izadifar, T. Chang, W.M. Kulyk, D. Chen, B.F. Eames, Analyzing biological performance of 3D-printed, cell-impregnated hybrid constructs for cartilage tissue engineering, *Tissue Eng. Part C. Methods.* 22 (2016) 173–188. doi:10.1089/ten.TEC.2015.0307.

- [15] J.-H. Shim, J. Lee, J.Y. Kim, D.-W. Cho, Bioprinting of a mechanically enhanced three-dimensional dual cell-laden construct for osteochondral tissue engineering using a multi-head tissue/organ building system, *J. Micromechanics Microengineering*. 22 (2012) 85014. doi:10.1088/0960-1317/22/8/085014.
- [16] C. Mota, D. Puppi, F. Chiellini, E. Chiellini, Additive manufacturing techniques for the production of tissue engineering constructs, *J. Tissue Eng. Regen. Med*. 9 (2015) 174–190.
- [17] M. Yeo, H. Lee, G.H. Kim, Combining a micro/nano-hierarchical scaffold with cell-printing of myoblasts induces cell alignment and differentiation favorable to skeletal muscle tissue regeneration, *Biofabrication*. 8 (2016) 35021.
- [18] S. Naghieh, M. Badrossamay, E. Foroozmehr, M. Kharaziha, Combination of PLA micro-fibers and PCL-gelatin nano-fibers for development of bone tissue engineering scaffolds, *Int. J. Swarm Intell. Evol. Comput*. 06 (2017) 1–4. doi:10.4172/2090-4908.1000150.
- [19] S. Naghieh, E. Foroozmehr, M. Badrossamay, M. Kharaziha, Combinational processing of 3D printing and electrospinning of hierarchical poly(lactic acid)/gelatin-forsterite scaffolds as a biocomposite: mechanical and biological assessment, *Mater. Des*. 133 (2017) 128–135. doi:10.1016/j.matdes.2017.07.051.
- [20] S. Khalil, W. Sun, Biopolymer deposition for freeform fabrication of hydrogel tissue constructs, *Mater. Sci. Eng. C*. 27 (2007) 469–478.
- [21] J.-H. Shim, J.Y. Kim, M. Park, J. Park, D.-W. Cho, Development of a hybrid scaffold with synthetic biomaterials and hydrogel using solid freeform fabrication technology, *Biofabrication*. 3 (2011) 34102.
- [22] W. Schuurman, V. Khristov, M.W. Pot, P.R. van Weeren, W.J. a Dhert, J. Malda, Bioprinting of hybrid tissue constructs with tailorable mechanical properties., *Biofabrication*. 3 (2011) 1–7. doi:10.1088/1758-5082/3/2/021001.
- [23] F. You, X. Wu, X. Chen, 3D Printing of Porous Alginate/gelatin Hydrogel Scaffolds and Their Mechanical Property Characterization, *J. Int. J. Polym. Mater. Polym. Biomater*. 66 (2016) 299–306. doi:10.1080/00914037.2016.1201830.
- [24] D. Macaya, M. Spector, Injectable hydrogel materials for spinal cord regeneration: a review, *Biomed. Mater*. 7 (2012) 12001.
- [25] M. Wang, P. Zhai, X. Chen, D.J. Schreyer, X. Sun, F. Cui, Bioengineered scaffolds for spinal cord repair, *Tissue Eng. Part B Rev*. 17 (2011) 177–194.
- [26] Q. Gao, Y. He, J. Fu, A. Liu, L. Ma, Coaxial nozzle-assisted 3D bioprinting with built-in microchannels for nutrients delivery, *Biomaterials*. 61 (2015) 203–215. doi:10.1016/j.biomaterials.2015.05.031.
- [27] X.Y. Tian, M.G. Li, N. Cao, J.W. Li, X.B. Chen, week 2- Characterization of the flow behavior of alginate/hydroxyapatite mixtures for tissue scaffold fabrication., *Biofabrication*. 1 (2009) 1–8. doi:10.1088/1758-5082/1/4/045005.
- [28] M.G. Li, X.Y. Tian, X.B. Chen, A brief review of dispensing-based rapid prototyping techniques in tissue scaffold fabrication: role of modeling on scaffold properties prediction., *Biofabrication*. 1

- (2009) 032001. doi:10.1088/1758-5082/1/3/032001.
- [29] V. Manojlovic, J. Djonlagic, B. Obradovic, V. Nedovic, B. Bugarski, Investigations of cell immobilization in alginate: rheological and electrostatic extrusion studies, *J. Chem. Technol. Biotechnol.* 81 (2006) 505–510.
- [30] M. Sarker, X.B. Chen, D.J. Schreyer, Experimental approaches to vascularisation within tissue engineering constructs., *J. Biomater. Sci. Polym. Ed.* 26 (2015) 683–734. doi:10.1080/09205063.2015.1059018.
- [31] S. Naghieh, A. Reihany, A. Haghighat, E. Foroozmehr, M. Badrossamay, F. Forooghi, Fused deposition modeling and fabrication of a three-dimensional model in maxillofacial reconstruction, *Regen. Reconstr. Restor.* 1 (2016) 139–144. doi:http://dx.doi.org/10.22037/triple%20r.v1i3.12543.
- [32] Y.S. Zhang, R. Oklu, M.R. Dokmeci, A. Khademhosseini, Three-Dimensional Bioprinting Strategies for Tissue Engineering, *Cold Spring Harb. Perspect. Med.* (2017) a025718. doi:10.1101/cshperspect.a025718.
- [33] F.C. Fierz, F. Beckmann, M. Huser, S.H. Irsen, B. Leukers, F. Witte, Ö. Degistirici, A. Andronache, M. Thie, B. Müller, The morphology of anisotropic 3D-printed hydroxyapatite scaffolds, *Biomaterials.* 29 (2008) 3799–3806.
- [34] A. Cazon, J. Aizpurua, A. Paterson, R. Bibb, R.I. Campbell, Customised design and manufacture of protective face masks combining a practitioner-friendly modelling approach and low-cost devices for digitising and additive manufacturing, *Virtual Phys. Prototyp.* 9 (2014) 251–261.
- [35] J.M. Otton, N.S. Birbara, T. Hussain, G. Greil, T.A. Foley, N. Pather, 3D printing from cardiovascular CT : a practical guide and review, *Cardiovasc. Diagn. Ther.* (2017). doi:10.21037/cdt.2017.01.12.
- [36] I. Martin, P.J. Simmons, D.F. Williams, Manufacturing challenges in regenerative medicine, *Sci. Transl. Med.* 6 (2014) 232fs16–232fs16.
- [37] S. V Murphy, A. Atala, 3D bioprinting of tissues and organs, *Nat. Biotechnol.* 32 (2014) 773–785. doi:10.1038/nbt.2958.
- [38] J.-S. Lee, J.M. Hong, J.W. Jung, J.-H. Shim, J.-H. Oh, D.-W. Cho, 3D printing of composite tissue with complex shape applied to ear regeneration, *Biofabrication.* 6 (2014) 024103. doi:10.1088/1758-5082/6/2/024103.
- [39] T.J. Hinton, Q. Jallerat, R.N. Palchesko, J.H. Park, M.S. Grodzicki, H. Shue, M.H. Ramadan, A.R. Hudson, A.W. Feinberg, Three-dimensional printing of complex biological structures by freeform reversible embedding of suspended hydrogels, *Sci. Adv.* 1 (2015) 1–10. doi:10.1126/sciadv.1500758.
- [40] C.B. Highley, C.B. Rodell, J.A. Burdick, Direct 3D printing of shear-thinning hydrogels into self-healing hydrogels, *Adv. Mater.* 27 (2015) 5075–5079.
- [41] F. You, X. Wu, N. Zhu, M. Lei, B.F. Eames, X. Chen, 3D Printing of porous cell-laden hydrogel constructs for potential applications in cartilage tissue engineering, *ACS Biomater. Sci. Eng.* 2 (2016) 1200–1210.

- [42] Addamay123, Human ear, (2017). <https://www.thingiverse.com/thing:304657>, date of access: June 2017.
- [43] S. Lv, T. Bu, J. Kayser, A. Bausch, H. Li, Towards constructing extracellular matrix-mimetic hydrogels: an elastic hydrogel constructed from tandem modular proteins containing tenascin FnIII domains, *Acta Biomater.* 9 (2013) 6481–6491.
- [44] C.J. Ferris, K.G. Gilmore, G.G. Wallace, Biofabrication: an overview of the approaches used for printing of living cells, *Appl. Microbiol. Biotechnol.* 97 (2013) 4243–4258.
- [45] L.Q. Ning, X.B. Chen, A Brief Review of Extrusion-based Tissue Scaffold Bio-Printing, *Biotechnol. J.* (2017) 1–47.
- [46] N.E. Fedorovich, J.R. De Wijn, A.J. Verbout, J. Alblas, W.J.A. Dhert, Three-dimensional fiber deposition of cell-laden, viable, patterned constructs for bone tissue printing, *Tissue Eng. Part A.* 14 (2008) 127–133.
- [47] J. Kundu, J.-H. Shim, J. Jang, S.-W. Kim, D.-W. Cho, An additive manufacturing-based PCL-alginate-chondrocyte bioprinted scaffold for cartilage tissue engineering, *J. Tissue Eng. Regen. Med.* 9 (2015) 1286–1297. doi:10.1002/term.1682.
- [48] M. Kim, S.B. Jo, J.H. Park, K. Cho, Flexible lateral organic solar cells with core–shell structured organic nanofibers, *Nano Energy.* 18 (2015) 97–108.
- [49] T. Andersen, P. Auk-Emblem, M. Dornish, 3D cell culture in alginate hydrogels, *Microarrays.* 4 (2015) 133–161.
- [50] S.H. Ahn, H.J. Lee, J.-S. Lee, H. Yoon, W. Chun, G.H. Kim, A novel cell-printing method and its application to hepatogenic differentiation of human adipose stem cell-embedded mesh structures, *Sci. Rep.* 5 (2015) 13427.
- [51] R.A. Perez, M. Kim, T.-H. Kim, J.-H. Kim, J.H. Lee, J.-H. Park, J.C. Knowles, H.-W. Kim, Utilizing core–shell fibrous collagen-alginate hydrogel cell delivery system for bone tissue engineering, *Tissue Eng. Part A.* 20 (2013) 103–114.
- [52] S.P.M. Bohari, D.W.L. Hukins, L.M. Grover, Effect of calcium alginate concentration on viability and proliferation of encapsulated fibroblasts, *Biomed. Mater. Eng.* 21 (2011) 159–170. doi:10.3233/BME-2011-0665.
- [53] C.J. Bettinger, E.J. Weinberg, K.M. Kulig, J.P. Vacanti, Y. Wang, J.T. Borenstein, R. Langer, Three-Dimensional Microfluidic Tissue-Engineering Scaffolds Using a Flexible Biodegradable Polymer, *Adv. Mater.* 18 (2006) 165–169.
- [54] M. Matyash, F. Despang, R. Mandal, D. Fiore, M. Gelinsky, C. Ikonomidou, Novel Soft Alginate Hydrogel Strongly Supports Neurite Growth and Protects Neurons Against Oxidative Stress, *Tissue Eng. Part A.* 18 (2012) 55–66. doi:10.1089/ten.tea.2011.0097.
- [55] N.O. Dhoot, C.A. Tobias, I. Fischer, M.A. Wheatley, Peptide-modified alginate surfaces as a growth permissive substrate for neurite outgrowth, *J. Biomed. Mater. Res. Part A.* 71 (2004) 191–200.
- [56] L.N. Novikova, A. Mosahebi, M. Wiberg, G. Terenghi, J. Kellerth, L.N. Novikov, Alginate hydrogel

- and matrigel as potential cell carriers for neurotransplantation, *J. Biomed. Mater. Res. Part A*. 77 (2006) 242–252.
- [57] M. Izadifar, Biomanufacturing versus superficial cell seeding: simulation of chondrocyte proliferation in a cylindrical cartilage scaffold, *Int. J. Tissue Eng.* 2013 (2013).
- [58] M. Izadifar, X. Chen, Radio frequency heating of implanted tissue engineered scaffolds: simulation and experimental studies, *Front. Heat Mass Transf.* 3 (2013).
- [59] J. Yang, Y.S. Zhang, K. Yue, A. Khademhosseini, Cell-laden hydrogels for osteochondral and cartilage tissue engineering, *Acta Biomater.* 57 (2017) 1–25. doi:10.1016/j.actbio.2017.01.036.
- [60] H. Martínez Ávila, S. Schwarz, N. Rotter, P. Gatenholm, 3D bioprinting of human chondrocyte-laden nanocellulose hydrogels for patient-specific auricular cartilage regeneration, *Bioprinting*. 1 (2016) 22–35. doi:10.1016/j.bprint.2016.08.003.
- [61] A. Rajaram, D. Schreyer, D. Chen, Bioplotting Alginate / Hyaluronic Acid Hydrogel Scaffolds with Structural Integrity and Preserved Schwann Cell Viability, *3D Print.* 1 (2014) 194–203. doi:10.1089/3dp.2014.0006.
- [62] V.K. Lee, A.M. Lanzi, H. Ngo, S.-S. Yoo, P.A. Vincent, G. Dai, Generation of multi-scale vascular network system within 3D hydrogel using 3D bio-printing technology, *Cell. Mol. Bioeng.* 7 (2014) 460–472.
- [63] W. Lee, V. Lee, S. Polio, P. Keegan, J.-H. Lee, K. Fischer, J.-K. Park, S.-S. Yoo, On-demand three-dimensional freeform fabrication of multi-layered hydrogel scaffold with fluidic channels, *Biotechnol. Bioeng.* 105 (2010) 1178.
- [64] F. Pati, J.-H. Shim, J.-S. Lee, D.-W. Cho, 3D printing of cell-laden constructs for heterogeneous tissue regeneration, *Manuf. Lett.* 1 (2013) 49–53.
- [65] T. Zehnder, B. Sarker, A.R. Boccaccini, R. Detsch, Evaluation of an alginate-gelatine crosslinked hydrogel for bioplotting., *Biofabrication*. 7 (2015). doi:10.1088/1758-5090/7/2/025001.
- [66] H. Lee, S. Ahn, L.J. Bonassar, G. Kim, Cell (MC3T3-E1)-Printed Poly (ϵ -caprolactone)/Alginate Hybrid Scaffolds for Tissue Regeneration, *Macromol. Rapid Commun.* 34 (2013) 142–149.
- [67] Z. Izadifar, X. Chen, W. Kulyk, Strategic design and fabrication of engineered scaffolds for articular cartilage repair, *J. Funct. Biomater.* 3 (2012) 799–838. doi:10.3390/jfb3040799.
- [68] S.-M. Lien, L.-Y. Ko, T.-J. Huang, Effect of pore size on ECM secretion and cell growth in gelatin scaffold for articular cartilage tissue engineering, *Acta Biomater.* 5 (2009) 670–679.
- [69] R. El-Ayoubi, C. DeGrandpré, R. DiRaddo, A.-M. Yousefi, P. Lavigne, Design and dynamic culture of 3D-scaffolds for cartilage tissue engineering, *J. Biomater. Appl.* 25 (2011) 429–444.
- [70] T.J. Hinton, A. Lee, A.W. Feinberg, 3D Bioprinting from the Micrometer to Millimeter Length Scales: Size Does Matter, *Curr. Opin. Biomed. Eng.* (2017). doi:10.1016/j.cobme.2017.02.004.
- [71] T.J. Klein, J. Malda, R.L. Sah, D.W. Hutmacher, Tissue engineering of articular cartilage with biomimetic zones, *Tissue Eng. Part B Rev.* 15 (2009) 143–157.
- [72] R. El-Ayoubi, N. Eliopoulos, R. Diraddo, J. Galipeau, A.-M. Yousefi, Design and fabrication of 3D

- porous scaffolds to facilitate cell-based gene therapy, *Tissue Eng. Part A*. 14 (2008) 1037–1048.
- [73] C.G. Spiteri, R.M. Pilliar, R.A. Kandel, Substrate porosity enhances chondrocyte attachment, spreading, and cartilage tissue formation in vitro, *J. Biomed. Mater. Res. Part A*. 78 (2006) 676–683.
- [74] D.L. Cohen, E. Malone, H.O.D. Lipson, L.J. Bonassar, Direct freeform fabrication of seeded hydrogels in arbitrary geometries, *Tissue Eng.* 12 (2006) 1325–1335.
- [75] B. Guillotin, A. Souquet, S. Catros, M. Duocastella, B. Pippenger, S. Bellance, R. Bareille, M. Rémy, L. Bordenave, J. Amédée, Laser assisted bioprinting of engineered tissue with high cell density and microscale organization, *Biomaterials*. 31 (2010) 7250–7256.
- [76] X.B. Chen, M.G. Li, H. Ke, Modeling of the Flow Rate in the Dispensing-Based Process for Fabricating Tissue Scaffolds, *J. Manuf. Sci. Eng.* 130 (2008) 021003. doi:10.1115/1.2789725.
- [77] J. Kundu, J.H. Shim, J. Jang, S.W. Kim, D.W. Cho, An additive manufacturing-based PCL-alginate-chondrocyte bioprinted scaffold for cartilage tissue engineering, *J. Tissue Eng. Regen. Med.* 9 (2015) 1286–1297. doi:10.1002/term.1682.
- [78] A.D. Olubamiji, Z. Izadifar, J.L. Si, D.M.L. Cooper, B.F. Eames, D.X. Chen, Modulating mechanical behaviour of 3D-printed cartilage-mimetic PCL scaffolds: influence of molecular weight and pore geometry, *Biofabrication*. 8 (2016) 025020. doi:10.1088/1758-5090/8/2/025020.
- [79] K. Hölzl, S. Lin, L. Tytgat, S. Van Vlierberghe, L. Gu, A. Ovsianikov, Bioink properties before, during and after 3D bioprinting, *Biofabrication*. 8 (2016) 032002. doi:10.1088/1758-5090/8/3/032002.
- [80] L. Moroni, J.R. De Wijn, C.A. Van Blitterswijk, Three-dimensional fiber-deposited PEOT/PBT copolymer scaffolds for tissue engineering: Influence of porosity, molecular network mesh size, and swelling in aqueous media on dynamic mechanical properties, *J. Biomed. Mater. Res. Part A*. 75 (2005) 957–965.
- [81] T.B.F. Woodfield, J. Malda, J. De Wijn, F. Peters, J. Riesle, C.A. van Blitterswijk, Design of porous scaffolds for cartilage tissue engineering using a three-dimensional fiber-deposition technique, *Biomaterials*. 25 (2004) 4149–4161.
- [82] S. Naghieh, M.R.R. Karamooz Ravari, M. Badrossamay, E. Foroozmehr, M. Kadkhodaei, Numerical investigation of the mechanical properties of the additive manufactured bone scaffolds fabricated by FDM: the effect of layer penetration and post-heating, *J. Mech. Behav. Biomed. Mater.* 59 (2016) 241–250. doi:10.1016/j.jmbbm.2016.01.031.
- [83] M.R.K. Ravari, M. Kadkhodaei, Finite element modeling of the elastic modulus of Ti6Al4V scaffold fabricated by SLM, in: *Poromechanics V5, Proc. Fifth Biot Conf. Poromechanics, 2013*: pp. 1021–1028.
- [84] M.R. Karamooz Ravari, M. Kadkhodaei, A. Ghaei, Effects of asymmetric material response on the mechanical behavior of porous shape memory alloys, *J. Intell. Mater. Syst. Struct.* (2015). doi:10.1177/1045389X15604232.
- [85] S. Naghieh, M.R.K. Ravari, M. Badrossamay, E. Foroozmehr, M. Kadkhodaei, Finite element analysis for predicting the mechanical properties of bone scaffolds fabricated by fused deposition modeling (FDM), in: *Modares Mech. Eng. Proc. Adv. Mach. Mach. Tools Conf., 2015*: pp. 450–454.

- [86] N.L. Nerurkar, S. Sen, A.H. Huang, D.M. Elliott, R.L. Mauck, Engineered disc-like angle-ply structures for intervertebral disc replacement, *Spine (Phila. Pa. 1976)*. 35 (2010) 867.
- [87] J.W.S. Hayami, D.C. Surrao, S.D. Waldman, B.G. Amsden, Design and characterization of a biodegradable composite scaffold for ligament tissue engineering, *J. Biomed. Mater. Res. Part A*. 92 (2010) 1407–1420.
- [88] D. Eyrich, H. Wiese, G. Maier, D. Skodacek, B. Appel, H. Sarhan, J. Tessmar, R. Staudenmaier, M.M. Wenzel, A. Goepferich, In vitro and in vivo cartilage engineering using a combination of chondrocyte-seeded long-term stable fibrin gels and polycaprolactone-based polyurethane scaffolds, *Tissue Eng.* 13 (2007) 2207–2218.
- [89] R.E. McMahon, X. Qu, A.C. Jimenez-Vergara, C.A. Bashur, S.A. Guelcher, A.S. Goldstein, M.S. Hahn, Hydrogel–electrospun mesh composites for coronary artery bypass grafts, *Tissue Eng. Part C Methods*. 17 (2011) 451–461.
- [90] J.L. Holloway, A.M. Lowman, G.R. Palmese, Mechanical evaluation of poly (vinyl alcohol)-based fibrous composites as biomaterials for meniscal tissue replacement, *Acta Biomater.* 6 (2010) 4716–4724.
- [91] A. Gloria, F. Causa, R. De Santis, P.A. Netti, L. Ambrosio, Dynamic-mechanical properties of a novel composite intervertebral disc prosthesis, *J. Mater. Sci. Mater. Med.* 18 (2007) 2159–2165.
- [92] L. Moroni, J.R. De Wijn, C.A. Van Blitterswijk, 3D fiber-deposited scaffolds for tissue engineering: influence of pores geometry and architecture on dynamic mechanical properties, *Biomaterials*. 27 (2006) 974–985.
- [93] M. Izadifar, P. Babyn, M.E. Kelly, D. Chapman, X. Chen, Bioprinting pattern-dependent electrical/mechanical behavior of cardiac alginate implants: characterization and ex-vivo phase-contrast microtomography assessment, *Tissue Eng.* (2017).
- [94] V.M. Correlo, L.F. Boesel, E. Pinho, A.R. Costa-Pinto, M.L. Alves da Silva, M. Bhattacharya, J.F. Mano, N.M. Neves, R.L. Reis, Melt-based compression-molded scaffolds from chitosan–polyester blends and composites: Morphology and mechanical properties, *J. Biomed. Mater. Res. Part A*. 91 (2009) 489–504.
- [95] M. Lebourg, R.S. Serra, J.M. Estellés, F.H. Sánchez, J.L.G. Ribelles, J.S. Antón, Biodegradable polycaprolactone scaffold with controlled porosity obtained by modified particle-leaching technique, *J. Mater. Sci. Mater. Med.* 19 (2008) 2047–2053.
- [96] A.S.P. Lin, T.H. Barrows, S.H. Cartmell, R.E. Guldberg, Microarchitectural and mechanical characterization of oriented porous polymer scaffolds, *Biomaterials*. 24 (2003) 481–489.
- [97] J.H. Wen, L.G. Vincent, A. Fuhrmann, Y.S. Choi, K.C. Hribar, H. Taylor-Weiner, S. Chen, A.J. Engler, Interplay of matrix stiffness and protein tethering in stem cell differentiation, *Nat. Mater.* 13 (2014) 979–987.
- [98] L. Santos, G. Fuhrmann, M. Juenet, N. Amdursky, C. Horejs, P. Campagnolo, M.M. Stevens, Extracellular stiffness modulates the expression of functional proteins and growth factors in endothelial cells, *Adv. Healthc. Mater.* 4 (2015) 2056–2063.
- [99] A. Shamloo, S.C. Heilshorn, Matrix density mediates polarization and lumen formation of

- endothelial sprouts in VEGF gradients, *Lab Chip*. 10 (2010) 3061–3068.
- [100] V. Mironov, R.P. Visconti, V. Kasyanov, G. Forgacs, C.J. Drake, R.R. Markwald, Organ printing: tissue spheroids as building blocks, *Biomaterials*. 30 (2009) 2164–2174.
- [101] J.J. Kim, L. Hou, N.F. Huang, Vascularization of three-dimensional engineered tissues for regenerative medicine applications, *Acta Biomater.* 41 (2016) 17–26. doi:10.1016/j.actbio.2016.06.001.
- [102] Y.S. Zhang, A. Khademhosseini, Seeking the right context for evaluating nanomedicine: from tissue models in petri dishes to microfluidic organs-on-a-chip, *Nanomedicine*. 10 (2015) 685–688.
- [103] M. Nomi, A. Atala, P. De Coppi, S. Soker, Principals of neovascularization for tissue engineering, *Mol. Aspects Med.* 23 (2002) 463–483.
- [104] H. Bae, A.S. Puranik, R. Gauvin, F. Edalat, B. Carrillo-Conde, N.A. Peppas, A. Khademhosseini, Building vascular networks, *Sci. Transl. Med.* 4 (2012) 160ps23-160ps23.
- [105] M. Nakamura, S. Iwanaga, C. Henmi, K. Arai, Y. Nishiyama, Biomatrices and biomaterials for future developments of bioprinting and biofabrication, *Biofabrication*. 2 (2010) 14110.
- [106] V. Mironov, V. Kasyanov, C. Drake, R.R. Markwald, Organ printing: promises and challenges, *Regen. Med.* 3 (2008) 93–103.
- [107] Y. Yu, Y. Zhang, I.T. Ozbolat, A Hybrid Bioprinting Approach for Scale-Up Tissue Fabrication, *J. Manuf. Sci. Eng.* 136 (2014) 061013. doi:10.1115/1.4028511.
- [108] W. Zhu, X. Ma, M. Gou, D. Mei, K. Zhang, S. Chen, 3D printing of functional biomaterials for tissue engineering, *Curr. Opin. Biotechnol.* 40 (2016) 103–112. doi:10.1016/j.copbio.2016.03.014.
- [109] J. Rouwkema, A. Khademhosseini, Vascularization and Angiogenesis in Tissue Engineering: Beyond Creating Static Networks, *Trends Biotechnol.* 34 (2016) 733–745. doi:10.1016/j.tibtech.2016.03.002.
- [110] H. Andersson, A. Van Den Berg, Microfabrication and microfluidics for tissue engineering: state of the art and future opportunities, *Lab Chip*. 4 (2004) 98–103.
- [111] C. Xu, W. Chai, Y. Huang, R.R. Markwald, Scaffold-free inkjet printing of three-dimensional zigzag cellular tubes, *Biotechnol. Bioeng.* 109 (2012) 3152–3160.
- [112] J. Yan, Y. Huang, D.B. Chrisey, Laser-assisted printing of alginate long tubes and annular constructs, *Biofabrication*. 5 (2012) 15002.
- [113] P. Datta, B. Ayan, I.T. Ozbolat, Bioprinting for vascular and vascularized tissue biofabrication, *Acta Biomater.* 51 (2017) 1–20. doi:10.1016/j.actbio.2017.01.035.
- [114] W. Wu, C.J. Hansen, A.M. Aragón, P.H. Geubelle, S.R. White, J.A. Lewis, Direct-write assembly of biomimetic microvascular networks for efficient fluid transport, *Soft Matter*. 6 (2010) 739–742.
- [115] J.S. Miller, K.R. Stevens, M.T. Yang, B.M. Baker, D.-H.T. Nguyen, D.M. Cohen, E. Toro, A.A. Chen, P.A. Galie, X. Yu, Rapid casting of patterned vascular networks for perfusable engineered three-dimensional tissues, *Nat. Mater.* 11 (2012) 768–774.

- [116] V.K. Lee, D.Y. Kim, H. Ngo, Y. Lee, L. Seo, S.-S. Yoo, P.A. Vincent, G. Dai, Creating perfused functional vascular channels using 3D bio-printing technology, *Biomaterials*. 35 (2014) 8092–8102.
- [117] J.P. Temple, D.L. Hutton, B.P. Hung, P.Y. Huri, C.A. Cook, R. Kondragunta, X. Jia, W.L. Grayson, Engineering anatomically shaped vascularized bone grafts with hASCs and 3D-printed PCL scaffolds, *J. Biomed. Mater. Res. - Part A*. 102 (2014) 4317–4325. doi:10.1002/jbm.a.35107.
- [118] R.A. Perez, H.-W. Kim, Core–shell designed scaffolds for drug delivery and tissue engineering, *Acta Biomater.* 21 (2015) 2–19.
- [119] Z. Zhang, B. Wang, D. Hui, J. Qiu, S. Wang, 3D bioprinting of soft materials-based regenerative vascular structures and tissues, *Compos. Part B Eng.* (2017).
- [120] W. Jia, P.S. Gungor-Ozkerim, Y.S. Zhang, K. Yue, K. Zhu, W. Liu, Q. Pi, B. Byambaa, M.R. Dokmeci, S.R. Shin, A. Khademhosseini, Direct 3D bioprinting of perfusable vascular constructs using a blend bioink, *Biomaterials*. 106 (2016) 58–68. doi:10.1016/j.biomaterials.2016.07.038.
- [121] C. Norotte, F.S. Marga, L.E. Niklason, G. Forgacs, Scaffold-free vascular tissue engineering using bioprinting, *Biomaterials*. 30 (2009) 5910–5917.
- [122] M.M. Martino, P.S. Briquez, A. Ranga, M.P. Lutolf, J.A. Hubbell, Heparin-binding domain of fibrin (ogen) binds growth factors and promotes tissue repair when incorporated within a synthetic matrix, *Proc. Natl. Acad. Sci.* 110 (2013) 4563–4568.
- [123] B.P. Purcell, D. Lobb, M.B. Charati, S.M. Dorsey, R.J. Wade, K.N. Zellars, H. Doviak, S. Pettaway, C.B. Logdon, J.A. Shuman, Injectable and bioresponsive hydrogels for on-demand matrix metalloproteinase inhibition, *Nat. Mater.* 13 (2014) 653–661.
- [124] A.S. Hoffman, Hydrogels for biomedical applications, *Adv. Drug Deliv. Rev.* 64 (2012) 18–23.
- [125] X. Wang, Q. Ao, X. Tian, J. Fan, Y. Wei, W. Hou, H. Tong, S. Bai, 3D bioprinting technologies for hard tissue and organ engineering, *Materials (Basel)*. 9 (2016) 1–23. doi:10.3390/ma9100802.
- [126] K.M. Chrobak, D.R. Potter, J. Tien, Formation of perfused, functional microvascular tubes in vitro, *Microvasc. Res.* 71 (2006) 185–196.
- [127] I.T. Ozbolat, Yin Yu, Bioprinting Toward Organ Fabrication: Challenges and Future Trends, *IEEE Trans. Biomed. Eng.* 60 (2013) 691–699. doi:10.1109/TBME.2013.2243912.
- [128] K. Nair, M. Gandhi, S. Khalil, K.C. Yan, M. Marcolongo, K. Barbee, W. Sun, Characterization of cell viability during bioprinting processes, *Biotechnol. J.* 4 (2009) 1168–1177.
- [129] M. Li, X. Tian, N. Zhu, D.J. Schreyer, X. Chen, Modeling Process-Induced Cell Damage, *Tissue Eng. Part C*. 16 (2010).
- [130] S. Ahn, H. Lee, L.J. Bonassar, G. Kim, Cells (MC3T3-E1)-laden alginate scaffolds fabricated by a modified solid-freeform fabrication process supplemented with an aerosol spraying, *Biomacromolecules*. 13 (2012) 2997–3003.
- [131] N.E. Fedorovich, W. Schuurman, H.M. Wijnberg, H.-J. Prins, P.R. van Weeren, J. Malda, J. Alblas, W.J.A. Dhert, Biofabrication of osteochondral tissue equivalents by printing topologically defined,

- cell-laden hydrogel scaffolds, *Tissue Eng. Part C Methods*. 18 (2011) 33–44.
- [132] R. Censi, W. Schuurman, J. Malda, G. Di Dato, P.E. Burgisser, W.J.A. Dhert, C.F. Van Nostrum, P. Di Martino, T. Vermonden, W.E. Hennink, A Printable Photopolymerizable Thermosensitive p (HPMAm-lactate)-PEG Hydrogel for Tissue Engineering, *Adv. Funct. Mater.* 21 (2011) 1833–1842.
- [133] H. Lee, Y.W. Koo, M. Yeo, S. Kim, G.H. Kim, Recent cell printing systems for tissue engineering, *Int. J. Bioprinting*. 3 (2017).
- [134] Y.S. and S.T. Hiroaki Onoe, Teru Okitsu, Akane Itou, Midori Kato-Negishi, Riho Gojo, Daisuke Kiriya, Koji Sato, Shigenori Miura, Shintaroh Iwanaga, Kaori Kuribayashi-Shigetomi, Yukiko T. Matsunaga, Metre-long cell-laden microfibrils exhibit tissue morphologies and functions, *Nat. Mater.* 12 (2013) 584–590.
- [135] N.E. Fedorovich, E. Kuipers, D. Gawlitta, W.J.A. Dhert, J. Alblas, Scaffold porosity and oxygenation of printed hydrogel constructs affect functionality of embedded osteogenic progenitors, *Tissue Eng. Part A*. 17 (2011) 2473–2486.
- [136] S.J. Hong, D.P. Jin, D.W. Buck, R.D. Galiano, T.A. Mustoe, Impaired response of mature adipocytes of diabetic mice to hypoxia, *Exp. Cell Res.* 317 (2011) 2299–2307.
- [137] A.B. Dababneh, I.T. Ozbolat, Bioprinting technology: a current state-of-the-art review, *J. Manuf. Sci. Eng.* 136 (2014) 61016.
- [138] Y. Koo, G. Kim, New strategy for enhancing in situ cell viability of cell-printing process via piezoelectric transducer-assisted three-dimensional printing, *Biofabrication*. 8 (2016) 25010.
- [139] M.W. Laschke, B. Vollmar, M.D. Menger, Inosculation: connecting the life-sustaining pipelines, *Tissue Eng. Part B Rev.* 15 (2009) 455–465.
- [140] Y. Zhang, Y. Yu, I.T. Ozbolat, Direct bioprinting of vessel-like tubular microfluidic channels, *J. Nanotechnol. Eng. Med.* 4 (2013) 20902.
- [141] W. Lee, J.C. Debasitis, V.K. Lee, J.-H. Lee, K. Fischer, K. Edminster, J.-K. Park, S.-S. Yoo, Multi-layered culture of human skin fibroblasts and keratinocytes through three-dimensional freeform fabrication, *Biomaterials*. 30 (2009) 1587–1595.
- [142] Y.-B. Lee, S. Polio, W. Lee, G. Dai, L. Menon, R.S. Carroll, S.-S. Yoo, Bio-printing of collagen and VEGF-releasing fibrin gel scaffolds for neural stem cell culture, *Exp. Neurol.* 223 (2010) 645–652.
- [143] J. Rouwkema, N.C. Rivron, C.A. van Blitterswijk, Vascularization in tissue engineering, *Trends Biotechnol.* 26 (2008) 434–441.

Chapter 3 Printability of 3D Printed Hydrogel Scaffolds: Influence of Hydrogel Composition and Printing Parameters

This chapter has been published as “Saman Naghieh, MD Sarker, N. K. Sharma, Zohra Barhoumo, and Xiongbiao Chen, Printability analysis of 3D printed modified hydrogel scaffolds: Influence of biomaterial composition and printing parameters, Journal of Biomedical Engineering” According to the Copyright Agreement, "the authors retain the right to include the journal article, in full or in part, in a thesis or dissertation".

(All the experimental work was conducted by me. MD Sarker, N. K. Sharma, and Zohra Barhoumi helped me in preparing Tables and Figures and performing some experiments. Professor Xiongbiao Chen guided and supervised the whole work.)

3.1 Abstract

Extrusion-based bioprinting has emerged as a promising method in tissue engineering and, specifically, the development of hydrogel scaffolds. However, bioprinting of hydrogel scaffolds is challenging due to printability-related issues, such as lack of capability to precisely deposit hydrogels to create the scaffold as per design. Printability is an index showing the difference between design and fabricated scaffold, yet under-explored. While some studies have attempted to improve either mechanical or biological characteristics of hydrogel scaffolds by means of mixing several types of hydrogels, limited known about the printability of such structures. In this study, sacrificial hydrogels (gelatin and MC) are used to discover the printability of pure and composite alginate scaffolds. As such, a stepwise study is undertaken to study the effect of the flow behavior of hydrogels used for scaffolds fabrication, as well as their mechanical properties, two-dimensional printability, and ultimately three-dimensional printability of pure alginate and a mixture of alginate, gelatin, and MC. Printability studies investigated pore size, strand diameter, and dimensions of scaffolds; and established several equations to define the printability – in terms of pore, strand, and angular printability, in addition to irregularity. Results indicated that the most important factors affecting the printability are biomaterial-related (such as viscosity) and fabrication-related ones (e.g. air pressure, nozzle speed, offset, and selected angular patterns). Finally, a linear regression model was developed to represent factors that have significant effects

on printability. The aim of this study is to present a clear picture of printability by introducing a framework to evaluate hydrogel printability in a systematic manner. Such an approach can be used to distinguish the most effective factors influencing the printability for different biomaterials.

3.2 Introduction

Extrusion-based bioprinting is one of the AM techniques used nowadays for various tissue engineering applications (Figure 3.1) [1]. Many studies have been carried out to create hydrogel scaffolds using this technique [2,3]. Generally speaking, a computer-aided design (CAD) is used to deposit biomaterials as per CAD [4]. However, scaffolds are rarely fabricated exactly according to CAD model. That is why the printability index is important as an element showing the difference between the scaffold design (typically in a CAD model) and the printed scaffold. 3D printability of a hydrogel biomaterial is defined as the ability of a hydrogel to form and maintain a reproducible 3D structure with structure integrity. Although the range of accuracy for extrusion-based machines is in the order of micron, there is still a challenge when it comes to shaping fidelity and the printability of scaffolds bio-fabricated using the extrusion-based technique.

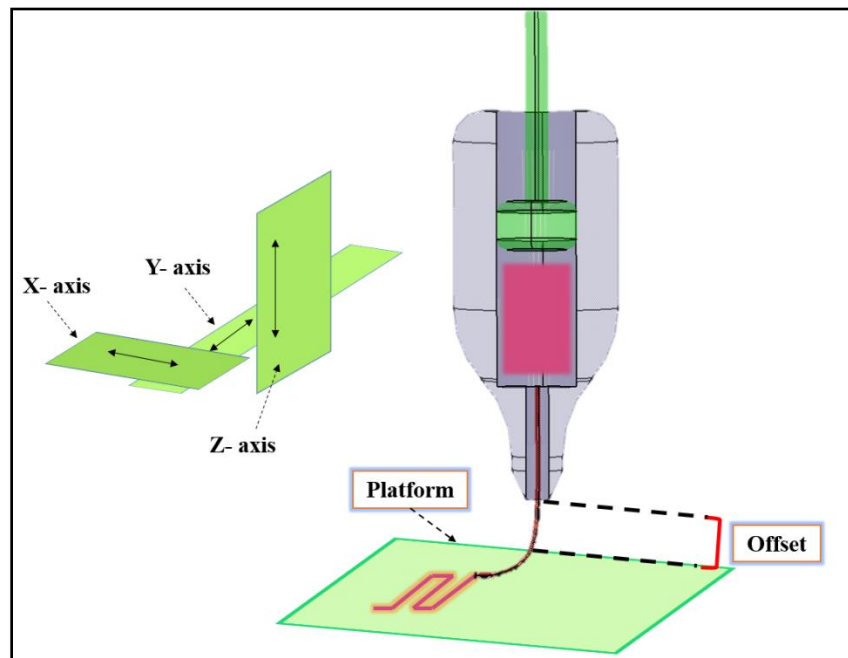


Figure 3.1. The schematic diagram of an extrusion-based 3D bio-printer.

The printability itself can influence other interrelated factors such as morphology and mechanical properties of scaffolds. Consequently, it can affect cell response [5]; it is well-accepted that the mechanical properties of scaffolds can influence cell faith [6]. Hence, it is important to study elements that can influence printability. Although there are a few studies on printability of different biomaterials, the real picture and definition of printability remain unclear and there are fundamental questions about how to map the relationships amongst printability and other interrelated factors such as biomaterial and fabrication. For example, in some studies, the flow behavior of biomaterials was considered to evaluate printability [7,8]. In these studies, the solely physical and rheological characteristics of materials were investigated [9]. In another study, the influence of ionic crosslinkers on printability has been investigated without considering other factors [10]. In some studies, only printing parameters have investigated as critical factors influencing printability [2,11]. In another study, the gelation properties of materials during the printing process were studied to achieve a mechanically stable structure [12]. Murphy et al. studies gelation time, swelling, and printability of various groups of hydrogels [13]. In another study, analytical methods were implemented to check the printability of materials [14]. Kyle et al. reported that printability is a matter of rheology, biomaterial composition, nozzle variables, pore and filament dimensions, geometry, and printing angle [15]. Hence, improving printability considering one of the factors solely is not a systematic approach to improve printability. As mentioned, different studies have investigated the effect of some factors on printability specifically. However, there is not a clear picture of printability considering interrelated factors influencing printability. In this study, rheological properties, printing parameters, and printing conditions are investigated systematically to map the relationship between these parameters and printability rather than considering each factor individually. As such, more studies should be performed in this area to define and establish novel approaches to define and measure printability. The key question of this study is how to measure printability [15].

Alginate is one of the hydrogels used widely for biofabrication of scaffolds used for tissue engineering applications as reported in numerous studies [16–23]. Specifically, one of the approaches to improve the printability of alginate scaffolds fabricated by extrusion-based bioprinting method is to mix alginate with other types of hydrogels [24]. Gelatin is one of these hydrogels usually mixed with alginate. Gelatin is a natural polymer derived from collagen and it

has a cell-friendly environment and this is one of the reasons for mixing alginate with this biomaterial [12]. MC is another biocompatible hydrocarbon polymer used commonly in scaffold fabrication due to its high hydrophilicity and water absorption, which is essential for nutrient delivery to the cells [25]. Hydrogels composed of multiple biomaterials have also been used in scaffold construction: for example, one study analyzed the properties of cell substrates composed of a scaffold containing both gelatin and alginate and found these scaffolds to have high water retention rates [26]. This suggests that combining different biomaterials may be a way to manipulate the scaffold characteristics and allow for better control in achieving desired scaffold functions.

The aim of this study is to present a clear picture of printability, identify factors that can affect it, and propose methods to measure 3D printability of hydrogel scaffolds with an alginate matrix. There are some studies on the effect of the flow behavior of biomaterials [27] ink consistency [7], and hydrogel mechanical characteristics [9] on printability. Nevertheless, little attention has been paid to the effect of printing parameters of scaffolds made of a mixture of hydrogels [2]. Here, the effect of hydrogel composition (alginate, alginate-gelatin, alginate-gelatin-MC, and alginate-MC) on swelling, mechanical, and degradation properties were tested over time. Then, a systematic study was implemented by characterizing the biomaterial flow behavior, 2D and 3D printability of hydrogels with different compositions. Finally, a linear regression model was developed to map the relationships amongst various biomaterial-related and fabricated-related elements affecting printability.

3.3 Materials and methods

3.3.1 Preparation of hydrogels

Medium viscosity Na-Alg from brown algae (Sigma-Aldrich Canada Ltd., P-code 1001172534, with a molecular weight of 80,000 – 120,000 g/mol), was used for the preparation of a 3% w/v alginate (group 1) using distilled water. Gelatin from porcine skin, Type A, Bioreagent, (Sigma-Aldrich Canada Ltd.) was used for the preparation of a 2% w/v alginate and 1% w/v gelatin solution (group 2). MC, phosphate buffer saline, and calcium chloride were obtained from Sigma-Aldrich Canada (Oakville, Ontario, Canada). 1.5% w/v alginate, 1% w/v gelatin and 0.5 % w/v MC were mixed together as group 3. Group 4 was consist of 1.5% w/v alginate and 1.5 % w/v MC

solution. For bulk gel experiments, hydrogels were pipetted into molds to a height of 4 millimeters and incubated with 50 mM calcium chloride at room temperature for cross-linking.

For the ease of discussion, different groups are named here. From now on, group 1 will refer to 3% (w/v) alginate while group 2 will refer to 2% (w/v) alginate and 1% (w/v) gelatin. The third group includes 1.5% (w/v) alginate, 1% (w/v) gelatin and 0.5 % (w/v) MC (group 3). Last group includes 1.5% (w/v) alginate and 1.5 % (w/v) MC (group 4). To have a uniform solution for printing, prepared solutions were stirred, centrifuged, and kept in a refrigerator to get rid of bubbles during the preparation procedure and to ensure complete hydration. In addition, solutions were kept in the nozzle for 20 minutes to have a uniform solution with a stable temperature in the printing head before starting the printing process.

3.3.2 Scaffold fabrication

A 3D Bioplotter (EvisionTec) was used to print scaffolds of 11×11×11 mm. All groups of hydrogels were deposited by using a 200 μm needle inner diameter (EFD, Nordson). Magics13 EnvisionTEC software and Bioplotter RP software were used for CAD model generation and slicing, respectively. Scaffolds were fabricated layer-by-layer, while hydrogel filaments were deposited into a CaCl₂ bath in a 12-well plate. The filament width, pore sizes, pore area, and the perimeter of scaffolds were measured using ImageJ[®] software. To check the uniformity of fabricated scaffolds, at least, 3 scaffolds were printed and evaluated in terms of pore size and strand diameter.

3.3.3 Testing hydrogel construct swelling properties

The initial weights of the hydrogel scaffolds were measured after removing them from the crosslinker solution and the scaffolds were then incubated in 10 mM Phosphate-buffered saline (PBS) solution at 37°C and 5% carbon dioxide. The weights of the samples were again measured after 1 hour, 3 hours, 12 hours, 3 days, 7 days, and 14 days for any change in mass due to swelling. A Kimwipe was used to eliminate excess or free liquid from the scaffold prior to weighing each sample. The swelling of the composite scaffolds was calculated with the following equation:

$$\% \text{ Swelling} = \frac{W_t - W_o}{W_o} \times 100 \quad (3.1)$$

where W_t is the hydrogel weight at the specific time and W_0 is the hydrogel weight at time 0 hours.

3.3.4 Testing the compressive strength of the hydrogel constructs

The hydrogel scaffolds were tested for compression strength using a compressive testing instrument from BOSE (load cell capacity: 20 Newtons). This device measured the forces required to compress a sample to a series of displacements until a maximum displacement of 2 mm was reached. The area and height of the scaffolds were measured using ImageJ® software prior to mechanical testing, and the resulting data were used to plot stress-strain curves for each construct. The elastic modulus was determined by finding the slope of the linear portion of the stress-strain curve.

3.3.5 Testing hydrogel construct degradation properties

Scaffolds were freeze-dried and then weighed to determine their initial masses. To obtain the degraded scaffolds, the samples were incubated in 10 mM PBS solution at 37°C and 5% carbon dioxide for 7, 14, 21, and 28 days. The PBS solution was then taken out of the samples and the samples were freeze-dried and weighed again using a digital scale. The hydrogel degradation was calculated with the following equation:

$$\% \text{ Degradation} = \frac{W_{FD0} - W_{FDt}}{W_{FD0}} \times 100 \quad (3.2)$$

where W_{FDt} is the freeze-dried hydrogel weight at a given time, and W_{FD0} is the freeze-dried hydrogel weight at the time 0.

3.3.6 Flow behavior tests

The flow behavior of various groups of 1 to 4 was investigated at 37°C. A Brookfield Ultra III Rheometer with the CP-41 spindle was used for the testing. The shear rate, shear stress, viscosity, and percentage of torque have been measured at various rotational speeds.

3.3.7 Printability studies on printing parameters and condition

Two dimensional (2D) studies were performed to check the printability of scaffolds by printing lines (scaffolds with two layers). Likewise, follow-up studies were carried out to check the 3D printability of different groups by printing 3D scaffolds. In the following subsections, the

experimental design on how to evaluate the effect of air pressure, nozzle speed, offset, and pattern selection on printability is discussed.

3.3.7.1 Air pressure

For this set of either 2D or 3D studies, air pressure (0.1 to 0.8 bar) and temperature (37, 45, and 55°C) were subjected to changes while other printing parameters such as nozzle speed and the temperature maintained constant.

3.3.7.2 Nozzle speed

For the second set of experiments, nozzle speed was changed starting from 4 mm/s for several pressures (0.1 to 0.4 bar). For this, scaffolds crosslinked mechanically and chemically through using a cold bed and CaCl₂, respectively (except for group 1 crosslinked chemically). For groups crosslinked physically, printing temperature was kept at 37°C while the printing bed temperature was 10°C (pressure: 0.1-0.5 bar, minimum nozzle speed of 10 mm/s). For all groups crosslinked chemically, minimum nozzle speed was 4 mm/s (pressure: 0.1 to 0.4 bar) and group 1 was printed at 24°C while other groups at 37°C.

3.3.7.3 Offset

For the third set of experiments, offset was the variable (-0.08 to 0.08 mm) and the selected temperature was the same as the one for the previous set of experiments (negative values is as per calibration and do not mean any kind of substrate scratching). The offset is the distance from the nozzle to the build platform (Figure 3.1), which was analyzed to determine the influence of the offset on the line width. The nozzle speed was maintained at 35 mm/s (pressure: 0.1 and 0.2 bar).

3.3.7.4 Angular pattern printing

As another part of printability investigation, scaffolds with various angular patterns were printed and evaluated from printability perspective. For this, scaffolds with angular patterns of 0-25°, 0-45°, and 0-90° were printed. Pressure and nozzle speed were maintained between 0.1 and 0.2 bar and 35 to 40 mm/s, respectively. The temperature was maintained as per the nozzle speed experiment.

3.3.8 Printability evaluation

In this study, different evaluations were performed in order to show methods on how to measure printability. For this, firstly, a standard diameter of strands (D_s) was calculated and compared with experimental strand diameter. For this, the following equations were used:

$$\rho = \frac{Mass}{Volume} \quad (3.3)$$

$$Q = \frac{Volume}{Time} \quad (3.4)$$

$$Nozzle\ speed = \frac{4Q}{\pi(D_s)^2} \quad (3.5)$$

where ρ , Q , and D_s are density, flow rate, and standard strand diameter, respectively. Here, different solutions of groups 1 to 4 were purged for a limited time and purged materials were weighted using the Sartorius Scale (model 225d). From Equation 3.3., the volume can be calculated and then using Equation 3.4 and 3.5, flow rate and standard strand diameter can be calculated respectively for different nozzle speeds. For this evaluation, pressure was maintained between 0.2 to 0.4 bar and temperature was same as the one reported in nozzle speed experiment. Based on Equation 3.5, strand printability was defined as:

$$Strand\ printability = 1 - \frac{D_s - D_{exp.}}{D_s} \quad (3.6)$$

where $D_{exp.}$ is experimental strand diameter. As another evaluation, pore printability was checked as it was reported elsewhere [8]. The following equation was used for this purpose.

$$Pore\ printability = \frac{p^2}{16\beta} \quad (3.7)$$

where β and p are the area and perimeter of a pore of a scaffold. As the last evaluation, pore irregularity was defined as:

$$I_{x,y} = \left| \frac{(x,y)_{th} - (x,y)_{exp.}}{(x,y)_{th}} \right| \quad (3.8)$$

where $I_{x,y}$ is the irregularity of the geometry of scaffolds in different directions of X and Y. $(x,y)_{th}$ shows the ideal length of a scaffold in X and Y directions as per design while $(x,y)_{exp.}$ represents experimental lengths in these directions.

3.3.9 Statistical significance

Statistical significance was calculated by performing a student's t-test. For each set of experiment, three replicas were considered at least and data were presented as a mean \pm standard deviation. Significant difference are shown with P-values of $p < 0.05$ and $p < 0.01$. Using Minitab® 17.1 software, a linear regression model was developed with two-sided intervals of confidence with 95% value.

3.4 Results

3.4.1 Mechanical characterization

The swelling properties of hydrogels are indicative of the ability of nutrients and wastes to be exchanged between the environment and cells that would be incorporated into the gels for the production of synthetic tissue. All samples in this study were incubated in PBS to assess the rate of water absorption over time. The change in mass of the hydrogels due to water absorption indicated a trend shown in Figure 3.2.

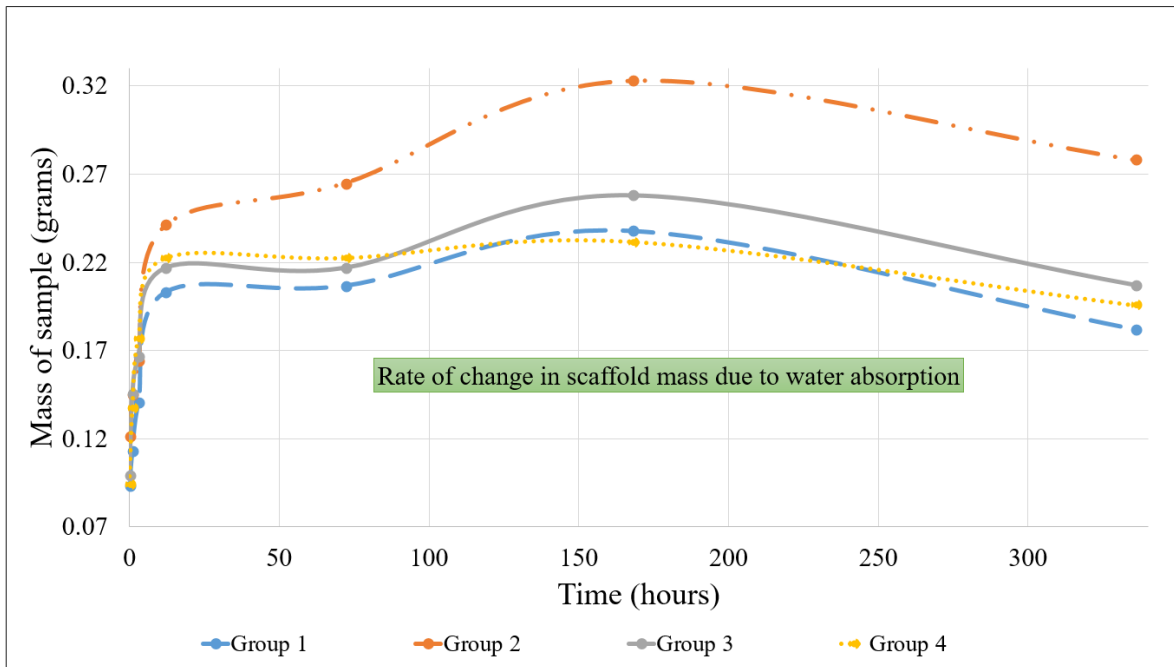


Figure 3.2. The rates of absorption of samples composed of various biomaterials were indicated by the change in mass of the samples over time.

Group 1 showed a 155.10% swelling, group 2 showed 165.95% swelling, group 3 showed 160.93% swelling, and group 4 showed 146.75% swelling after 168 hours of incubation with PBS. According to the data, group 2's hybrid hydrogels showed the highest rate of absorption indicated by the highest change in mass over time of incubation. The degradation rate of each sample was also measured by observing the change in mass of the samples after immersion in PBS over time. The pure alginate samples (group 1), group 2, group 3, and group 4 showed 32.53%, 13.33%, 40.00%, and 19.70% degradation, respectively, over time incubated in PBS. PBS has been used widely to evaluate the degradation rate of scaffolds as reported by [11,28–30]. Notably, as future work, other solutions such as fetal bovine serum and penicillin-streptomycin contained medium can be used to check the degradation rate of scaffolds. The alginate-gelatin-MC and pure alginate gels showed the greatest rate of degradation. The compressive strength of all groups was determined by finding the elastic modulus of each sample over weekly intervals of time, and the results are shown in Figure 3.3.

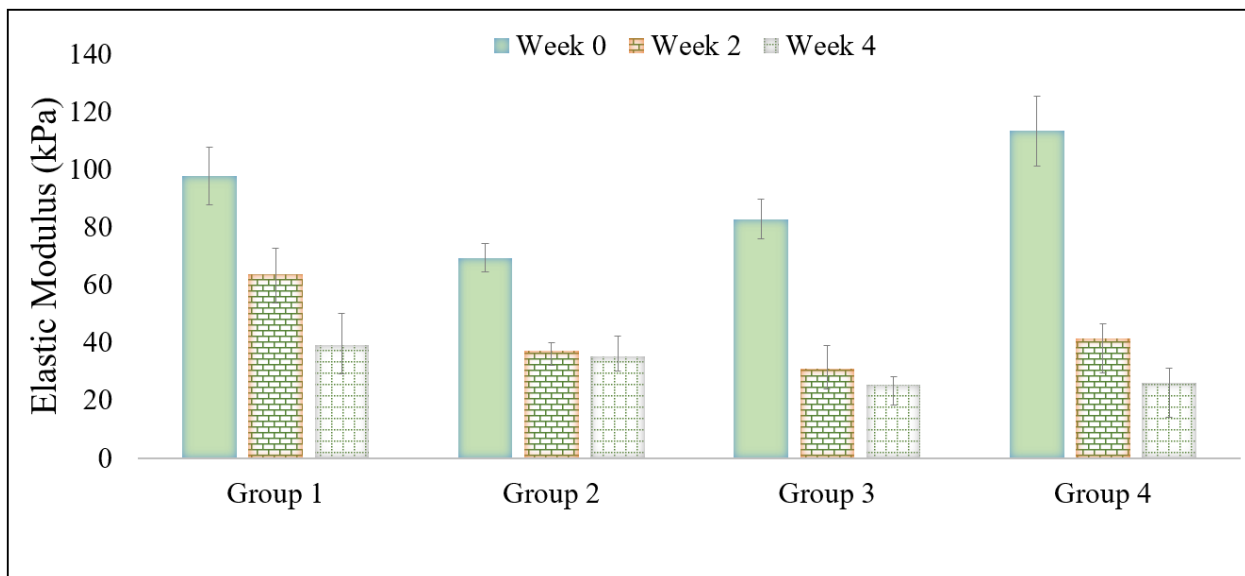


Figure 3.3. The compressive strength of the scaffolds of varying composition over time is shown here. Statistical significance was calculated using a Student's t-test (was and ** were used to represent $p < 0.05$ and $p < 0.01$, respectively).*

The elastic moduli of group 1's samples was 97.7 kPa, 63.8 kPa, and 39.1 kPa while for group 2's samples, it was 69.4 kPa, 37.1 kPa, and 35.2 kPa during the 0, 2, and 4 weeks of incubation in PBS, respectively. The values for group 3's samples were 82.85 kPa, 31 kPa, and 25.4 kPa, and the values for group 4's samples were 113.3 kPa, 41.45 kPa, and 26.1 kPa. Results

indicated that there was a decline in the compressive strength of each of the hydrogels that was especially evident in the first two weeks. After the first two weeks of immersion, the decline in compressive strength was more pronounced in pure alginate gels than the composite polymer samples. Furthermore, scaffolds of group 4 had a significantly higher elastic modulus compared to the hybrid constructs containing gelatin.

3.4.2 Flow behavior results

The flow behavior of all four groups was analyzed and Figure 3.4 shows the results of shear rate versus shear stress. At the same shear rate, group 1 showed higher shear stresses. Both groups of 3 and 4, which contain MC had a linear stress/strain behavior while other groups of 1 and 2 showed a non-Newtonian behavior.

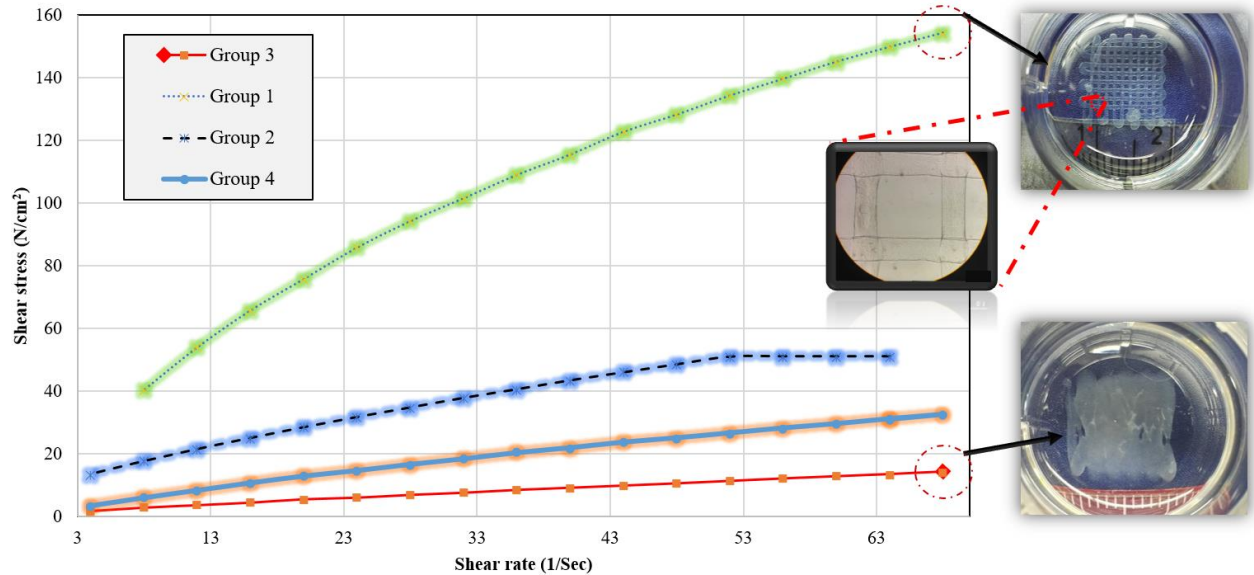


Figure 3.4. Shear stress as a function of the Shear rate for each solution.

Based on results obtained from Figure 3.4, the viscosity was calculated and the results showed high viscosity of group 1 followed by other groups of 2, 4, and 3. It was reported that 300 to 30000 cps is a suitable range of viscosity for printable biomaterials [2]. Our results showed that all groups except for group 3 are in this range (Table 3.1).

Table 3.1. Viscosity behavior for different groups.

Groups	Min viscosity (cps)	Max viscosity (cps)
1	2245.435 ± 37.29	6582.08 ± 55.73
2	783.21 ± 56.95	1375.36 ± 69.46
3	205.15 ± 12.26	466.64 ± 34.73
4	476.62 ± 4.27	835.04 ± 69.47

3.4.3 Effect of printing parameters on 2D printability

3.4.3.1 Pressure test

The air pressure is one of the most critical factors affecting printability [2]. Every biomaterial has a surface tension and in order to print a biomaterial, a pressure more than the surface tension of biomaterials should be applied. Figure 3.5 shows the effect of printing pressure on purging status of group 2 and 4 at different temperatures, as an illustration. We defined D_s as the distance between the end of the needle and the position that the droplet of biomaterial separates. As such, for different biomaterials, D_s can be measured and to this end, suitable pressure and temperature can be selected. As shown, for some groups, even at 0.3 bar, the biomaterial is not printable and it is like a droplet hanging from the needle. On the other hand, higher pressures cause instability of extruded biomaterial and subsequently, poor printability. Group 1 behaved like a highly viscous biomaterial and was not printable at 37 °C (0.2 bar). At higher pressures, D_s was between 4.8 to 25.8 mm and higher pressures showed higher D_s . Group 3 showed a non-viscous behavior and even at 0.2 bar pressure, D_s more than 7.5 mm was observed. Our results showed that 0.2 bar is a suitable pressure to dominate the surface tension of biomaterials for group 1, 2, and 4 while 0.1 bar was found more suitable for group 3.

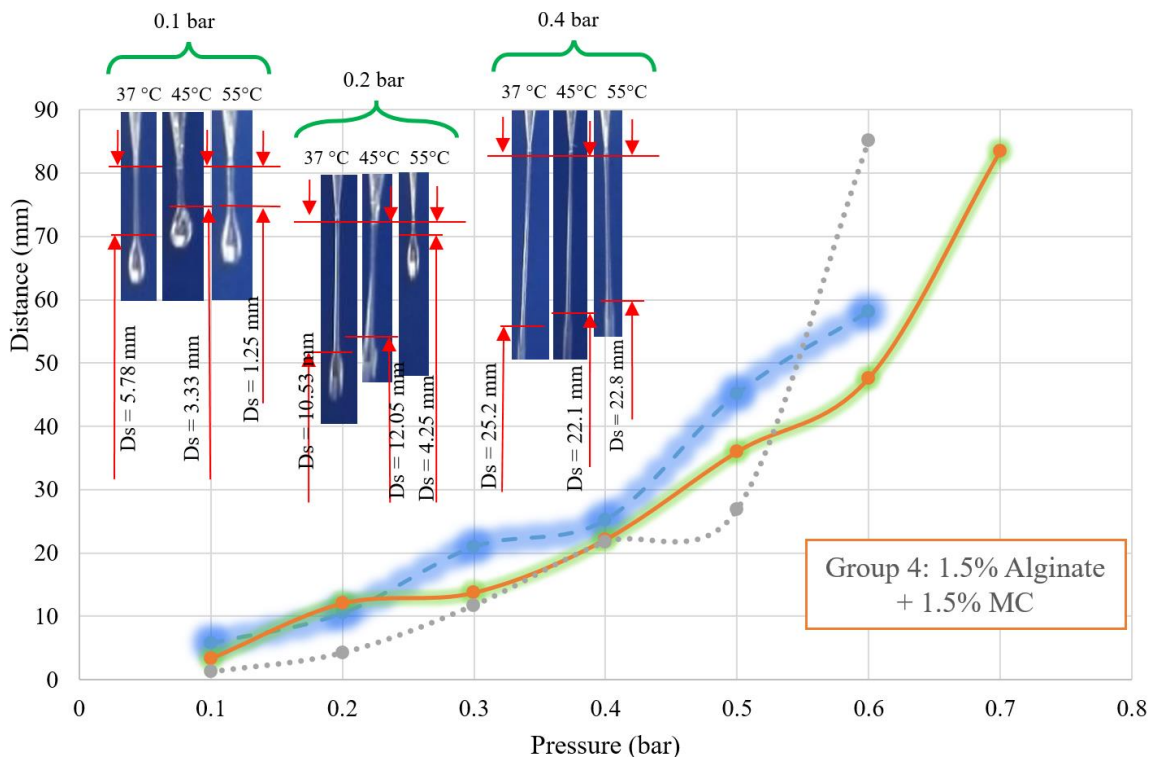
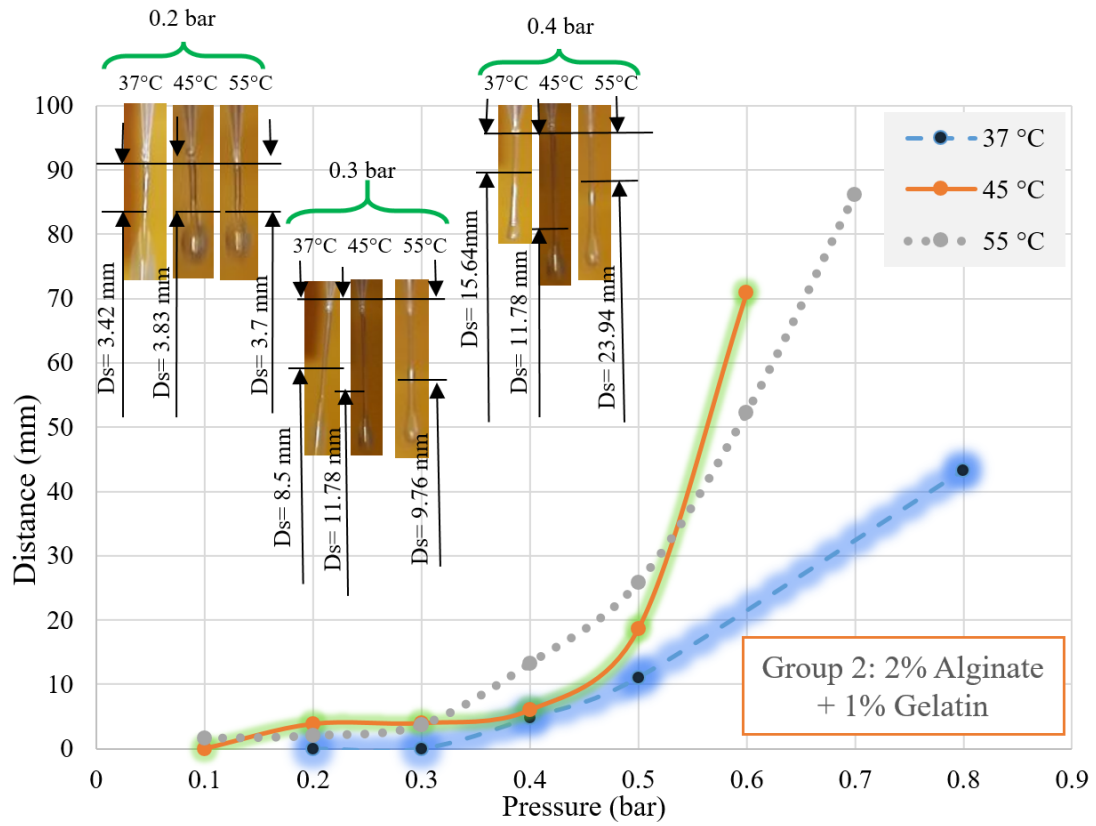


Figure 3.5. Effect of printing pressure on D_s for groups 2 and 4, as an illustration.

3.4.3.2 Nozzle speed test

For this set of experiments, nozzle speed was subjected to changes. Firstly, physical crosslinking was used and groups 2, 3, and 4 were printed on a cold bed (10°C). However, poor printability was observed for all groups. Hence, chemical crosslinking was implemented by using a 50 mM CaCl₂. Using Equations 3.3 to 3.5, the standard strand diameter was calculated for all groups. Figure 3.6 shows results for all groups including experimental and standard strand diameter (inset images are printed scaffolds for group 2 at different nozzle speeds of 6, 14, 18, and 26 mm/s, as an illustration). Results showed that the experimental and theoretical values of strand diameter for group 1 are similar at nozzle speed of less than 8 mm/s while 12 mm/s was observed as a suitable speed for group 2. For group 3, experimental and theoretical values were more similar at higher speeds of more than 30 mm/s while 18 to 24 mm/s were identified more suitable for group 4. Overall, in all groups, there was a range of nozzle speed that theoretical and experimental values were close and speeds that fall under or above that range caused poor strand printability. In addition, generally speaking, by increasing the nozzle speed, thinner strand diameters were achieved.

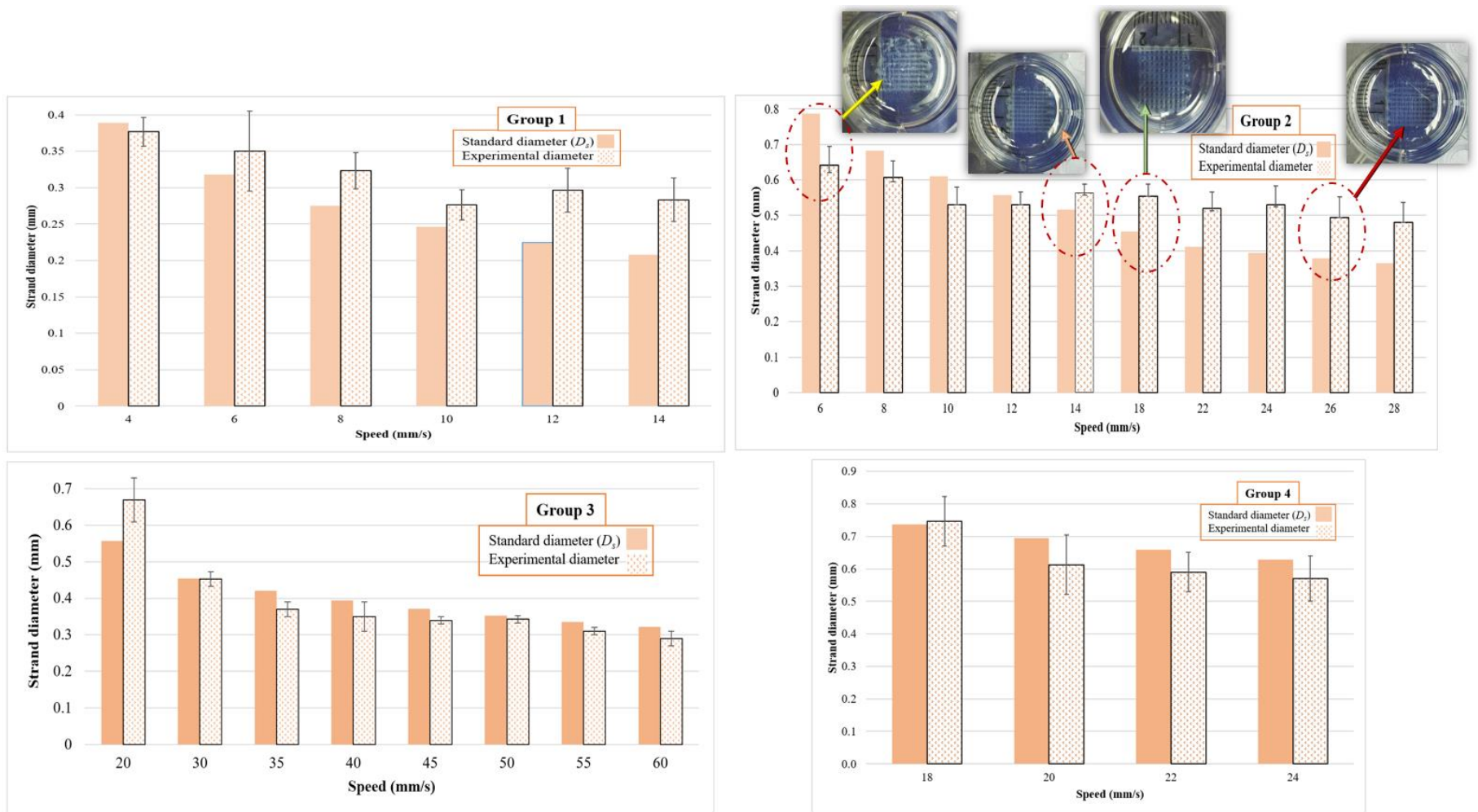


Figure 3.6. Effect of nozzle speed on printability of groups 1 to 3 (pressure: 0.2 bar) and 4 (pressure: 0.1 bar): comparison between D_s and experimental strand diameter (inset images are printed scaffolds for group 2 at different nozzle speeds of 6, 14, 18, and 26 mm/s, as an illustration).

Strand printability and pore printability results have been shown in Table 3.2. Those values that were close to 1 ± 0.1 were considered acceptable for both pore and strand printability.

Table 3.2. Effect of nozzle speed on strand and pore printability.

Groups	Pressure (bar)	Speed	Strand printability	Pore printability	
1	0.2	4	0.97 ± 0.060	1.01 ± 0.002	
	0.2	6	1.10 ± 0.180	1.01 ± 0.012	
	0.2	8	1.18 ± 0.090	1.01 ± 0.009	
	0.2	10	1.12 ± 0.140	1.01 ± 0.003	
	0.2	12	1.32 ± 0.150	1.00 ± 0.003	
	0.2	14	1.36 ± 0.150	0.98 ± 0.022	
2	0.2	6	0.81 ± 0.066	1.139 ± 0.086	
	0.2	8	0.89 ± 0.069	1.050 ± 0.042	
	0.2	10	0.91 ± 0.083	1.066 ± 0.070	
	0.2	12	0.95 ± 0.062	1.010 ± 0.006	
	0.2	14	1.09 ± 0.049	1.048 ± 0.054	
	0.2	18	1.22 ± 0.077	1.002 ± 0.015	
3	0.2	22	1.26 ± 0.111	1.04 ± 0.027	
	3	0.1	20	1.203 ± 0.136	1.152 ± 0.135
		0.1	30	0.997 ± 0.067	1.012 ± 0.019
		0.1	35	0.871 ± 0.059	1.010 ± 0.010
		0.1	40	0.897 ± 0.106	1.010 ± 0.018
		0.1	45	0.925 ± 0.056	1.045 ± 0.065
		0.1	50	0.975 ± 0.059	1.033 ± 0.041
0.1		55	0.923 ± 0.052	0.937 ± 0.122	
4	0.2	18	1.075 ± 0.110	1.338 ± 0.488	
	0.2	20	0.931 ± 0.138	0.974 ± 0.036	
	0.2	22	0.939 ± 0.097	0.982 ± 0.056	
	0.2	24	0.947 ± 0.116	1.039 ± 0.029	

3.4.3.3 Offset test

For this section of studies, the offset was subjected to changes. Figure 3.7 shows results of offset, showing that offset can significantly affect strand diameter. All groups printed with $200 \mu\text{m}$ needle but a wide range of strand diameter (between 0.1 to 0.6 mm) was observed modulating the offset.

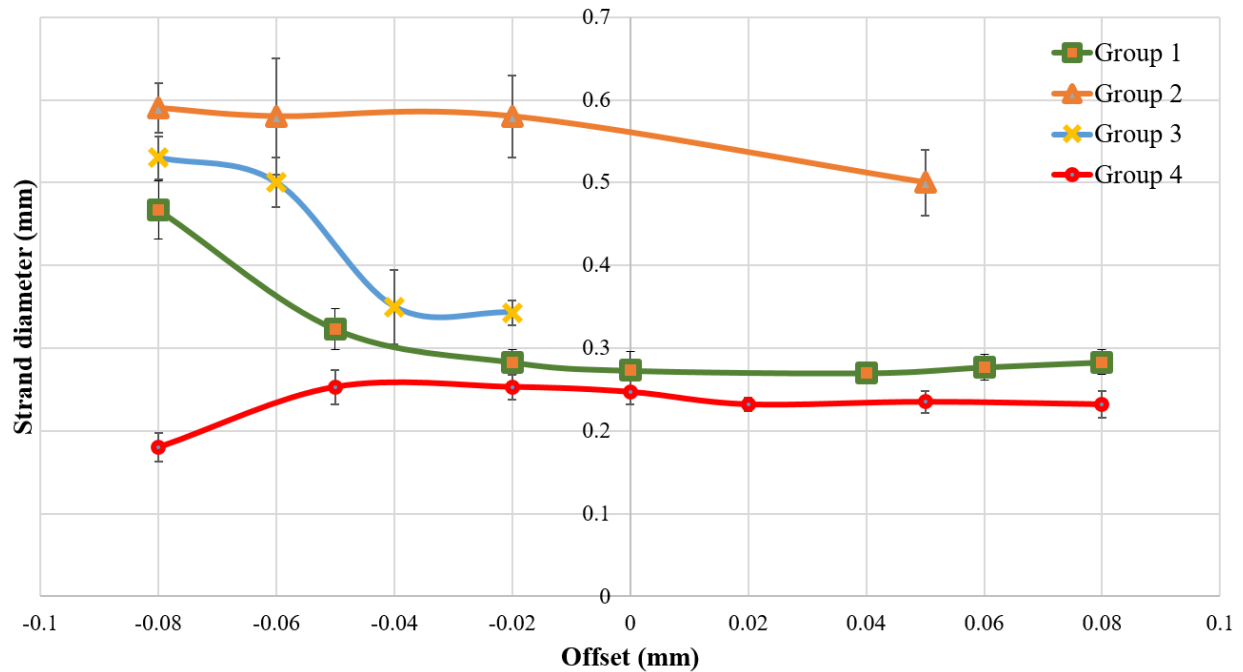


Figure 3.7. Effect of offset on the strand diameter of scaffolds made of groups 1 to 4.

3.4.3.4 Printing angular patterns

Scaffolds with acute, right, and obtuse angles were printed (Figure 3.8). Angular pattern printability results showed that not all groups can have good angle printability for 25° and 45° . The printing quality became worst at right angles so that a huge difference was observed in those that printed with $0-90^\circ$ laydown pattern than $0-25^\circ$ ones.

Groups	CAD angle (°)	Measured angle (°)
1	0-25	26.94 ± 6.95
	0-45	45.42 ± 4.16
	0-90	100.60 ± 4.32
2	0-25	24.84 ± 2.93
	0-45	46.41 ± 9.48
	0-90	111.56 ± 16.30
3	0-25	25.943 ± 7.48
	0-45	42.340 ± 1.06
	0-90	138.353 ± 8.03
4	0-25	21.82 ± 2.94
	0-45	33.33 ± 3.84
	0-90	122.46 ± 17.30

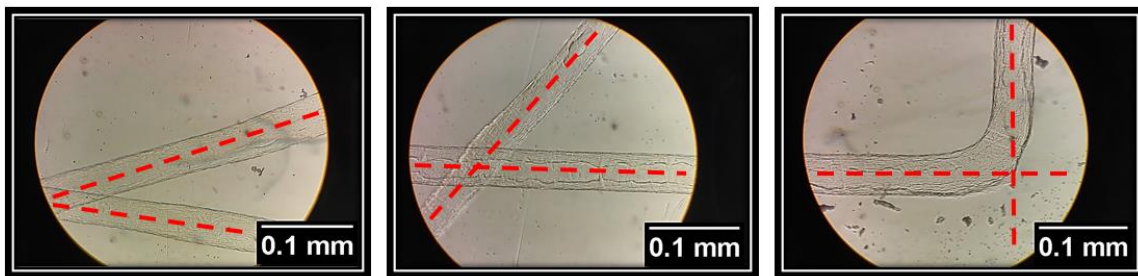
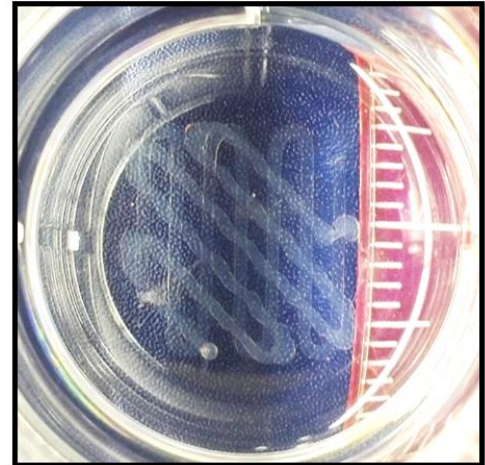
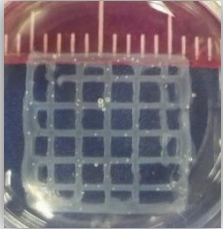
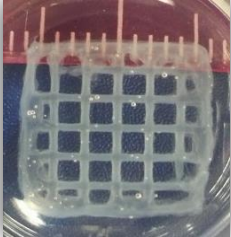
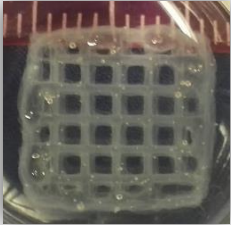



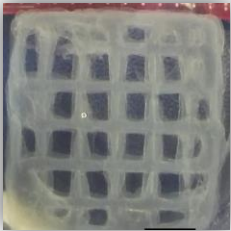
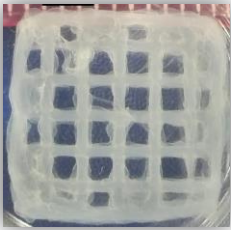
Figure 3.8. Effect of the angular pattern on printability of scaffolds with acute, right, and obtuse angles.

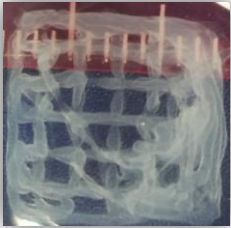
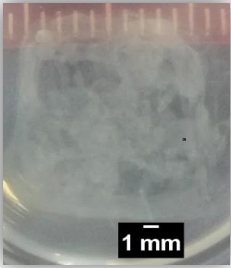

3.4.4 Effect of printing parameters on 3D printability

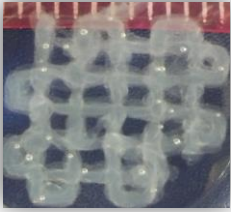

In the proceeding sections, 2D printability was presented and in this sections, 3D printability is discussed in terms of irregularity in the X and Y directions, pore printability, and strand printability for scaffolds made from different groups of given biomaterials (5, 10, and 15 layers). Table 3.3 shows results for irregularity, pore and strand printability, as well as top views of scaffolds with 5, 10, and 15 layers.

Table 3.3. 3D printability results for bioplotted scaffolds made from groups 1 to 4 (✗ shows that biomaterials were not printable or a large deviation has been observed).

Groups	Printed layers	Irregularity X	Irregularity Y	Pore printability	Strand printability	Printed scaffold (top view)
1	5	0.08	0.05	0.96 ± 0.02	1.29 ± 0.07	
	10	0.05	0.06	1.00 ± 0.04	1.71 ± 0.07	
	15	0.10	0.07	1.00 ± 0.01	1.64 ± 0.09	

2	5	0.07	0.03	0.97 ± 0.02	1.22 ± 0.02	
	10	0.09	0.03	1.01 ± 0.01	1.92 ± 0.27	
	15	0.09	0.08	0.97 ± 0.02	1.70 ± 0.25	

3	5	0.07	0.03	1.02 ± 0.07	×	
	10	×	×	×	×	
4	5	0.11	0.06	1.05 ± 0.45	1.10 ± 0.34	

	10	0.08	0.07	0.97 ± 0.05	1.01 ± 0.11	
	15	×	×	×	×	

3.5 Discussion

Different methods of scaffold design can be used to manipulate the mechanical properties of hydrogel scaffolds to those that are best suited for cell support. Various studies have shown that it is crucial for the mechanical properties of scaffolds to be carefully controlled to successfully simulate the ECM which supports cells in human tissue because there is a dynamic relationship between cell growth and viability and the ECM [25,31–34]. These experiments have shown that water retention rate, elasticity, and degradation rate of a hydrogel construct can, to some extent, be controlled by changing the material composition of the scaffold. In this study, hydrogels containing alginate-gelatin showed a higher water retention capacity than the pure alginate gels. One possible explanation for this observation is that pure alginate molecules experience stronger intermolecular forces with one another than when they are part of hybrid hydrogels. Adding gelatin or MC may interfere with the intermolecular forces between adjacent alginate molecules, and as a result, the attraction between the alginate molecules and surrounding water molecules may be stronger than in pure alginate hydrogels, which leads to greater water absorption. Furthermore, the melting point of gelatin is about 35°C [35], therefore at 37°C gelatin would be in liquid form, and as a result, there would be gaps in the scaffold which would be replaced by the surrounding water molecules. This would lead to a higher absorption rate when compared to a pure alginate hydrogel sample. This high water retention capacity allows cells to readily exchange important molecules such as ions and signaling molecules with their environment [25].

Additionally, hybrid hydrogels containing gelatin had a lower elastic modulus compared to alginate-MC hybrid hydrogels, possibly because of the degradation of gelatin at physiological temperatures. The decomposition of gelatin due to its melting point of around 35°C would cause the formation of gaps in the construct, and this could compromise its mechanical stability and result in a lower elastic modulus. These results indicate that hydrogels can be constructed with different materials depending on the degree of stiffness that is necessary for the tissue type that requires regeneration. This allows for better specificity and control in scaffold design and construction.

Group 3 showed the highest percentage of degradation in comparison to the other hydrogels. MC is soluble in water at temperatures lower than 40°C-50°C, as mentioned earlier,

has a melting point of about 35°C [35,36]. The weakened intermolecular interactions of MC and gelatin at physiological temperature would, therefore, lead to a high rate of degradation of this gel over time. Here, we proposed some compositions with various mechanical and swelling/degradation rates.

Our results also showed different flow behavior from Newtonian to non-Newtonian ones. Group 1, having the highest viscosity, showed a good printability discussed elaborately later on. It means that the more viscous biomaterial, the more appropriate printability achieved. However, high viscous biomaterials may not be printable. Referring back to the mentioned general rule, an appropriate range of viscosity from 300 to 30000 cps is recommended. Group 4 was not in the recommended range, which was in agreement with our printability results so that a poor printability was observed for this group. Notably, as we use lower viscous biomaterials, likewise, higher speeds should be implemented and it may cause difficulties for printing such as sudden direction changes in the edges of scaffolds.

From an air pressure perspective, group 1 behaved like a highly viscous biomaterial but as mentioned, it is always recommended to mix alginate with other biomaterials to achieve synergistic properties. However, adding gelatin or MC to alginate reduced the viscosity of the final solutions, as we discussed previously on the variation of viscosity observed in different groups. That being said, comparing to group 1, for other groups a lower amount of pressure is required to dominate the surface tension of biomaterials. Studying the effect of pressure on D_s can clarify an appropriate range of pressure, suitable for printing. Due to having several groups with different viscosities, pressures in between 0.1 to 0.2 showed good results and at either lower or higher pressures, the biomaterials were not printable or had an unstable printing condition due to applying a high pressure. Referring to the changes in viscosity of different groups, lower viscous groups were printable at relatively higher nozzle speeds. It means that due to having relatively lower viscosities (e.g. groups 3 and 4), biomaterials flow easily and so at the same pressure, it is required to increase the nozzle speed to prevent extra deposition of biomaterials. As mentioned, group 1 was printable appropriately at speeds around 10 mm/s while the starting point of speed for group 3 and 4 was more than 18 mm/s (Figure 3.6).

From 2D strand and pore printability point of view, group 1 had acceptable strand printability for speeds ranging from 4 to 8 mm/s whereas pore printability showed acceptable results for speeds in between 4 to 14 mm/s. However, group 2 had not acceptable strand printability for the speed of less than 8 mm/s. This might be due to having a lower viscosity than group 1, and so higher speeds are required to reach acceptable printability. In addition, speeds higher than 14 mm/s showed poor strand printability for group 2 whereas, for all speeds in between 6 to 22 mm/s, pore printability was acceptable. It means that using some speeds we may have acceptable pore printability while strand printability may not be acceptable. Hence, both pore and strand printability should be considered together to find suitable nozzle printing speed rather than taking either pore or strand printability into account separately. It should be noted that the criteria used keeps account only of pore shape. In this case, it means that for the cited parameters, the scaffolds still present perfectly square pores but with different size from the design. For group 3, speeds more than 30 mm/s showed an appropriate range of pore and strand printability. For the last group, all speeds in between 18 to 24 mm/s showed acceptable printability.

Using offset of -0.02 to 0.08 mm, strand diameter in between 200 to 300 μm was observed for groups 1 and 4. At offset less than -0.02 mm, a significant change in strand diameter was observed. For group 3, strand diameters of more than 300 μm were observed and this may be due to having low viscosity resulting in having quick biomaterial flow leading to having a relatively large strand diameter. Group 4 showed a decrease in strand diameter by increasing the offset. The offset should be selected carefully because having large space between printing bed and needle lead to non-continuous printing and having small offset may lead to squeezing the biomaterial and preventing the proper flow of biomaterial during the deposition.

Regarding angle printing, at acute angles, angle printability was acceptable while, for example, at 90° poor printability was observed in terms of angle. These results were interpreted as meaning that changing the needle direction by having a sharp angle of more than 90 may lead to poor angle printability due to a sudden change of the direction of the nozzle. Such a change in direction may cause stretching of strands and results in modulating the strand diameter as well.

In agreement with 2D printability results, 3D printability studies showed that all printed scaffolds have acceptable pore printability while strand printability was not acceptable (most

values were more than 1 ± 0.1). As mentioned, the criteria used keeps account only of pore shape. Hence, both pore and strand printability should be considered. Surprisingly, strand printability has been neglected in the literature and our results showed that while having acceptable pore printability, scaffolds can have poor strand printability. One possible solution to address poor strand printability is to modulate the nozzle speed at constant pressures to get closer to the theoretical values. However, using such an approach, other interrelated factors, such as pore printability, can be affected. Except for group 4, all groups showed less than 10 percent irregularity in the *X* and *Y* directions. For groups 1 and 2, scaffolds with 15 layers were printed but groups 3 and 4 showed poor printability for scaffolds made from more than 5 layers. Referring back to flow behavior results, groups 3 and 4 with relatively lower viscosities showed poor printability whereas other groups showed better printability. The viscosity of biomaterials can significantly influence the printability of bioplotted scaffolds so as high viscosity biomaterials need higher pressure and low viscous ones require less pressure to be extruded.

Overall, there are many factors causing a deviancy between experimental and theoretical values including pressure, nozzle speed, and offset, as interrelated elements from printability perspective and modulating one of them can affect the other elements. That being said, all elements should be selected carefully so as to avoid, on one hand, any strand coiling owing to over-extrusion of an extruded strand, and on the other hand, using a low pressure that cannot dominate the surface tension of the biomaterial. To make a clear picture of printability and significantly effective elements, the following linear regression models were developed (R^2 more than 85%) to map the relationship amongst the studied parameters including nozzle speed, pore and strand printability for 2D printing (Table 3.4), based on results presented in Table 3.2.

Table 3.4 Linear regression models created based on experimental results reported in Table 3.2.

Groups	Applied pressure (bar)	linear regression models (nozzle speed: N_s, pore printability: P, strand printability: S)
1	0.2	$S = 51.5 - 3.39 N_s - 50.1 P + 3.38 N_s \times P$

2	0.2	$S = 0.08 + 0.108 N_s + 0.53 P - 0.075 N_s \times P$
3	0.1	$S = -2.06 + 0.0528 N_s + 2.96 P - 0.0525 N_s \times P$
4	0.2	$S = -0.6298 + 0.06394 N_s + 1.534 P - 0.06222 N_s \times P$

It is worthwhile to cite the fact that a high concentration of alginate is not an appropriate environment for cells [37]. High concentrations of alginate can interrupt diffusion mass transfer mechanism and lead to low cell viability. Inhabitation of cell migration/proliferation is another reason for avoiding high concentration alginate. That being said, the present study showed that we may mix other cell-friendly hydrogels such as gelatin in order to have a low concentration of alginate along with improving the printability of such a low concentration alginate.

3.6 Conclusions

Hydrogels are valuable with respect to their ability to serve as an appropriate environment for cells due to their ease of preparation and similarity to the ECM of many human tissues. Extrusion-based bioprinting method is used widely to create hydrogel scaffolds used extensively for different tissue engineering applications. In this regard, it is highly recommended to mix hydrogels to achieve synergistic properties. Here we examined the swelling, as well as degradation, rate and mechanical properties (elastic moduli) of hydrogels with various compositions of alginate, gelatin, and MC. Results showed that composite hydrogels have better water absorption ability compared to pure alginate hydrogel. Additionally, all combinations of hydrogels showed a decreasing pattern of elastic modulus with time, while alginate-MC combination gels showed the highest elastic moduli. After evaluating scaffolds from the mechanical perspective, more experiments were conducted to investigate the hydrogel printability. Results showed that biomaterial-related elements such as viscosity and fabrication-related ones such as air pressure, nozzle speed, offset, and selected angular pattern can influence the printing quality. Modulating these parameters, it is possible to improve the printability of different groups of hydrogels including alginate, gelatin, and MC. Conducting research studies on printability can

open the door for further improvement in the fabrication of hydrogel scaffolds using the extrusion-based technique. To conclude, taking biomaterial- and fabrication-related elements, printability can be improved and accordingly, scaffolds can be specialized depending on which tissue requires regenerative tissue therapy.

3.7 References

- [1] S. Naghieh, M. Sarker, M. Izadifar, X. Chen, Dispensing-based bioprinting of mechanically-functional hybrid scaffolds with vessel-like channels for tissue engineering applications – a brief review, *J. Mech. Behav. Biomed. Mater.* 78 (2018) 298–314. doi:10.1016/j.jmbbm.2017.11.037.
- [2] Y. He, F. Yang, H. Zhao, Q. Gao, B. Xia, J. Fu, Research on the printability of hydrogels in 3D bioprinting, *Sci. Rep.* 6 (2016) 29977. doi:10.1038/srep29977.
- [3] S. Naghieh, M.R. Karamooz-Ravari, M. Sarker, E. Karki, X. Chen, Influence of crosslinking on the mechanical behavior of 3D printed alginate scaffolds: Experimental and numerical approaches, *J. Mech. Behav. Biomed. Mater.* 80 (2018) 111–118. doi:10.1016/j.jmbbm.2018.01.034.
- [4] A. Skardal, A. Atala, Biomaterials for integration with 3-D bioprinting, *Ann. Biomed. Eng.* 43 (2015) 730–746.
- [5] H. Ding, R.C. Chang, Printability Study of Bioprinted Tubular Structures Using Liquid Hydrogel Precursors in a Support Bath, *Appl. Sci.* 8 (2018) 403.
- [6] J.H. Wen, L.G. Vincent, A. Fuhrmann, Y.S. Choi, K.C. Hribar, H. Taylor-Weiner, S. Chen, A.J. Engler, Interplay of matrix stiffness and protein tethering in stem cell differentiation, *Nat. Mater.* 13 (2014) 979–987.
- [7] J.H.Y. Chung, S. Naficy, Z. Yue, R. Kapsa, A. Quigley, S.E. Moulton, G.G. Wallace, Bio-ink properties and printability for extrusion printing living cells, *Biomater. Sci.* 1 (2013) 763–773.
- [8] L. Ouyang, R. Yao, Y. Zhao, W. Sun, Effect of bioink properties on printability and cell viability for 3D bioplotting of embryonic stem cells, *Biofabrication.* 8 (2016) 35020. doi:10.1088/1758-5090/8/3/035020.
- [9] L.E. Bertassoni, J.C. Cardoso, V. Manoharan, A.L. Cristino, N.S. Bhise, W.A. Araujo, P. Zorlutuna, N.E. Vrana, A.M. Ghaemmaghami, M.R. Dokmeci, Direct-write Bioprinting of Cell-laden

- Methacrylated Gelatin Hydrogels, *Biofabrication*. 6 (2014) 1–19. doi:10.1088/1758-5082/6/2/024105.Direct-write.
- [10] M. Sarker, M. Izadifar, D. Schreyer, X. Chen, Influence of ionic crosslinkers (Ca²⁺/Ba²⁺/Zn²⁺) on the mechanical and biological properties of 3D Bioprinted Hydrogel Scaffolds, *J. Biomater. Sci. Polym. Ed.* 29 (2018) 1126–1154.
- [11] M.D. Sarker, S. Naghieh, A.D. McInnes, L. Ning, D. Schreyer, X. Chen, Bio-fabrication of peptide-modified alginate scaffolds: Printability, mechanical stability and neurite outgrowth assessments, *Bioprinting*. (2019) e00045.
- [12] F. You, X. Wu, X. Chen, 3D Printing of Porous Alginate/gelatin Hydrogel Scaffolds and Their Mechanical Property Characterization, *J. Int. J. Polym. Mater. Polym. Biomater.* 66 (2016) 299–306. doi:10.1080/00914037.2016.1201830.
- [13] S. V Murphy, A. Atala, 3D bioprinting of tissues and organs, *Nat. Biotechnol.* 32 (2014) 773–785. doi:10.1038/nbt.2958.
- [14] J. Göhl, K. Markstedt, A. Mark, K. Håkansson, P. Gatenholm, F. Edelvik, Simulations of 3D bioprinting: predicting bioprintability of nanofibrillar inks, *Biofabrication*. 10 (2018) 34105.
- [15] S. Kyle, S. Kyle, Z.M. Jessop, A. Al-sabah, I.S. Whitaker, 'Printability' of Candidate Biomaterials for Extrusion Based 3D Printing : State-of-the-Art 'Printability' of Candidate Biomaterials for Extrusion Based 3D Printing : State-of-the-Art, *Adv. Healthc. Mater.* (2017). doi:10.1002/adhm.201700264.
- [16] M. Müller, E. Öztürk, Ø. Arlov, P. Gatenholm, M. Zenobi-Wong, Alginate Sulfate-Nanocellulose Bioinks for Cartilage Bioprinting Applications, *Ann. Biomed. Eng.* 45 (2016) 1–14. doi:10.1007/s10439-016-1704-5.
- [17] J.K. Gandhi, E.C. Opara, E.M. Brey, Alginate-based strategies for therapeutic vascularization., *Ther. Deliv.* 4 (2013) 327–41. doi:10.4155/tde.12.163.
- [18] F.E. Freeman, D.J. Kelly, Tuning Alginate Bioink Stiffness and Composition for Controlled Growth Factor Delivery and to Spatially Direct MSC Fate within Bioprinted Tissues, *Sci. Rep.* (2017) 1–12. doi:10.1038/s41598-017-17286-1.

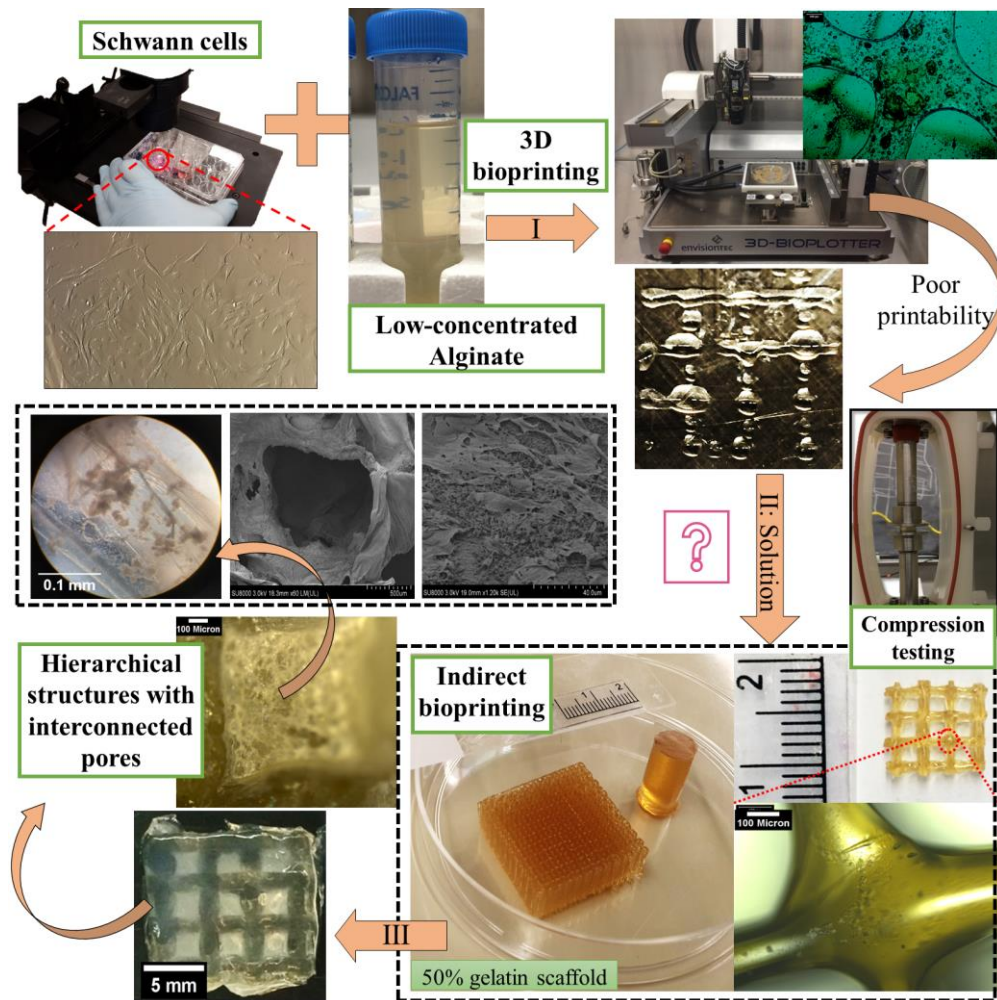
- [19] J. Ivanovska, T. Zehnder, P. Lennert, B. Sarker, A.R. Boccaccini, A. Hartmann, R. Schneider-Stock, R. Detsch, Biofabrication of 3D Alginate-Based Hydrogel for Cancer Research: Comparison of Cell Spreading, Viability, and Adhesion Characteristics of Colorectal HCT116 Tumor Cells, *Tissue Eng. Part C Methods*. 22 (2016) 708–715. doi:10.1089/ten.tec.2015.0452.
- [20] S.P.M. Bohari, D.W.L. Hukins, L.M. Grover, Effect of calcium alginate concentration on viability and proliferation of encapsulated fibroblasts, *Biomed. Mater. Eng.* 21 (2011) 159–170. doi:10.3233/BME-2011-0665.
- [21] Y. Luo, G. Luo, M. Gelinsky, P. Huang, C. Ruan, 3D bioprinting scaffold using alginate/polyvinyl alcohol bioinks, *Mater. Lett.* (2016). doi:10.1016/j.matlet.2016.12.009.
- [22] L. Ning, Y. Xu, X. Chen, D.J. Schreyer, Influence of mechanical properties of alginate-based substrates on the performance of Schwann cells in culture, *J. Biomater. Sci. Polym. Ed.* 27 (2016) 898–915. doi:10.1080/09205063.2016.1170415.
- [23] K. Markstedt, A. Mantas, I. Tournier, H. Martínez Ávila, D. Hägg, P. Gatenholm, 3D Bioprinting Human Chondrocytes with Nanocellulose Alginate Bioink for Cartilage Tissue Engineering Applications, *Biomacromolecules*. 16 (2015) 1489–1496. doi:10.1021/acs.biomac.5b00188.
- [24] A. Habib, V. Sathish, S. Mallik, B. Khoda, 3D printability of alginate-carboxymethyl cellulose hydrogel, *Materials (Basel)*. 11 (2018) 454.
- [25] C. Ivanov, M. Popa, M. Ivanov, A.A. Popa, Synthesis of poly (vinyl alcohol) - methyl cellulose hydrogel as possible scaffolds in tissue engineering, *J. Optoelectron. Adv. Mater.* 9 (2007) 3440–3444.
- [26] T. Pan, W. Song, X. Cao, Y. Wang, 3D bioplotting of gelatin/alginate scaffolds for tissue engineering: influence of crosslinking degree and pore architecture on physicochemical properties, *J. Mater. Sci. Technol.* 32 (2016) 889–900.
- [27] T. Gao, G.J. Gillispie, J.S. Copus, A.K.P.R. Asari, Y.-J. Seol, A. Atala, J.J. Yoo, S.J.J. Lee, Optimization of gelatin-alginate composite bioink printability using rheological parameters: a systematic approach, *Biofabrication*. (2018).
- [28] S.-H. Lee, J.H. Lee, Y.-S. Cho, Analysis of degradation rate for dimensionless surface area of well-

- interconnected PCL scaffold via in-vitro accelerated degradation experiment, *Tissue Eng. Regen. Med.* 11 (2014) 446–452.
- [29] S. Naghieh, M.D. Sarker, E. Abelseh, X. Chen, Indirect 3D bioprinting and characterization of alginate scaffolds for potential nerve tissue engineering applications, *J. Mech. Behav. Biomed. Mater.* (2019).
- [30] T. Huang, C. Fan, M. Zhu, Y. Zhu, W. Zhang, L. Li, 3D-printed scaffolds of biomaterialized hydroxyapatite nanocomposite on silk fibroin for improving bone regeneration, *Appl. Surf. Sci.* 467 (2019) 345–353.
- [31] R. Singhvi, A. Kumar, G.P. Lopez, G.N. Stephanopoulos, D.I. Wang, G.M. Whitesides, D.E. Ingber, Engineering cell shape and function., *Science*. 264 (1994) 696–8. doi:10.1126/science.8171320.
- [32] C.S. Chen, Geometric Control of Cell Life and Death, *Science* (80-.). 276 (1997) 1425–1428. doi:10.1126/science.276.5317.1425.
- [33] S. Nanda, N. Sood, B.V.K. Reddy, T.S. Markandeywar, Preparation and Characterization of Poly (vinyl alcohol) -chondroitin Sulphate Hydrogel as Scaffolds for Articular Cartilage Regeneration, 2013 (2013).
- [34] M.W. Tibbitt, K.S. Anseth, Hydrogels as extracellular matrix mimics for 3D cell culture, *Biotechnol. Bioeng.* 103 (2009) 655–663.
- [35] S. Shariff, A.K. Kaler, Principles & Interpretation of Laboratory Practices in Surgical Pathology, JP Medical Ltd, 2016.
- [36] E. Ruel-Gariepy, J.-C. Leroux, In situ-forming hydrogels—review of temperature-sensitive systems, *Eur. J. Pharm. Biopharm.* 58 (2004) 409–426.
- [37] M. Matyash, F. Despang, R. Mandal, D. Fiore, M. Gelinsky, C. Ikonomidou, Novel Soft Alginate Hydrogel Strongly Supports Neurite Growth and Protects Neurons Against Oxidative Stress, *Tissue Eng. Part A.* 18 (2012) 55–66. doi:10.1089/ten.tea.2011.0097.

Chapter 4 Indirect 3D bioprinting and characterization of alginate scaffolds for potential nerve tissue engineering applications

This chapter has been published as “Saman Naghieh, MD Sarker, Emily Abelseth, and Xiongbiao Chen, Indirect 3D bioprinting and characterization of alginate scaffolds for potential nerve tissue engineering applications, Journal of the Mechanical Behavior of Biomedical Materials” According to the Copyright Agreement, "the authors retain the right to include the journal article, in full or in part, in a thesis or dissertation".

(All the experimental work was conducted by me. MD Sarker and Emily Abelseth helped me to conduct some experiments. Professor Xiongbiao Chen guided and supervised the whole work.)



4.1 Abstract

Low-concentration hydrogels have favorable properties for many cell functions in tissue engineering but are considerably limited from a scaffold fabrication point of view due to poor 3D printability. Here, we developed an indirect-bioprinting process for alginate scaffolds and characterized the potential of these scaffolds for nerve tissue engineering applications. The indirect-bioprinting process involves (1) printing a sacrificial framework from gelatin, (2) impregnating the framework with low-concentration alginate, and (3) removing the gelatin framework by an incubation process, thus forming low-concentration alginate scaffolds. The scaffolds were characterized by compression testing, swelling, degradation, and morphological and biological assessment of incorporated or seeded Schwann cells. For comparison, varying concentrations of alginate scaffolds (from 0.5 to 3%) were fabricated and sterilized using either ultraviolet light or ethanol. Results indicated that scaffolds can be fabricated using the indirect-bioprinting process, wherein the scaffold properties are affected by the concentration of alginate and sterilization technique used. These factors provide effective means of regulating the properties of scaffolds fabricated using the indirect-bioprinting process. Cell-incorporated scaffolds demonstrated better cell viability than bulk gels. In addition, scaffolds showed better cell functionality when fabricated with a lower concentration of alginate compared to a higher concentration. The indirect-bioprinting process that we implemented could be extended to other types of low-concentration hydrogels to address the tradeoffs between printability and properties for favorable cell functions.

4.2 Introduction

Recent progress in tissue engineering has placed the possibility of meeting the growing worldwide demand for tissue and organ replacements within reach in the near future. To this end, extrusion-based bioprinting has played an important role in fabricating complex structures layer-by-layer to mimic native tissues [1–3]. Hydrogels have often been used in the extrusion-based technique as a bioink to incorporate large cell populations, growth factors, proteins, and peptides [4]. Notably, properties of a hydrogel bioink depend on its hydrogel concentration and affect cell viability [5], printability [6,7], and mechanical strength of the printed scaffolds [8]. At low concentrations, hydrogels are difficult, and at times even impossible, to print 3D constructs. In

contrast, hydrogels at relatively high concentrations can reduce cell viability due to the increased mechanical strength of hydrogels [9] and higher induced forces that cells experience during the fabrication process [10]. The hydrogel concentration can also influence mechanical properties [11]. Further investigation into these influences is urged [7].

By means of the extrusion-based technique, scaffolds made from hydrogels have been explored for nerve tissue engineering [9,12,13]. In nerve tissue engineering, considerable evidence supports the use of low-concentration hydrogels due to their favorable effects on cell responses or functions [5]. It has also been reported that low-concentration alginate (0.2 and 1% (w/v) is able to provide a better environment for neurite growth and cell viability [5,14]. While low-concentration alginate can support nerve tissue regeneration, poor printability makes it an undesirable material for printing scaffolds [5,15]. Hydrogels at higher concentrations have been used to enhance the printability and structural fidelity but at the cost of reduced in-growth of new tissue [16]. Therefore, approaches that allow for addressing this issue are greatly needed. Among these approaches, indirect printing has been evolved promising to tackle the poor printability of low concentration hydrogels [17–19].

Indirect bioprinting involves the creation of a sacrificial framework, which is used temporarily to support the formation of a scaffold made of a polymer [20]. Using indirect bioprinting, different materials, including bioactive materials and cells, can be strategically incorporated in a scaffold. Furthermore, indirect bioprinting allows for control over both the external and internal structure, thus creating scaffolds with advanced architecture [19]. As such, indirect bioprinting offers a great degree of versatility with respect to materials and structures, making it an attractive technique for the creation of complex hydrogel scaffolds. Notably, indirect 3D bioprinting of hydrogel scaffolds for nerve tissue regeneration has not been explored. Specifically, the mechanical and biological properties of hydrogel scaffolds fabricated by the indirect approach remain unclear, raising the need to discover their applications in nerve tissue regeneration.

As inspired, we developed an indirect bioprinting process for fabricating alginate scaffolds so as to address the issue of poor printability of low-concentration alginate. Our stepwise study included i) fabricating 0.5, 1.5, and 3% alginate scaffolds via the indirect bioprinting process where

50% gelatin is used as the sacrificial framework; ii) investigating the effects of UV and ethanol sterilization techniques on the mechanical properties of the indirectly-bioprinted scaffolds; iii) examining the degradation and swelling of the indirectly-bioprinted scaffolds; and iv) assessing the biological properties of the indirectly-bioprinted scaffolds. In addition, bulk gels and directly-bioplotted scaffolds were assessed and compared in terms of the viability of incorporated Schwann cells using a live/dead assay. The novelty of this work lies in the development of a method to create scaffolds from low-concentration alginate to circumvent its poor printability occurring in the direct bioprinting process. To the best of our knowledge, this is the first report of mechanically-stable scaffolds fabricated by an indirect printing technique and made of low-concentration alginate, with potential for nerve tissue engineering.

4.3 Materials and Methods

4.3.1 Materials and equipment

Gelatin (from bovine skin), medium viscosity Na-Alg (sodium salt from brown algae, medium viscosity), CaCl₂, Dulbecco's modified Eagle's medium (DMEM), fetal bovine serum (FBS), trypsin, ethylene-diaminetetraacetic acid (EDTA), and fluorescent dyes (propidium iodide (PI), calcein, Hoechst 33342) were all obtained from Sigma Aldrich (St. Louis, MO). Phosphate buffered saline (PBS; 0.0067 M) was obtained from HyClone (Logan, Utah). Primary rat Schwann cells (PRSCs) were supplied by Saskatoon City Hospital. A Sartorius scale (model 225d; Shanghai, China) was used for weighing samples. A 0.22- μ m bottle-top filter (Thermo Scientific, Ann Arbor, MI, USA) was used to filter alginate solutions. A freeze-dryer (FreeZone, Labconco, USA) was used to freeze-dry samples. Sterile circular coverslips (Thermo Scientific™) and 12/24-well tissue culture plates (Thermo Fisher Scientific, MA, USA) were used for experiments.

4.3.2 Directly bioprinting of scaffolds and preparation of cell-incorporated bulk gels

4.3.2.1 Direct bioprinting of scaffolds

3D scaffolds were directly printed on a 3D bioplotter (EnvisionTEC, Germany). For this, 12-well plates were coated with polyethyleneimine (PEI) for the purpose of enhancing the attachment of first printing layer to the plate during the printing process [21] and then the coated plates were placed in an incubator over a day for the subsequent use in scaffold printing. Three

hydrogels, comprised of 0.5, 1.5, and 3% alginate, representing low to reasonably high concentrations, were chosen to investigate the mechanical and biological performance of scaffolds fabricated by using a direct printing technique. For all groups, 300 μL of sterile alginate were mixed with 20 μL of cell media. The mixture was transferred to a 200- μm needle and three samples of each concentration were printed in a lattice pattern into PEI-coated wells (Figure 4.1). Printing parameters were chosen based on a printability study, which aimed to identify the appropriate temperature, pressure, and linear speed for each alginate concentration. The print temperature for the 3% alginate was set at 20 $^{\circ}\text{C}$, and the pressure and linear speed of the head were 0.3 bar and 14 mm/s, respectively. The print temperature for the 1.5% alginate was also 20 $^{\circ}\text{C}$ and the pressure and linear speed were set to 0.1 bar and 26 mm/s, respectively. The inter-strand distance was 3.5 mm for all groups. After printing one layer, 1 mL of CaCl_2 was added, then removed after 2 min and replaced with 1 mL of DMEM. The 0.5% alginate solution had poor printability (inconsistent strands and beading) and was not printable with a 100- μm needle (Figure 4.1c); using a 200- μm needle resulted in a bulk gel with no visible lattice structure. Therefore, instead of direct bioprinting of 0.5% alginate, bulk gel was used for further studies. To this end, 100 μL of the mixture (0.5% alginate and cells) was transferred into three separate wells. Then 1 mL of CaCl_2 was immediately added to each well, removed, and replaced with 1 mL of DMEM. The plates were incubated at 37 $^{\circ}\text{C}$ and 5% CO_2 .

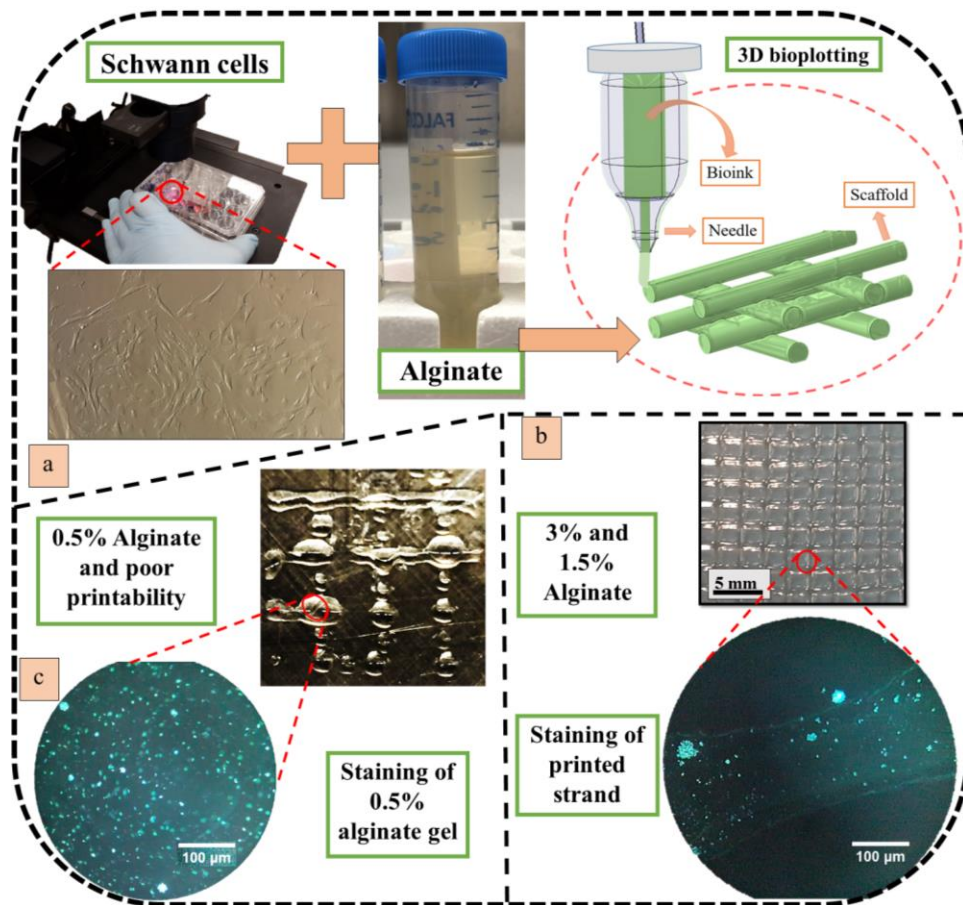


Figure 4.1. 3D biplotting of alginate hydrogels: a) cultivated Schwann cells mixed with alginate hydrogel and then biplotted, b) cell-incorporated alginate scaffold and staining result showing one strand, and c) poor printability of 0.5% alginate printed with a 100- μ m needle and staining result of cell-incorporated gel.

4.3.2.2 Preparation of alginate solutions with cells

A culture dish with PRSCs was examined under a microscope to assess the confluency of cells for that 85-100% is required for cell passing; and for all cell-viability studies, the passage number of cells were maintained between 6 and 14. The culture medium was completely aspirated, then 5 mL of 10 mM sterile PBS was added along the sides of the plate, gently swirled, then completely aspirated. One mL of sterile trypsin + EDTA was added, and the plate was gently swirled so the mixture coated the entire surface of the plate. The trypsin + EDTA was aspirated, and the plate was incubated for 5 min at 37°C and 5% CO₂. Six mL of DMEM + 10% FBS were added and gently re-pipetted to create an even suspension. The entire contents of the culture dish were transferred to a 14-mL Falcon tube and centrifuged at 800 rpm for 5 min. After centrifuging,

300 μL of the solution were kept in the Falcon tube and the cell pellet redistributed in the solution. Cell density was 500,000 cells per 300 μL of solution. Then 80 μL of this solution were added to each alginate sample (0.5, 1.5, and 3.0%), and then mixed with a multi-rotator for 5 min.

4.3.2.3 Preparation of cell-incorporated Bulk Gels

A 0.22- μm bottle-top filter was used to filter 0.5% (w/v) medium viscosity Na-Alg solution, which was kept in a freezer at $-80\text{ }^{\circ}\text{C}$ for 24 h and then freeze-dried for 48 h, while maintaining a sterile environment. The freeze-dried alginate was re-dissolved in sterile calcium-free DMEM to prepare 0.5, 1.5, and 3% (w/v) alginate precursors. PRSCs were cultured and trypsinized. Alginate precursors were thoroughly mixed with the cells at a density of 5×10^5 cells/mL to obtain a homogeneous cell distribution in the hydrogel. The mixture of alginate/cell suspension (100 μL) was poured onto sterile circle coverslips coated with 0.1% w/v PEI solution, and then 1 mL CaCl_2 (50 mM) solution was layered over the dispensed alginate solution to facilitate crosslinking for 6 min in a 24-well tissue culture plate.

4.3.3 Indirect bioprinting of alginate scaffolds

A 50% (w/v) gelatin solution was prepared by dissolving 20 g of gelatin in 40 mL of distilled water using a magnetic stir plate heated to $50\text{ }^{\circ}\text{C}$. The gelatin framework was designed using Magics CAD software (Materialise, Belgium), and then printed using a 3D bioplotter (EnvisionTEC, Germany), as shown in Figure 4.2. Strands were printed and layered on top of one another to form a $25\text{ mm} \times 25\text{ mm} \times 2.50\text{ mm}$ square lattice structure with a pore size of 2.5 mm. A print pressure of 0.8 bar, temperature of $50\text{ }^{\circ}\text{C}$, speed of 16 mm/s, and a 24-gauge printing needle were used for printing; and structures were printed with 20 layers.

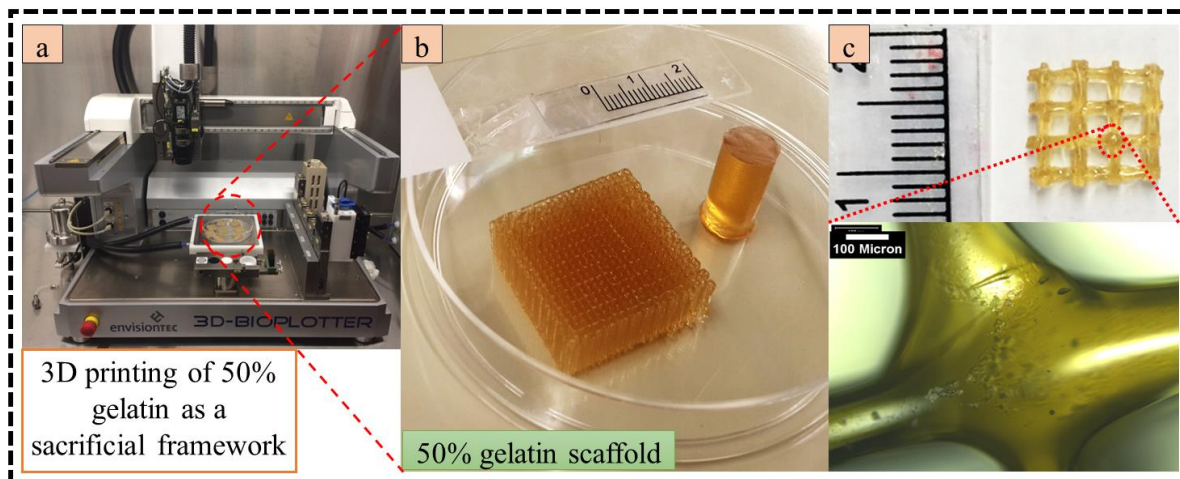


Figure 4.2. Indirect biofabrication: a) 3D bioplotter used for the fabrication of gelatin scaffolds, b) gelatin scaffold and bulk gel samples, and c) gelatin scaffold used for indirect biofabrication and a close-up view of this sacrificial framework.

The 0.5, 1.5, and 3.0% alginate solutions were prepared by dissolving 0.2, 0.6, or 1.2 g of alginate, respectively, into 40 mL of distilled water using a multi-rotator. A 50 mM CaCl_2 solution was prepared by mixing 2.2 g of CaCl_2 with 300 mL of distilled water. Gelatin frameworks were cut into smaller samples of approximately $8 \text{ mm} \times 8 \text{ mm} \times 2.5 \text{ mm}$ and then placed in separate dishes. Alginate solution was added or impregnated to each of the gelatin frameworks and then 0.1 mL of 50 mM CaCl_2 added on top of the frameworks. The frameworks were then flipped and impregnated with more alginate. Excess alginate and bubbles in the pores were removed using a pipette, and 50 mM CaCl_2 was poured into the dishes. Dishes were refrigerated for 18 h, then placed in an incubator at $37 \text{ }^\circ\text{C}$ and 5.0% CO_2 for 48 h in order to melt and remove gelatin. Scanning electron microscopy (SEM) was used to investigate the morphology of the indirectly-printed scaffolds. SEM images were captured using a Hitachi microscope on gold-coated samples. Images were taken at each stage of the indirect-fabricated scaffold preparation to determine pore size and strand thickness and analyzed using ImageJ[®] software.

4.3.4 Sterilization of scaffolds by ethanol disinfection or UV irradiation

Ethanol disinfection was carried out as per the previous study [22]. Three samples from each group of scaffolds were placed in separate dishes, and then 250 mL of 70% ethanol was pipetted into each dish. The samples were exposed for 20 min and then the ethanol was removed and replaced with 250 mL of distilled water. The samples were soaked in distilled water for 10

min before mechanical testing. UV sterilization involved placing samples in separate dishes underneath a 254 nm UV light source for 20 min, with aluminum foil used to enclose the area. Other sterilization techniques such as lyophilization, gamma-irradiation, and ethylene oxide treatment were not explored as they have been shown to negatively affect the alginate structure [22]. Disinfection via ethanol or UV light was chosen to be investigated as these techniques have not been investigated in many studies.

For post-seeding of indirect-fabricated scaffolds, scaffolds of each concentration group were sterilized by soaking in 70% ethanol for 20 min, then transferred to sterile Falcon tubes, and freeze-dried for 48 h. Freeze-dried samples were placed in PEI-coated wells of a 12-well plate, then covered with 10 μ L of cell mixture and 2 mL of DMEM. After 2 min, the DMEM was removed and an additional 5 μ L of cell mixture was added along with 1 mL of DMEM. Scaffolds were kept in an incubator at 37 °C and 5% CO₂.

4.3.5 Mechanical tests

The mechanical properties of the scaffolds were tested by uniaxial unconfined compression on a BioDynamic 5010 testing machine (Bose, USA). Tests were repeated three times for each group of scaffolds. In each test, the geometrical features of scaffolds were measured and characterized by taking pictures of scaffolds and analyzing them using ImageJ software. The scaffolds were then placed between the two smooth plates of the testing machine and subjected to compression at a rate of 0.017 mm/s. A stress-strain curve was generated for each group of scaffolds, and the slope of the linear portion of the curve was evaluated to calculate the elastic modulus.

4.3.6 Assessment of the swelling and degradation rates

Swelling correlates with a hydrogel's ability to retain water and is an important property to understand to prevent adverse effects on the surrounding tissue when a scaffold is implanted *in vivo*. The rate of degradation is an important property to consider when creating a biomimetic scaffold as well [23]. Samples made of varying concentrations of alginate scaffolds (from 0.5 to 3%) were removed from the crosslinker solution and placed separately in pre-weighed dishes. Excess liquid was removed with a Kimwipe tissue and the weights of the dishes were recorded. In the next step, 2 mL of PBS were added to each dish, which were then incubated at 37 °C and 5%

CO₂. At various time points (1, 2, 3, 4, 6, and 12 h, 1 d and 7 d), the dishes were removed from the incubator, the PBS was removed, the dishes were reweighed. Percent swelling was calculated as:

$$\% \text{ Swelling} = \frac{w_t - w_0}{w_0} \times 100 \quad (4.1)$$

where w_0 is the initial weight of the sample and w_t is the weight measured at one the above time points.

To study the degradation rate, 10 samples from each group were placed in pre-weighed Falcon tubes and then stored in the freezer at -40 °C for 4 h. Samples were then freeze-dried and weighed to determine their initial mass. Samples were then soaked in 1 mL of 70% ethanol for 20 min, the ethanol removed, and 2 mL of PBS added to each Falcon tube. The samples were then placed in an incubator at 37 °C and 5% CO₂ for 1, 3, 6, 24, or 48 h. At these time points, the PBS solution was removed, then the Falcon tubes placed in the freezer, freeze-dried, and reweighed. Degradation rate was calculated as:

$$\% \text{ Degradation} = \frac{w_{FD0} - w_{FDt}}{w_{FD0}} \times 100 \quad (4.2)$$

where w_{FD0} is the initial weight of the freeze-dried scaffold and w_{FDt} is the weight of the freeze-dried scaffold at one the above time points (1, 2, 3, 4, 6, and 12 h, 1 d and 7 d).

4.3.7 Cell viability and morphological assessment

Fluorescent microscope imaging of the bulk gels took place on days 1, 3, and 8 using a Zeiss Germany microscope (Axiovert 100) and X-cite® EXFO (series 120). Samples were stained with 5 mg/mL Hoechst and 50 mg/mL PI/Calcein dye. Imaging of the cell-incorporated scaffolds occurred on days 1, 4, and 8. Samples were stained with 5 mg/mL Hoechst and 1 mg/mL calcein, with 2 μL of each dye added to the samples and mixed with a pipette. Samples were then incubated for 1 h. DMEM was removed, samples were washed with PBS, 1 mL of fresh DMEM was added, and then the samples were imaged using fluorescent microscopy. Images were analyzed with ImageJ to determine the circularity of cells as well as the number of live and dead cells. Fractional cell viability was calculated as:

$$\text{Fractional Viability} = \frac{\text{Live Cells}}{\text{Dead Cells}} \times 100 \quad (4.3)$$

4.3.8 Statistical analysis

T-tests were conducted to investigate differences between groups. Results were considered significant at $P < 0.05$. All results are reported as mean \pm standard deviation. Minitab 17 statistics software was used to check the significant effect of the duration of culture and the concentration of alginate for cell viability studies using ANOVA (general linear model).

4.4 Results and discussion

4.4.1 Morphology of scaffolds

The architectural properties of a scaffold are characterized in terms of its external geometry and internal structure. Figure 4.3 shows the indirect fabrication of scaffolds from alginate with different concentrations and the morphology of gelatin and alginate scaffolds (after refrigeration and incubation) using microscopic and SEM imaging. It shows distinct differences in the appearance of the scaffolds as well. All samples were visibly larger in area than the sacrificial gelatin, as a temporary framework.

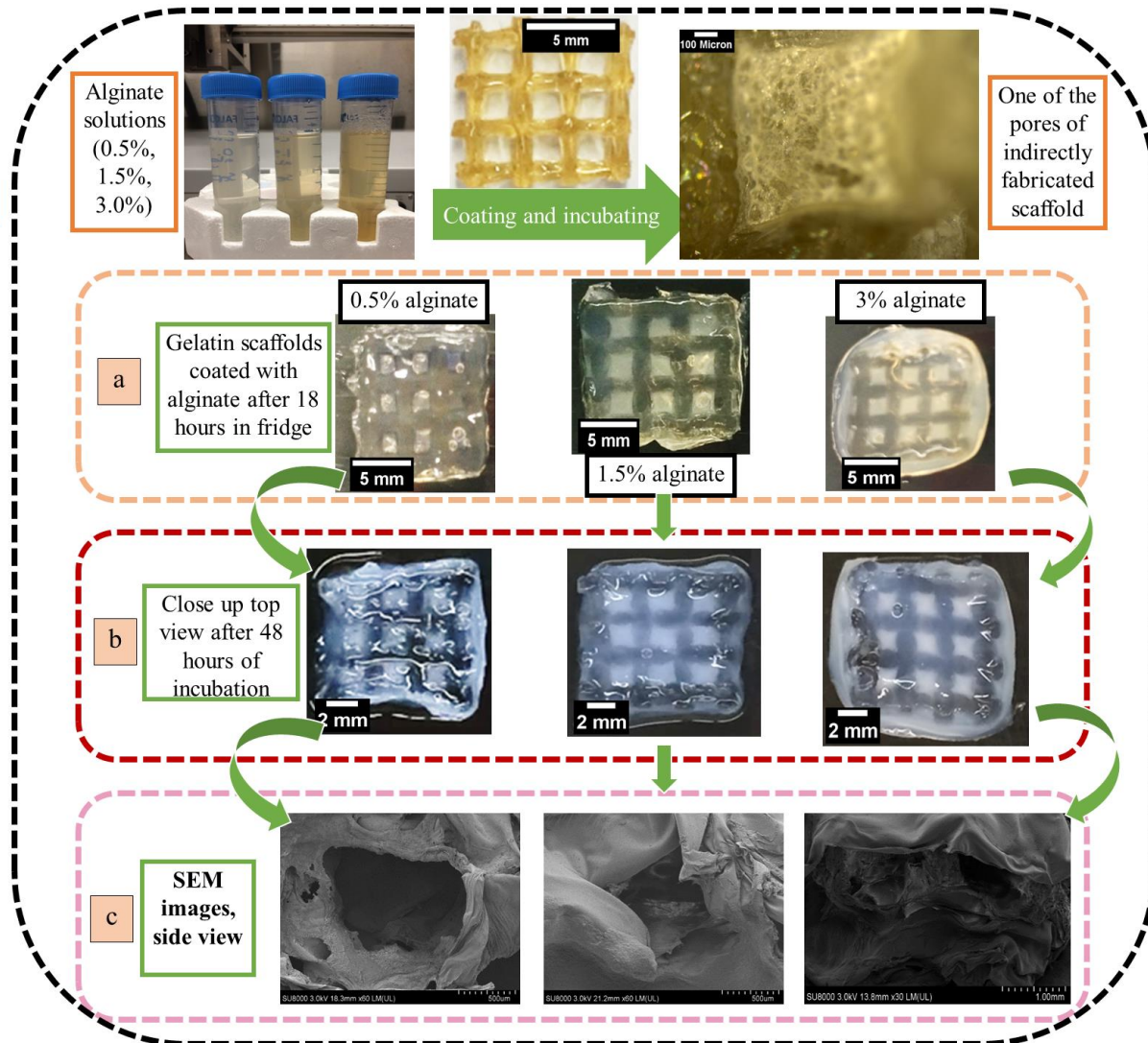


Figure 4.3. Indirect biofabrication of alginate scaffolds using sacrificial gelatin [from left to right: 0.5, 1.5, and 3% alginate solutions, sacrificial framework (scale bar 5 mm), and pore of indirect-fabricated scaffold after freeze-drying (scale bar 100 μm)]: a) impregnated gelatin scaffolds after 18 h refrigeration, b) removing the sacrificial material after 48 h incubation, and c) SEM images of the side view of indirectly fabricated scaffolds with 0.5%, 1.5% (scale bar 500 μm), and 3% (scale bar 1 mm) alginate concentrations after freeze-drying.

Figure 4.4 compares the pore size in the X and Y directions, strand diameter, and sample thickness across all sacrificial gelatin and indirectly fabricated samples after 18 h of refrigeration and 48 h of incubation. After both refrigeration and incubation, the strand diameter of all scaffolds increased compared to the original gelatin scaffold (0.763 ± 0.004 mm). A slight initial increase in pore size in all scaffolds occurred after impregnation of sacrificial frameworks with alginate and refrigeration. However, after incubation, the pore size of all scaffolds decreased to

significantly less than the original gelatin scaffold with a pore size of 1.507 ± 0.055 mm and 1.518 ± 0.061 mm in X and Y directions, respectively. Pore size, shape, and interconnectivity have a profound influence on tissue regeneration and integration. Different pore sizes are preferable for different anatomical locations to obtain functional tissue regeneration. For example, scaffolds employed in bone tissue engineering having 160-700 μm average pore size [24], while in vascular tissue engineering pore sizes larger than 400 μm inhibit the formation of a vascular network [25,26].

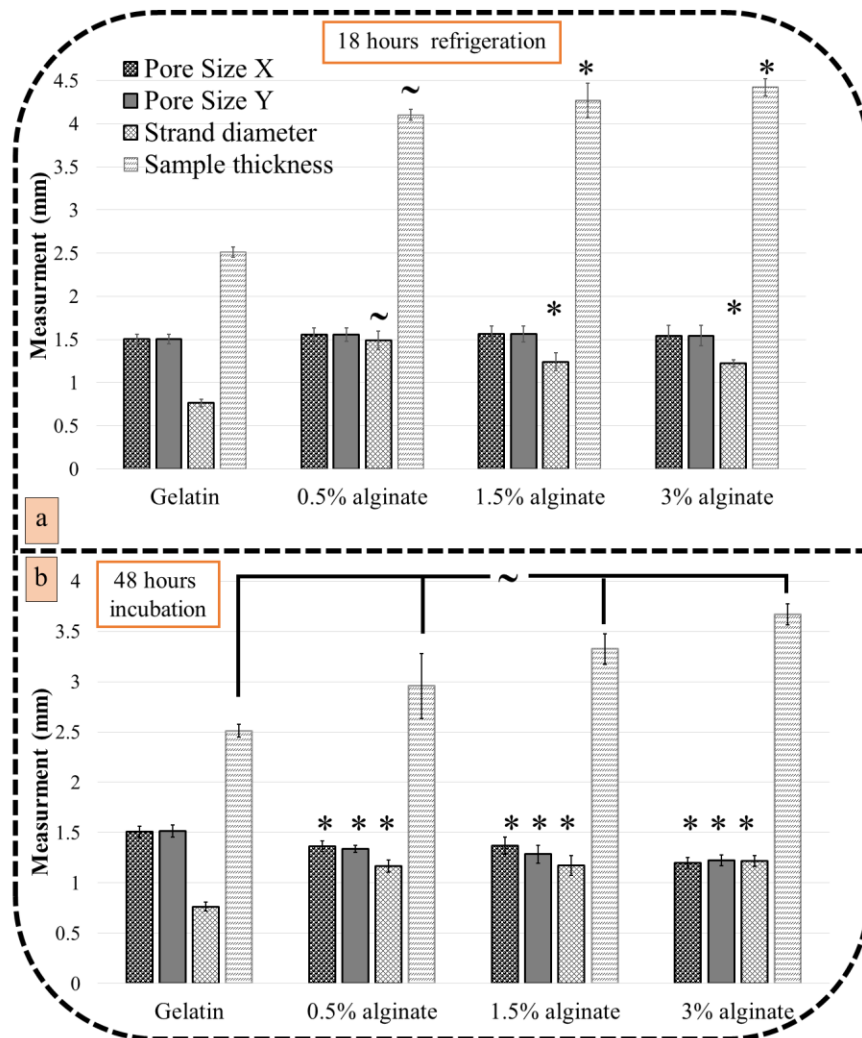


Figure 4.4. A comparison of pore size, strand diameter, and sample thickness from sacrificial gelatin scaffolds to samples after a) 18 h of refrigeration and b) subsequent 48 h of incubation. (*) and (~) indicate a significant difference from the original scaffold and the two other sample types, respectively ($p \leq 0.05$, $n = 9$).

4.4.2. Mechanical properties

Scaffolds indirectly fabricated from 0.5, 1.5, and 3.0% alginate were subjected to either ethanol disinfection, UV irradiation, or no sterilization. Compressive stress-strain tests were conducted to analyze the effect of varying % w/v concentration and method of sterilization on mechanical strength. We note here other factors beyond sterilization technique, such as crosslinking mechanism and molecular weight of the alginate, also affect mechanical properties [5,27,28]. Figure 4.5 shows that scaffolds with a higher % w/v concentration of alginate have a higher elastic modulus. This corresponds to scaffolds with a higher solids concentration displaying greater mechanical strength. Scaffolds treated with ethanol had the highest elastic modulus, followed by unsterilized scaffolds, and then UV irradiated scaffolds. Polymers degrade when exposed to UV light [29,30], which is likely the cause for the decrease elastic modulus in samples sterilized with UV irradiation. Similarly, bacterial degradation might alter the structure integrity of the nonsterile hydrogel and thus affect the elastic modulus of alginate scaffolds [31]. Based on the results above, the scaffolds treated with ethanol were determined to have the best mechanical properties (from having a higher elastic modulus point of view) and thus were subjected to swelling and degradation tests.

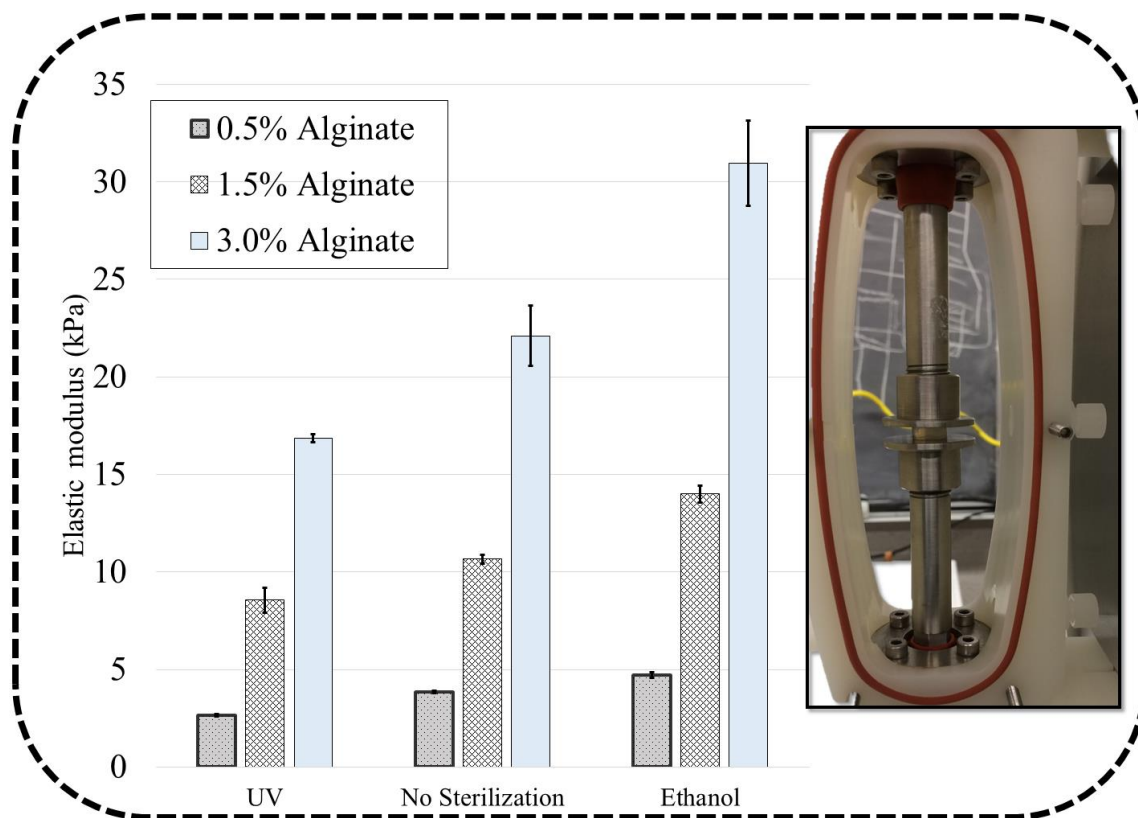


Figure 4.5. Elastic modulus for different scaffolds (fabricated from 0.5, 1.5, and 3% alginate) for control samples and those sterilized using UV or ethanol (results for all groups are significantly different at $p \leq 0.05$).

4.4.3 Swelling properties

In this study, the hydrogels were soaked in PBS. An exchange reaction occurs between the calcium (Ca^{2+}) ions in the scaffold and the sodium (Na^+) ions in the PBS, causing the crosslinks in the alginate formed by CaCl_2 to break, releasing Ca^{2+} ions into solution [32]. Water then enters the hydrogel and causes it to swell. Figure 4.6a shows the trend over 24 h for all hydrogel precursors considered (0.5, 1.5, 3%), which reflects initial swelling followed thereafter by degradation. Rapid swelling occurred in the first hour due to ion exchange, polymer chain relaxation, and water uptake. The low-concentration alginate precursor contains less mannuronic and glucuronic acid compared to the high concentration alginate precursor. In particular, carboxylate ions (COOH^-) supplied by either mannuronic or glucuronic acid participate in the crosslinking process by forming a bond with divalent ions (i.e., Ca^{2+}). The strength and density of crosslinking depends on the availability of divalent and carboxylate ions in the hydrogel. In this study, the swelling rate of the scaffolds occurred in the order $0.5\% > 1.5\% > 3\%$ alginate precursor in the first hour of incubation. After

the first hour, the swelling of the 1.5 and 3% alginate scaffolds continued at a slower rate due to the effect of saturation, whereas the swelling of the 0.5% alginate scaffold started decreasing at a rapid rate due to the initiation of degradation mechanisms. The swelling of 1.5 and 3% hydrogels appeared to decline after 3 and 6 h, respectively. The slower swelling rate of the 3.0% alginate compared to 1.5% alginate is attributed to its high crosslinking density and strength. The lower crosslinking density in low-concentration alginate hydrogels (0.5 and 1.5%) caused rapid degradation that reduced the swelling of these scaffolds in the PBS earlier than for the higher concentration (3%) alginate. Samples were weighed again after 1 week, but no significant change in swelling was observed. All tests were conducted in a constant volume of PBS, meaning no extra Na^+ ions were added to each well of the tissue culture plate. Once the samples reached equilibrium with surrounding Na^+ ions after 8 h of incubation, little change in the amount of swelling was identified in all samples due to insignificant polymer chain relaxation, water uptake, and degradation, in agreement with [33].

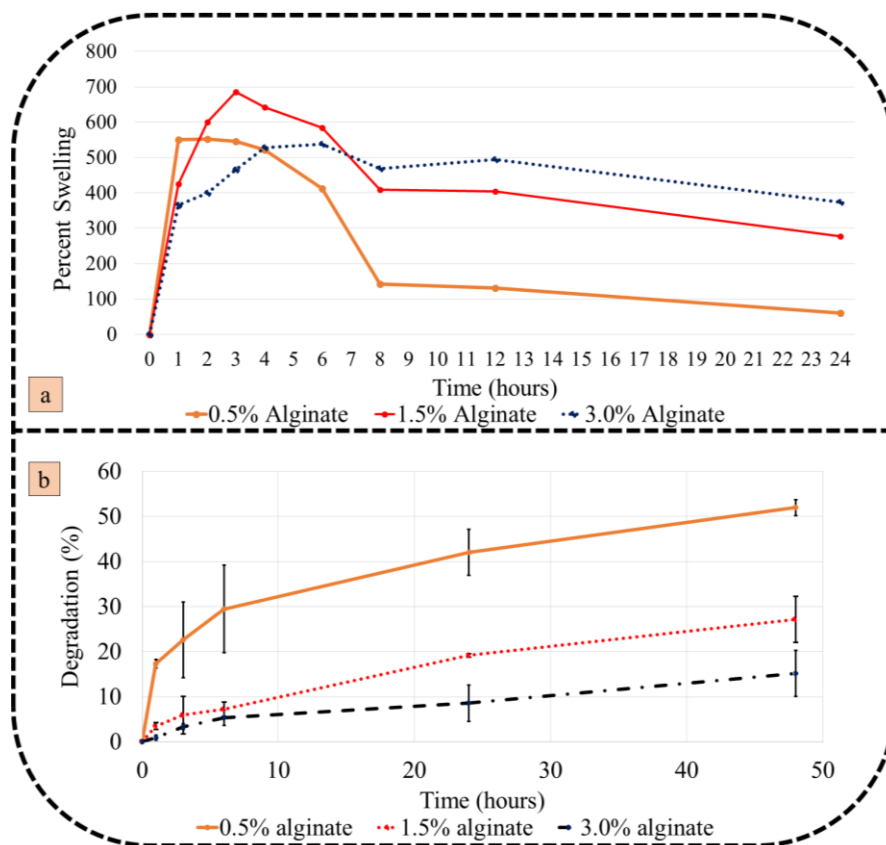


Figure 4.6. Percent a) swelling over 24 h and b) degradation over 48 h of the three types of alginate scaffolds created using the indirect fabrication technique.

4.4.4 Degradation properties

Alginate hydrogels were degraded by the release of divalent ions crosslinking the gel, in this case Ca^{2+} , into the surrounding solution by an exchange reaction with monovalent cations [32], in this case the Na^+ ions found in the PBS solution. Figure 4.6b shows the degradation trends of the three scaffold types (0.5, 1.5, 3% alginate precursor) over 48 h. The 0.5% alginate scaffold shows the most dramatic change, degrading $52\% \pm 1.74$ at 48 h. In comparison, the 1.5% scaffold and the 3% scaffold both changed more gradually, degrading $27.4\% \pm 5.11$ and $15.14\% \pm 5.09$, respectively, after 48 h. The degradation profile of 0.5, 1.5 and 3% alginate scaffolds increased in the order $0.5\% > 1.5\% > 3\%$. Similar to the observations related to swelling, rapid degradation occurred in all alginate scaffolds from 0 to 3 h and then slowed due to ionic equilibrium ($\text{Na}^+/\text{Ca}^{2+}$) with the surroundings (due to the fixed volume of PBS in each culture well). Notably, both the 0.5

and 1.5% alginate samples became structurally unstable after 48 h but the 3% alginate samples maintained their structure for almost one week.

Figure 4.7a shows the progression of the degradation of the alginate scaffolds. The 0.5% alginate scaffolds degraded rapidly, completely losing their physical structure after only 3 h; the 1.5% scaffolds began losing their structure after 3 h, with almost complete loss after 48 h; the 3.0% scaffolds underwent no dramatic visible change in structure over 48 h. The inner structure of the different groups was investigated using SEM imaging. Figure 4.7b shows the internal structure of indirect-fabricated scaffolds made from different concentrations of alginate after 24 h. Scaffolds fabricated from low-concentration alginate (0.5%) had more porous structures than those made from 3% alginate, which had a rigid structure; the porous structure might facilitate the higher rate of degradation observed in the 0.5% alginate group. After 1 hour of incubating in the PBS solution, 0.5% and 1.5% scaffolds had a smoother inner structure than the 3% scaffold, which is good evidence of surface/bulk degradation as well as the dissolution of the lower concentration alginate. The 3% alginate scaffold demonstrated a rough surface even after 24 h in contrast to the other groups that showed evidence of erosion. The visual changes in Figure 4.7 closely follow the degradation trend in Figure 4.6b. The structure integrity of the 3% alginate scaffolds over 48 h suggests their possible application in tissue engineering. As the scaffolds retain well-interconnected internal channels, created using sacrificial gelatin, this type of scaffold would be useful in studying micro-fluidics and vascularization [34]. In contrast, the relatively rapid degradation of the 0.5 and 1.5% alginate scaffolds could be useful in drug or cell release studies. Low-concentration hydrogels have promise in terms of neurite outgrowth for nerve tissue engineering; being rapidly degradable, such low-concentration hydrogels could be used as a filler material inside a conduit for their possible application in nerve guidance conduits, as reported in detail elsewhere [35].

The degradation experiments were conducted in a fixed volume of PBS and at a temperature designed to simulate the physiologic environment. Under these conditions, ion exchange takes place during the first few hours until equilibrium with the PBS is achieved. Because ion exchange is associated with degradation, observation of the degradation rate during the first few hours is critical for understanding the mechanical behavior of alginate/gelatin scaffolds in the physiologic buffer.

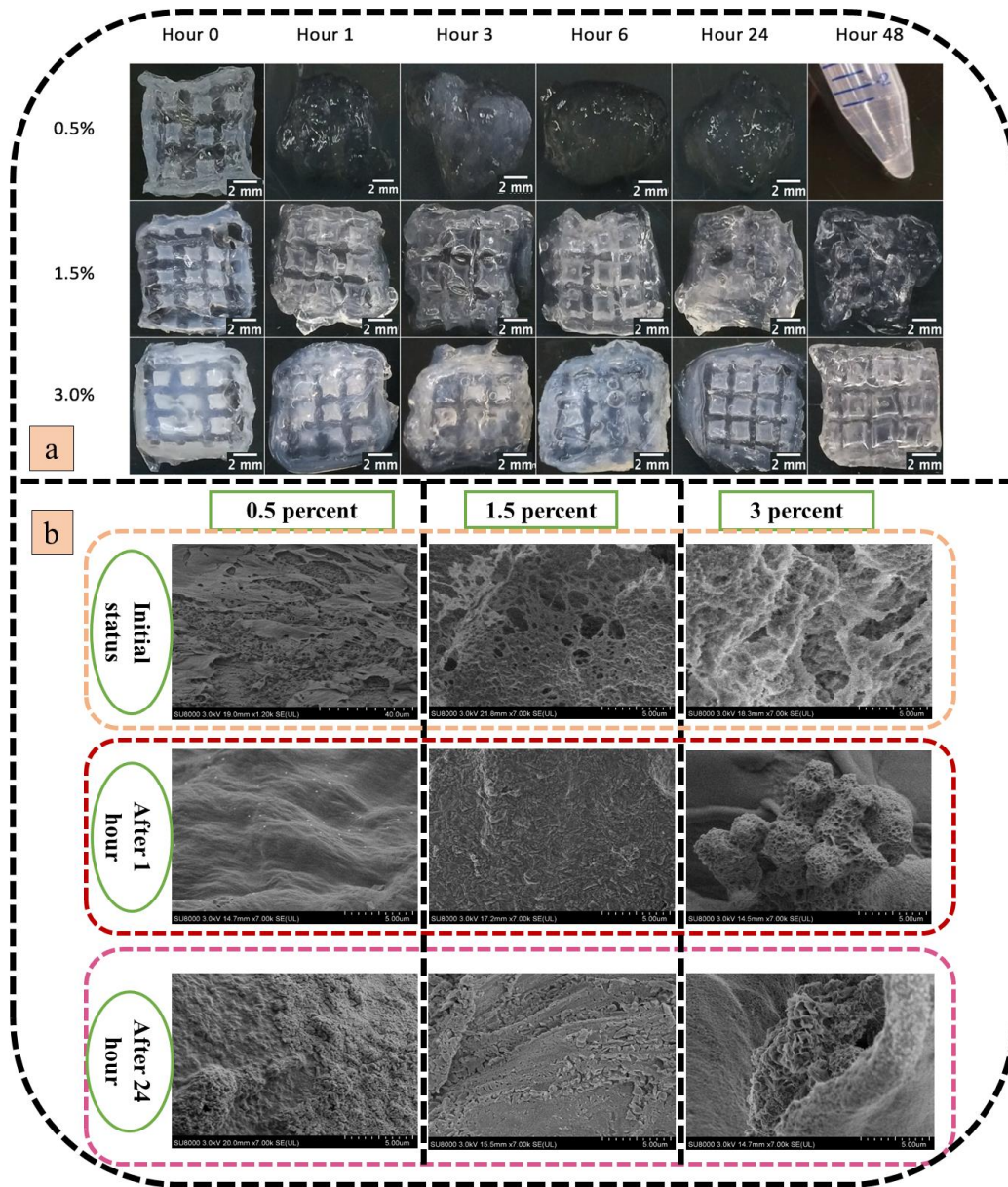


Figure 4.7. Progression of degradation for 1.5 and 3.0% alginate scaffolds over 48 h: a) visual observation and b) SEM images of indirect-fabricated scaffolds with 0.5, 1.5, and 3% alginate.

4.4.5 Cell viability and circularity assessment

4.4.5.1 Fluorescent imaging of bulk gels

Each bulk gel was stained with Hoechst and PI to show the number of total cells and dead cells, respectively. All hydrogels experienced a decrease in cell viability over the course of 8 d (Figure 4.8). The 3% and 1.5% alginate hydrogels experienced a steep drop in fractional viability

from day 1 to day 8 (less than 40% and 30% for 1.5% and 3% alginate hydrogels, respectively), while the 0.5% gel had higher cell viability at the end of day 8 (more than 50%). The cells seeded onto the 0.5% bulk gel had a higher fractional viability over 8 days than those on 1.5 and 3.0% bulk gels. This might be due to the lower concentration of this hydrogel making it a favorable substrate for cells, as reported elsewhere [5]. Increasing alginate precursor concentration results in a stiffer internal structure of the bulk gel, which interrupts diffusion mass transfer mechanism between the cells and culture media and significantly affects the metabolic mechanism of incorporated cells. In addition, strong bonds among the polymer chains in the high-concentration alginate inhibit cell migration/proliferation as well as cell to cell interactions. Therefore, high concentration alginate is not a promising biomaterial in terms of cell viability but demonstrates relatively suitable mechanical properties for tissue engineering applications. In contrast, low-concentration (0.5%) alginate demonstrates better cell viability compared to high-concentration alginate but has poorer mechanical stability. Hence, the optimum concentration of alginate precursor needs to be determined prior to fabrication to achieve both satisfactory mechanical stability and cell viability. The decreased cell viability in all alginate hydrogels with time could be improved by introducing interconnected channels through indirect printing and the creation of scaffolds with a porous structure. Such an interconnected structure would facilitate diffusive mass transfer (i.e., nutrients, oxygen gas, proteins, metabolites etc.) between the incorporated cell population and the surrounding culture medium.

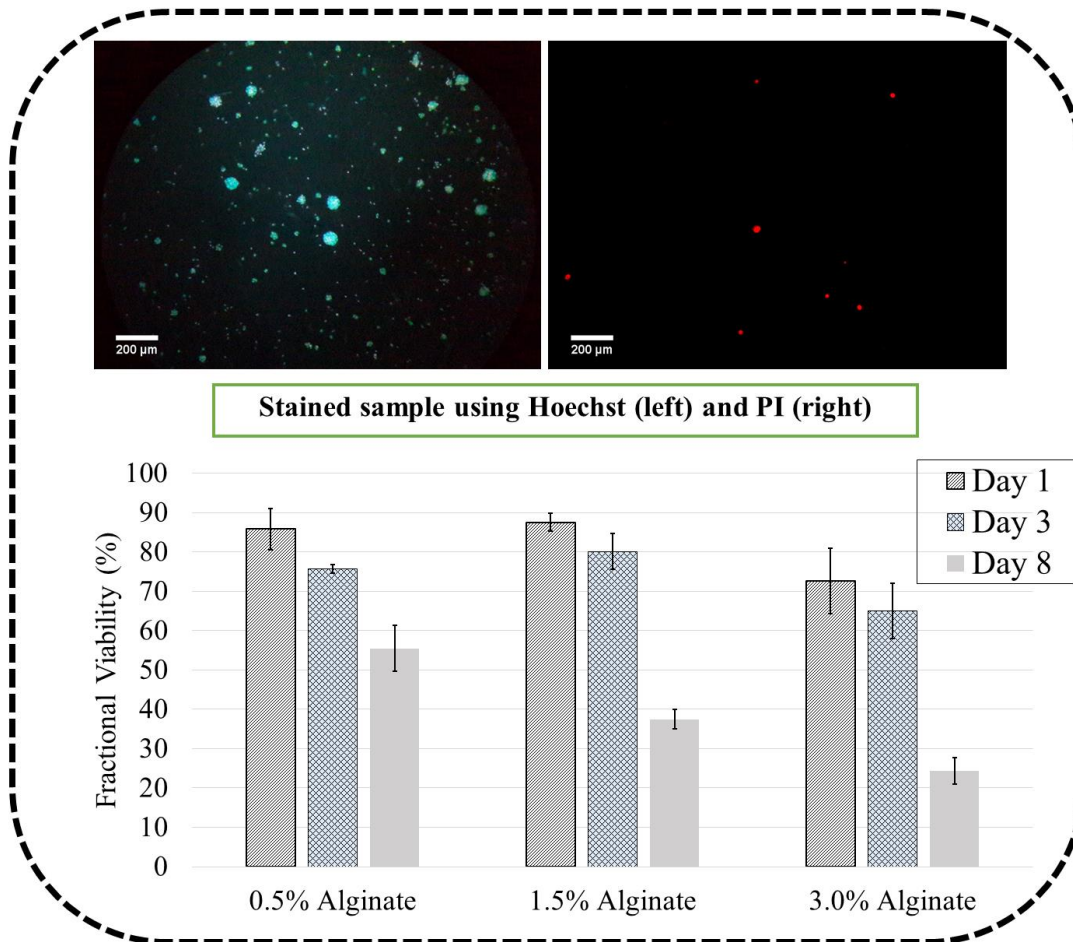


Figure 4.8. Fractional cell viability in 0.5, 1.5, and 3% bulk alginate gels over 8 d. Based on ANOVA (general linear model), time, concentration, and their interaction are statistically significant ($p < 0.05$) (top pictures are fluorescence microscope images of the total (left) and dead (right) staining of Schwann cells using Hoechst and PI).

4.4.5.2 Fluorescent imaging of cell-incorporated scaffolds

Scaffolds were stained with calcein and Hoechst to show the number of live cells and total cells, respectively. Calcein staining and optical images captured from the cell-incorporated scaffolds after bioprinting are shown in Figure 4.9. The 0.5% alginate had poor printability (Figure 4.1) and so 0.5% alginate scaffolds were not considered; images in Figure 4.9I are for bulk gel. Optical microscopy was used to illustrate cell development, with the images showing pores were open and cells were well distributed (partially elongated cells with high cell density; Figure 4.9II and III). Alginate scaffolds fabricated with 1.5 or 3.0% hydrogel precursor showed better cell viability compared to 0.5% alginate gel on day 3 and 8 due to the interconnected bioplotted structures (Figure 4.10). However, alginate scaffolds printed with 3% alginate precursor

demonstrated poorer cell viability than the 1.5% alginate scaffold, indicating the effect of shear stress-induced cell damage during the biplotting process. Live cells within the 0.5% bulk alginate gel showed a decreasing trend over the 8 d of *in vitro* culture; this is attributed to rapid degradation and the non-porous structure. Incorporated Schwann cells in 1.5 and 3.0% alginate scaffolds had a higher cell viability at day 3 than day 1 or 8 that might be due to the high proliferation rate; the observed decrease in cell viability thereafter is likely due to the effect of tissue remodeling. Compared to 3% alginate scaffolds, 1.5% alginate scaffolds maintained better cell viability over the 1 to 8 day culture period, suggesting the efficacy of less stiff polymer in the 3D cell incorporation approach. These results suggest the potential for scaffolds biplotted with sequential layers of soft and stiff hydrogel strands, which would simultaneously address both biological and mechanical performance for specific tissue engineering applications.

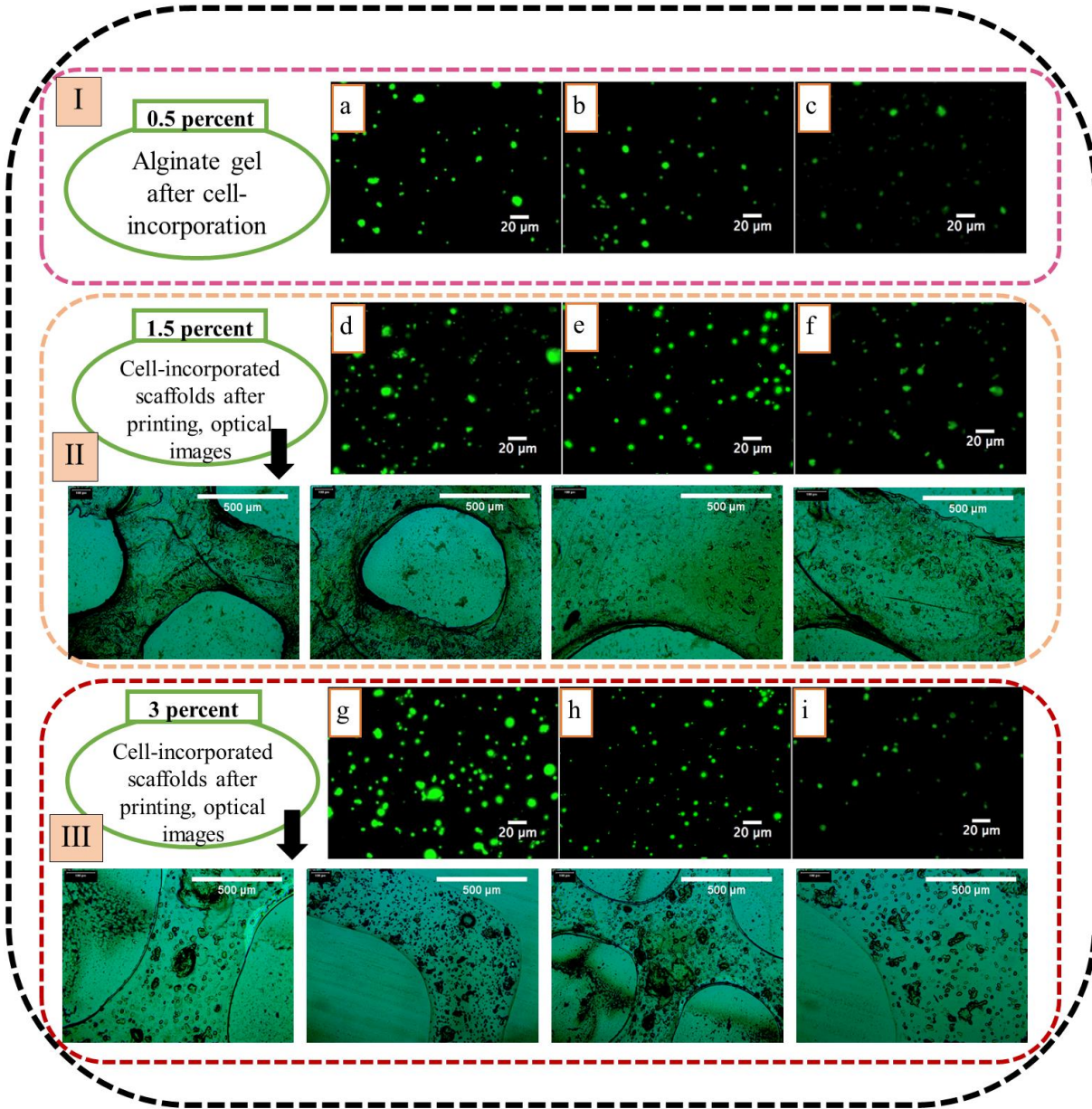


Figure 4.9. Fluorescence microscope images of live staining of Schwann cells (scale bar 20 μm) showing live cells: I) 0.5% alginate bulk gel: a) day 1, b) day 4, c) day 8; II) 1.5% alginate scaffold: d) day 1, e) day 4, f) day 8; III) 3% alginate scaffold: g) day 1, h) day 4, i) day 8 (optical images in II and III were captured after fabrication of the cell-incorporated scaffolds; all scale bars are 500 μm).

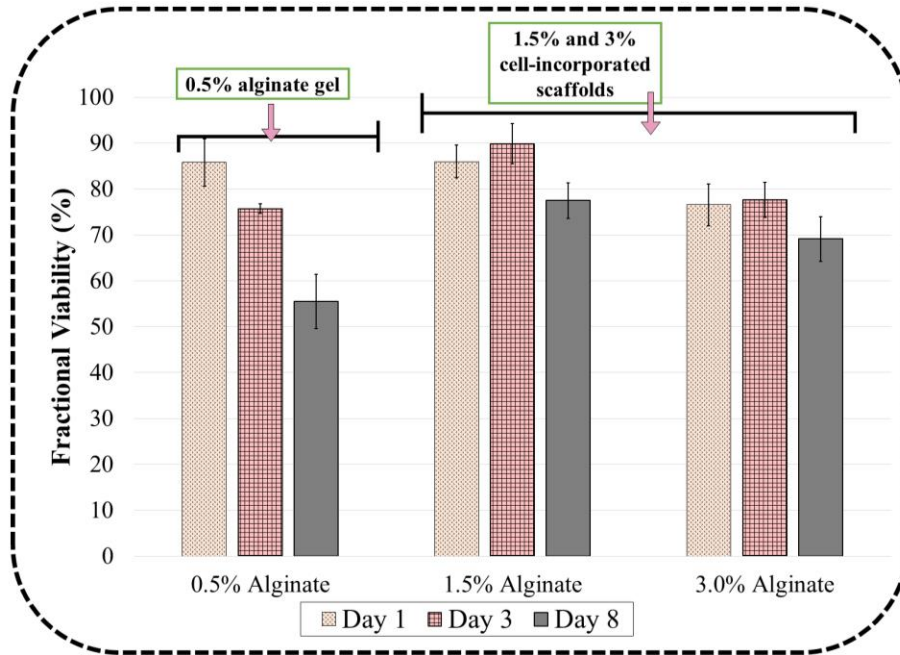


Figure 4.10. Fractional cell viability in each cell-incorporated scaffold after 8 d. Error bars are standard deviation. Based on ANOVA (general linear model), time, concentration, and their interaction are statistically significant ($p < 0.05$).

4.4.5.3 Cell morphology in bulk gels and cell-incorporated/post-seeded scaffolds

Calcein assay was used to stain the cytoplasm of Schwann cells to assess the morphology of cells over time [36]. The circularity of cells in the three types of alginate structures was analyzed using ImageJ. Circularity is measured on a 0.0-1.0 scale, with 1.0 being a perfect circle. Low circularity values are associated with a more stretched, attached, or differentiated state of incorporated cells. The circularity of cells in the 0.5, 1.5, and 3.0% alginate bulk gels was 0.423 ± 0.118 , 0.768 ± 0.034 , and 0.799 ± 0.064 , respectively, after 8 d (Figure 4.11a). The lower circularity of cells in the 0.5% alginate gel at day 8 compared to other groups occurred concurrently with rapid degradation during the culture period due to significant polymer chain relaxation, swelling, and medium uptake within the bulk gel. Absorption of culture medium facilitated the availability of various protein molecules within the matrix that helped Schwann cells in the 0.5% alginate hydrogel express multipolar morphology. The higher values for cell circularity for the other bulk gels (3 and 1.5%; Figure 4.11a) suggest the lower concentration of alginate is more favorable for 3D Schwann cell cultures over time.

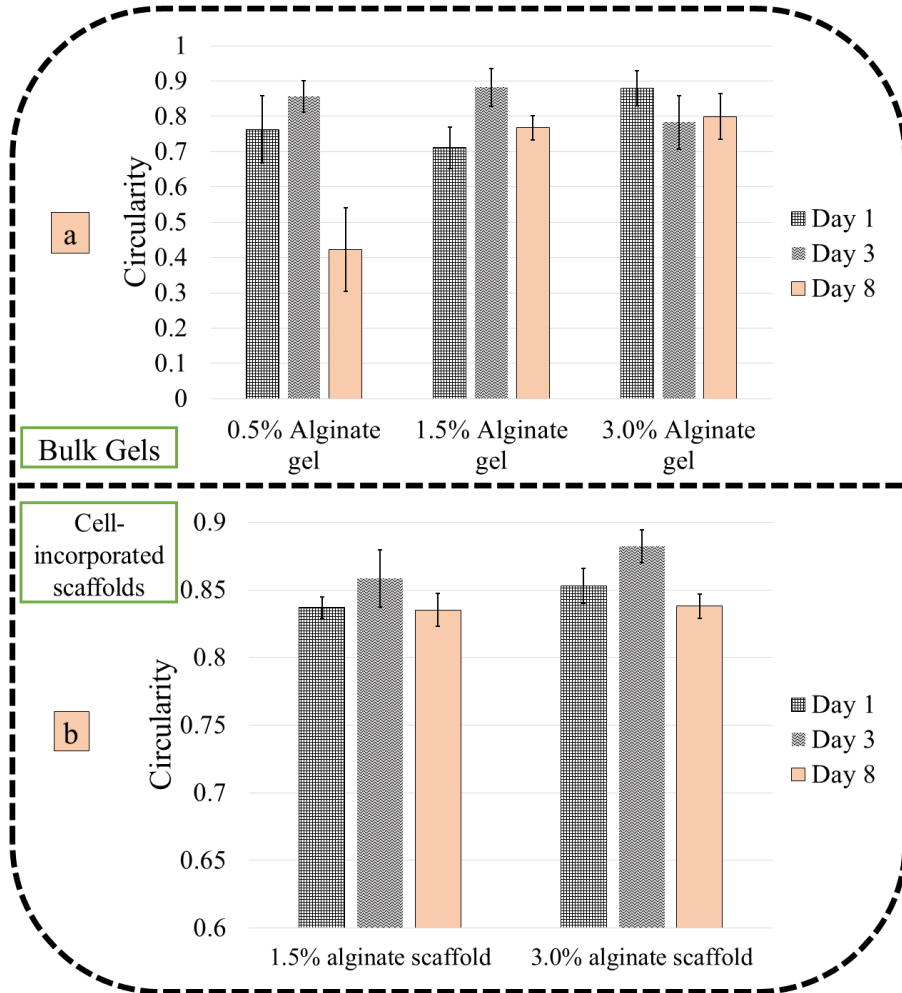


Figure 4.11. Cell circularity on bulk gels and cell-incorporated scaffolds over 8 d.

In the 1.5 and 3% alginate scaffolds fabricated using direct bioplotting (Figure 4.11b), incorporated cells were more circular than in the 0.5% alginate bulk gel (Figure 4.11a). The high circularity is attributed to confined cells that are unable to migrate and interact with each other inside the alginate strands of the bioplotting scaffolds. Furthermore, the trend in Figure 4.11b indicates that the circularity of cells in the 1.5 and 3% alginate scaffolds are close to 0.9 at day 3. This might be due to a large number of cells, resulting from cell proliferation, becoming trapped in a confined space, where they tend to remain in a more circular shape. This could also explain the spike in circularity on day 3 for both the 1.5 and 3.0% alginate scaffolds (cell retraction due to proliferation). On a 2D tissue culture plate, Schwann cells usually demonstrate multipolar morphology, extending multiple processes that are indicative of attachment, differentiation, and

migrated states. In the *in vivo* state, the morphology might differ from cell to cell as per the location and function of the tissue or organ. In some applications, spherical morphology of cells (such as chondrocytes and pancreatic islet cells) incorporated into alginate hydrogel can form functional tissues [37,38]; however, the elongated morphology of Schwann cells is expected in a 3D culture to facilitate the formation Bands of Büngner necessary for the regeneration of damaged peripheral nerves.

Figure 4.12a shows an increase in circularity over 8 days for post-seeded scaffolds. Figure 4.12b demonstrates an increase in cells and cell clumping, and therefore the increased circularity again might be due to the retraction of cells to make space for proliferating cells. Figure 4.12b also shows the Schwann cells attached to the surface of the indirect-fabricated scaffolds. Schwann cells continued to proliferate on the surface of the 0.5% alginate scaffold to day 8 (Figure 4.12b), but this was less evident for the other alginate scaffolds (1.5 and 3%). This is consistent with reports demonstrating the limitations of cell migration, growth, and differentiation using high-density hydrogels [39]. As shown in Figure 4.7b, pores are evident in the inner structure of the 0.5% indirect-fabricated scaffolds and could facilitate the observed cell growth. Furthermore, not only were more cells observed on the surface of 0.5% alginate scaffold, for all sample groups, the seeded cells showed more spherical morphology over time in particular spots on the alginate surface, indicative of cell proliferation. It is well-established that polysaccharide molecules lacking peptides in their structure do not facilitate cell attachment on the surface. However, absorption of gelatin molecules released from the indirectly-fabricated framework on the surface of alginate strands might enhance the surface properties of alginate scaffolds fabricated by the proposed indirect approach. Moreover, some amount of gelatin might get absorbed in the alginate hydrogel during the removal process, and thereafter have a positive effect on the cellular behavior [40].

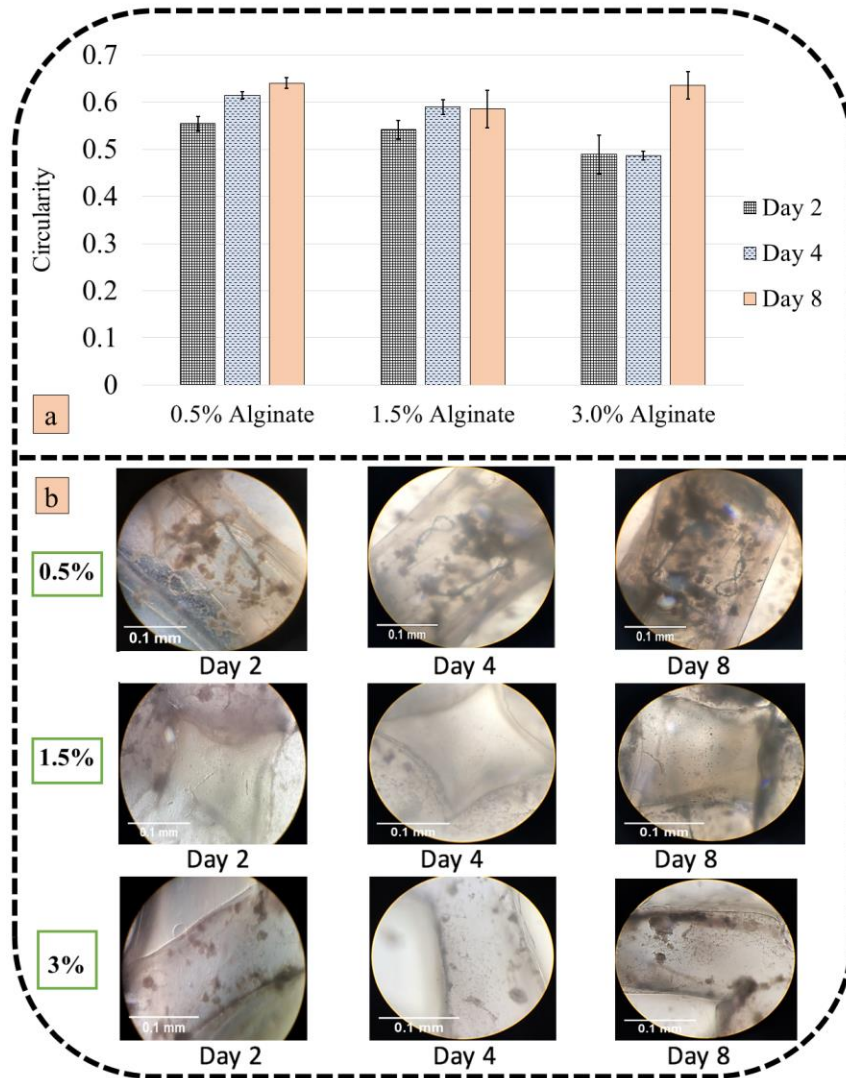


Figure 4.12. Cell circularity of Schwann cells in post-seeded scaffolds over 8 d: a) cell viability for different groups of indirect-fabricated scaffolds and b) optical images from samples from different days indicating the morphology of cells (100× magnification).

4.5 Conclusions

Hydrogels are widely used in the bioprinting of scaffolds for tissue engineering applications. Low-concentration hydrogels create a favorable environment for many cell functions but are limited from the fabrication point of view due to poor printability. Here, we illustrated the feasibility of fabricating scaffolds from low-concentration alginate using an indirect-bioprinting process by means of a sacrificial gelatin framework. Scaffolds were fabricated with varying concentrations of alginate and then sterilized using either UV or ethanol. Next, the scaffolds were

characterized biologically using Schwann cells for potential nerve tissue engineering applications. Our results indicate that scaffolds can be fabricated by the indirect-bioprinting process at precursor alginate concentrations of 0.5-3%. Scaffolds created from 0.5, 1.5, and 3% alginate and sterilized with ethanol have a higher elastic modulus than those treated with UV. Scaffolds made from 0.5 and 1.5% alginate experienced significant changes in swelling, while those fabricated from 3.0% alginate demonstrated much more gradual changes. In addition, 0.5% alginate scaffolds experienced dramatic degradation compared to those fabricated from 1.5 or 3.0% alginate. The low-concentration alginate scaffolds provided a more favorable environment for Schwann cells. Taken together, our results show the indirect-bioprinting process successfully addresses the poor printability of low-concentration alginate for scaffold fabrication. The results further show that both the mechanical and biological properties of fabricated scaffolds are affected by the concentration of alginate as well as the sterilization technique utilized. These results provide an effective means of regulating scaffold properties during the indirect-bioprinting process. Furthermore, the results indicate the possibility of extending the proposed indirect-bioprinting process to other types of low-concentration hydrogels to address the tradeoffs between printability and properties favorable for cell functioning.

4.6 References

- [1] S. Vijayavenkataraman, W.-C. Yan, W.F. Lu, C.-H. Wang, J.Y.H. Fuh, 3D bioprinting of tissues and organs for regenerative medicine, *Adv. Drug Deliv. Rev.* (2018).
- [2] S. Naghieh, X.B. Chen, Scaffold Design, in: *Extrus. Bioprinting Scaffolds Tissue Eng. Appl.*, Springer International Publishing Switzerland, 2019. doi:10.1007/978-3-030-03460-3.
- [3] S. Naghieh, M. Sarker, M. Izadifar, X. Chen, Dispensing-based bioprinting of mechanically-functional hybrid scaffolds with vessel-like channels for tissue engineering applications – a brief review, *J. Mech. Behav. Biomed. Mater.* 78 (2018) 298–314. doi:10.1016/j.jmbbm.2017.11.037.
- [4] Y.J. Tan, X. Tan, W.Y. Yeong, S.B. Tor, Hybrid micro scaffold-based 3D bioprinting of multi-cellular constructs with high compressive strength: A new biofabrication strategy, *Sci. Rep.* 6 (2016) 39140.
- [5] M. Matyash, F. Despang, R. Mandal, D. Fiore, M. Gelinsky, C. Ikonomidou, Novel Soft Alginate

- Hydrogel Strongly Supports Neurite Growth and Protects Neurons Against Oxidative Stress, *Tissue Eng. Part A*. 18 (2012) 55–66. doi:10.1089/ten.tea.2011.0097.
- [6] L.E. Bertassoni, J.C. Cardoso, V. Manoharan, A.L. Cristino, N.S. Bhise, W.A. Araujo, P. Zorlutuna, N.E. Vrana, A.M. Ghaemmaghami, M.R. Dokmeci, Direct-write Bioprinting of Cell-laden Methacrylated Gelatin Hydrogels, *Biofabrication*. 6 (2014) 1–19. doi:10.1088/1758-5082/6/2/024105.Direct-write.
- [7] Y. He, F. Yang, H. Zhao, Q. Gao, B. Xia, J. Fu, Research on the printability of hydrogels in 3D bioprinting, *Sci. Rep.* 6 (2016) 29977. doi:10.1038/srep29977.
- [8] A. Skardal, M. Devarasetty, H.-W. Kang, I. Mead, C. Bishop, T. Shupe, S.J. Lee, J. Jackson, J. Yoo, S. Soker, A hydrogel bioink toolkit for mimicking native tissue biochemical and mechanical properties in bioprinted tissue constructs, *Acta Biomater.* 25 (2015) 24–34.
- [9] L. Ning, H. Sun, T. Lelong, R. Guilloteau, N. Zhu, D.J. Schreyer, D.X. Chen, 3D bioprinting of scaffolds with living Schwann cells for potential nerve tissue engineering applications, *Biofabrication*. (2018).
- [10] M. Li, X. Tian, N. Zhu, D.J. Schreyer, X. Chen, Modeling process-induced cell damage in the biodispensing process, *Tissue Eng. Part C Methods*. 16 (2009) 533–542.
- [11] M. a LeRoux, F. Guilak, L. a Setton, Compressive and shear properties of alginate gel: Effects of sodium ions and alginate concentration, *J. Biomed. Mater. Res.* 47 (1999) 46–53. doi:10.1002/(SICI)1097-4636(199910)47.
- [12] G. Potjewyd, S. Moxon, T. Wang, M. Domingos, N.M. Hooper, Tissue Engineering 3D Neurovascular Units: A Biomaterials and Bioprinting Perspective, *Trends Biotechnol.* (2018).
- [13] S. England, A. Rajaram, D.J. Schreyer, X. Chen, Bioprinted fibrin-factor XIII-hyaluronate hydrogel scaffolds with encapsulated Schwann cells and their in vitro characterization for use in nerve regeneration, *Bioprinting*. 5 (2017) 1–9. doi:10.1016/j.bprint.2016.12.001.
- [14] N. Cao, X.B. Chen, D.J. Schreyer, Influence of Calcium Ions on Cell Survival and Proliferation in the Context of an Alginate Hydrogel, *ISRN Chem. Eng.* 2012 (2012) 1–9. doi:10.5402/2012/516461.
- [15] L. Ning, Y. Xu, X. Chen, D.J. Schreyer, Influence of mechanical properties of alginate-based substrates on the performance of Schwann cells in culture, *J. Biomater. Sci. Polym. Ed.* 27 (2016)

898–915.

- [16] A.D. Augst, H.J. Kong, D.J. Mooney, Alginate hydrogels as biomaterials, *Macromol. Biosci.* 6 (2006) 623–633.
- [17] J.Y. Tan, C.K. Chua, K.F. Leong, Indirect fabrication of gelatin scaffolds using rapid prototyping technology, *Virtual Phys. Prototyp.* 5 (2010) 45–53. doi:10.1080/17452751003759144.
- [18] A. Houben, J. Van Hoorick, J. Van Erps, H. Thienpont, S. Van Vlierberghe, P. Dubruel, Indirect Rapid Prototyping: Opening Up Unprecedented Opportunities in Scaffold Design and Applications, *Ann. Biomed. Eng.* 45 (2017) 58–83. doi:10.1007/s10439-016-1610-x.
- [19] W. Yeong, C. Chua, K. Leong, M. Chandrasekaran, M. Lee, Indirect fabrication of collagen scaffold based on inkjet printing technique, *Rapid Prototyp. J.* 12 (2006) 229–237. doi:10.1108/13552540610682741.
- [20] E. Tamjid, A. Simchi, Fabrication of a highly ordered hierarchically designed porous nanocomposite via indirect 3D printing: Mechanical properties and in vitro cell responses, *Mater. Des.* 88 (2015) 924–931.
- [21] A. Rajaram, D.J. Schreyer, D.X.B. Chen, Use of the polycation polyethyleneimine to improve the physical properties of alginate–hyaluronic acid hydrogel during fabrication of tissue repair scaffolds, *J. Biomater. Sci. Polym. Ed.* 26 (2015) 433–445.
- [22] W. Stoppel, J.C. White, S.D. Horava, S.C. Roberts, W.L. Stoppel, J.C. White, S.D. Horava, A.C. Henry, S.C. Roberts, S.R. Bhatia, Terminal sterilization of alginate hydrogels : Efficacy and impact on mechanical properties on mechanical properties, (2014). doi:10.1002/jbm.b.33070.
- [23] J. Sun, H. Tan, Alginate-Based Biomaterials for Regenerative Medicine Applications, (2013) 1285–1309. doi:10.3390/ma6041285.
- [24] S. Naghieh, M.R.R. Karamooz Ravari, M. Badrossamay, E. Foroozmehr, M. Kadkhodaei, Numerical investigation of the mechanical properties of the additive manufactured bone scaffolds fabricated by FDM: the effect of layer penetration and post-heating, *J. Mech. Behav. Biomed. Mater.* 59 (2016) 241–250. doi:10.1016/j.jmbbm.2016.01.031.
- [25] F. Bai, Z. Wang, J. Lu, J. Liu, G. Chen, R. Lv, J. Wang, K. Lin, J. Zhang, X. Huang, The correlation between the internal structure and vascularization of controllable porous bioceramic materials in

- vivo: a quantitative study, *Tissue Eng. Part A.* 16 (2010) 3791–3803.
- [26] M.C. Kruyt, J.D. de Bruijn, C.E. Wilson, F.C. Oner, C.A. van Blitterswijk, A.J. Verbout, W.J.A. Dhert, Viable Osteogenic Cells Are Obligatory for Tissue-Engineered Ectopic Bone Formation in Goats, *Tissue Eng.* 9 (2003) 327–336. doi:10.1089/107632703764664792.
- [27] F.E. Freeman, D.J. Kelly, Tuning Alginate Bioink Stiffness and Composition for Controlled Growth Factor Delivery and to Spatially Direct MSC Fate within Bioprinted Tissues, *Sci. Rep.* (2017) 1–12. doi:10.1038/s41598-017-17286-1.
- [28] S. Naghieh, M.R. Karamooz-Ravari, M. Sarker, E. Karki, X. Chen, Influence of crosslinking on the mechanical behavior of 3D printed alginate scaffolds: Experimental and numerical approaches, *J. Mech. Behav. Biomed. Mater.* 80 (2018) 111–118. doi:10.1016/j.jmbbm.2018.01.034.
- [29] J.M. Wasikiewicz, F. Yoshii, N. Nagasawa, R.A. Wach, H. Mitomo, Degradation of chitosan and sodium alginate by gamma radiation, sonochemical and ultraviolet methods, *Radiat. Phys. Chem.* 73 (2005) 287–295. doi:10.1016/j.radphyschem.2004.09.021.
- [30] N. Nagai, T. Matsunobe, T. Imai, Infrared analysis of depth profiles in UV-photochemical degradation of polymers, *Polym. Degrad. Stab.* 88 (2005) 224–233. doi:10.1016/j.polymdegradstab.2004.11.001.
- [31] C. Arnosti, D.J. Repeta, N. V Blough, Rapid bacterial degradation of polysaccharides in anoxic marine systems, *Geochim. Cosmochim. Acta.* 58 (1994) 2639–2652.
- [32] K.Y. Lee, D.J. Mooney, Alginate : properties and biomedical applications, *Prog. Polym. Sci.* 37 (2013) 106–126. doi:10.1016/j.progpolymsci.2011.06.003.Alginate.
- [33] M. Mendoza García, M. Izadifar, X. Chen, Evaluation of PBS Treatment and PEI Coating Effects on Surface Morphology and Cellular Response of 3D-Printed Alginate Scaffolds, *J. Funct. Biomater.* 8 (2017) 48. doi:10.3390/jfb8040048.
- [34] G.Y. Huang, L.H. Zhou, Q.C. Zhang, Y.M. Chen, W. Sun, F. Xu, T.J. Lu, Microfluidic hydrogels for tissue engineering, *Biofabrication.* 3 (2011) 12001.
- [35] M. d. Sarker, S. Naghieh, A.D. Mcinnes, D.J. Schreyer, X. Chen, Strategic design and fabrication of nerve guidance conduits for peripheral nerve regeneration, *Biotechnol. J.* (2018) 1700635. doi:10.1002/biot.201700635.

- [36] M.A. DeCoster, S. Maddi, V. Dutta, J. McNamara, Microscopy and image analysis of individual and group cell shape changes during apoptosis, *Microsc. Sci. Technol. Appl. Educ.* (2010) 836–843.
- [37] R. Calafiore, Alginate microcapsules for pancreatic islet cell graft immunoprotection: struggle and progress towards the final cure for type 1 diabetes mellitus, (2003).
- [38] S.H. Chia, B.L. Schumacher, T.J. Klein, E.J. Thonar, K. Masuda, R.L. Sah, D. Watson, Tissue-engineered human nasal septal cartilage using the alginate-recovered-chondrocyte method, *Laryngoscope*. 114 (2004) 38–45.
- [39] T. Zehnder, B. Sarker, A.R. Boccaccini, R. Detsch, Evaluation of an alginate-gelatine crosslinked hydrogel for bioplotting, *Biofabrication*. 7 (2015) 025001. doi:10.1088/1758-5090/7/2/025001.
- [40] F. You, X. Wu, X. Chen, 3D Printing of Porous Alginate/gelatin Hydrogel Scaffolds and Their Mechanical Property Characterization, *J. Int. J. Polym. Mater. Polym. Biomater.* 66 (2016) 299–306. doi:10.1080/00914037.2016.1201830.

Chapter 5 Modeling of the Mechanical Behavior of 3D-Bioplotting Scaffolds Considering the Penetration in Interlocked Strands

This chapter has been published as “Saman Naghieh, MD Sarker, Mohammad Reza Karamooz-Ravari, Adam D McInnes, and Xiongbiao Chen, Modeling of the Mechanical Behavior of 3D-Bioplotting Scaffolds Considering the Penetration in Interlocked Strands, Journal of Applied Sciences” According to the Copyright Agreement, "the authors retain the right to include the journal article, in full or in part, in a thesis or dissertation".

(All the experimental work was conducted by me. MD Sarker and Adam D McInnes helped me to conduct some experiments. Professor Xiongbiao Chen and Mohammad Reza Karamooz-Ravari guided and supervised the whole work.)

5.1 Abstract

(3D bioplotting has been widely used to print hydrogel scaffolds for tissue engineering applications. One issue involved in 3D bioplotting is to achieve the scaffold structure with the desired mechanical properties. To overcome this issue, various numerical methods have been developed to predict the mechanical properties of scaffolds, but limited by the imperfect representation of one key feature of scaffolds fabricated by 3D bioplotting, i.e., the penetration or fusion of strands in one layer into the previous layer. This paper presents our study on the development of a novel numerical model to predict the elastic modulus (one important index of mechanical properties) of 3D bioplotting scaffolds considering the aforementioned strand penetration. For this, the finite element method was used for the model development, while medium-viscosity alginate was selected for scaffold fabrication by the 3D bioplotting technique. The elastic modulus of the bioplotting scaffolds was characterized using mechanical testing and results were compared with those predicted from the developed model, demonstrating a strong congruity between them. Once validated, the developed model was also used to investigate the effect of other geometrical features on the mechanical behavior of bioplotting scaffolds. Our results show that the penetration, pore size, and number of printed layers have significant effects on the elastic modulus of bioplotting scaffolds; and also suggest that the developed model can be used as a powerful tool to modulate the mechanical behavior of bioplotting scaffolds.

5.2 Introduction

One aim of tissue engineering is to develop tissue/organ substitutes or scaffolds, based on the principles of biology and engineering, for the repair or replacement of damaged tissues and organs [1,2]. For this, scaffolds, typically of a 3D porous structure made from biomaterials, play an important role in supporting and/or promoting cell growth, tissue regeneration, and transport of nutrients and wastes. Design and fabrication of scaffolds have proven to be a challenging task [3]. One important issue in the design and fabrication of scaffolds is achieving the desired mechanical properties to match those of tissue at the site of implantation. More specifically, the scaffold must be strong enough to resist structural collapse upon implantation, yet sufficiently compliant so as not to damage the surrounding tissues.

Tissue scaffolds can be fabricated by either conventional or modern techniques. Conventional methods, like electrospinning, are limited for the fabrication of 3D scaffolds with interconnected pores [4,5] and in some cases, organic solvents have to be used, thus being detrimental for cellular proliferation/differentiation [6]. Nowadays, AM techniques have been drawn considerable attention since it allows to fabricate scaffolds layer-by-layer [7], and thus opens a new door to create scaffolds with complex 3D microstructure and controllable pore shape and size [8]. Among various AM techniques, extrusion-based 3D bioplotting shows promise, where bioinks are extruded from either one or multiple needles and thus form 3D scaffolds [9,10], as shown in Figure 5.1 (a pneumatic-based 3D bioplotter extruding biomaterials from one needle). Notably, the bioink for bioplotting can be prepared from the biomaterials favorable for cells, thus being capable of incorporating cells and proteins in the scaffold fabrication process [11,12]. For this, hydrogels have been widely utilized as they are able to provide an appropriate environment for encapsulating cells and growth factors [13]. This is mainly due to the fact the hydrogels involve a large amount of water in their polymeric 3D network, which is favorable to cell growth and tissue regeneration [14,15]. Alginate is one of the widely-used natural polymers with properties of good biocompatibility and ease of gelation and has found many applications in tissue engineering, such as wound healing and drug delivery [16]. As inspired, we selected alginate in the present study for the scaffold fabrication.

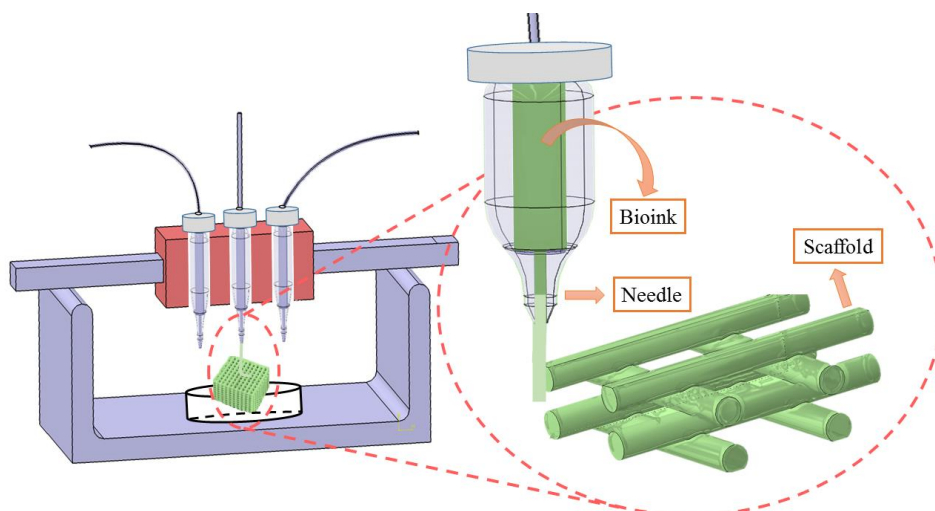


Figure 5.1. Schematic of 3D bioplotting.

As noted previously, scaffolds should have the mechanical properties similar to those of targeted tissue. To this end, research has been performed to fabricate scaffolds with desired mechanical properties by taking the aforementioned advantages of 3D bioplotting [17,18]. The experimental results illustrate the mechanical properties of 3D-bioplotting scaffolds can be affected by the scaffold-material properties and the geometrical features of scaffolds (including pore size, strand diameter, and orientation of strands) [17,19]. Notably, experimental measurements and characterization of the mechanical properties of scaffolds are time-consuming, even impractical once implanted *in vivo*. Therefore, there is a need to develop alternative methods, like numerical modeling, to represent or predict the mechanical properties of scaffolds instead of the use of experimental tests.

Recently, FEM has been introduced as a method to represent the mechanical properties of scaffolds fabricated by means of 3D extrusion-based printing. In our previous studies [8,20], models based on FEM have been developed to predict the elastic modulus of printed scaffolds. By these models, the elastic modulus of scaffolds was predicted with a good agreement with the measured ones [8,20]. FEM-based models can also be used to represent the change of mechanical properties of scaffolds with time due to the scaffold degradation [21] and the mechanical behavior of Poly(ethylene glycol) diacrylate hydrogels with complex geometric shapes [6]. It has been illustrated that FEM is a powerful tool to model the scaffold mechanical properties. However, the accurate representation of the structure of the scaffolds in the development of the FEM-based

model is an essential, yet challenging, task. This is particularly true when the printed scaffold structure is significantly different from the scaffold design due to the penetration or fusion of strands in one layer into the previous layer during the scaffold fabrication process. This difference, however, has been ignored in the reported models including those reviewed above for 3D biplotted scaffolds specifically. It is noted that the penetration amongst interlocked strands, analogous to a saddle notch, can affect the mechanical properties significantly [8], which should be considered in the FEM-based models.

In this study, FEM was used for the development of a model to predict the mechanical behavior of biplotted scaffolds considering the effect of penetration in interlocked strands. In the model development, the structural features of the scaffolds, including diameter and orientation of strands, strand penetration, and pore size, were considered as the inputs to the model, along with the scaffold-material properties. Scaffolds and bulk gels were fabricated from alginate by 3D biplotting and then evaluated mechanically through compression tests. Based on the developed model, the stress-strain curves were simulated and compared to those of experimental measurements to validate the developed model.

5.3 Materials and methods

5.3.1 Material preparation for fabrication

Materials utilized in this experiment were alginic acid sodium salt from brown algae (medium viscosity) with P-code 1001172534 and calcium chloride dehydrate with P-code 1001911753 (Sigma-Aldrich Canada Ltd., Toronto, ON, Canada). In addition, a tissue culture plate was treated with 0.5% (w/v) polyethylenimine (PEI, Alfa Aesar, Mw: 60000) and incubated overnight at 37°C. This coating can improve the surface adhesion of alginate strands during the printing process to achieve successful printing [22]. To prepare a 3% w/v alginate solution, 7.5 g of alginate powder was weighted using an analytical balance (Sartorius, CP 225 D), then added to 250 mL distilled water in a beaker covered by a parafilm. The solution was mixed overnight using a magnetic stirrer to create a homogenous solution. The solution was centrifuged for 5 minutes at 800 rpm (Sorvall T6000 B Centrifuge) to remove bubbles that had formed during mixing. To crosslink alginate, 50 mM CaCl₂ was added to the print bath to induce immediate crosslinking as the material was extruded in the scaffold fabrication process, as described below.

5.3.2 Design and fabrication of scaffolds

A CAD model of a scaffold, with a cuboid shape of $7 \times 7 \times 5$ mm, was generated using Magics EnvisionTEC (V13, Materialise, Belgium), which was then sliced into 31 layers with the Bioplotter RP software (V2.9, EnvisionTEC GmbH, Germany). The slice thickness was considered as 88% of the strand diameter. VisualMachine software (BP, V2.2, EnvisionTEC GmbH, Germany) was utilized to control the printing and assign the print parameters for the model (Figure 5.2). A perpendicular pattern with alternating angles of 0° and 90° was used between the two adjacent layers, each layer consisting of strands with a distance of 1 mm. A 3D-Bioplotter™ system (EnvisionTEC GmbH) was used to fabricate scaffolds by printing alginate solution into the 50 mM CaCl_2 solution to induce crosslinking layer-by-layer. Specifically, the 3% alginate solution was maintained at 10°C for 10 min in a low-temperature dispensing head. Alginate was dispensed at $18\text{-}20^\circ\text{C}$ using a conical needle with the inner diameter of $200\ \mu\text{m}$. The scaffolds were printed in a 12-well tissue culture plate coated with PEI, with each well containing 1 mL of 50 mM CaCl_2 to crosslink alginate immediately after dispensing. The pressure was set at 0.2 bar and head speed of 8 mm/s selected during printing. Printing conditions are presented in Table 5.1. After fabrication, scaffolds were maintained in the crosslinking solution for a time period sufficient to allow the Ca^{2+} ions to penetrate and crosslink the whole structure.

For assessing the elastic modulus of bulk gel, bulks of alginate were also created on the 3D-Bioplotter™ system by employing the procedure and printing conditions similar to the above scaffold fabrication except the zero distance set between two adjacent strands.

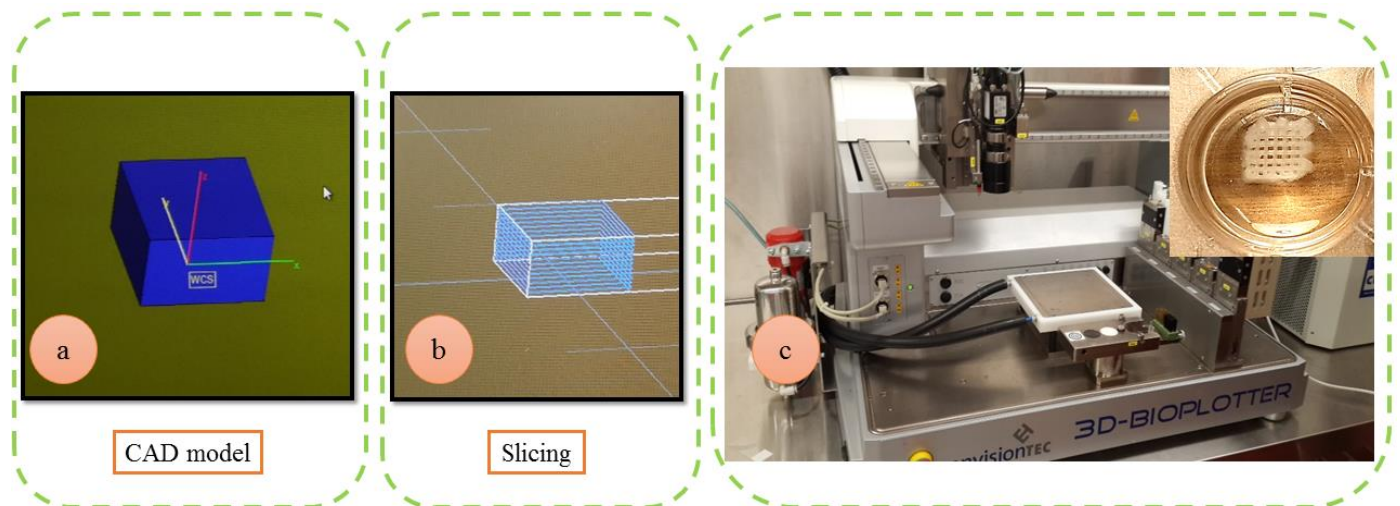


Figure 5.2. Illustration of printing alginate scaffolds: a) CAD model, b) sliced layers, and c) 3D-Bioplotter used for scaffold printing, with an inserted image showing the alginate scaffold printed in a tissue culture plate.

Table 5.1. Printing condition used in scaffold fabrication.

Concentration	Needle diameter (μm)	Head speed (mm/s)	Pressure (bar)	Temperature ($^{\circ}\text{C}$)	Crosslinker
3% (w/v)	200	8	0.2	18-20	CaCl ₂ (50 mM)

5.3.3 Image analyzing

For capturing the geometry of the samples, a 13 MP, f/2.2, 31mm, autofocus camera (Samsung, Korea) was used, and images were analyzed by Image J[®] 1.48v Software (National Institute of Health, USA). The strand diameter, height, and pore size of the fabricated scaffold were obtained using the aforementioned software (n=10). Moreover, the projected area on the plane of loading, which is needed for the calculation of stress was obtained using the dimensions obtained from these images prior to performing mechanical testing.

5.3.4 Mechanical testing

Using a texture machine (Texture Technologies Corp., New York, USA), uniaxial unconfined compression tests were performed. Three specimens were prepared for each group of bulk alginate and porous scaffold. All tests were carried out at a speed of 0.1 mm/s (strain rate of 0.035 S⁻¹) with a defined preload of 1 N. Before doing any experiment, specimens were placed between the loading plates of the machine and the load cell was set to zero. ASTM D-695 standard was used to assess the elastic modulus of both bulk gels and porous scaffolds of alginate [23], as reported in the standard guide for characterization and testing of biomaterial scaffolds used in tissue-engineered medical products (ASTM: F2150 – 13) [24]. Porous scaffolds were kept in a CaCl₂ crosslinking solution and extracted from the solution immediately prior to mechanical testing. It should be noted that keeping fabricated samples of alginate in the incubator with 37 $^{\circ}\text{C}$ temperature (humidified environment containing 5% CO₂) did not have any significant effect on the elastic modulus. Hence, to simplify the experiment, samples were kept in a refrigerator (4 $^{\circ}\text{C}$) before the experiment. It is noted that there was a nonlinear region at the beginning of the stress-strain curves, termed as the toe-region. This region makes the calculation of the elastic modulus (the slope of the first linear part of the curve) difficult. Based on the method provided in ASTM

D-695 standard, a line was used to fit the first linear section of the curves and the intersection of this line and the strain axis is terms as the corrected zero-strain point.

5.3.5 Finite element modeling

A Python script was used to develop a parametric finite element model through the finite element package ABAQUS 6.11-1 with the detailed information provided as follows. Figure 5.3.a shows the model generated using cylinders with the diameter of D and alternating strand orientation of $0-90^\circ$ to mimic the structure of fabricated scaffolds. The number of strands in each plane is denoted by N with corresponding subscripts, the amount of penetration within layers by Δ_0 , the pore size in the X and Z directions by P_x and P_z , respectively, and the length of material exceeding the main borders of the scaffold by E_x and E_z (Figure 5.3.a). It should be mentioned that for applying the compressive load, the upper and lower sides of the modeled scaffolds were trimmed with the value of Δ_L . Using these parameters, the dimensions of the scaffold can be calculated using the following relationships:

$$L_x = 2E_x + N_x D + (N_x - 1)P_x \quad (5.1)$$

$$L_z = 2E_z + N_z D + (N_z - 1)P_z \quad (5.2)$$

$$L_y = \begin{cases} 2\left(\frac{D}{2} - \Delta L + N_{yz}(D - \Delta_0)\right) & N_{yz} = N_{yx} - 1 \\ 2\left(\frac{D}{2} - \Delta L + N_{yz}(D - \Delta_0)\right) - (D - \Delta_0) & N_{yz} = N_{yx} \end{cases} \quad (5.3)$$

where L_x , L_y , and L_z are the length of the scaffold in each direction.

As shown in Figure 5.3.b, to simulate the compression test, all the translational degrees of freedom of the bottom side of the scaffold were fixed while the upper face was moved downward with the value of the desired deformation. Since the model has some symmetric planes, the computational efforts might be reduced by decreasing the size of the model. Hence, the model was considered symmetric in X and Z directions. In addition, appropriate boundary conditions, e.g. fixing the degree of freedom parallel to the plane of symmetry were applied.

To run the developed model, 20% displacement was applied and the Poisson's ratio was considered as 0.31 as per the previous studies [25,26]. Ten-node modified quadratic tetrahedron

elements (four integration points, C3D10) were used to mesh the model (the configuration of the meshed model is available in Figure 5.3.b). In addition, convergence was achieved by using the criteria or conditions that the displacement function within an element is continuous, of rigid-body one, and under the constant strain [27].

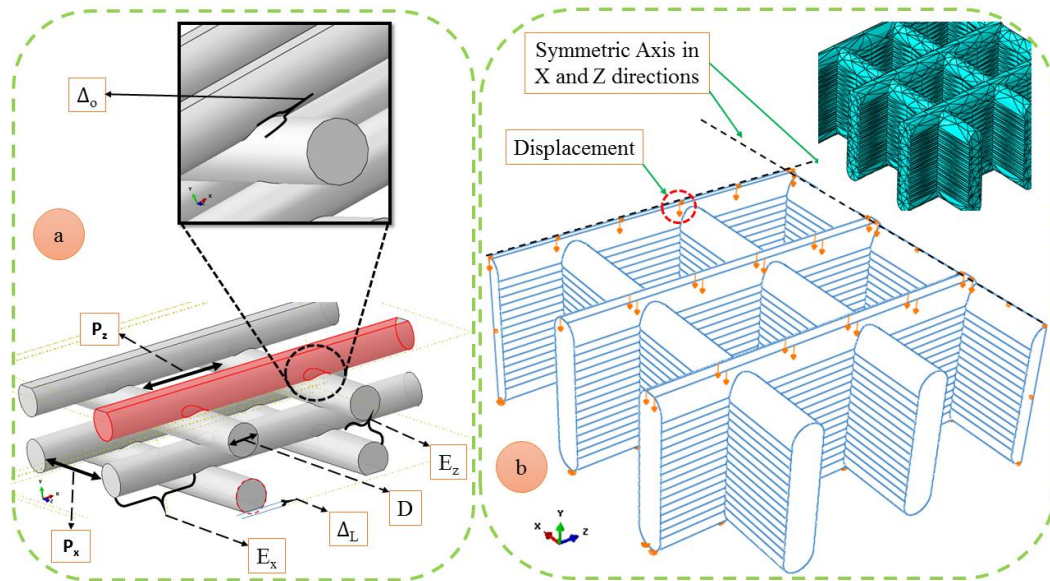


Figure 5.3. a) Applied parameters in finite element model including the amount of penetration within layers (Δ_0), pore size in the X and Z directions (P_x and P_z), E_x and E_z as the extra material exceeding the main borders of the scaffold. Δ_L is also the amount of trimmed value of the upper and lower sides of the modeled scaffolds for applying the compressive load and D is the strand diameter b) applied boundary conditions and meshed part.

5.3.6 Statistical analysis

Experimental data are presented as mean \pm standard deviation. A linear regression equation was extracted using Minitab[®] 17.1 software and confidence level for all intervals was considered as two-sided intervals with 95% value and, thus, P-value less than 0.05 was considered significant.

5.4 Results and discussion

5.4.1 Model verification

In this section, the geometrical features of the fabricated scaffold are evaluated according to the analysis of the captured images using Image J[®] Software, the elastic modulus of bulk gel and porous scaffolds are then examined and reported, and finally the results of the developed finite element model are presented and compared with the experimental measurements.

Geometrical features of scaffolds were measured using captures images analyzed in Image J® Software. The average pore size was 0.39 ± 0.03 mm and 0.47 ± 0.06 mm in Z and X directions, respectively. The strand diameter and height of the scaffold were also measured as 0.58 ± 0.06 mm and 2.63 ± 0.12 mm in Z and X directions, respectively. To measure the penetration, the original CAD design and the printed scaffolds were compared in terms of the layer height. The penetration was calculated based on the difference in heights, giving a value of 510 μm . Table 5.2 shows the parameters obtained from geometrical features of the fabricated scaffold and they were used in the simulation of the model, as input data.

Table 5.2. Parameter values used in simulation by the finite element model.

Parameters	Values (μm)
N_X	7
N_{YX}	15
N_{YZ}	16
N_Z	7
D	580
Δ_o	510
Δ_L	10
P_x	470
P_z	390
E_x	10
E_z	10

The compressive stress-strain response of the porous scaffolds and bulk alginate was used to calculate their corresponding elastic modulus. The elastic modulus of the bulk gel and alginate scaffold were calculated to be 42.3 ± 1.58 KPa and 32.1 ± 0.6 KPa, respectively.

For finite element simulations, a mesh sensitivity analysis on the finite element model was performed by comparing the predicted elastic modulus using different mesh sizes, with the results shown in Figure 5.4. To do so, the mesh size was reduced until the change of the obtained results was negligible. Using this method, the mesh size value of 0.3 was obtained and used for all the simulations.

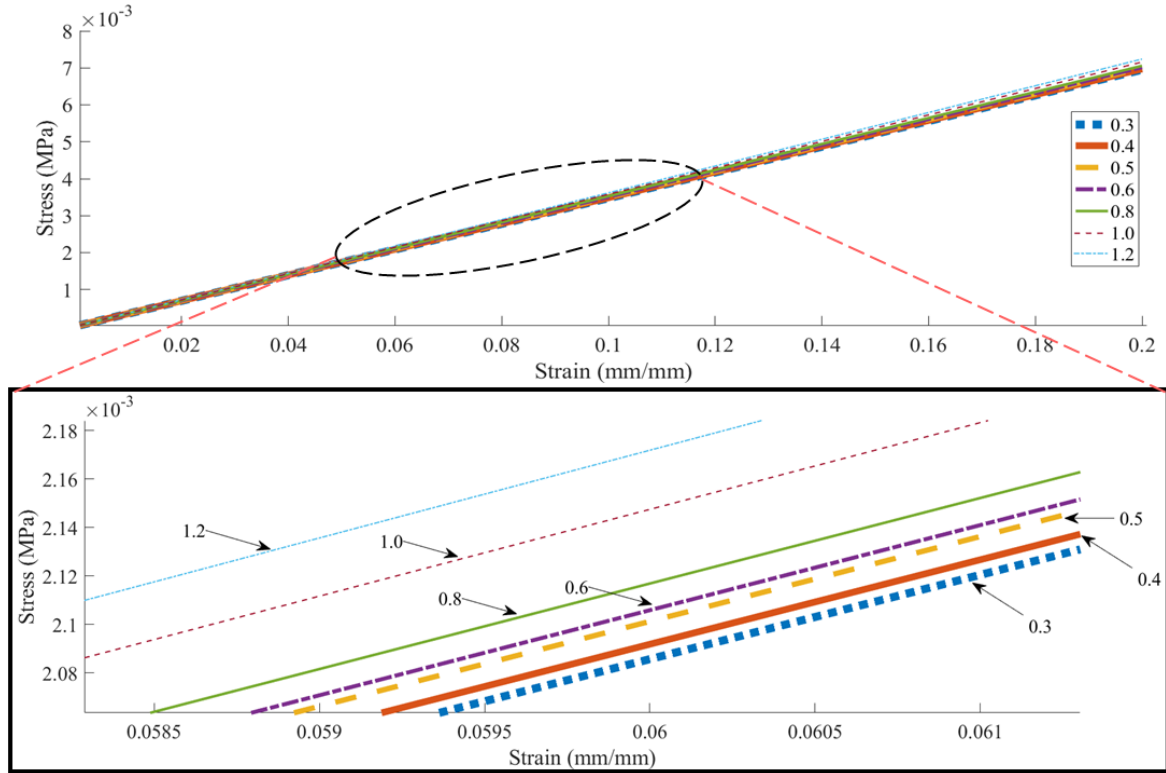


Figure 5.4. Mesh sensitivity study.

Using the developed finite element model, the elastic modulus of the fabricated scaffold was predicted to be 28.76 KPa, which is in agreement with the experimentally measured one, i.e., 32.1 ± 0.6 KPa. To further study the effectiveness of the model, more experiments were conducted by changing the penetration, pore size, and number of layers. For this, three sets of experiments were performed and for each set, one factor was subjected to changes and other parameters were taken the same as the ones listed in Table 5.2.

For the first set, the penetration element was changed. Initially, the slice thickness, which was 88% of the strand diameter (i.e. 580 μm), calculated as 510 μm . Then, the slice thickness was selected as 35% of strand diameter to reach 200 μm penetration by trial and error. The model predicted 14.92 KPa for scaffolds with approximately 0.2mm penetration within layers (the elastic modulus based on the experiment was 15.47 ± 1.03 KPa). As mentioned, the model predicted 28.76 KPa as the elastic modulus of scaffolds with 510 μm penetration which was in good agreement with experimental results (32.1 ± 0.6 KPa), as shown in Figure 5.5.

For the second set of experiments, the pore size of scaffolds was subjected to changes. Experimental results showed the elastic modulus of 22.43 ± 0.49 KPa for scaffolds with $P_x=551$ μm and $P_z=487$ μm , while the model predicted 21.35 KPa (Figure 5.6). As it was mentioned, the elastic modulus of scaffolds fabricated based on parameters reported in Table 5.2 ($P_x= 470$ μm and $P_z=390$ μm) was $32.1 \pm .0.6$ KPa, while the model predicted 28.76 KPa. In addition, for bulk gel, the elastic modulus of 42.3 ± 1.58 KPa was calculated experimentally, while the simulation predicted 37.94 KPa, as the elastic modulus. In case of bulk gel, $P_x=P_z=0$ was considered for the modeling purpose.

For the last set of experiments, the number of layers was changed and scaffolds with 16 and 24 number of layers were printed and experimental results showed 24.25 ± 0.64 KPa and $26.85 \pm .0.92$ KPa, while model predictions were 24.97 KPa and 27.34 KPa, respectively (Figure 5.7). As mentioned earlier, for scaffolds fabricated based on parameters mentioned in Table 5.2, 32.1 ± 0.60 KPa was obtained experimentally as the elastic modulus of scaffolds with 31 layers (the model prediction was 28.76 KPa).

5.4.2 Some more simulation results

Using the developed model, simulations were further performed to study the influence of penetration on the elastic modulus of scaffolds. For this, the value of penetration was changed from 0.01 mm, to 0.2, 0.3, 0.4, and 0.51, while the values of other parameters were taken the same as the ones listed in Table 5.2. The simulation results are presented in Figure 5.5, which shows a larger penetration lead to the higher elastic modulus. Elastic modulus achieved from experiment and model were discussed earlier for 0.2 and 0.51 mm penetration. More simulations were performed and the model predicted 3.64 KPa, 23.9 KPa, and 25.95 KPa for scaffolds with 0.01, 0.3, and 0.4 mm penetration amongst layers. Additionally, as shown in Figure 5.5, as the penetration is increased, the model predicts higher elastic modulus and results become closer to the elastic modulus of a bulk gel (experimental elastic modulus = 42.3 KPa). It means that by increasing the penetration, a scaffold with a rigid structure and high mechanical stability is obtained.

It should be noted the penetration between layers is an important index to measure the printability of hydrogels (i.e., alginate in the present study) in 3D bioplotting, which is defined as

the ability of a hydrogel to form and maintain a 3D structure and characterized by the difference between the printed scaffold structure and the designed one [28,29]. Larger penetration suggests the bigger difference between the printed structure and designed one, thus poorer printability of the hydrogel. In this study, the measured height of the fabricated scaffolds (2.63 ± 0.12 mm) was inputted to the numerical model to predict the elastic modulus of the printed structure (CAD model height was not considered for modeling).

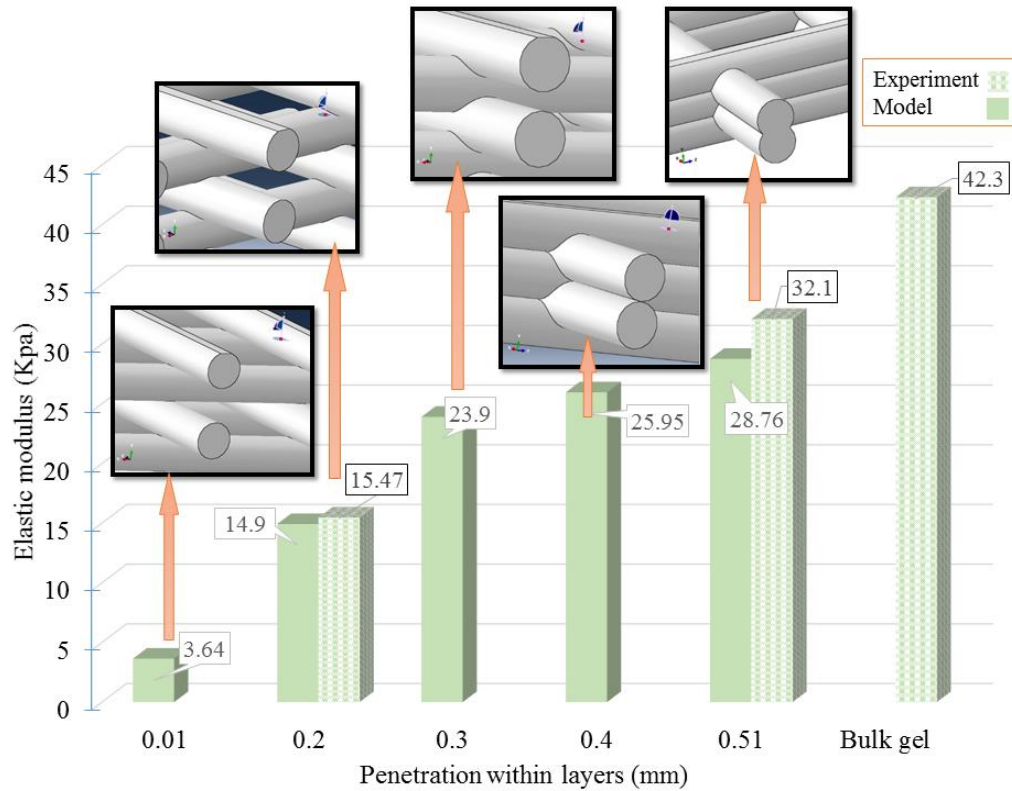


Figure 5.5. Effect of penetration within layers on the elastic modulus of alginate scaffolds with a strand diameter of 0.58 mm and a distance of 1 mm between two adjacent strands.

Based on the developed model, a numerical analysis was also carried out to study the effect of pore size on the elastic modulus of scaffolds. In these simulations, the pore size value was changed from 0 to 551 μm , with other parameter values the same as the ones listed in Table 5.2. The simulation results are shown in Figure 5.6, showing that a smaller pore size can result in a higher elastic modulus. As such, the pore size of scaffolds can be adjusted in order to obtain the mechanical properties similar to the native tissues. While there are many experimental studies in this regard [17,19], the use of finite element method would provide a more effective approach to

adjust the pore size or other geometrical parameters to achieve the desired mechanical properties. It should be noted that measured pore sizes in different directions of fabricated scaffolds were not the same as shown in Figure 5.6. Here more simulations were performed. Modeling results showed 30.42 KPa, 26.61 KPa, and 24.62 KPa for scaffolds with 300, 400, and 500 μm pore sizes in the X and Z directions defined in Figure 5.3.

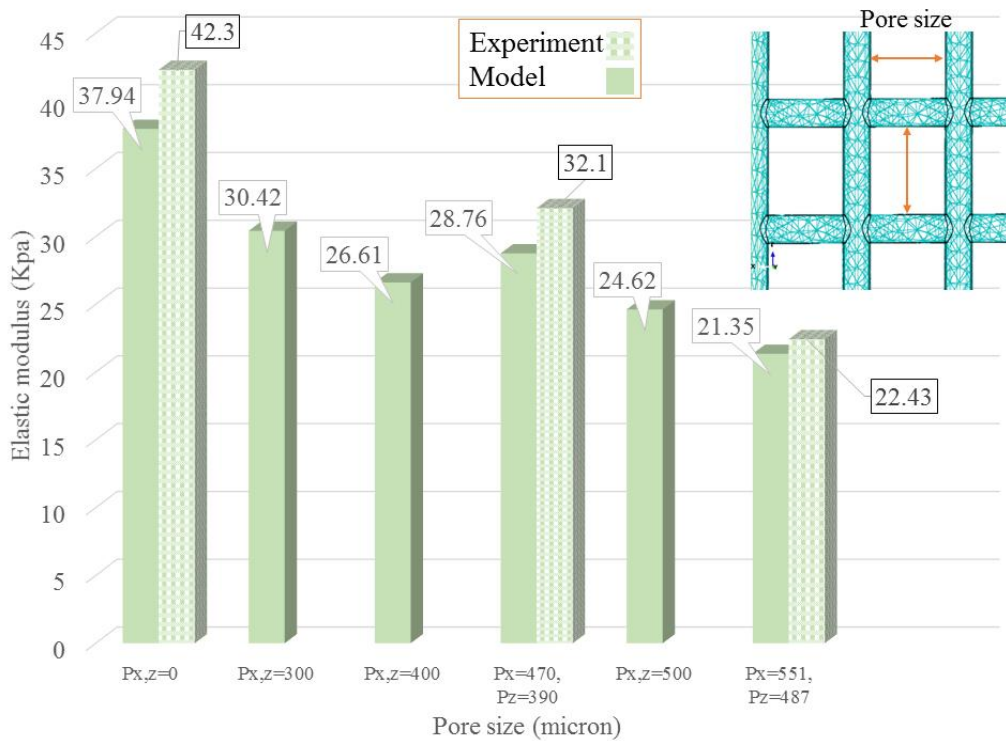


Figure 5.6. Effect of pore size on the elastic modulus (pattern fill column bars show experimental results for bioplotted scaffolds with $(P_x, z=0)$, $(P_x=470$ and $P_z=390)$, and $(P_x=551$ and $P_z=487)$).

The number of layers in the Y direction was investigated to determine the effect of the height of the scaffold on its elastic modulus. The penetration and strand diameter were considered as 0.51 mm and 0.58 mm, respectively. As demonstrated in 5.7, increasing the number of layers causes a higher elastic modulus numerically and experimentally. This is likely due to having more layers and, consequently, a thicker scaffold with a more mechanically stable structure has a higher elastic modulus. For a scaffold made of 10 layers, the model predicted 22.14 KPa as the elastic modulus of a porous scaffold. The model predicted 24.97 KPa, 27.34 KPa, and 28.76 KPa for scaffolds with 16, 24, and 31 layers, respectively.

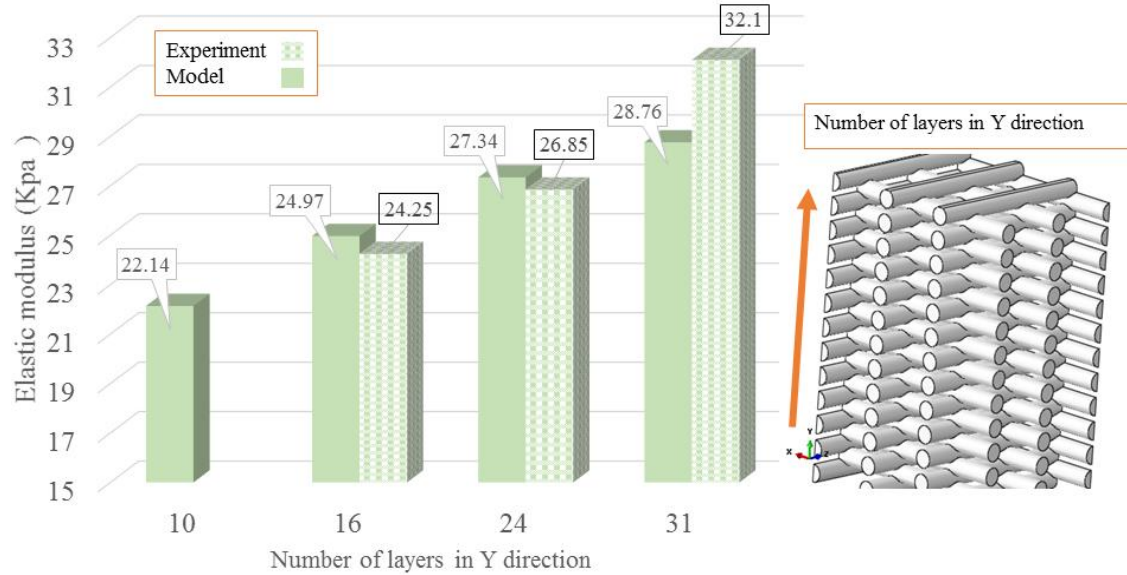


Figure 5.7. Effect of the number of layers on the elastic modulus (pattern fill column bars show experimental results for biplotted scaffolds with 16 (24.25 ± 0.64 KPa), 24 (26.85 ± 0.92 KPa), and 31 layers (32.1 ± 0.60 KPa)).

A strong congruity was observed between experimental and numerically predicted values of elastic modulus. Although the model was developed based on the assumption of a symmetric structure, biplotted scaffolds might be asymmetric in different directions due to random variables that affect extrusion. This asymmetry might cause an increase in the error between predicted and real values because of numerous variables associated with the 3D biofabrication regulate the structural uniformity and geometry of the scaffold. Fluid viscosity, temperature, dispensing pressure, needle speed, and crosslinker concentration have a profound effect on the strand diameter, porosity, and pore size distribution [22]. In this study, the scaffolds were printed in a static volume of the crosslinking solution of 1 mL and 50 mM CaCl_2 , the number of available Ca^{2+} ions in the crosslinking media decreases gradually with the fabrication of successive layers. Such a variable concentration of Ca^{2+} ions can affect the structure and thus the mechanical properties of the printed scaffolds [30]. As such, the effect of the crosslinker mechanism can be taken into consideration for improving the accuracy of model prediction. Also, fluid viscosity is temperature-dependent and therefore temperature, changing during the printing process, can affect the fluid flow, which is also responsible for degraded structures in the biplotted scaffolds. Another important factor influencing the mechanical behavior of porous scaffolds is microstructure degradation from the designed one [31–34]. Thus, in order to enhance the accuracy of numerical

models, one way is to identify these changes and degradations and specify them or their effects in the model. Moreover, it was reported that pore distribution and orientation of strands are not stable throughout the printed scaffold and it can influence the mechanical properties of scaffolds [35]. All of these can result in the degradation of the structure of scaffolds, thus affecting the error between the predicted and real values of scaffolds mechanical properties.

According to the results obtained from the developed model, Equation 5.4 was derived by fitting a linear regression model ($R^2=99.61\%$) to quantitatively specify the effect of each term on the elastic modulus. For this purpose, the degree of penetration, strand diameter, pore size, and extra materials in X and Z directions, and the number of layers in Y direction were considered in the model. The number of layers in X and Z directions were assumed as five. In addition, considering the effect of major factors (Δo , D , P_z , P_x , E_z , E_x and N_y), all the interactions amongst the aforementioned factors were considered in the model. Accordingly, with respect to P-value, some parameters were not appeared to be significant. However, regarding the interaction between various terms, these factors showed a significant effect Significant interactions were identified amongst many factors including penetration* N_y , $D*N_y$, $D*P_z$, $D*P_x$, N_y*P_z , and N_y*P_x . Figure 5.8 shows the effect of each factor on the elastic modulus demonstrating the significant effect of different terms on the elastic modulus.

$$\begin{aligned}
 \text{Elastic modulus} = & (136 \Delta o) + (651.9 D) - (10.37 N_y) + (2024 P_z) - (1956 P_x) - (497.7 E_x) + \\
 & (569 E_z) - (822 \Delta o \times D) + (98.5 \Delta o \times N_y) - (22463 \Delta o \times P_z) + (22209 \Delta o \times P_x) + \\
 & (4982 \Delta o \times E_x) - (5749 \Delta o \times E_z) - (49.9 D \times N_y) + (1357 D \times P_z) - (1796 D \times P_x) - 31.4 \\
 & \hspace{15em} (5.4)
 \end{aligned}$$

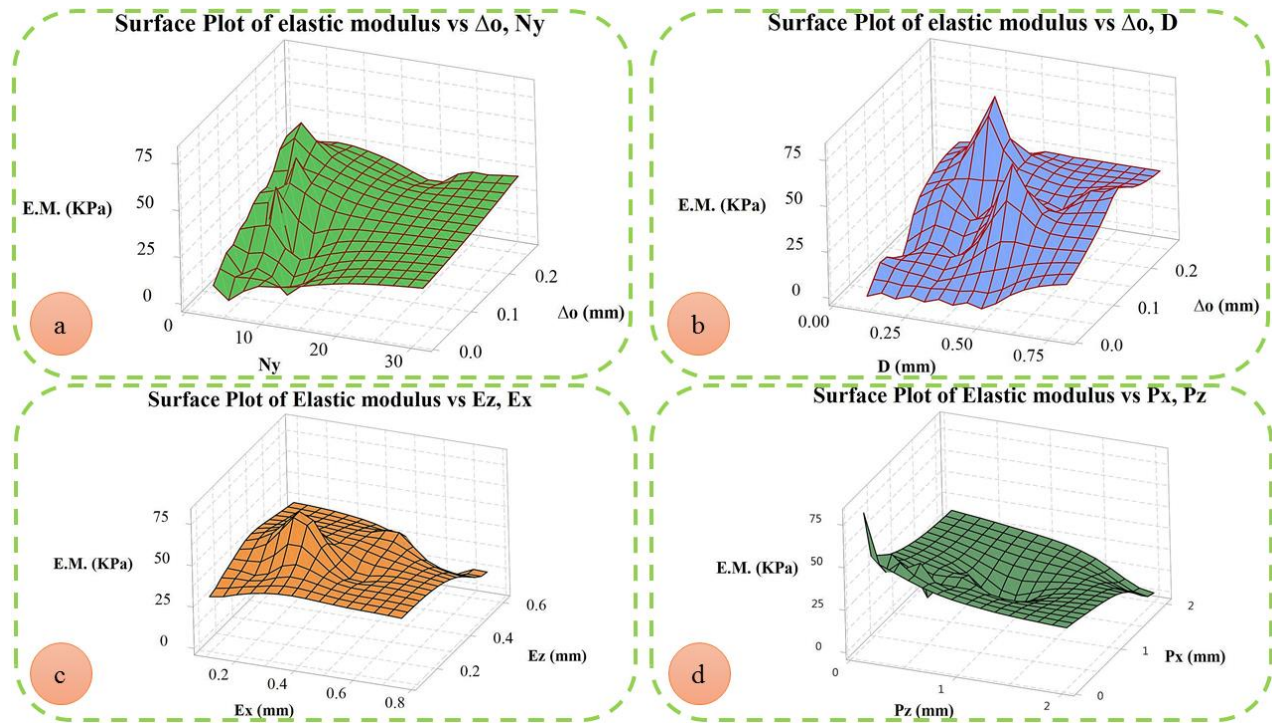


Figure 5.8. Effect of a) Δo and N_y , b) Δo and D, c) E_x and E_z , and d) P_z and P_x on the elastic modulus (E.M.).

It should also be noted that degradation of the scaffold over time can affect the mechanical properties of scaffolds and in this regard, many studies have been made to predict the mechanical behavior of scaffolds considering the effect of degradation in physiological condition [36–38]. In this study, we focused on the effect of penetration without the consideration of scaffold degradation over time. As an improvement of the model presented in this study, the effect of degradation on the mechanical properties of alginate scaffolds might be included in the future. As another extension of the present work, this model can be applied to study the mechanical behavior of hybrid scaffolds printed from more than two biomaterials. Similarly, this model can also be expanded to represent or predict the mechanical behavior of bioprinted scaffolds made from cell-incorporated hydrogels. To this end, cell-incorporated hydrogels can be evaluated mechanically and results can be used as an input of the presented model to predict the mechanical behavior of them.

5.5 Conclusions

In this study, a novel finite element model, by taking into account of the penetration of strands in one layer into the previous layer, was developed to represent and predict the mechanical properties of scaffolds fabricated by 3D Bioplotting technique. Our experimental results show the penetration within layers has a significant influence on the mechanical properties of printed scaffolds, along with the number of layers and pore size of scaffolds. To these experimental results, the predictions from our model were compared, showing a strong congruity between them. Based on the simulations from the developed model, a simple regression equation was developed to show the effects of penetration, pore size and number of layers on the elastic modulus of printed scaffolds. The method used to develop both finite element model and regression equation for alginate in the present study can also be implemented for other hydrogels so as to achieve the desired mechanical properties in tissue engineering.

5.6 References

- [1] M.G. Li, X.Y. Tian, X.B. Chen, A brief review of dispensing-based rapid prototyping techniques in tissue scaffold fabrication: role of modeling on scaffold properties prediction., *Biofabrication*. 1 (2009) 032001. doi:10.1088/1758-5082/1/3/032001.
- [2] M. Sarker, X.B. Chen, D.J. Schreyer, Experimental approaches to vascularisation within tissue engineering constructs., *J. Biomater. Sci. Polym. Ed.* 26 (2015) 683–734. doi:10.1080/09205063.2015.1059018.
- [3] X.-B.B. Chen, Dispensed-Based Bio-Manufacturing Scaffolds for Tissue Engineering Applications, *Int. J. Eng. Appl.* 2 (2014) 1–31.
- [4] S. Naghieh, M. Badrossamay, E. Foroozmehr, M. Kharaziha, Combination of PLA micro-fibers and PCL-gelatin nano-fibers for development of bone tissue engineering scaffolds, *Int. J. Swarm Intell. Evol. Comput.* 06 (2017) 1–4. doi:10.4172/2090-4908.1000150.
- [5] S. Naghieh, E. Foroozmehr, M. Badrossamay, M. Kharaziha, Combinational processing of 3D printing and electrospinning of hierarchical poly(lactic acid)/gelatin-forsterite scaffolds as a biocomposite: mechanical and biological assessment, *Mater. Des.* 133 (2017) 128–135. doi:10.1016/j.matdes.2017.07.051.

- [6] T. Jin, I. Stanciulescu, Numerical investigation of the influence of pattern topology on the mechanical behavior of PEGDA hydrogels, *Acta Biomater.* 49 (2017) 247–259.
- [7] S. Naghieh, A. Reihany, A. Haghighat, E. Foroozmehr, M. Badrossamay, F. Forooghi, Fused deposition modeling and fabrication of a three-dimensional model in maxillofacial reconstruction, *Regen. Reconstr. Restor.* 1 (2016) 139–144.
doi:<http://dx.doi.org/10.22037/triple%20r.v1i3.12543>.
- [8] S. Naghieh, M.R.R. Karamooz Ravari, M. Badrossamay, E. Foroozmehr, M. Kadkhodaei, Numerical investigation of the mechanical properties of the additive manufactured bone scaffolds fabricated by FDM: the effect of layer penetration and post-heating, *J. Mech. Behav. Biomed. Mater.* 59 (2016) 241–250. doi:10.1016/j.jmbbm.2016.01.031.
- [9] M. d. Sarker, S. Naghieh, A.D. Mcinnes, D.J. Schreyer, X. Chen, Strategic design and fabrication of nerve guidance conduits for peripheral nerve regeneration, *Biotechnol. J.* (2018) 1700635. doi:10.1002/biot.201700635.
- [10] S. Naghieh, M. Sarker, M. Izadifar, X. Chen, Dispensing-based bioprinting of mechanically-functional hybrid scaffolds with vessel-like channels for tissue engineering applications – a brief review, *J. Mech. Behav. Biomed. Mater.* 78 (2018) 298–314. doi:10.1016/j.jmbbm.2017.11.037.
- [11] B. Basu, *Fundamentals of Scaffolds Fabrication Using Low Temperature Additive Manufacturing*, in: *Biomater. Musculoskelet. Regen.*, Springer, 2017: pp. 127–173.
- [12] S. Das, F. Pati, Y.-J. Choi, G. Rijal, J.-H. Shim, S.W. Kim, A.R. Ray, D.-W. Cho, S. Ghosh, Bioprintable, cell-laden silk fibroin–gelatin hydrogel supporting multilineage differentiation of stem cells for fabrication of three-dimensional tissue constructs, *Acta Biomater.* 11 (2015) 233–246.
- [13] B.K. Singh, R. Sirohi, D. Archana, A. Jain, P.K. Dutta, Porous chitosan scaffolds: A systematic study for choice of crosslinker and growth factor incorporation, *Int. J. Polym. Mater. Polym. Biomater.* 64 (2015) 242–252.
- [14] D.N. Heo, N.J. Castro, S.-J. Lee, H. Noh, W. Zhu, L.G. Zhang, Enhanced bone tissue regeneration using a 3D printed microstructure incorporated with a hybrid nano hydrogel, *Nanoscale.* 9 (2017) 5055–5062. doi:10.1039/C6NR09652B.

- [15] Z. Izadifar, T. Chang, W.M. Kulyk, D. Chen, B.F. Eames, Analyzing biological performance of 3D-printed, cell-impregnated hybrid constructs for cartilage tissue engineering, *Tissue Eng. Part C. Methods*. 22 (2016) 173–188. doi:10.1089/ten.TEC.2015.0307.
- [16] K.Y. Lee, D.J. Mooney, Alginate : properties and biomedical applications, *Prog. Polym. Sci.* 37 (2013) 106–126. doi:10.1016/j.progpolymsci.2011.06.003.Alginate.
- [17] F. You, X. Wu, X. Chen, 3D Printing of Porous Alginate/gelatin Hydrogel Scaffolds and Their Mechanical Property Characterization, *J. Int. J. Polym. Mater. Polym. Biomater.* 66 (2016) 299–306. doi:10.1080/00914037.2016.1201830.
- [18] L.G. Bracaglia, B.T. Smith, E. Watson, N. Arumugasaamy, A.G. Mikos, J.P. Fisher, 3D printing for the design and fabrication of polymer-based gradient scaffolds, *Acta Biomater.* (2017).
- [19] A.D. Olubamiji, Z. Izadifar, J.L. Si, D.M.L. Cooper, B.F. Eames, D.X. Chen, Modulating mechanical behaviour of 3D-printed cartilage-mimetic PCL scaffolds: influence of molecular weight and pore geometry, *Biofabrication*. 8 (2016) 025020. doi:10.1088/1758-5090/8/2/025020.
- [20] S. Naghieh, M.R.K. Ravari, M. Badrossamay, E. Foroozmehr, M. Kadkhodaei, Finite element analysis for predicting the mechanical properties of bone scaffolds fabricated by fused deposition modeling (FDM), in: *Modares Mech. Eng. Proc. Adv. Mach. Mach. Tools Conf.*, 2015: pp. 450–454.
- [21] N.K. Bawolin, Modeling Material-Degradation-Induced Elastic Property of Tissue Engineering Scaffolds, *J. Biomech. Eng.* 132 (2010) 111001–7. doi:10.1115/1.4002551.
- [22] M. Sarker, X.B. Chen, Modeling the flow behavior and flow rate of medium viscosity alginate for scaffold fabrication with a 3D bioplotter, (2017).
- [23] ASTM: D 695 15, Standard Test Method for Compressive Properties of Rigid Plastics, 2015. https://compass.astm.org/EDIT/html_annot.cgi?D695+15.
- [24] ASTM: F1635, Standard Guide for Characterization and Testing of Biomaterial Scaffolds Used in Tissue-Engineered Medical Products, 2013.
- [25] V.B. Nguyen, C.X. Wang, C.R. Thomas, Z. Zhang, Mechanical properties of single alginate microspheres determined by microcompression and finite element modelling, *Chem. Eng. Sci.* 64 (2009) 821–829. doi:10.1016/j.ces.2008.10.050.

- [26] Y. Zhang, Y. Yu, H. Chen, I.T. Ozbolat, Characterization of printable cellular micro-fluidic channels for tissue engineering., *Biofabrication*. 5 (2013) 025004. doi:10.1088/1758-5082/5/2/025004.
- [27] Module: 2 Finite Element Formulation Techniques Lecture 3: Finite Element Method: Displacement Approach, (n.d.) <http://nptel.ac.in/courses/105105041/m2l7.pdf>.
- [28] Y. He, F. Yang, H. Zhao, Q. Gao, B. Xia, J. Fu, Research on the printability of hydrogels in 3D bioprinting, *Sci. Rep.* 6 (2016) 29977. doi:10.1038/srep29977.
- [29] F. You, B.F. Eames, X. Chen, Application of Extrusion-Based Hydrogel Bioprinting for Cartilage Tissue Engineering, *Int. J. Mol. Sci.* 18 (2017) 1597.
- [30] S. Naghieh, M.R. Karamooz-Ravari, M. Sarker, E. Karki, X. Chen, Influence of crosslinking on the mechanical behavior of 3D printed alginate scaffolds: Experimental and numerical approaches, *J. Mech. Behav. Biomed. Mater.* 80 (2018) 111–118. doi:10.1016/j.jmbbm.2018.01.034.
- [31] M.R. Karamooz Ravari, M. Kadkhodaei, M. Badrossamay, R. Rezaei, Numerical investigation on mechanical properties of cellular lattice structures fabricated by fused deposition modeling, *Int. J. Mech. Sci.* 88 (2014) 154–161.
- [32] M.R. Karamooz Ravari, M. Kadkhodaei, A. Ghaei, A Unit Cell Model for Simulating The Stress-Strain Response of Porous Shape Memory Alloys, *J. Mater. Eng. Perform.* (2015) 1–10.
- [33] M.R. Karamooz Ravari, M. Kadkhodaei, A. Ghaei, Effects of asymmetric material response on the mechanical behavior of porous shape memory alloys, *J. Intell. Mater. Syst. Struct.* (2015). doi:10.1177/1045389X15604232.
- [34] M.R. Karamooz Ravari, M. Kadkhodaei, A Computationally Efficient Modeling Approach for Predicting Mechanical Behavior of Cellular Lattice Structures, *J. Mater. Eng. Perform.* 24 (2015) 245–252.
- [35] R. Singh, P.D. Lee, T.C. Lindley, C. Kohlhauser, C. Hellmich, M. Bram, T. Imwinkelried, R.J. Dashwood, Characterization of the deformation behavior of intermediate porosity interconnected Ti foams using micro-computed tomography and direct finite element modeling, *Acta Biomater.* 6 (2010) 2342–2351.
- [36] N.K. Bawolin, X. Chen, Synchrotron-Based in Situ Characterization of the Scaffold Mass Loss from

Erosion Degradation, *J. Funct. Biomater.* 7 (2016) 17.

[37] N.K. Bawolin, A.T. Dolovich, D.X.B. Chen, C.W.J. Zhang, Characterization of mechanical properties of tissue scaffolds by phase contrast imaging and finite element modeling, *J. Biomech. Eng.* 137 (2015) 81004.

[38] N.K. Bawolin, X.B. Chen, Remote Determination of Time-Dependent Stiffness of Surface-Degrading-Polymer Scaffolds Via Synchrotron-Based Imaging, *J. Biomech. Eng.* 139 (2017) 41004.

Chapter 6 Influence of crosslinking on the mechanical behavior of 3D printed alginate scaffolds: experimental and numerical approaches

This chapter has been published as “Saman Naghieh, Mohammad Reza Karamooz-Ravari, MD Sarker, Eva Karki, and Xiongbiao Chen, Influence of Crosslinking on the Mechanical Behavior of 3D Printed Alginate Scaffolds: Experimental and Numerical Approaches, Journal of the Mechanical Behavior of Biomedical Materials, 2018, DOI: 10.1016/j.jmbbm.2018.01.034, <https://www.youtube.com/watch?v=puT4-xGI54Y&t=31s>.” According to the Copyright Agreement, "the authors retain the right to include the journal article, in full or in part, in a thesis or dissertation".

(All the literature review was conducted by me. MD Sarker and Eva Karki helped me in performing experiments. Professor Xiongbiao Chen and Mohammad Reza Karamooz-Ravari guided and supervised the whole review work.)

6.1 Abstract

Tissue scaffolds fabricated by 3D bioprinting are attracting considerable attention for tissue engineering applications. Because the mechanical properties of hydrogel scaffolds should match the damaged tissue, changing various parameters during 3D bioprinting has been studied to manipulate the mechanical behavior of the resulting scaffolds. Crosslinking scaffolds using a cation solution (such as CaCl_2) is also important for regulating the mechanical properties, but has not been well documented in the literature. Here, the effect of varied crosslinking agent volume and crosslinking time on the mechanical behavior of 3D bioplotted alginate scaffolds was evaluated using both experimental and numerical methods. Compression tests were used to measure the elastic modulus of each scaffold, then a finite element model was developed and a power model used to predict scaffold mechanical behavior. Results showed that crosslinking time and volume of crosslinker both play a decisive role in modulating the mechanical properties of 3D bioplotted scaffolds. Because mechanical properties of scaffolds can affect cell response, the findings of this study can be implemented to modulate the elastic modulus of scaffolds according to the intended application.

6.2 Introduction

Extrusion-based techniques are widely used to print large tissue scaffolds with cells and in such a system, biopolymers dispensed simultaneously from a 3D biofabrication system [1,2] and provide custom-made scaffolds using imaging technology [3]. It has also been combined with other techniques like electrospinning to come up with newly developed scaffolds [4,5]. Such fabrication requires biocompatible bioink to maintain a hydrated environment essential for cell survival [6]. Over the last decade, several hydrogel precursors have been investigated to develop suitable bioinks for extrusion-based systems [7]. Seaweed-derived Na-Alg is a potential bioink for fabricating cell-incorporated 3D structures with remarkable geometric precision [8]. In an extrusion-based biofabrication system, a cell-hydrogel precursor mixture is extruded layer-by-layer through a nozzle as per a pre-designed structure. The extruded alginate precursor must gel quickly to assist the fabrication process and support cell survival [9,10]. In this regard, divalent ionic crosslinkers have frequently been used to crosslink extruded hydrogel-based bioink because the ions cause rapid gelation and the gels can have acceptable printability and support the viability of any incorporated cells [11].

Although alginate offers several attractive features for 3D biofabrication, the poor mechanical stability of alginate scaffolds has been a major issue that requires further investigation [12]. Several efforts have improved the mechanical stability of 3D alginate constructs. For instance, alginate composites have been explored but complexities associated with multi-polymer handling may limit their application [2]. Other studies have been conducted to improve the mechanical stability of hydrogel scaffolds by manipulating the type and concentration of ionic crosslinkers [13]. Among various divalent ions, Ca^{2+} ions facilitate superb printability for alginate precursors while maintaining reasonable cell viability [14]. Mechanically stable alginate scaffolds can be successfully fabricated using CaCl_2 solution at higher concentrations [15], but the incorporated cells can be adversely affected [1]. Therefore, extruding the alginate precursor into a lower concentration CaCl_2 solution has been recommended to limit effects on cell viability [16]. Cell-incorporated scaffolds should also be crosslinked immediately after printing to prevent significant decreases in cell viability [1]. If the alginate precursor is extruded in a constant, low-concentration, and small volume of CaCl_2 solution, the number of available Ca^{2+} ions in the media

might decline significantly with the progression of scaffold height; this, in turn, might affect the mechanical stability of the extruded hydrogel. Accordingly, an appropriate quantity of low concentration CaCl_2 solution should be employed in the biofabrication process to minimize the depletion effect of Ca^{2+} ions. However, this effect has not been thoroughly examined to date and so the appropriate volume and concentration of CaCl_2 solution required for an extrusion-based system without compromising the mechanical stability of the alginate scaffolds is not known.

Furthermore, extrusion-based biofabrication techniques require a specific amount of time to print a 3D structure and, during this period, scaffolds remain immersed in the crosslinker. Similar to concentration, crosslinking time in Ca^{2+} ions affects the viability of incorporated cells [1]. In an extrusion-based system, the CaCl_2 solution is often aspirated upon biofabrication without allowing sufficient time for the alginate scaffolds to achieve equilibrium with the Ca^{2+} ions. While quick removal of the CaCl_2 solution improves cell viability, the mechanical stability of the alginate scaffolds could be significantly compromised. Scaffolds crosslinked for an extended period could potentially be used for post-seeding applications, but the effect of immersing bioplotted alginate scaffolds in CaCl_2 solution for a prolonged period on the mechanical stability of the hydrogel construct has not been assessed.

This study investigated the volume of CaCl_2 and gelation time as potential significant parameters in the biofabrication process of alginate scaffolds. While some studies have focused on the concentration of crosslinker [1], here we exclusively concentrate on the effect of crosslinking time and volume for a fixed concentration of the crosslinking solution. The effect of these factors on the mechanical characteristics of the bioplotted scaffolds was investigated using experimental and numerical approaches. Alginate precursor was used as a bioink to print scaffolds with a 3D bioplotting machine. Bioink was extruded in CaCl_2 solution layer-by-layer to fabricate a cuboid structure. The gelation time was varied from 0 to 24 h, with the volume of 50 mM CaCl_2 solution maintained between 1 and 5 mL. The elastic modulus of the scaffolds produced was measured to evaluate the effect of varying volumes and gelation times of CaCl_2 solution, and then numerical models used to predict the elastic modulus of alginate scaffolds crosslinked with various volumes of crosslinker at a fixed concentration. Such models will be very useful for predicting the elastic modulus of alginate scaffolds *in situ* where the gelation time in the ionic crosslinkers must vary.

6.3 Materials and methods

6.3.1 Preparation of alginate solution and other required materials

Medium viscosity alginic acid sodium salt from brown algae (Sigma-Aldrich Canada Ltd., P-code 1001172534, with a molecular weight of 80,000-120,000 g/mol) was used for the preparation of a 3% w/v alginate solution using distilled water. Calcium chloride dehydrate (Sigma-Aldrich Canada Ltd., P-code 1001911753) was used for the preparation of a 50 mM CaCl₂ crosslinking solution. Tissue culture plates were treated with 0.5% (w/v) PEI (Alfa Aesar) and then incubated overnight at 37 °C and 5% carbon dioxide to improve the attachment of the first printed layer of alginate to the culture plate during the ensuing scaffold fabrication [8].

6.3.2 Design and fabrication of alginate scaffolds

The CAD model for scaffolds with dimensions of 10 × 10 × 5 mm was created using Magics EnvisionTEC (V13, Materialise, Belgium) and then sliced into 15 layers using Bioplotter RP software (V2.9, EnvisionTEC GmbH, Germany). The thickness of each layer was set at 160 μm and the distance between two adjacent strands at 1.5 mm.

A 3D bioplotter (EnvisionTEC GmbH) was used to fabricate the scaffolds with the alginate solution dispensed through a conical needle (EFD Nordson, Westlake, OH) with an inner diameter of 200 μm at a temperature of 20 °C. During dispensing, the applied pressure was set to 0.2 bar and the horizontal movement speed of the dispensing head to 6 mm/s. Scaffolds were fabricated layer-by-layer as per the CAD design by dispensing alginate solution into the wells of a 12-well tissue culture plate that held 1, 3, or 5 mL of 50 mM CaCl₂ as a crosslinking agent. Scaffolds were then either immediately subjected to mechanical testing or kept in the crosslinking solution at 37 °C for 2, 4, or 24 h before mechanical testing. The experimental groups are summarized in Table 6.1.

Table 6.1. Groups of scaffolds subjected to mechanical testing.

Group	Crosslinking time in CaCl₂ upon fabrication (h)	Volume of CaCl₂ used for crosslinking (mL)	Storage temperature before mechanical testing (°C)
1	0	1	n/a
2	0	3	n/a
3	2	1	37

4	2	3	37
5	4	1	37
6	4	3	37
7	24	1	37
8	24	3	37
9	24	5	37

6.3.3 Mechanical testing

Compression tests were performed to calculate the elastic modulus of the scaffolds from the recorded stress-strain curves. To this end, a Bose BioDynamic™ machine (with a load cell of 20 N) was used for compression tests on the scaffolds done at a speed of 0.01 mm/s (or a strain ratio of 0.0037 s⁻¹). Based on a method explained elsewhere [17], the elastic modulus of the scaffolds was calculated using the linear section of the stress-strain curves and by defining the ϵ_0 (corrected zero strain point) as the intersection of the linear region of the curve and the zero-stress point (Figure 6.1). Compression tests were also performed on bulk alginate gels. Bulk gels were 3D bioplotted layer by layer to create an environment for their crosslinking similar to that used for the scaffolds (Figure 6.1a, b). The same volume of alginate used to create the scaffolds was used to fabricate the bulk gels. The elastic modulus values for the bulk gels were used to run the finite element model presented below.

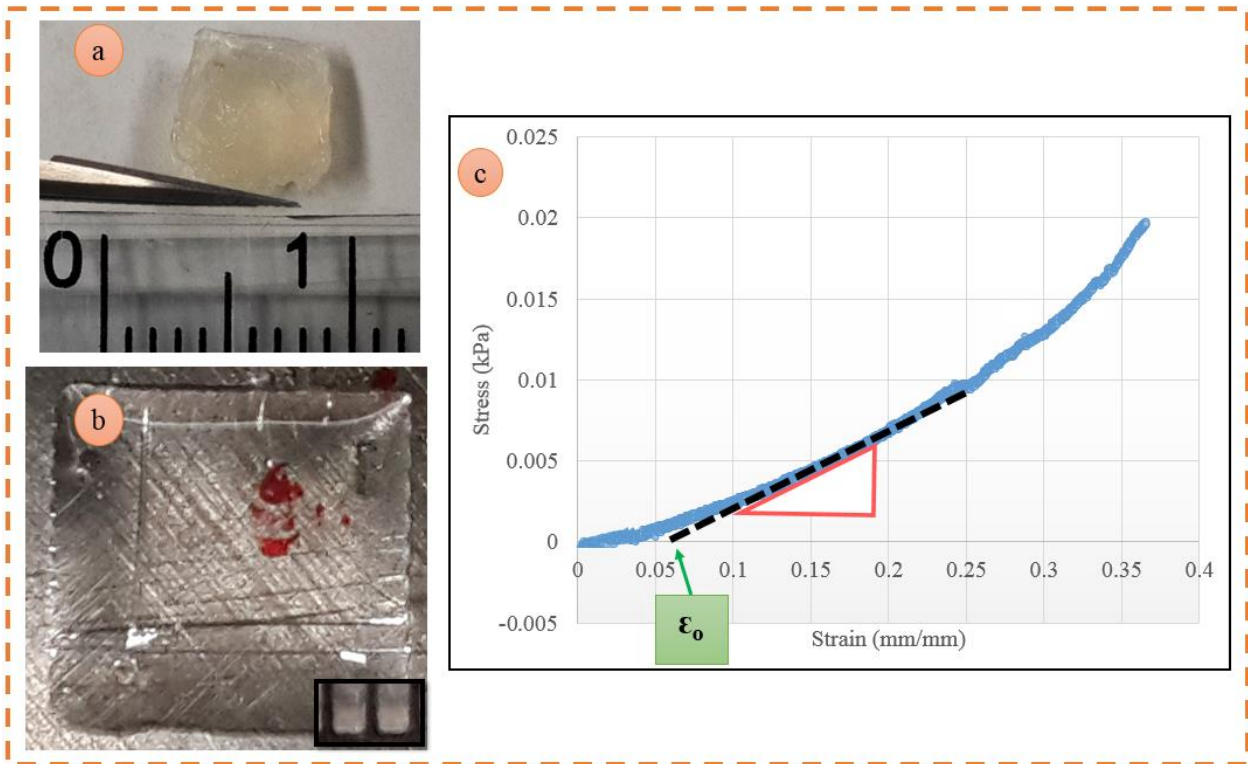


Figure 6.1. a) 3D bioplotting bulk gel, b) first printed layer of the bulk gel, and c) corrected stress-strain curve using corrected zero strain point.

6.3.4 Numerical modeling of the linear/non-linear behavior of 3D bioplotting scaffolds

Two approaches were implemented to predict the mechanical behavior of 3D bioplotting scaffolds: linear elastic finite element modeling and non-linear regression modeling. The main goal of these numerical models are to predict the mechanical behavior of scaffolds prior to fabrication to optimize scaffold parameters pre-production, as producing various iterations for experimental characterization is costly and time consuming [18,19].

To develop the linear finite element model, a Python script was developed using the finite element package ABAQUS 6.11-1. The proposed finite element model was developed to predict the elastic modulus of 3D bioplotting scaffolds immediately after printing. One of the inputs of this model is the elastic modulus of bulk gel, which can be affected by crosslinking time and volume; hence, the effect of crosslinking mechanism was taken into consideration. The details of the model developed are discussed elsewhere [17,20]. Briefly, scaffolds were considered as combinations of strands with 0° and 90° orientations and an interstrand distance representing the pore size in the X

and Z directions. Figure 6.2 depicts the geometrical model used to define the structure of a 3D bioplotted scaffold. The number of strands (N) was chosen to represent the structure of the fabricated scaffolds and D was defined as the diameter of each strand. Additionally, the amount of penetration among layers (Δ_0) was considered in the model. According to the stress-strain curves of the compressed samples, the displacement of this elastic model was defined as 25%. A Poisson ratio of 0.31 was selected for alginate from the literature [21,22] and Δ_L was defined as the value of deformed sections at the top and bottom of the scaffold. Finally, E_x and E_z were defined in the model so that the real structure of the printed scaffold could be represented (Figure 6.2). Equations 6.1 to 6.3 were added to the developed Python script to mathematically represent the structure of the alginate scaffolds:

$$L_x = 2E_x + N_x D + (N_x - 1)P_x \quad (6.1)$$

$$L_z = 2E_z + N_z D + (N_z - 1)P_z \quad (6.2)$$

$$L_y = \begin{cases} 2 \left(\frac{D}{2} - \Delta L + N_{YZ}(D - \Delta_0) \right) & N_{YZ} = N_{YX} - 1 \\ 2 \left(\frac{D}{2} - \Delta L + N_{YZ}(D - \Delta_0) \right) - (D - \Delta_0) & N_{YZ} = N_{YX} \end{cases} \quad (6.3)$$

where L_x , L_y , and L_z are dimensions of the scaffold in the X, Y, and Z directions, respectively. To reduce the computational effort, the model assumed symmetry in the X and Z directions and a strand diameter that was the mean of diameters measured from different points on the scaffold.

Ten-node modified quadratic tetrahedron elements with four integration points, denoted as C3D10 in ABAQUS, were used to mesh the model. The size of the mesh was initially set at 1 and then reduced until the change in the simulation results was negligible. Using this method, a mesh size of 0.3 was found appropriate and thus utilized for all simulations. Furthermore, the layer penetration was defined in the model as the amount of penetration of one layer into the next; full-attachment amongst layers was taken into account by merging nodes. Additionally, all geometrical features, i.e., pore size in different directions, strand diameter, thickness, etc., were obtained using captured images and added as model inputs. As such, the model considered all changes that might occur after printing, such as shrinkage, and was representative of the actual scaffolds fabricated.

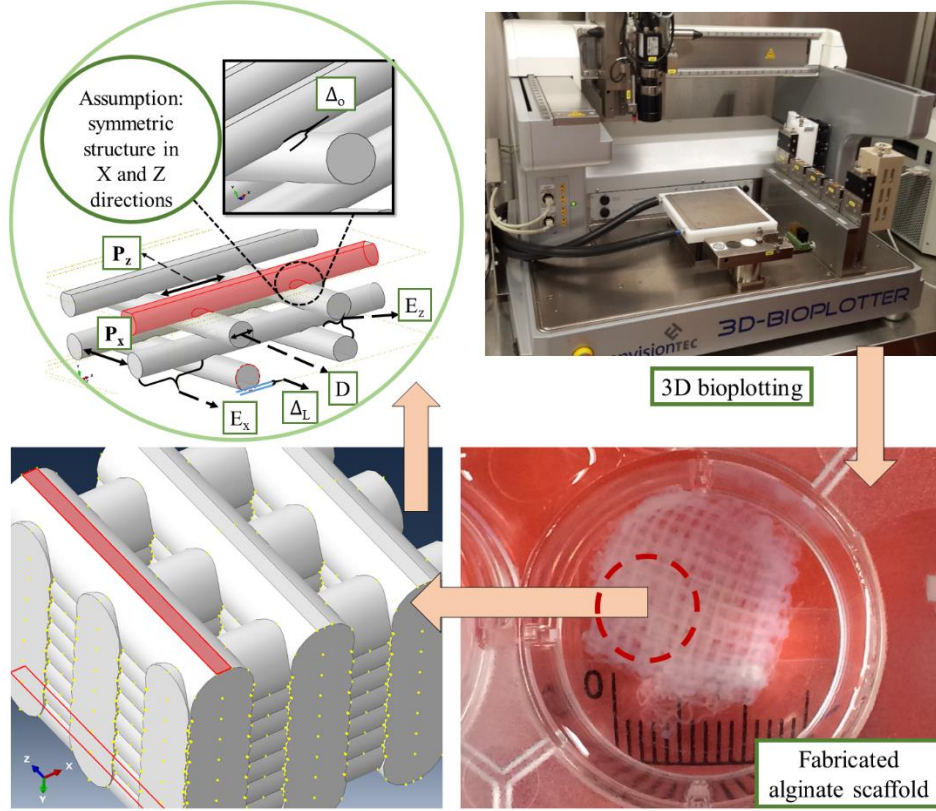


Figure 6.2. The model developed to represent the structure of the alginate scaffold fabricated using a 3D bioplotter: penetration within layers (Δ_0), strand diameter (D), pore size in the X (P_x) and Z (P_z) directions, exceeding distance after the last strand in X and Z directions (E_x and E_z), and the amount of deformation at the upper and lower sides of the scaffold (Δ_L).

In addition, consideration of the nonlinear mechanical behavior of the scaffolds has been taken into account in many studies to date because the tissues being replaced by scaffolds are homogeneous materials with non-linear responses. Accordingly, a non-linear (empirical power) model was also developed to investigate the non-linear behavior of the bioplotted scaffolds and bulk gels. Power models have been widely reported in the literature for modeling the non-linear behavior of materials [23], according to:

$$\sigma_E = K \epsilon_E^n \quad (6.4)$$

where K is the rigidity constant (index of stiffness), n is the degree of concavity (index for the deviation from linearity), and σ_E , ϵ_E are stress and strain, respectively. For $n=1$, this equation is equal to Hooke's law and k represents the elastic modulus.

In some tissue engineering applications, such as peripheral nerve [24], bone [17], and articular cartilage [25] regeneration, scaffolds undergo compressive force exerted by over- and underlying tissues in one direction. In such cases, the compressive elastic modulus is important in one direction while the scaffold mechanical behavior in other directions might be different; indeed, bioprinted scaffolds are not isotropic [26].

6.3.5 Imaging and morphology evaluation

SEM was used to investigate the scaffold morphology and open source software (ImageJ 1.5i) used to process the captured images.

6.3.6 Statistical analysis

All results are reported as mean values \pm standard deviation. T-tests were used to compare the means of groups and determine statistical significance.

6.4 Results and discussion

6.4.1 Effect of the crosslinking time

Figure 6.3 shows the effect of crosslinking time on the elastic modulus of alginate scaffolds in a fixed volume (3 mL) of CaCl_2 crosslinker. Compression tests indicated elastic modulus values of 39.8 ± 6.36 kPa (immediately after printing), 99.3 ± 1.8 kPa (2 h after printing), 153.60 ± 16.10 kPa (4 h after printing), and 273.35 ± 5.55 kPa (24 h after printing). The larger elastic modulus observed with increasing time is attributed to more Ca^{+2} ions being involved in chemically crosslinking the alginate.

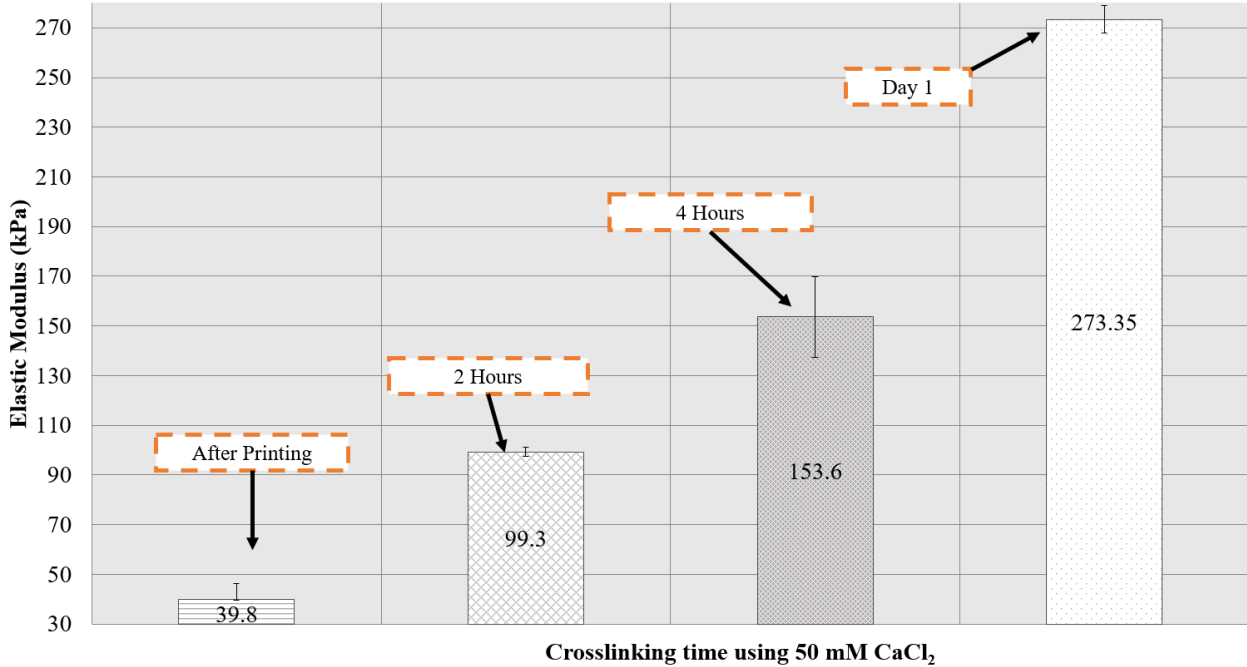


Figure 6.3. Effect of crosslinking time on the elastic modulus of alginate scaffolds immersed in 3 mL of 50 mM CaCl₂.

6.4.2 Effect of crosslinker volume

Figure 6.4 shows the effect of varying the volume of CaCl₂ on the elastic modulus. The focus here was on the first 4 h after printing, which should provide sufficient time for the Ca⁺² ions to penetrate the entire structure. As showed in Figure 6.3, samples exposed to the crosslinking agent for a greater amount of time had a higher elastic modulus; for example, Figure 6.4 shows values of 21.65 ± 1.91 kPa immediately after printing vs. 80.25 ± 2.35 kPa measured 2 h later for scaffolds printed into 1 mL of CaCl₂. The elastic modulus of other samples with the same condition except for exposing to 3 mL of crosslinker agent was 39.8 ± 6.36 kPa, 99.3 ± 1.8 kPa, 153.60 ± 16.10 kPa, and 273.35 ± 5.55 kPa, as mentioned before. Comparing the mechanical properties of samples that were crosslinked in 1 vs. 3 mL of CaCl₂ for the same crosslinking time shows that a larger volume of crosslinking agent leads to better mechanical stability immediately after printing. Notably, samples crosslinked using either 3 or 5 mL of CaCl₂ had no significant difference in terms of elastic modulus after 24 h, which is attributed to the scaffolds reaching equilibrium with the crosslinking solution. For 3D bioplotting of cell-incorporated alginate scaffolds, crosslinking time is critical because cell viability can decrease significantly with exposure to the crosslinking solution [1]. The results here indicate that the volume of crosslinker plays a decisive role in

determining the elastic modulus of alginate scaffolds immediately after printing. These findings could be implemented to modulate the mechanical behavior of scaffolds to match those of the target tissue. In the next section, a finite element model is proposed to predict the elastic modulus of scaffolds immediately after printing.

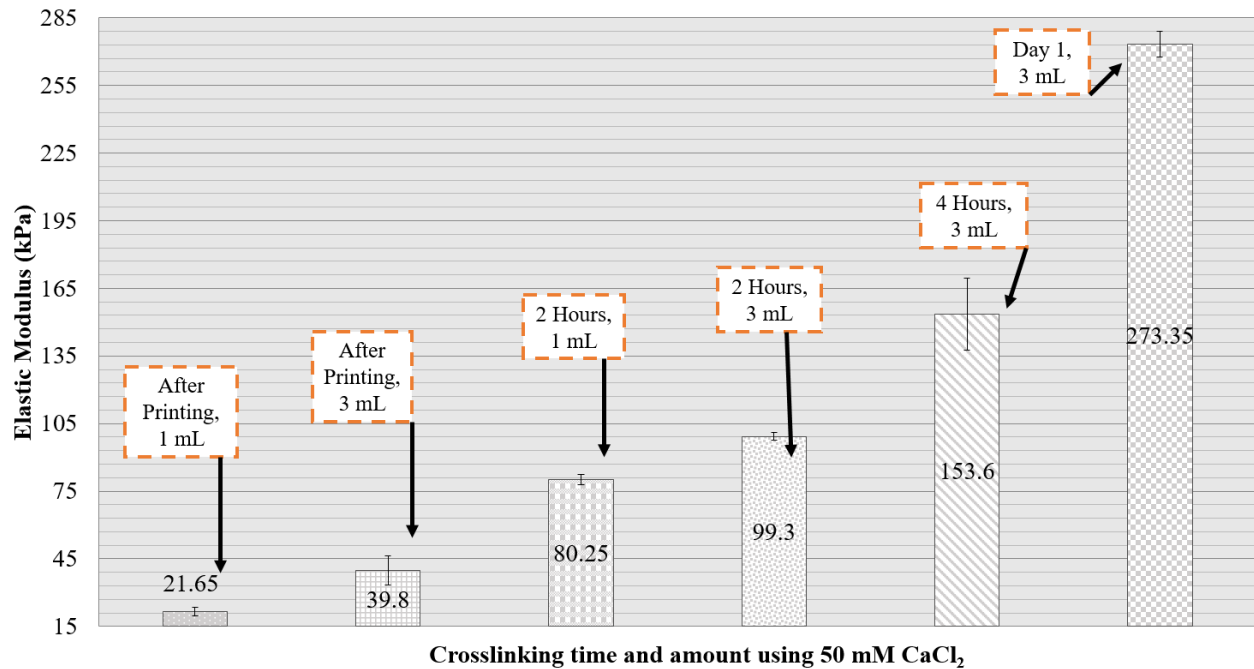


Figure 6.4. Effect of crosslinking time and crosslinker volume on the elastic modulus of alginate scaffolds immersed in 1 mL or 3 mL of crosslinking agent.

6.5 Follow-up computational analysis

6.5.1 Linear elastic finite element model to predict the elastic modulus of scaffolds immediately after printing

An elastic linear model was developed to predict the elastic modulus of scaffolds exposed to 1 mL or 3 mL of crosslinker immediately after the 3D bioplotting process. As noted above, predicting the mechanical behavior of scaffolds immediately after printing would be useful for cell-incorporated scaffolds that cannot remain in crosslinking solution for a long time without compromising cell viability. To calculate the elastic modulus of the bulk materials, bulk alginate gels were exposed to 1 mL or 3 mL of crosslinker and immediately subjected to mechanical testing (data not shown). The significant difference between the elastic modulus of scaffolds crosslinked with 1 mL vs. 3 mL of crosslinker and compressed immediately after printing was shown in Figure

6.4; this is attributed to the porous structure of the scaffolds. SEM images of alginate scaffolds crosslinked for 24 h in 50 mM CaCl_2 indicate the presence of nanopores throughout the scaffold strands (Figure 6.5). These pores can increase the surface area and, consequently, more surface is exposed to the crosslinking agent. Hence, using 3 mL vs. 1 mL of crosslinker, and therefore more Ca^{2+} ions, can improve the mechanical stability of 3D bioplotted scaffolds immediately after printing.

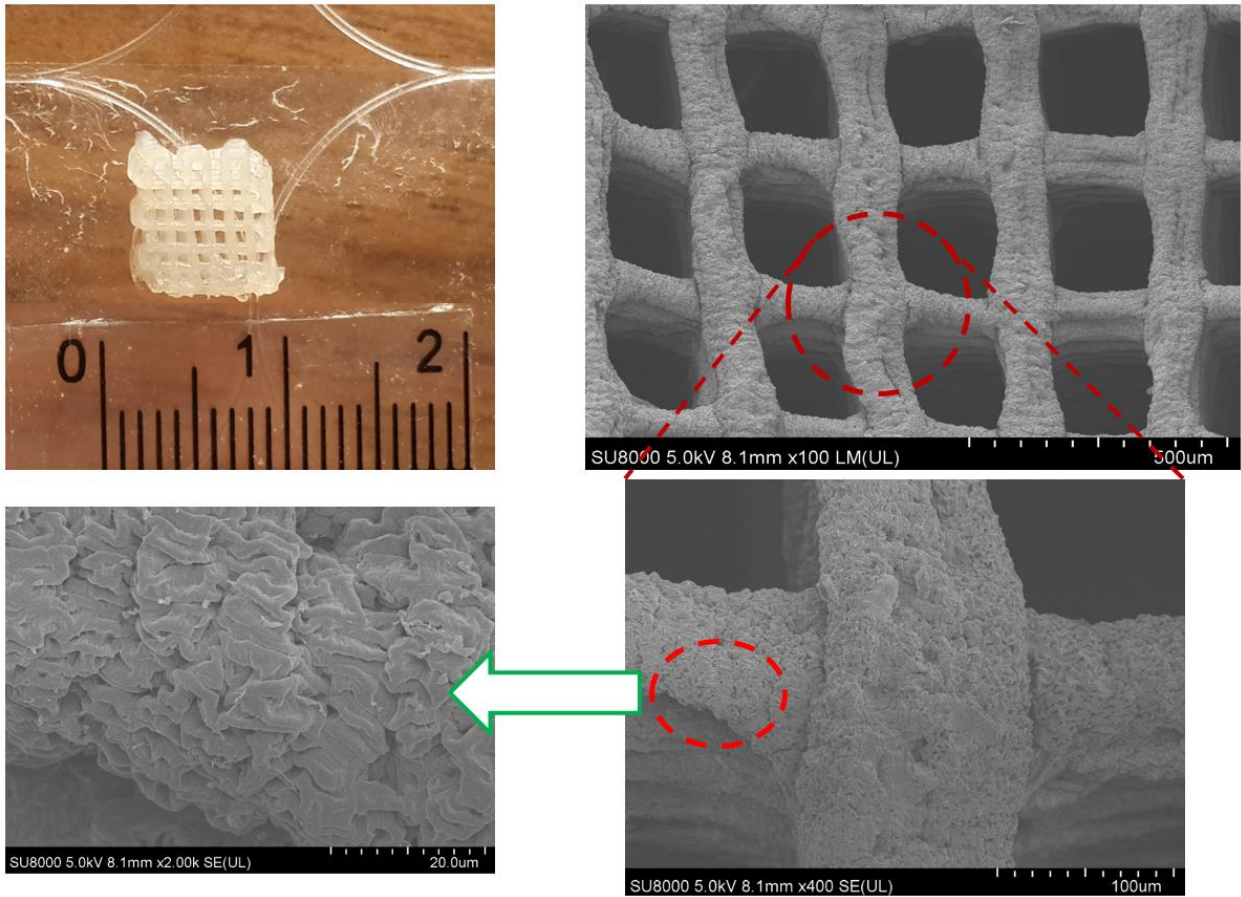


Figure 6.5. Morphology of bulk alginate gel (top left) and SEM images of an alginate scaffold immersed in 50 mM CaCl_2 for 24 h.

Inputs for the linear elastic model were as follows. The elastic modulus values determined for the 3D bioplotted bulk gels immersed in 3 mL or 1 mL of CaCl_2 and subjected to mechanical testing immediately after printing were 79.2 ± 3.04 kPa (linear section, $R^2=95.12\%$) and 42.3 ± 1.58 kPa (linear section, $R^2=92.57\%$), respectively. Figure 6.6 demonstrates the stress-strain curves of the scaffolds and bulk gels, the boundary conditions applied in the model, the meshed

part, and the collapsed scaffold after compression. The pore size ($P=0.652 \pm 0.04$ mm), number of strands (N_X and $N_Z=6$, $N_{YX}=7$, $N_{YZ}=8$), diameter of each strand ($D=0.516 \pm 0.06$ mm), amount of penetration among layers ($\Delta_0=0.392$ mm), and the value of deformation ($\Delta_L=0.01$ mm) were defined based on analyzing the images captured of the bioplotted scaffolds.

The model predicted an elastic modulus for scaffolds immersed in 3 mL of crosslinker and immediately subjected to compression testing of 38.59 kPa, which is in good agreement with values obtained experimentally (39.8 ± 6.36 kPa). Good agreement was also noted between the predicted elastic modulus of scaffolds immersed in 1 mL of crosslinker (20.58 kPa) and experimental results (21.65 ± 1.91 kPa).

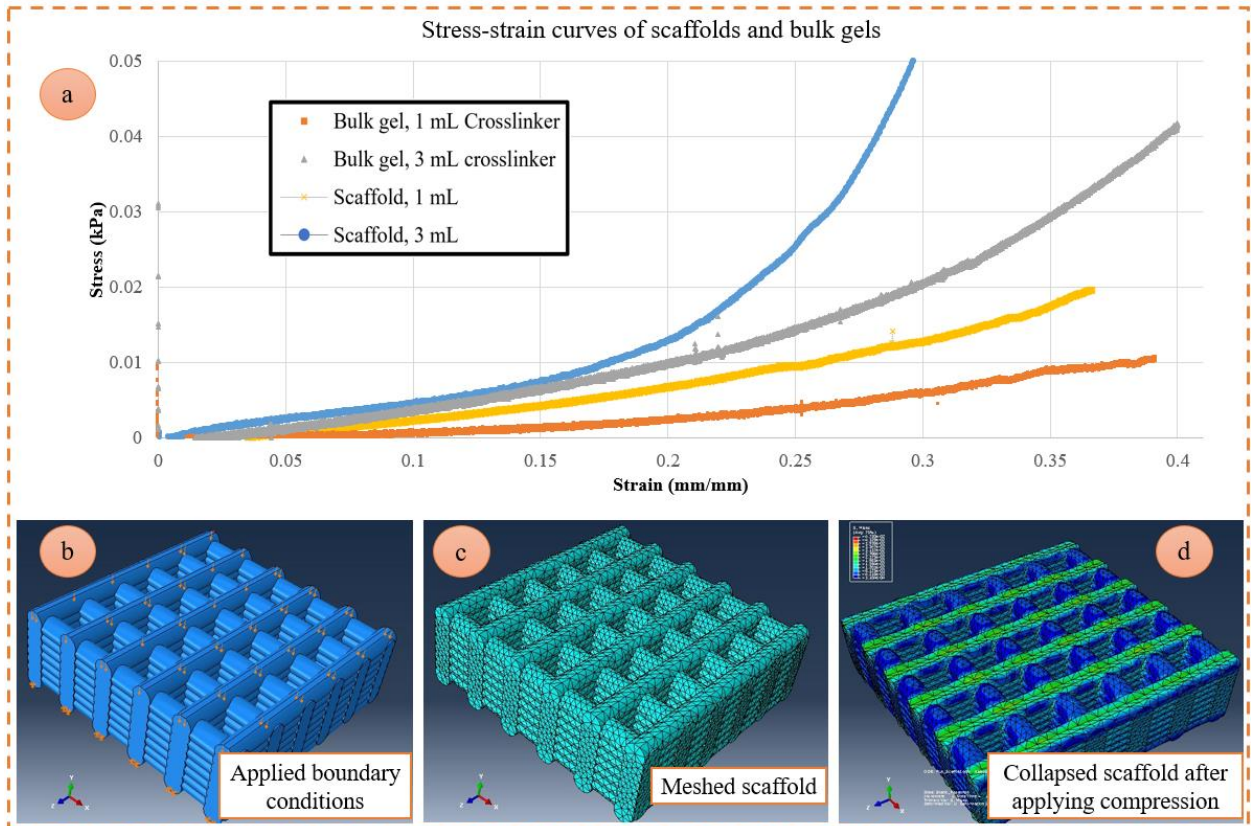


Figure 6.6. a) Stress-strain curves of alginate samples of scaffolds and bulk gels (compressed after 3D bioplotting), b) finite element model: I) applied boundary conditions, II) meshed part, and III) collapsed scaffold after compression.

This linear elastic model might, therefore, be useful for predicting the elastic modulus of cell-incorporated scaffolds based on the relationship between crosslinking time and cell viability [1]. Using the model developed, the volume of CaCl_2 crosslinker could be calculated in advance

to modulate the mechanical properties of scaffolds so that the elastic modulus is matched according to the mechanical properties of the target tissue. As mentioned, the finite element model proposed only predicts the low-strain region of the stress-strain curve (linear elastic region). In some tissue engineering applications, such as nerve and skin regeneration, the linear, low-strain region of the stress-strain curve was used to calculate the elastic modulus of samples and considered to represent physiological behavior in the human vasculature [27]. In a similar study, isotropic linear elastic behavior was reported and 10% strain used to calculate the elastic modulus of scaffolds fabricated as cardiac-mimetic structures; furthermore, 10 to 25% strain was reported as the cardiac-relevant strain range in physiological conditions [28]. Finally, a finite element study assigned linear elastic elements to a model to predict the mechanical properties of tissue-engineered cartilage constructs [29]. Hence, the direct determination of elastic modulus from the linear section of stress-strain curve is appropriate if the possible applications are taken into account. For example, cartilage undergoes loading and unloading with periodic stress relaxation. Therefore, the stress-strain curve is reproduced many times and determination of the elastic modulus from the linear section of a stress-strain curve of the material is appropriate. In the next, subsection, the non-linear behavior of bioplotting gels, as well as scaffolds, are investigated.

6.5.2 Non-linear numerical model to predict the non-linear behavior of 3D bioplotting scaffolds and bulk gels

The linear section of the stress-strain curve was predicted using the aforementioned linear elastic finite element model. Here, Equation 6.4 (empirical power model) was used to predict the non-linear behavior of scaffolds crosslinked for 24 h. The power model obtained for more than 50% strain was ($R^2=96\%$):

$$\sigma_E = 0.126 \epsilon_E^{0.9917} \quad (6.5)$$

The n value of close to 1 (here 0.9917) in Equation 6.5 indicates the alginate behaves in a near linear elastic fashion according to Hooke's law. However, this equation demonstrates the dependency of the elastic modulus of alginate gels on the strain (strain-rate dependent behavior). Table 6.2 indicates the power models obtained for other samples at different times (immediately, 2h, and 4h after printing) and volumes (1 mL and 3 mL) of crosslinker. The majority of models have R^2 values greater than 90%, which indicates good agreement with experimental values. All

also have n values larger than 1, which is evidence that they have completely non-linear behavior at higher values of strain. However, the proposed linear elastic finite element model (subsection 6.5.1) has utility for predicting the behavior of the scaffolds at lower values of strain, such as would be expected for the intended applications.

Table 6.2. Numerical models predicting the non-linear mechanical behavior of 3D bioplotting alginate gels and scaffolds.

Crosslinker volume Time	1 mL	3 mL
Gel: After printing	$\sigma_E = 0.0299\varepsilon_E^{1.4336}$ $R^2 = 91\%$	$\sigma_E = 0.1986\varepsilon_E^{1.8158}$ $R^2 = 97\%$
Gel: 2 hours	$\sigma_E = 0.0819\varepsilon_E^{1.1411}$ $R^2 = 86\%$	$\sigma_E = 1.0137\varepsilon_E^{2.3338}$ $R^2 = 90\%$
Gel: 4 hours	$\sigma_E = 0.3862\varepsilon_E^{1.7681}$ $R^2 = 98\%$	$\sigma_E = 0.1264\varepsilon_E^{1.3187}$ $R^2 = 96\%$
Scaffold: after printing	$\sigma_E = 0.0939\varepsilon_E^{1.6298}$ $R^2 = 99\%$	$\sigma_E = 0.1437\varepsilon_E^{1.3866}$ $R^2 = 92\%$

The power model $\sigma_E = 0.0939\varepsilon_E^{1.6298}$ ($R^2=99\%$) was obtained for alginate scaffolds fabricated by the 3D bioplotting technique, crosslinked in 1 mL of CaCl_2 , and subjected to mechanical testing immediately after printing (Table 6.2). The degree of concavity ($n=1.6298$) is greater than one and indicates non-linear behavior and an upward concavity, which is obvious from the stress-strain curve (Figure 6.6). Additionally, the rigidity constant for both the bulk gel and alginate scaffold is related to the alginate concentration, guluronic residue fraction, and viscosity. The alginate used in this study is composed of approximately 61% mannuronic acid and 39% guluronic acid (M/G ratio of 1.56), which under low strain behaves like an elastic material and returns to its initial shape after removing the applied force. The power model for the scaffolds crosslinked in 3 mL of CaCl_2 and subjected to compression testing immediately after printing was $\sigma_E = 0.1437\varepsilon_E^{1.3866}$ ($R^2=92\%$, Table 6.2).

Equation 6.6 was used to predict the stress at failure (σ_D , strength needed to break the material with a unitary surface), as reported by [23]:

$$\sigma_D = K \varepsilon_D^n \quad (6.6)$$

where σ_D and ε_D are the stress and strain at failure, respectively. Here, we considered 25% strain as the failure point for the scaffolds. Equation 6.6 predicted values of stress at failure of 9.8 kPa (1 mL CaCl₂) and 21.02 kPa (3 mL CaCl₂), which align well with experimental values of 9.77 kPa (1 mL CaCl₂) and 25.14 kPa (3 mL CaCl₂).

6.6 Conclusions

This study investigated the effect of crosslinking mechanism on the mechanical behavior of 3D bioprinted alginate scaffolds by varying the volume of 50 mM CaCl₂ crosslinker employed as well as the crosslinking time. Both immersion time and volume of crosslinker play a decisive role in modulating the elastic modulus of 3D bioprinted alginate scaffolds. These two previously unexplored factors can be used to modulate the mechanical properties of scaffolds to match those of the target tissue. Furthermore, numerical models (linear and non-linear) were developed to predict the elastic modulus of alginate scaffolds. The results from the models were in good agreement with experimental results and, as such, the models could be implemented to predict the mechanical properties of 3D bioprinted scaffolds.

6.7 References

- [1] N. Cao, X.B. Chen, D.J. Schreyer, Influence of Calcium Ions on Cell Survival and Proliferation in the Context of an Alginate Hydrogel, *ISRN Chem. Eng.* 2012 (2012) 1–9. doi:10.5402/2012/516461.
- [2] S. Naghieh, M. Sarker, M. Izadifar, X. Chen, Dispensing-based bioprinting of mechanically-functional hybrid scaffolds with vessel-like channels for tissue engineering applications – a brief review, *J. Mech. Behav. Biomed. Mater.* 78 (2018) 298–314. doi:10.1016/j.jmbbm.2017.11.037.
- [3] S. Naghieh, A. Reihany, A. Haghighat, E. Foroozmehr, M. Badrossamay, F. Forooghi, Fused deposition modeling and fabrication of a three-dimensional model in maxillofacial reconstruction, *Regen. Reconstr. Restor.* 1 (2016) 139–144. doi:http://dx.doi.org/10.22037/triple%20r.v1i3.12543.
- [4] S. Naghieh, M. Badrossamay, E. Foroozmehr, M. Kharaziha, Combination of PLA micro-fibers and PCL-gelatin nano-fibers for development of bone tissue engineering scaffolds, *Int. J. Swarm Intell.*

- Evol. Comput. 06 (2017) 1–4. doi:10.4172/2090-4908.1000150.
- [5] S. Naghieh, E. Foroozmehr, M. Badrossamay, M. Kharaziha, Combinational processing of 3D printing and electrospinning of hierarchical poly(lactic acid)/gelatin-forsterite scaffolds as a biocomposite: mechanical and biological assessment, *Mater. Des.* 133 (2017) 128–135. doi:10.1016/j.matdes.2017.07.051.
- [6] A. Rajaram, D. Schreyer, D. Chen, Bioplotting Alginate / Hyaluronic Acid Hydrogel Scaffolds with Structural Integrity and Preserved Schwann Cell Viability, *3D Print.* 1 (2014) 194–203. doi:10.1089/3dp.2014.0006.
- [7] F. You, B.F. Eames, X. Chen, Application of Extrusion-Based Hydrogel Bioprinting for Cartilage Tissue Engineering, *Int. J. Mol. Sci.* 18 (2017) 1597.
- [8] A. Rajaram, D.J. Schreyer, D.X.B. Chen, Use of the polycation polyethyleneimine to improve the physical properties of alginate–hyaluronic acid hydrogel during fabrication of tissue repair scaffolds, *J. Biomater. Sci. Polym. Ed.* 26 (2015) 433–445.
- [9] R. Tripathi, B. Mishra, Development and evaluation of sodium alginate–polyacrylamide graft–copolymer-based stomach targeted hydrogels of famotidine, *AAPS PharmSciTech.* 13 (2012) 1091–1102.
- [10] C.H. Yang, M.X. Wang, H. Haider, J.H. Yang, J.-Y. Sun, Y.M. Chen, J. Zhou, Z. Suo, Strengthening alginate/polyacrylamide hydrogels using various multivalent cations, *ACS Appl. Mater. Interfaces.* 5 (2013) 10418–10422.
- [11] M. Sarker, X.B. Chen, Modeling the Flow Behavior and Flow Rate of Medium Viscosity Alginate for Scaffold Fabrication With a Three-Dimensional Bioplotter, *J. Manuf. Sci. Eng. Trans. ASME.* 139 (2017). doi:10.1115/1.4036226.
- [12] Y. Zhang, J. Liu, L. Huang, Z. Wang, L. Wang, Design and performance of a sericin-alginate interpenetrating network hydrogel for cell and drug delivery, *Sci. Rep.* 5 (2015) 12374.
- [13] A.S. Hoffman, Hydrogels for biomedical applications, *Adv. Drug Deliv. Rev.* 64 (2012) 18–23.
- [14] S. Swioklo, P. Ding, A.W. Pacek, C.J. Connon, Process parameters for the high-scale production of alginate-encapsulated stem cells for storage and distribution throughout the cell therapy supply

- chain, *Process Biochem.* (2016).
- [15] F. You, X. Wu, N. Zhu, M. Lei, B.F. Eames, X. Chen, 3D Printing of porous cell-laden hydrogel constructs for potential applications in cartilage tissue engineering, *ACS Biomater. Sci. Eng.* 2 (2016) 1200–1210.
- [16] A.G. Tabriz, M.A. Hermida, N.R. Leslie, W. Shu, Three-dimensional bioprinting of complex cell laden alginate hydrogel structures, *Biofabrication.* 7 (2015) 045012. doi:10.1088/1758-5090/7/4/045012.
- [17] S. Naghieh, M.R.R. Karamooz Ravari, M. Badrossamay, E. Foroozmehr, M. Kadkhodaei, Numerical investigation of the mechanical properties of the additive manufactured bone scaffolds fabricated by FDM: the effect of layer penetration and post-heating, *J. Mech. Behav. Biomed. Mater.* 59 (2016) 241–250. doi:10.1016/j.jmbbm.2016.01.031.
- [18] P.F. Egan, *PLOS ONE* Computationally designed lattices with tuned properties for tissue engineering using 3D printing, *PLoS One.* 12 (2017) 1–20. doi:10.1371/journal.pone.0182902.
- [19] J. Wieding, A. Wolf, R. Bader, Numerical optimization of open-porous bone scaffold structures to match the elastic properties of human cortical bone, *J. Mech. Behav. Biomed. Mater.* 37 (2014) 56–68.
- [20] S. Naghieh, M.R.K. Ravari, M. Badrossamay, E. Foroozmehr, M. Kadkhodaei, Finite element analysis for predicting the mechanical properties of bone scaffolds fabricated by fused deposition modeling (FDM), in: *Modares Mech. Eng. Proc. Adv. Mach. Mach. Tools Conf.*, 2015: pp. 450–454.
- [21] V.B. Nguyen, C.X. Wang, C.R. Thomas, Z. Zhang, Mechanical properties of single alginate microspheres determined by microcompression and finite element modelling, *Chem. Eng. Sci.* 64 (2009) 821–829. doi:10.1016/j.ces.2008.10.050.
- [22] Y. Zhang, Y. Yu, H. Chen, I.T. Ozbolat, Characterization of printable cellular micro-fluidic channels for tissue engineering., *Biofabrication.* 5 (2013) 025004. doi:10.1088/1758-5082/5/2/025004.
- [23] M. Mancini, M. Moresi, R. Rancini, Mechanical properties of alginate gels: empirical characterisation, *J. Food Eng.* 39 (1999) 369–378.
- [24] L. Ning, Y. Xu, X. Chen, D.J. Schreyer, Influence of mechanical properties of alginate-based

- substrates on the performance of Schwann cells in culture, *J. Biomater. Sci. Polym. Ed.* 27 (2016) 898–915.
- [25] F. You, X. Wu, N. Zhu, M. Lei, B.F. Eames, X. Chen, 3D Printing of Porous Cell-Laden Hydrogel Constructs for Potential Applications in Cartilage Tissue Engineering, *ACS Biomater. Sci. Eng.* 2 (2016) 1200–1210. doi:10.1021/acsbiomaterials.6b00258.
- [26] A.D. Olubamiji, Z. Izadifar, J.L. Si, D.M.L. Cooper, B.F. Eames, D.X. Chen, Modulating mechanical behaviour of 3D-printed cartilage-mimetic PCL scaffolds: influence of molecular weight and pore geometry, *Biofabrication.* 8 (2016) 025020. doi:10.1088/1758-5090/8/2/025020.
- [27] S. Amensag, P.S. McFetridge, Tuning scaffold mechanics by laminating native extracellular matrix membranes and effects on early cellular remodeling, *J. Biomed. Mater. Res. Part A.* 102 (2014) 1325–1333.
- [28] R.A. Neal, A. Jean, H. Park, P.B. Wu, J. Hsiao, G.C. Engelmayr Jr, R. Langer, L.E. Freed, Three-dimensional elastomeric scaffolds designed with cardiac-mimetic structural and mechanical features, *Tissue Eng. Part A.* 19 (2012) 793–807.
- [29] B.G. Sengers, C.C. Van Donkelaar, C.W.J. Oomens, F.P.T. Baaijens, The local matrix distribution and the functional development of tissue engineered cartilage, a finite element study, *Ann. Biomed. Eng.* 32 (2004) 1718–1727.

Chapter 7 Conclusions and future recommendations

7.1 Conclusions

Extrusion-based bioprinting has been used for various types of tissue engineering applications. Using extrusion-based bioprinting, biomimetic structures, called scaffolds, are fabricated by considering mechanical and biological factors. Printability is a key issue in extrusion-based bioprinting, though. It is an index to measure the difference between the designed and fabricated scaffold in the printing process. As a result of printability, the mechanical behavior of the printed scaffolds is different from the designed one (original scaffold design). Hence, it is important to study printability and the factors affecting it significantly. The main elements affecting printability (bioink, design, and fabrication) were studied in this dissertation. In particular, the flow rate of bioink and printing parameters, such as needle geometry and printing pressure, were studied. Specifically, hydrogels are the main focus of this dissertation, and all the results obtained here can be extended to any type of hydrogel. Besides, the crosslinking mechanism was studied in terms of crosslinking time and concentration, as it has a significant influence on printability and, as a result, the mechanical behavior of scaffolds. Furthermore, low-concentration hydrogels were used widely in extrusion-based bioprinting due to their cell-friendly environment. However, the poor printability of low-concentration hydrogels prevents further studies on bioprinted scaffolds. Hence, in this dissertation, indirect bioprinting was presented to address this issue. Finally, yet importantly, a numerical model was developed and presented in this dissertation because it is always time-consuming and labor-intensive to investigate scaffolds mechanically. Therefore, numerical modeling is recommended to study the mechanical behavior of bioprinted scaffolds ahead of time and before fabrication to save time and resources. Moreover, printability elements, such as crosslinking agents, can be considered in such numerical models to develop precise models that can predict the mechanical characteristics of scaffolds accordingly. The obtained conclusions have been highlighted as follows:

- The swelling, as well as degradation, rate, and mechanical properties (elastic moduli) of hydrogels can be modulated based on the compositions of hydrogels. In this dissertation, alginate, gelatin, and MC were combined, and the results showed that composite hydrogels have better water absorption ability compared to pure

alginate hydrogel. Additionally, all groups of hydrogels showed a decreasing pattern of elastic modulus with time. In particular, alginate-MC hydrogels showed the highest elastic modulus. As per printability assessment, results showed that bioink-related elements (e.g. viscosity), fabrication-related ones (e.g. air pressure, nozzle speed, offset), and design-related factors (e.g. selected angular pattern) can affect printability. Hence, in this dissertation, the outlined factors were modulated to improve the printability of alginate, gelatin, and MC hydrogel scaffolds. To conclude, scaffolds with modulated mechanical properties (e.g. swelling, degradation, and elastic modulus) can be fabricated to have a customized structure as per the respected tissue requirements.

- An indirect-bioprinting process was developed to fabricate low-concentration alginate scaffolds using a sacrificial gelatin framework. Indirectly-fabricated scaffolds were successfully printed while maintaining high cell viability. The directly and indirectly printed scaffolds have their advantages and disadvantages that were discussed in this dissertation.
- Sterilization can affect the mechanical behavior of hydrogel scaffolds. Alginate scaffolds sterilized using ethanol had higher elastic modulus than the ones sterilized by UV. Results showed that precursor alginate scaffolds (0.5-3%) could be fabricated by the indirect-bioprinting process.
- Although 0.5% alginate scaffolds can provide a cell-friendly environment (compared with the control group, which is the culture dish), they had a dramatic degradation rate than 1.5 or 3.0% alginate scaffolds. Hence, the developed indirect-bioprinting process can be used to successfully address the poor printability of low-concentration alginate. However, not all low-concentration scaffolds can be implemented due to poor mechanical properties. So, depending on the application, low to high concentration scaffolds can be fabricated as a trade-off between having a scaffold with a cell-friendly environment (low-concentration hydrogel) and a scaffold with more mechanical stability (high concentration hydrogel). Results also showed that both the mechanical and biological properties of fabricated scaffolds

could be affected by the concentration of hydrogel as well as the sterilization technique used.

- Numerical models are an asset to fabricate scaffolds with appropriate mechanical properties. These models can be used in advance and before fabrication to evaluate scaffolds to make sure that they satisfy the required mechanical properties. In this dissertation, a novel finite element model was developed considering the penetration of strands in one layer into the previous layer. Results showed the significant effect of the penetration within layers on the elastic modulus of printed scaffolds. After verification, the model was used to predict the elastic modulus of scaffolds with a different number of layers and pore sizes. Results indicated that scaffolds with smaller pore sizes and a higher number of layers had higher elastic modulus. The developed model can be used for other hydrogels to achieve the desired mechanical properties in tissue engineering.
- In this dissertation, the effect of crosslinker was taken into account by developing a numerical model that can take the effect of the crosslinking mechanism in terms of elastic modulus as an input. For this, the elastic modulus of bulk alginate scaffolds crosslinked with different volumes of crosslinker and crosslinking time was added as an input to predict the mechanical behavior of porous scaffolds. Results showed that the developed model is in good agreement with experimental results. It was concluded that scaffolds, crosslinked in a higher volume of the crosslinker with more crosslinking time, have higher elastic modulus.

7.2 Recommendations for future research

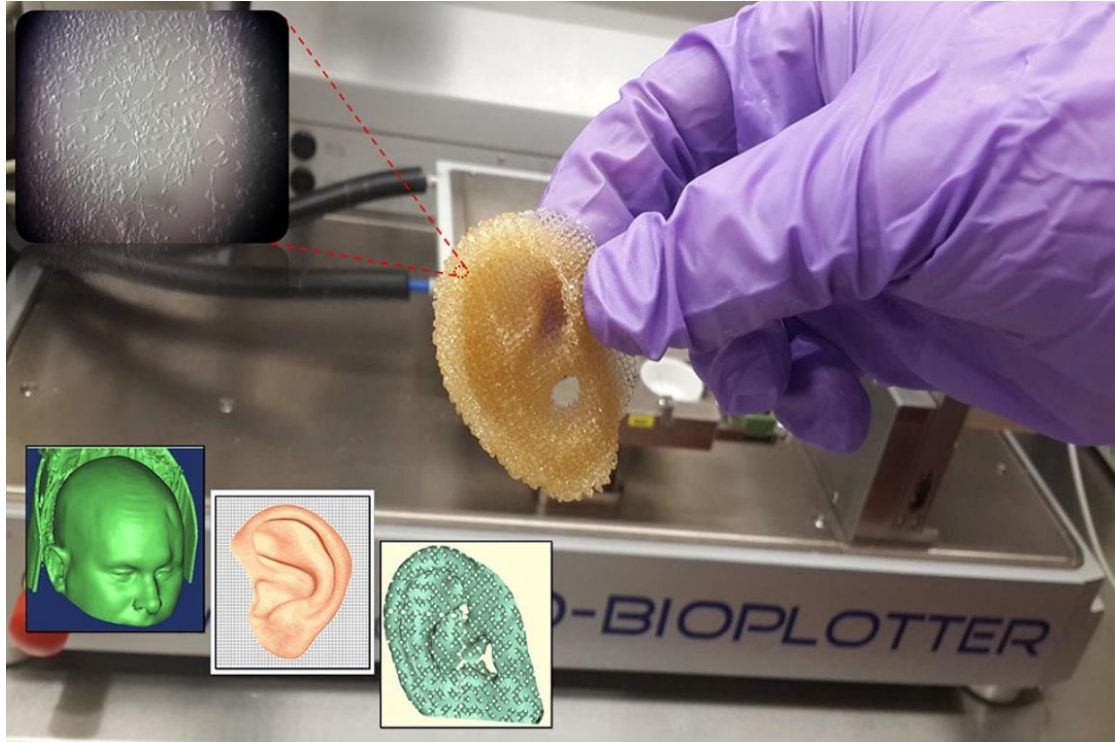
In this dissertation, fabrication-, design, and bioink-related elements were investigated to map the relationship between them and printability. In addition, numerical models were developed to consider the penetration amongst bioprinted layers and the crosslinking mechanism. Close investigations on the following issues might be considered as recommendations for future research, including:

- In this dissertation, only one type of crosslinker (CaCl_2) was used to crosslink the bioprinted scaffolds. However, different types of crosslinking agents might be used

to bioprint hydrogels into them (various concentrations). This approach might be a potential pathway to achieve scaffolds with enhanced mechanical and/or biological performance. Hence, further investigation into different types of crosslinkers at various concentrations is recommended.

- In this dissertation, measurement tools to evaluate printability were discussed. However, other guidelines should be specified in the future to assess scaffold design, material selection, and printing parameters from a manufacturability point of view (e.g. using a benchmark).
- All the mechanical experiments were conducted under a static condition. However, in some cases, the dynamic behavior of scaffolds should be investigated. In the future, it might be a potential study to evaluate the mechanical properties of 3D bioprinted scaffolds in a dynamic condition (physiologic buffer can be circulated during the test performance). Additionally, for modeling purposes, fluid flow can be considered in the model to study the effect of shear stress on cell damage. Degradation of scaffolds is another area yet to be explored, and it can be modeled using numerical approaches in the future.
- In this dissertation, only one type of cell, called Schwann cells, was used to evaluate the biological performance of indirectly printed scaffolds made of low-concentration alginate. It is recommended to study the behavior of other cell sources to gain more insight into the biological performance of such an indirectly-printed structure.
- In the future, cell studies carried out in this dissertation can be extended to animal studies to evaluate the fabricated scaffolds *in vivo*.

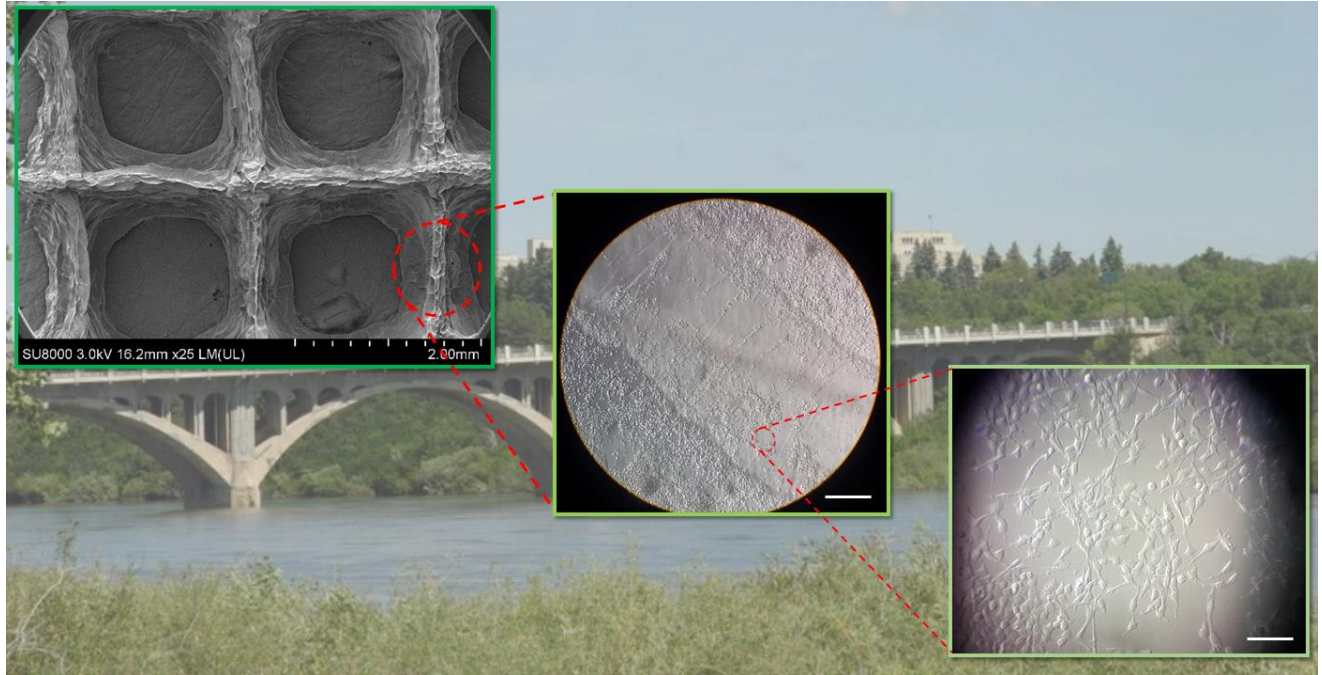
Appendix A: Images of Research Competition 2018



Let's Create an Artificial Organ with Cells! *Research in action, runner up*

You have probably heard about the global organ shortage due to limited donors. Creating organs artificially through 3D bioprinting is a promising way to help people who are waiting for life-saving surgeries. The picture is showing the 3D ear fabricated using a 3D bioprinter. The inset images show the patient's medical imaging data, creating the model of the ear from the patient's imaging data, designing the porous ear, and the microscopic image of the incorporated cells inside the ear. The idea behind 3D printing is like a normal inkjet printer. My research focuses on the development of customized scaffolds, like the ear in this picture as a temporary construct, including a mixture of patient's cells and biomaterials. Hopefully, this magical technique will help millions of people around the world waiting for tissues and organs (With help from Adam McInnes).

Appendix B: Images of Research Competition 2019



Building a bridge in the world of neural cells!

Building a bridge is a common approach in civil engineering to connect two sides. What if we want to do the same thing inside the body? Bridging two sides of a damaged nerve? That sounds weird, but it is much easier than you think. Peripheral nervous system (PNS) injuries cause various types of disabilities. When a damaged nerve is more than 2 mm long, the body cannot heal. If this is the case, the body needs a temporary structure—known as a scaffold—to help the damaged tissue recover itself. The picture shows the 3D scaffold fabricated using a 3D bioprinter to treat a damaged peripheral nerve. This scaffold is made of alginate, a natural polymer, and neural cells to bridge the gap between the two sides of a damaged nerve. My research focuses on developing scaffolds to build a bridge for nerve regeneration (with help from MD Sarker).